"If anybody says he can think about quantum problems
without getting giddy, that only shows he has not understood
the first thing about them."

Max Planck

"Very strange people, physicists - in my experience the
ones who aren't dead are in some way very ill."

Mr. Standish
"The Long Dark Tea-Time Of The Soul" by Douglas Adams

University of Alberta

NEUTRAL SCALAR HIGGS SEARCHES USING VECTOR BOSON FUSION AT ATLAS

by

Jeffrey Kelvin de Jong ©

A thesis submitted to the Faculty of Graduate Studies and Research in partial fulfillment of the requirements for the degree of **Doctor of Philosophy.**

Department of Physics

Edmonton, Alberta
Spring 2006

Library and
Archives Canada

Bibliothèque et
Archives Canada

Published Heritage
Branch

Direction du
Patrimoine de l'édition

395 Wellington Street
Ottawa ON K1A 0N4
Canada

395, rue Wellington
Ottawa ON K1A 0N4
Canada

NOTICE:
The author has granted a non-exclusive license allowing Library and Archives Canada to reproduce, publish, archive, preserve, conserve, communicate to the public by telecommunication or on the Internet, loan, distribute and sell theses worldwide, for commercial or non-commercial purposes, in microform, paper, electronic and/or any other formats.

The author retains copyright ownership and moral rights in this thesis. Neither the thesis nor substantial extracts from it may be printed or otherwise reproduced without the author's permission.

AVIS:
L'auteur a accordé une licence non exclusive permettant à la Bibliothèque et Archives Canada de reproduire, publier, archiver, sauvegarder, conserver, transmettre au public par télécommunication ou par l'Internet, prêter, distribuer et vendre des thèses partout dans le monde, à des fins commerciales ou autres, sur support microforme, papier, électronique et/ou autres formats.

L'auteur conserve la propriété du droit d'auteur et des droits moraux qui protège cette thèse. Ni la thèse ni des extraits substantiels de celle-ci ne doivent être imprimés ou autrement reproduits sans son autorisation.

In compliance with the Canadian Privacy Act some supporting forms may have been removed from this thesis.

While these forms may be included in the document page count, their removal does not represent any loss of content from the thesis.

Conformément à la loi canadienne sur la protection de la vie privée, quelques formulaires secondaires ont été enlevés de cette thèse.

Bien que ces formulaires aient inclus dans la pagination, il n'y aura aucun contenu manquant.

Canada

Abstract

The Higgs boson is the last undiscovered particle predicted by the Standard Model. Its discovery is key to our understanding of the electroweak symmetry breaking process and the origin of mass. The primary purpose of the ATLAS detector at the Large Hadron Collider is the discovery of this particle. This thesis evaluates the discovery potential of the ATLAS experiment for a Heavy Neutral Scalar Higgs boson, $M_H \geq 170$ GeV/c^2, produced through vector boson fusion and decaying through the four physics channels : H$\rightarrow$ZZ$\rightarrow l^+l^-$+jj and H$\rightarrow$WW$\rightarrow l\nu_l$+jj where l = e,μ.

The analysis has been performed using the PYTHIA 6.227 Monte-Carlo generator and the ATLAS fast simulation package ATLFAST. This fast simulation package has been modified such that the results are in agreement with the full simulation program DICE/ATRECON. The ATLFAST package has also been modified to include electronic noise and low and high luminosity pileup.

This thesis demonstrates that even when the large systematic uncertainties are addressed a neutral scalar Higgs boson can be discovered after 3 years of running at low luminosity (collecting 30 fb^{-1}at L=1×10^{33} cm^{-2}s^{-1}) if its mass were between 170 GeV/c^2 < M_H < 190 GeV/c^2 or above 280 GeV/c^2. The Higgs boson can also be discovered after running for 1 year at high luminosity (collecting 100 fb^{-1}at L=1×10^{34} cm^{-2}s^{-1}) if its mass were between 170 GeV/c^2 < M_H < 180 GeV/c^2 or above 290 GeV/c^2.

Acknowledgements

They say that it takes a village to raise a child. In a similar manner I would not be submitting this thesis if it were not for the vast multitude who have helped me along the way.

I would first like to thank my supervisor, Dr. James L. Pinfold. He was a never ending source of different approaches and new ideas that I hope will make this thesis stand out.

I would also like to thank Bryan Caron for his dedication to the CSR computing network and answering an endless barrage of "basic" computing questions.

To all my fellow graduate students as well as the academic and non-academic staff at the CSR who have made my years at the University of Alberta very enjoyable.

To my parents. From a young age you taught me that with hard work and much prayer I could accomplish anything. I hope that I've made you proud.

And lastly, to my wife Heather. You were there to celebrate with me in my moments of triumph and comfort me when nothing in this thesis seemed to be going right. You patiently waited. You never complained when the completion time-line kept getting pushed back, or when I had to stay late in the office or couldn't come to bed because I found a groove. I love you.

Contents

List of Figures

List of Tables

Chapter 1

Introduction

Particle Physics is the study of elementary particles and their interactions. For almost 40 years particle physicists have used the Standard Model to understand the behaviour of such interactions. In the past 10 years Fermilab has discovered 2 of the 3 remaining particles predicted by the Standard Model: the top quark in 1995 [1] in the CDF and D0 collaborations, and most recently (2001) the tau neutrino [2] in DONUT. Despite such success Fermilab does not possess sufficient centre of mass energy, nor does it possess the luminosity to record enough data to discover the Standard Model's most elusive particle, the Higgs boson.

The Large Hadron Collider (LHC) is due to come on-line in 2007, it is 7 times more energetic than the Tevatron at Fermilab, with a centre of mass energy of 14 TeV. The LHC and the ATLAS detector have been designed with the express purpose of being able to search for and discover the Higgs Boson.

The theory pertaining to the Standard Model, as well as theories detailing particle interaction with matter, are both quite well understood. Therefore, it is possible to utilize Monte-Carlo methods to simulate Higgs production and decay, along with the interactions that will occur in the ATLAS detector. Such simulations will allow physicists to determine what will be seen in the ATLAS detector once the LHC is turned on.

1.1 The Standard Model

Elementary particles can be grouped into two different categories: spin 1/2 fermions, and integer spin bosons. Fermions can be further broken down into two *families*: quarks, which carry colour charge and interact via the strong and electroweak forces, and leptons, which only interact through electroweak forces. Fermions are typically grouped in three genera-

tions, in which each successive generation increases in mass.

$$
\begin{array}{cccc}
 & \text{Generation} & & \\
1^{st} & 2^{nd} & 3^{rd} & \text{Charge}(e) \\
\begin{pmatrix} u \\ d \end{pmatrix} & \begin{pmatrix} c \\ s \end{pmatrix} & \begin{pmatrix} t \\ b \end{pmatrix} & \begin{array}{c} +\frac{2}{3} \\ -\frac{1}{3} \end{array} \\
\begin{pmatrix} \nu_e \\ e^- \end{pmatrix} & \begin{pmatrix} \nu_\mu \\ \mu^- \end{pmatrix} & \begin{pmatrix} \nu_\tau \\ \tau^- \end{pmatrix} & \begin{array}{c} 0 \\ -1 \end{array}
\end{array}
$$

$$\overrightarrow{\text{Increasing Mass}}$$

Matter in the visible universe is predominantly composed of only 3 particles from the first generation: the (u)p and (d)own quarks, and the electron(e^-). Heavier, unstable particles, like the Higgs boson, are only produced in high energy collisions such as those which will take place at the LHC. The mass [1] hierarchy of the fundamental fermions is listed in table 1.1 [3].

Quarks		Leptons	
Particle	Mass	Particle	Mass
d	1.5-4 MeV/c^2	e	0.511 MeV/c^2
u	4-8 MeV/c^2	ν_e	$\leq$3 eV/c^2
s	80-130 MeV/c^2	μ	105.66 MeV/c^2
c	1.15-1.35 GeV/c^2	ν_μ	$\leq$0.19 MeV/c^2
b	4.1-4.4 GeV/c^2	τ	1777.0$\pm$0.3 MeV/c^2
t	174.3$\pm$5.1 GeV/c^2	ν_τ	$\leq$18.2 MeV/c^2

Table 1.1: The fermions in the Standard Model.

The integral spin bosons, table 1.2, are the particles which mediate the four fundamental forces : electromagnetism, strong and weak forces, and gravitation. The massless photon is

Force	Mediator	Mass (GeV)	Spin	Mediates Between
Strong	8 gluons	0	1	Coloured Particles
Weak	W$^\pm$	80.425$\pm$0.038	1	Quarks,Leptons,EW bosons
	Z^0	91.1876$\pm$0.0021	1	
Electromagnetic	photon(γ)	0	1	Charged Particles

Table 1.2: The force carriers of the Standard Model

the force carrier for electromagnetism and acts on all particles which carry electric charge. The weak force, which acts on all particles that possess weak hyper-charge, is mediated by the massive W$^\pm$ and Z^0 bosons and is responsible for processes such as nuclear β-decay. The strong force is mediated by an octet of massless gluons and acts only on other coloured particles. It is responsible for the confinement of quarks inside colourless mesons and baryons.

---

[1]Unit conversion between the particle standard and metric is $GeV/c^2 = 1.78 \times 10^{-27}$ kg. In natural units we set $\hbar$=c=1. As such the mass term is often given in units of GeV.

2

The first unification of fundamental forces occurred over one hundred years ago, in 1865, James Maxwell unified the electric force and the magnetic force with the now famous Maxwell's Equations. The quantum formulation of electrodynamics (QED) was developed in the 1940s with the photon as the propagator of the $U(1)_{EM}$ symmetry group. Electromagnetism was unified with the weak force as the electro-weak force by Glashow-Weinberg-Salam [4][5] in the late 1960s. The underlying group structure of the electro-weak theory is $SU(2)_L \times U(1)_Y$ where L refers to the handedness of the weak interaction and Y is the weak hypercharge Quantum-chromodynamics(QCD), which transforms under the $SU(3)_C$ symmetry group and explains the strong force, was introduced to the Standard Model in the 1970s[6].

While the Standard Model works very well, there are several indications that it must be interpreted only as an effective theory. It does not yet incorporate gravity, it has no solution to the gauge hierarchy problem. Also, the Standard Model provides no fundamental explanation as to why there are only three generations of fermions or why the model contains exactly 19 free parameters. These 19 free parameters are summarized in table 1.3. Lack of completeness and the large number of free parameters indicate to physicists that the Standard Model is only an approximation of a more fundamental underlying theory.

Description	Free Parameters
Quark Masses	m_u, m_c, m_b
	m_d, m_s, m_t
Lepton Masses	m_e, m_μ, m_τ
CKM mixing Matrix	θ_{12}, θ_{23}, θ_{13}, δ
Gauge coupling constants	g_e, g_w, g_s
Higgs Parameters	m_H, m_W
Strong CP	θ_{CP}

Table 1.3: There are 19 free parameters in the Standard Model.

Further, in the construction of the Standard Model Lagrangian, the gauge boson mass terms violate gauge invariance and the mass terms for fermions violate the symmetry of the $SU(2)_L \times U(1)_Y$ group. These issues would lead to a theory containing only massless particles but experiments have shown that the only massless particle in the Standard Model is the photon[2] and the gluon.

In 1964, Peter Higgs postulated a mechanism [9] that breaks the symmetry of the vacuum and generates masses for 3 of the 4 electroweak bosons, along with masses for the fermions. This mechanism also predicts the existence of a neutral scalar particle known as the Higgs

---

[2]Neutrino oscillation experiments have proven that even the neutrino has mass[7], and as such add additional free parameters to table 1.3. [8] nicely summarizes the bounds on the upper mass of the photon.

3

boson. The search for this particle and the understanding of the Higgs mechanism is one of the primary goals of the LHC and the ATLAS detector.

1.2 Gauge Invariance

1.2.1 Abelian Gauge

Consider the Lagrangian of a free Dirac particle :

$$\mathcal{L} = \bar{\psi}\gamma^\mu \partial_\mu \psi - m\bar{\psi}\psi \tag{1.1}$$

The Lagrangian is invariant under the global U(1) gauge transformation, $\psi \rightarrow \psi e^{i\alpha}$. Performing a local gauge transformation:

$$\psi \rightarrow \psi e^{iQ\alpha(x)}$$

the second term in equation 1.1 is manifestly invariant. To maintain the invariance of the first term we must define a "covariant derivative":

$$\mathcal{D}_\mu = \partial_\mu + iQA_\mu$$

which introduces a vector field A_μ that transforms as:

$$A_\mu \rightarrow A_\mu - \partial_\mu \alpha(x)$$

Recognizing this new field as the photon and assigning the coupling strength Q=-e, we can substitute these equations back into 1.1 and, including the kinetic energy term for the photon, the Lagrangian becomes:

$$\mathcal{L} = \bar{\psi}(i\gamma^\mu \partial_\mu - m)\psi + e\bar{\psi}\gamma^\mu A_\mu \psi - \frac{1}{4}F_{\mu\nu}F^{\mu\nu} \tag{1.2}$$

where the electromagnetic field strength tensor is defined as:

$$F_{\mu\nu} = \frac{1}{iQ}[\mathcal{D}_\nu, \mathcal{D}_\mu] = \partial_\nu A_\mu - \partial_\mu A_\nu + iQ[A_\nu, A_\mu] \tag{1.3}$$

The commutator in the last term vanishes in this Abelian theory.

We are left with a Lagrangian that describes a fermionic field interacting with a vector field. In this Lagrangian local gauge invariance prohibits the addition of a mass term for the gauge field as the mass term is not invariant under the transformation:

$$\frac{1}{2}m^2 A_\mu A^\mu \rightarrow \frac{1}{2}m^2(A_\mu - \partial_\mu \alpha)(A^\mu - \partial^\mu \alpha) \neq \frac{1}{2}m^2 A_\mu A^\mu \tag{1.4}$$

4

1.2.2 Non-Abelian Gauge Invariance

The Yang-Mills Lagrangian for two non-interacting spin-1/2 Dirac particles can be written as:

$$\mathcal{L} = \overline{\psi_1}(i\gamma^\mu\partial_\mu - m_1)\psi_1 + \overline{\psi_2}(i\gamma^\mu\partial_\mu - m_2)\psi_2 \tag{1.5}$$

Making the following definitions:

$$\Psi = \begin{pmatrix} \psi_1 \\ \psi_2 \end{pmatrix} \quad M = \begin{pmatrix} m_1 & 0 \\ 0 & m_2 \end{pmatrix} \tag{1.6}$$

equation 1.5 reduces to

$$\mathcal{L} = \overline{\Psi}(i\gamma^\mu\partial_\mu - M)\Psi \tag{1.7}$$

Equation 1.7 is invariant under the global SU(2) transformation $\Psi = e^{ig\vec{\tau}\cdot\vec{\alpha}}\Psi$, where g is the coupling strength, $\vec{\tau}$ are the three Pauli matrices (the generators of SU(2)), and $\vec{\alpha}$ is a three vector. Local gauge invariance requires that 1.7 is invariant under the transformation:

$$\Psi = e^{\frac{ig}{2}\tau\cdot\alpha(x)}\Psi \tag{1.8}$$

So as in the Abelian case we introduce the covariant derivative,

$$\mathcal{D}_\mu = \partial_\mu + igB_\mu \tag{1.9}$$

which has 3 independent vector fields $B_\mu = \frac{1}{2}\vec{\tau}\cdot\vec{b_\mu}$ and these vector fields can be shown [10], to transform as

$$\vec{b_\mu'} = \vec{b_\mu} - \alpha(\vec{x}) \times \vec{b_\mu} - \frac{1}{g}\partial_\mu\alpha(\vec{x}) \tag{1.10}$$

The field strength tensor for SU(2) is comparable to that in U(1) but with a non-zero commutator we have :

$$F_{\mu\nu} = \frac{\vec{\tau}}{2} \cdot \underbrace{((\partial_\nu\vec{b_\mu} - \partial_\mu\vec{b_\nu}) - g(\vec{b_\nu} \times \vec{b_\mu}))}_{\vec{f_{\mu\nu}}} \tag{1.11}$$

The gauge invariant SU(2) Lagrangian, including the 3 kinetic terms for the 3 vector particles, is then :

$$\mathcal{L} = \overline{\Psi}i\gamma^\mu\partial_\mu\Psi - g\overline{\Psi}\gamma^\mu B_\mu\Psi - \overline{\Psi}M\Psi - \frac{1}{4}\vec{f_{\mu\nu}} \cdot \vec{f^{\mu\nu}} \tag{1.12}$$

As in equation 1.2 a gauge field mass term of the form $\frac{1}{2}M^2\vec{b_\mu} \cdot \vec{b^\mu}$ would break the gauge invariance of this Lagrangian.

It would seem that we would have a workable theory by combining equations 1.2 and 1.12 to form a SU(2)xU(1) group, and somehow generate masses for the gauge bosons and fermions. The following sections outline how masses for the bosons and fermions in a gauge theory can be generated through the process of spontaneous symmetry breaking.

5
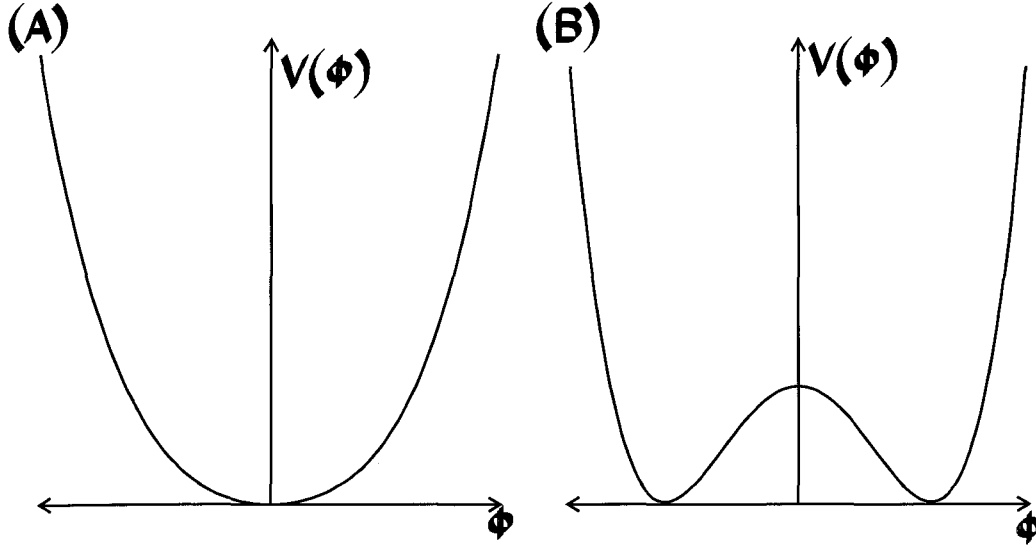
Figure 1.1: Graphical representation of the Higgs Mexican hat potential: (a) $\mu^2 > 0$ and (b)$\mu^2 < 0$.

1.3 Symmetry Breaking

1.3.1 Goldstone's Theorem

The symmetry of a Lagrangian is said to be broken when the symmetry inherent in the Lagrangian is not shared by the vacuum. To illustrate this principle consider the following Lagrangian for a complex scalar field $\phi = \frac{1}{\sqrt{2}}(\phi_1 + i\phi_2)$:

$$
\begin{aligned}
\mathcal{L} &= T - V(\phi) \\
&= (\partial_\mu \phi)^* \partial^\mu \phi - (\mu^2 \phi^* \phi + \lambda(\phi^* \phi)^2)
\end{aligned}
\tag{1.13}
$$

The potential $V(\phi)$, represented graphically in figure 1.1 and defined in equation 1.13, is that of the Higgs field. It is required that $\lambda > 0$ so that the potential be bounded. The minimum, or ground state, of this potential corresponds to the vacuum. If the value μ^2 is positive the minimum of the potential occurs at $\phi^* \phi = 0$. If instead μ^2 is negative then a non-trivial degenerate vacuum is obtained at a radius :

$$
\sqrt{(\phi^* \phi)} = \sqrt{(\frac{-\mu^2}{2\lambda})} e^{i\theta}, 0 \le \theta \le 2\pi
\tag{1.14}
$$

Since the Lagrangian in equation 1.13 is invariant under the global U(1) transformation we can arbitrarily choose the minimum with $\theta = 0$ such that :

$$
\phi_1 = \sqrt{\frac{-\mu^2}{2\lambda}} = \frac{v}{\sqrt{2}}
\tag{1.15}
$$

Rewriting the original fields by expanding around the vacuum in terms of two real fields η and ρ :

$$
\phi = \frac{1}{\sqrt{2}}(v + \eta(x) + i\rho(x))
\tag{1.16}
$$

6

Substituting equation 1.16 back into the original Lagrangian to obtain:

$$\mathcal{L}_0 = \begin{aligned}&\tfrac{1}{2}(\partial_\mu\rho\partial^\mu\rho) + (\tfrac{1}{2}(\partial_\mu\eta\partial^\mu\eta) + \mu^2\eta^2)\\ &-\tfrac{1}{4}\lambda(\eta^4 + 2\eta^2\rho^2 + \rho^4) - \lambda v(\eta\rho^2 + \eta^3)\\ &-\tfrac{1}{4}\mu^2 v^2\end{aligned} \tag{1.17}$$

Recalling that $\mu^2 < 0$ this Lagrangian represents a field theory involving a massive scalar field η with a mass $m^2 = 2|\mu|^2$, and a massless field ρ. This massless spin-0 field is known as the Goldstone boson, and is a direct result of the spontaneous breaking of a continuous global symmetry. By expanding this theory to include local gauge symmetry masses can be generated for the gauge bosons.

To make equation 1.13 invariant under local SU(1) gauge transformations, $\phi' = e^{iQ\alpha(x)}\phi$, it is necessary to include the gauge covariant derivative $\mathcal{D}$ which was defined in equation 1.9. The Lagrangian for a massless vector-field A_μ and a massive complex scalar field (ϕ) is :

$$\mathcal{L} = (\mathcal{D}_\mu\phi)^*\mathcal{D}^\mu\phi - V(\phi) - \frac{1}{4}F_{\mu\nu}F^{\mu\nu} \tag{1.18}$$

Expanding about the vacuum as in equation 1.16 :

$$\mathcal{L} = \begin{aligned}&\mathcal{L}_0 - \tfrac{1}{4}F_{\mu\nu}F^{\mu\nu} + \tfrac{1}{2}Q^2 v^2 A_\mu A^\mu\\ &+\tfrac{1}{2}Q^2 A_\mu A^\mu(\eta^2 + \rho^2) + Q^2 A_\mu A^\mu(\eta v)\\ &+Qv A_\mu\partial^\mu\rho + Q(\eta\partial_\mu\rho - \rho\partial_\mu\eta)A^\mu\end{aligned} \tag{1.19}$$

This equation represents a massive scalar field η, a massless Goldstone boson ρ, and now a massive vector field A_μ with a mass $M_A = Qv$. Equation 1.19 includes interaction terms of the form $A_\mu\partial^\mu\rho$. These problematic terms can be gauged away with the transformations :

$$\begin{aligned}A'_\mu &= A_\mu + \tfrac{1}{Qv}\partial_\mu\rho\\ \phi' &= e^{-\frac{i\rho(x)}{v}}\phi(x) = (v + \eta(x))\end{aligned} \tag{1.20}$$

giving:

$$\mathcal{L} = \begin{aligned}&(\tfrac{1}{2}\partial_\mu\eta\partial^\mu\eta + \mu^2\eta^2)\\ &+\tfrac{1}{2}Q^2 v^2 A_\mu A^\mu - \tfrac{1}{4}F_{\mu\nu}F^{\mu\nu}\\ &+\eta v Q^2 A_\mu A^\mu + \tfrac{1}{2}Q^2\eta^2 A_\mu A^\mu\\ &-\tfrac{1}{4}(\mu^2 v^2 + \lambda\eta^4 + 4\lambda\eta^3 v)\end{aligned} \tag{1.21}$$

This final Lagrangian includes a massive scalar "Higgs" particle(η) and a massive vector field A_μ.

1.4 Higgs Mechanism and the Standard Model

It was discovered in the mid 1950s [11] that the weak interaction maximally violated parity in that all neutrinos are left handed and all anti-neutrinos are right handed. The particle grouping in section 1.1 can be modified to express the nature of the weak interaction. For the sake of simplicity we will just focus on the first family:

$$\left[\begin{pmatrix} u \\ d \end{pmatrix}_L \quad d_R, u_R \right] \quad \left[\begin{pmatrix} \nu_e \\ e \end{pmatrix}_L \quad e_R \right] \tag{1.22}$$

7

We construct the Standard Model Lagrangian out of a $SU(2)_L \times U(1)_Y$ theory where L is the left-handed nature of SU(2) and Y is the weak hypercharge of U(1) defined by the Gell-Mann-Nishijima formula:

$$Q = T_3 + \frac{Y}{2} \qquad (1.23)$$

Q is the electric charge, and T_3 is the third component of weak isospin. Table 1.4 summarizes these values for the first family of leptons.

Lepton	T_3	Q	Y	Quark	T_3	Q	Y
ν_e	$\frac{1}{2}$	0	-1	u_L	$\frac{1}{2}$	$\frac{2}{3}$	$\frac{1}{3}$
e_L	$-\frac{1}{2}$	-1	-1	d_L	$-\frac{1}{2}$	$-\frac{1}{3}$	$\frac{1}{3}$
e_R	0	-1	-2	u_R	0	$\frac{2}{3}$	$\frac{4}{3}$
				d_R	0	$-\frac{1}{3}$	$-\frac{2}{3}$

Table 1.4: The Gell-Man-Nishijima relationships for the first family of leptons.

The Lagrangian for the leptons in the first family can be written:

$$\mathcal{L}_0 = \overline{R}i\gamma^\mu \underbrace{(\partial_\mu + ig_a\frac{Y_R}{2}a_\mu)}_{U(1)_Y \, derivative} R + \overline{L}i\gamma^\mu \underbrace{(\partial_\mu + ig_a\frac{Y_L}{2}a_\mu + ig_b\frac{\vec{\tau}}{2}\cdot\vec{b_\mu})}_{SU(2)_L \times U(1)_Y \, derivative} L \qquad (1.24)$$

where $L = \begin{pmatrix} \nu_e \\ e \end{pmatrix}_L$ and $R = (e_R)$.

The 4 kinetic energy terms corresponding to the gauge fields defined in equations 1.3 and 1.11 (U(1) and SU(2) respectively), must be added to the Lagrangian

$$\mathcal{L}_{gauge} = -\frac{1}{4}F_{\mu\nu}F^{\mu\nu} - \frac{1}{4}f_{\mu\nu}\cdot f^{\mu\nu} \qquad (1.25)$$

The combined Lagrangian, $\mathcal{L}_0 + \mathcal{L}_{gauge}$, is invariant under local and global rotations of $SU(2)\times U(1)$.

A Dirac particle can be written as the sum of its left and right handed components : $e = e_R + e_L$; e_R and e_L are defined in terms of the projection operators:

$$e_L = P_L e = \tfrac{1}{2}(1 - \gamma^5)e$$
$$e_R = P_R e = \tfrac{1}{2}(1 + \gamma^5)e$$

The mass term of a Dirac particle is then:

$$\mathcal{L}_{mass} = -m_e\overline{e}e = -m_e(\overline{e_R}e_L + \overline{e_L}e_R) \qquad (1.26)$$

But e_L transforms as a member of an isospin doublet, and e_R as a singlet. Therefore the standard Dirac mass term violates gauge invariance. As noted previously, the gauge boson mass terms ($\frac{1}{2}M^2A_\mu A^\mu$) break the gauge invariance of the Lagrangian.

8

The required mass terms can be produced by the addition of the complex Y=1 Higgs doublet :

$$\phi = \frac{1}{\sqrt{2}} \begin{pmatrix} \phi_1 + i\phi_2 \\ \phi_3 + i\phi_4 \end{pmatrix} \tag{1.27}$$

The Higgs Lagrangian can be written :

$$\mathcal{L}_{Higgs} = \frac{1}{2}(\mathcal{D}_\mu \phi)^\dagger \mathcal{D}^\mu \phi - (\mu^2 \phi^\dagger \phi + \lambda(\phi^\dagger \phi)^2) \tag{1.28}$$

where the $SU(2)_L \times U(1)_Y$ covariant derivative is taken to be :

$$\mathcal{D}_\mu = \partial_\mu + ig_a \frac{Y_H}{2} a_\mu + ig_b \frac{\vec{\tau}}{2} \cdot \vec{b_\mu} \tag{1.29}$$

The masses for the SU(2) gauge bosons are generated by gauging away three of the terms in the Higgs doublet through the expansion around the vacuum ($\frac{v}{\sqrt{2}} = \sqrt{\frac{-\mu^2}{2\lambda}}$) :

$$\phi(x) = \frac{1}{\sqrt{2}} \begin{pmatrix} 0 \\ v + H(x) \end{pmatrix} \tag{1.30}$$

where we have introduced a scalar Higgs Boson H(x). According to the Gell-Man-Nishijima formula this Higgs field has values: Y=1, Q=0 and $T_3 = -\frac{1}{2}$.

Additional manipulation of the Lagrangian is necessary to write it in Standard Model form. The charged gauge fields are defined as:

$$W_\mu^+ \equiv \frac{b_\mu^1 - ib_\mu^2}{\sqrt{2}}, W_\mu^- \equiv \frac{b_\mu^1 + ib_\mu^2}{\sqrt{2}} \tag{1.31}$$

and the orthogonal neutral fields :

$$Z_\mu \equiv \frac{-g_a a_\mu + g_b b_\mu^3}{\sqrt{g_a^2 + g_b^2}}, A_\mu \equiv \frac{g_b a_\mu + g_a b_\mu^3}{\sqrt{g_a^2 + g_b^2}} \tag{1.32}$$

After these substitutions, and the addition of the kinetic terms for the gauge bosons the Lagrangian can be written :

$$
\begin{aligned}
\mathcal{L} = \;& \frac{1}{2}\partial_\mu H \partial^\mu H - \frac{\lambda}{4}(2vH + H^2)^2 && \text{Free Higgs field} \\
& -\frac{1}{4}F_{\mu\nu}F_{\mu\nu} + 0A_\mu A^\mu + \frac{v^2(g_a^2 + g_b^2)}{8}Z_\mu Z^\mu && \text{Free Gauge Fields} \\
& -\frac{1}{4}\mathbf{f}_{\mu\nu} \cdot \mathbf{f}^{\mu\nu} + \frac{g_b^2 v^2}{8}(|W_\mu^+|^2 + |W_\mu^-|^2) && \\
& +\frac{g_b^2 v}{4}H(|W_\mu^+|^2 + |W_\mu^-|^2) + \frac{g_b^2}{8}H^2(|W_\mu^+|^2 + |W_\mu^-|^2) && \text{Interaction terms} \\
& +\frac{v(g_a^2 + g_b^2)}{4}HZ_\mu Z^\mu + \frac{(g_a^2 + g_b^2)}{8}Z_\mu Z^\mu H^2 &&
\end{aligned} \tag{1.33}
$$

While the Lagrangian may appear to be complicated, several important properties can be identified including the mass of the W-boson, $M_W = \frac{g_b v}{2}$; and the mass of the Z-boson, $M_Z = \frac{v\sqrt{g_a^2 + g_b^2}}{2}$. The W and Z masses are related via the weak mixing angle(θ_W):

$$\frac{M_W}{M_Z} = cos(\theta_W) \tag{1.34}$$

9

The photon, A_μ, does not couple to the Higgs, nor does it have mass. The Higgs Boson has a mass $M_H = \sqrt{2\lambda v^2}$, where v is the vacuum expectation value and can be calculated as $v = \frac{2M_W \sin(\theta_W)}{e}$ =246 GeV. The Higgs boson mass cannot be theoretically derived from this Lagrangian due to the inclusion of the variable λ which cannot be determined from any currently measurable quantity.

The Higgs boson couples to the generic lepton via the Yukawa interaction term ($\mathcal{L}_f$), which is both Lorentz invariant and symmetric under $SU(2)_L \times U(1)_Y$

$$\mathcal{L}_f = -G_f[\overline{R}(\phi^\dagger L) + (\overline{L}\phi)R] \tag{1.35}$$

Taking the generic lepton to be the electron and expanding the Higgs field about the vacuum, as in equation 1.30, the fermionic Lagrangian becomes:

$$\mathcal{L}_f = -m_e\overline{e}e - \frac{m_e}{v}\overline{e}eH \tag{1.36}$$

where the electron mass is defined as $m_e = \frac{G_e v}{\sqrt{2}}$. The Higgs boson couples to leptons with a strength directly proportional to the lepton's mass.

For first the generation of quarks, the Yukawa coupling is written as :

$$\begin{aligned}\mathcal{L}_Q = \quad &-G_u[(\overline{L_q\phi})u_R + \overline{u_R}(\overline{\phi}^\dagger L_q)] \\ &-G_d[(\overline{L_q}\phi)d_R + \overline{d_R}(\phi^\dagger L_q)]\end{aligned} \tag{1.37}$$

where the complex conjugate of the Higgs doublet $\overline{\phi} = i\sigma^2\phi^*$. Defining the quark masses as $m_u = \frac{G_u v}{\sqrt{2}}$, and $m_d = \frac{G_d v}{\sqrt{2}}$ the quark Lagrangian is:

$$\mathcal{L}_Q = [-m_u\overline{u}u - \frac{m_u}{v}\overline{u}uH] + [-m_d\overline{d}d - \frac{m_d}{v}\overline{d}dH] \tag{1.38}$$

Spontaneous symmetry breaking provides a simple method to generate particle masses in the Standard Model while still satisfying Lorentz and gauge invariance. This procedure produces a neutral scalar field, of indeterminate mass, which couples to elementary particles with a strength proportional to their mass. Provided that the Higgs boson exists, the Large Hadron Collider and the ATLAS detector provide a means through which physicists will be able to discover and study the Higgs boson irregardless of its mass.

The Standard Model makes no prediction on the actual mass of the Higgs boson[3]. Neutral scalar Higgs searches are typically broken into 3 mass regions:

- The *light* Higgs boson has a mass $M_H < M_Z$.

- The *intermediate* mass Higgs boson lies between $M_Z < M_H < 2M_Z$.[12] [13]

---

[3]The Higgs mass is given in terms of the variable λ which is used to describe the Higgs potential, this is not a calculable quantity.

10
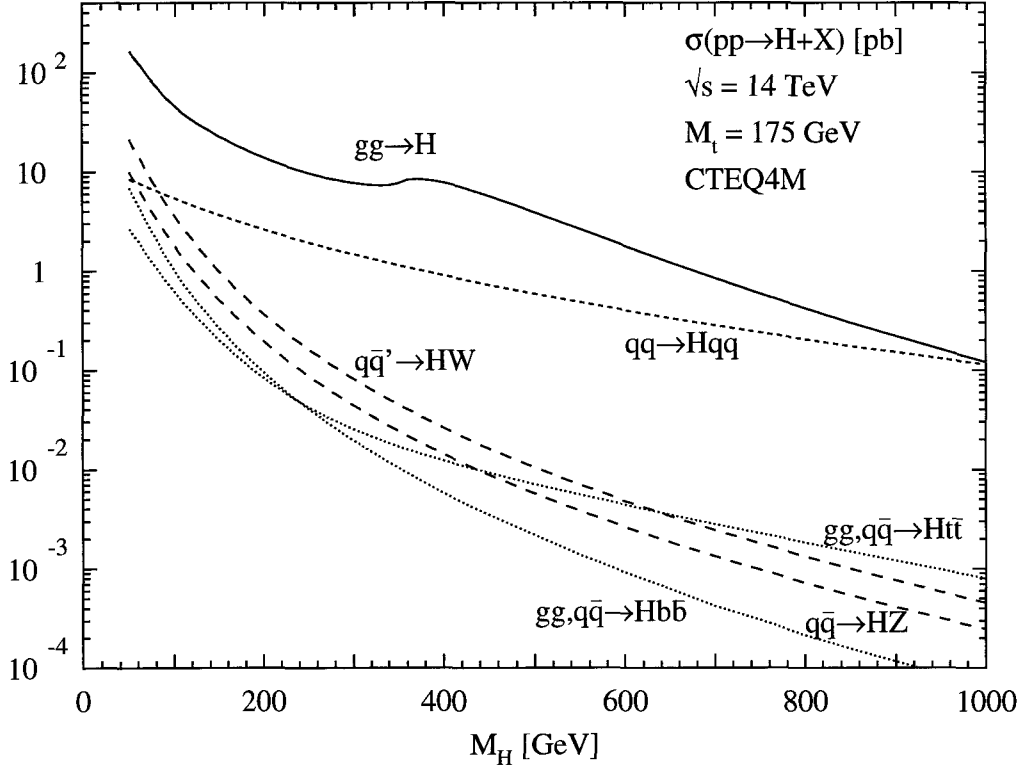
Figure 1.2: The cross section for various Higgs production modes in proton proton collisions at 14 TeV as a function of Higgs mass[17].

- The *heavy* Higgs which lies at masses above $2M_Z$.[14] [15] [16]

The dominant mechanism for detectable Higgs boson production is dependent on the type and energy of the colliding particles, and the mass of the Higgs boson being generated. This thesis will focus exclusively on the search for a heavy Higgs boson. For a heavy Higgs boson the dominant production modes at the Large Hadron Collider are gluon and vector boson fusion. The cross sections for these processes are given in figure 1.2. The Feynman diagrams are given in figure 1.3.

While the mass of the Higgs boson is not predicted by the Standard Model, we can calculate in terms of measured quantities how it couples to the other particles of the Standard Model. Using the relevant Feynman rules and Fermi's golden rule for two-body decays it is possible to calculate the branching widths for the various Higgs decays. Recall that in the Standard Model, the Higgs boson couples to mass, therefore the partial widths that are dominant in the heavy Higgs regime, shown in figure 1.4(a), are H→ZZ and H→WW, where [19] :

$$
\begin{aligned}
\Gamma_{H \to ZZ} &= \frac{g^2}{128\pi} \frac{m_H^3}{m_W^2} \sqrt{1 - x_Z}(1 - x_Z + \tfrac{3}{4}x_Z^2) \\
\Gamma_{H \to WW} &= \frac{g^2}{64\pi} \frac{m_H^3}{m_W^2} \sqrt{1 - x_W}(1 - x_W + \tfrac{3}{4}x_W^2)
\end{aligned}
\tag{1.39}
$$
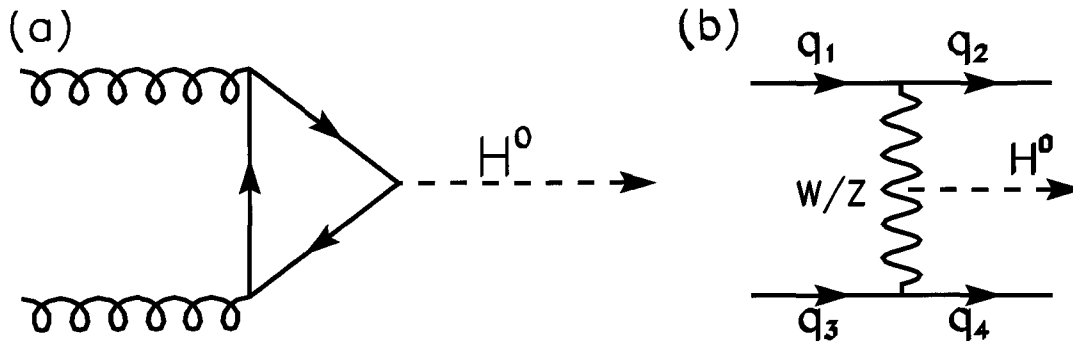
Figure 1.3: The Feynman diagrams for the two dominant Higgs boson production modes at the LHC (a) gluon fusion and (b) Vector boson fusion.
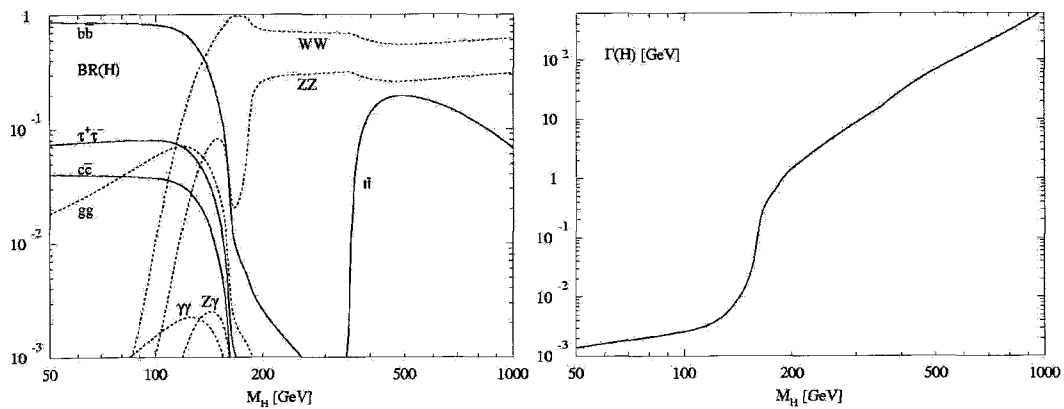
Figure 1.4: (a) A plot of Higgs branching ratios as a function of Higgs mass; for the heavy Higgs, the dominant channels are decays to the vector bosons[18].(b) The growth of the Higgs width with respect to its mass.

12
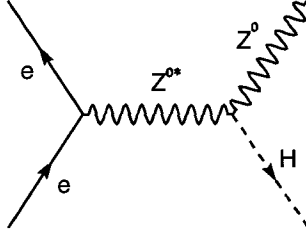
Figure 1.5: The dominant Higgs production mode in the LEP accelerator was Higgsstrahlung.

with $x_Z = 4\frac{m_Z^2}{m_H^2}$, $x_W = 4\frac{m_W^2}{m_H^2}$ and $g = g_b$. For a large Higgs mass the terms including x_W and x_Z become negligible and the total width of the Higgs is approximately.

$$\Gamma_{TOT} = \frac{3g^2}{128\pi} \frac{m_H^3}{m_W^2} \tag{1.40}$$

The width of the Higgs boson grows with its mass as shown in figure 1.4(b). The interpretation of the Higgs as a physical particle looses meaning when its mass is equal to its width; this occurs at roughly 1.4 TeV/c^2. Results from both theory and experiment allow the placement of more strict limits on the allowed mass range of the Higgs.

1.5 Higgs Mass limits

The experimental lower limit of the Higgs mass comes from the LEP project. The LEP experiments collected 2461 pb^{-1} of e$^+$e$^-$collisions between the energies of 189 and 209 GeV. Focusing on Higgs production via Higgsstrahlung; production of a Higgs off an excited Z^{0*} as shown in figure 1.5, the LEP Higgs working group was able to place a lower limit on the Higgs mass of 114.4 GeV/c^2 with 95% confidence [20][4]. The CDF collaboration[21] has estimated the potential for a Higgs boson discovery at the Tevatron based on 8 fb^{-1}(4 fb^{-1}at CDF and 4 fb^{-1}at D0) of data . Their predictions are shown in figure 1.6. If the Higgs boson has a mass below 120 GeV/c^2 D0 and CDF will be able to obtain a 3 σ significance[5]. If no signal is seen a lower limit can be set on the Higgs boson mass of 135 GeV/c^2 with 95% confidence. An actual 5 σ discovery of the Higgs boson will not be possible utilizing the CDF and D0 collider experiments.

1.5.1 Unitarity

The scattering amplitude for vector bosons $W^+W^- \to W^+W^-$ grows as the center of mass energy; and at high energies violates Unitarity. When the Higgs boson is introduced the

---

[4]The phrase "95% confidence" is not to be taken as a 5% possibility that the Higgs is less than the given value. Rather, if the Higg's mass was 114.4 GeV/c^2 , there is a 5% chance experimentalists missed it.

[5]The significance indicates a possible (S)ignal excess over the expected (B)ackground. The significance is defined as $S/\sqrt{B}$, or the number of signal events passing a cut, divided by the square root of the number of background events passing the same cut.

13
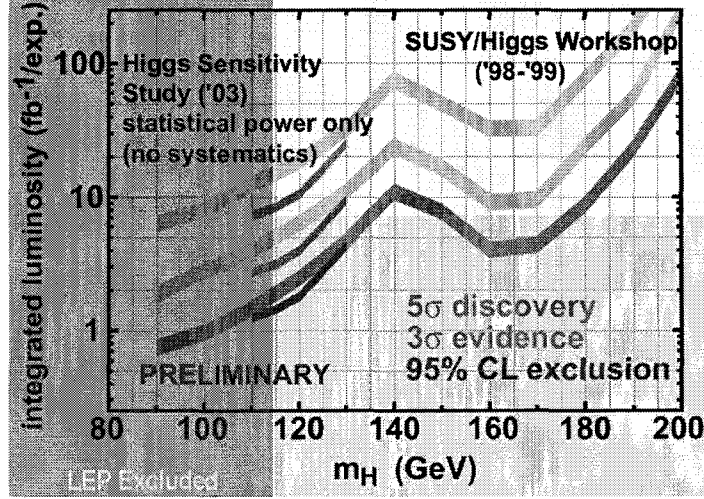
Figure 1.6: The vertical band indicates the Higgs mass region excluded by the LEP results. The horizontal band indicates the possible limits if the CDF and D0 experiments collect 8 fb^{-1} of data.

tree level amplitudes either vanish or approach a constant at large energies. The Unitarity condition on the largest eigenvalue of the partial s-wave analysis for vector boson scattering provides a loose upper limit on the Higgs of:

$$m_H = \left(\frac{8\pi\sqrt{2}}{3G_F}\right)^{1/2} \approx 1\text{TeV}/c^2 \tag{1.41}$$

If this bound is violated the perturbative nature of the theory breaks down and the interactions between the W$^{\pm}$,Z^0, H become strong around the 1 TeV scale.[22]

1.5.2 Triviality

Using the renormalization notation in [23], first order loop corrections to the Higgs coupling λ (as in equation 1.33) run as:

$$\frac{1}{\lambda(\mu)} = \frac{1}{\lambda(\Lambda)} + \frac{3}{2\pi^2}\log(\frac{\Lambda}{\mu}) \tag{1.42}$$

where μ is some small energy scale, and Λ is a much larger scale at which we expect new physics. In order for the Higgs (with mass $m_H = v\sqrt{2\lambda(\mu)}$) potential to be bounded and stable, $\lambda(\Lambda)$ must never be negative. If we let the upper scale Λ approach infinity while holding v at some physical scale this forces $\lambda(v) \to 0$, implying a trivial, non-interacting scalar field. Requiring a non-negative value for $\lambda(\Lambda)$ equation 1.42 can be written as an inequality.

$$m_H \leq \sqrt{\frac{4v^2\pi^2}{3 \cdot \log(\frac{\Lambda}{m_H})}} \tag{1.43}$$

For example, assuming that the Electroweak theory is good up to the Planck scale $\Lambda = 10^{19}$ GeV, this bounds the Higgs mass to be $M_H \leq 175$ GeV/c^2. Lowering the scale of new

14
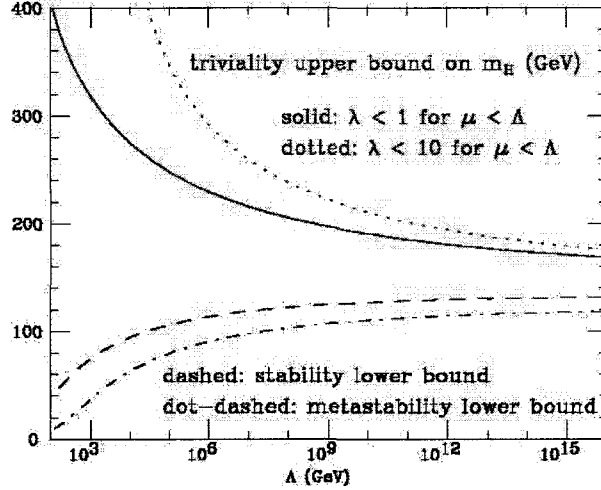
Figure 1.7: The upper bound on the Higgs mass(vertical axis) is set by triviality, the lower mass limit is defined by vacuum stability.

physics Λ, the coupling constant enters a non-perturbative region and the above equations are no longer sufficient. Lattice simulations[24] place a stricter bound on the Higgs mass in the low Λ region of $m_H \leq 630$ GeV/c^2 .

1.5.3 Vacuum Stability

A lower limit can be placed on the mass of the Higgs by requiring vacuum stability. That is, for the Higgs potential defined in equation 1.13: $V(v)<V(0)$. One loop corrections [23] lead to the lower limit

$$M_H^2 \geq \frac{3G_F\sqrt{2}}{8\pi^2}(2M_W^4 + M_Z^4 - 4m_t^4)\log(\frac{\Lambda^2}{v^2}) \geq -4500log(\frac{\Lambda}{v}) \tag{1.44}$$

While one loop corrections give a negative lower bound, two loop corrections [25] are sizable and yield a positive definite lower bound summarized in figure 1.7.

The requirement that $V(v)<V(0)$ ensures that the vacuum in its current state is perfectly stable. The lower mass limit on the Higgs boson can be loosened somewhat if the vacuum is meta-stable, that is the probability of the vacuum decaying is less than the lifetime of the universe. If the Standard Model is to remain valid up to the unification scale of 10^{16} GeV, the Higgs boson is required to have a mass between 145 GeV/c^2 and 170 GeV/c^2 .

1.6   Indirect Measurements

The top quark, and the Higgs boson appear as radiative corrections to the electroweak propagators. Therefore, precision measurements of the electroweak parameters can give indirect

15
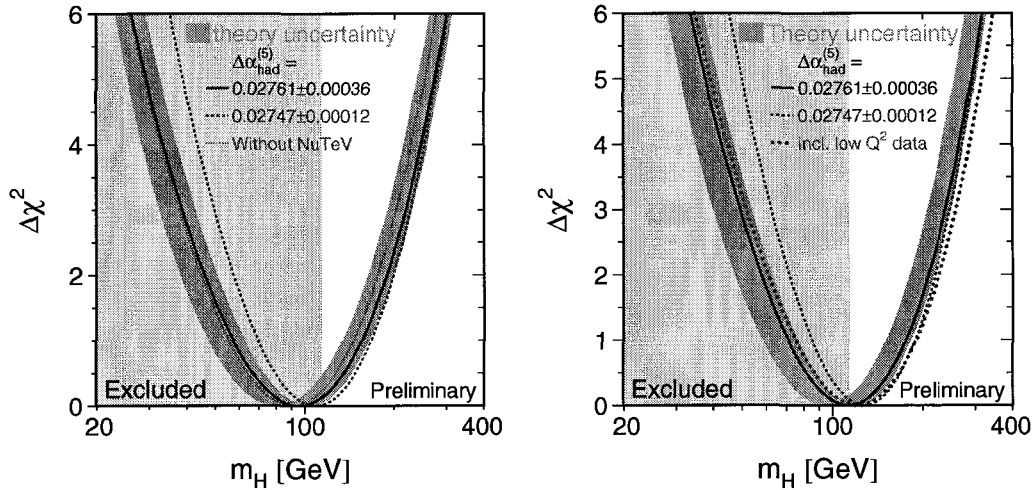
Figure 1.8: (a) Prior to the new top quark measurements the optimal Higgs mass value was below the LEP limit. (b) The increase in the top quark mass reported by CDF and D0[31] [32] shifted the optimal value to be above the LEP limit.

indications of the Higgs boson mass.

Fits of all the available electroweak data have been performed by the LEP Electroweak working group. The fits from 2003 [26] and 2004 [30] produced the two different Higgs mass limit curves seen in figure 1.8. The CDF collaboration recently published [31] a new measurement of the top quark mass of 178.0 ± 4.3 GeV/c^2. The 2004 LEP results, which include the new top quark mass, give a Higgs boson mass of 114^{+69}_{-45}GeV/c^2 [20], with an upper bound of 260 GeV/c^2 at the 95% confidence level.

It has been argued in [33] and [34] that the large inconsistencies in the electroweak data, specifically the values of $\sin^2\theta_W(\nu N)$ (the weak mixing angle measured by neutrino-nucleon scattering at NuTeV [35]) and $A^{0,b}_{fb}$ (forward-backward asymmetry in ee$\rightarrow$Z$\rightarrow$b$\bar{\text{b}}$ events at LEP) shown in figure 1.9 should reduce our confidence in the overall Electroweak fit. The authors go on to argue that if these two values are not simply statistical errors they could be taken as a sign of new physics. They suggest modifications to the Standard Model, such as a fourth generation of fermions or additional massive vector bosons, to account for these discrepancies. As a result the upper bound on the Higgs mass can be extended to 400 GeV/c^2.

Supersymmetry (SUSY) states that every fundamental particle has a supersymmetric

16

Winter 2003

	Measurement	Pull	$(O^{meas}-O^{fit})/\sigma^{meas}$
			-3 -2 -1 0 1 2 3
$\Delta\alpha_{had}^{(5)}(m_Z)$	0.02761 ± 0.00036	-0.16	
m_Z [GeV]	91.1875 ± 0.0021	0.02	
Γ_Z [GeV]	2.4952 ± 0.0023	-0.36	
σ_{had}^0 [nb]	41.540 ± 0.037	1.67	
R_l	20.767 ± 0.025	1.01	
$A_{fb}^{0,l}$	0.01714 ± 0.00095	0.79	
$A_l(P_\tau)$	0.1465 ± 0.0032	-0.42	
R_b	0.21644 ± 0.00065	0.99	
R_c	0.1718 ± 0.0031	-0.15	
$A_{fb}^{0,b}$	0.0995 ± 0.0017	-2.43	
$A_{fb}^{0,c}$	0.0713 ± 0.0036	-0.78	
A_b	0.922 ± 0.020	-0.64	
A_c	0.670 ± 0.026	0.07	
A_l(SLD)	0.1513 ± 0.0021	1.67	
$\sin^2\theta_{eff}^{lept}(Q_{fb})$	0.2324 ± 0.0012	0.82	
m_W [GeV]	80.426 ± 0.034	1.17	
Γ_W [GeV]	2.139 ± 0.069	0.67	
m_t [GeV]	174.3 ± 5.1	0.05	
$\sin^2\theta_W(\nu N)$	0.2277 ± 0.0016	2.94	
Q_W(Cs)	-72.83 ± 0.49	0.12	

-3 -2 -1 0 1 2 3

Figure 1.9: A view of how well the electroweak data fits with the LEP 2003 prediction for the Higgs mass [26].

17

partner: fermions are paired with SUSY gauge bosons, and the bosons are paired with SUSY fermions. The simplest SUSY theory consistent with the standard model is the Minimal Supersymmetric Standard Model (MSSM)[27][28]. In the MSSM the vacuum symmetry is broken by two complex Higgs doublets[6], leading to a total of 5 Higgs bosons: two neutral CP even Higgs bosons (h^0,H^0), 1 neutral CP odd (A^0) and two charged Higgs bosons ($H^\pm$). For the two CP even Higgs bosons SUSY favours that one be light and the other be heavy. Taking the top mass to be M_t=178 GeV/c^2, the MSSM places an upper limit on the mass of the lightest neutral Higgs boson[29] to be M_{h^0} <136 GeV/c^2.

Consequently, it is important not to limit searches to that of a medium mass Higgs, but we must look for signals of a heavy Higgs boson as well.

1.7 Physics Channels

This thesis will focus on a heavy neutral scalar Higgs boson produced through vector boson fusion and decaying through the four channels listed below.

$$q_1 q_2 \rightarrow \quad H \quad q_3 q_4 \quad \left\{ \begin{array}{ll} H \rightarrow ZZ & \rightarrow e^+ e^- jj \\ & \rightarrow \mu^+ \mu^- jj \\ H \rightarrow WW & \rightarrow e^+ \nu_e jj \\ & \rightarrow \mu^+ \nu_\mu jj \end{array} \right. \qquad (1.45)$$

The reconstruction of the H$\rightarrow Z^0 Z^0$ channel is the focus of chapter 4. The H$\rightarrow W^+ W^-$ channel will be discussed in chapter 5.

The Feynman diagram given in figure 1.10 represents the four processes listed in equation 1.45. The Higgs Boson is formed through a process called vector boson fusion: individual quarks from protons in opposing bunches radiate virtual vector bosons which fuse to form the Higgs boson. After they radiate, provided they gain enough transverse momentum (P_T), these quarks will shower and produce jets that enter the forward regions[7] of the detector. These "forward tagging jets" in the Vector Boson Fusion signal are not present in gluon-gluon fusion nor are they present in the dominant background processes. It is for this reason that we consider Higgs boson production through vector boson fusion.

When the Higgs boson mass is large figure 1.4 shows that it will decay preferentially to a pair of real vector bosons, which further decay into leptons and quarks. The energy stored in the mass of the Higgs boson gets transferred through to these decay products producing

---

[6]One of the free parameters in the MSSM is tan(β); this is the ratio of the vacuum expectation values of the Higgs doublets.

[7]The forward region of the detector is that region which lies closest, in angle, to the beamline.

18
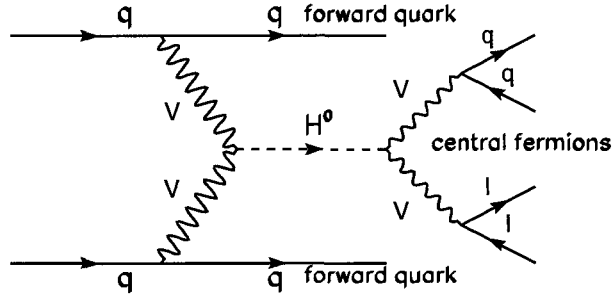
Figure 1.10: The Higgs signal is characterized by two high P_T central jets(with a combined mass $M_{W/Z}$), two isolated high P_T central leptons (also with mass $M_{W/Z}$), and two highly energetic tagging jets.

Higgs Mass (GeV/c^2)	200	600	1000
σ(qq→Hqq)(pb)	2.41	0.345	0.0891
BR$_H$(H→ZZ)	25.7%	28.2%	30.8%
BR$_l$(ZZ→4l)		1.01%	
$\sigma \times$BR$_H \times$BR$_l$(fb)	6.26	0.98	0.277
BR$_{lq}$(ZZ→l$\bar{l}$q$\bar{q}$)		14.07%	
$\sigma \times$BR$_H \times$BR$_{lq}$(fb)	87.1	13.7	3.86
BR(H→WW)	73.9%	58.1%	62.2%
BR$_l$(WW→lνlν)		10.52%	
$\sigma \times$BR$_H \times$BR$_l$(fb)	187.4	21.1	5.83
BR$_{lq}$(WW→lνqq)		43.82%	
$\sigma \times$BR$_H \times$BR$_{lq}$(fb)	780.0	87.8	24.3

Table 1.5: The production cross section for a Higgs boson produced through vector boson fusion. The mixed decay channel has a much larger branching ratio than the purely leptonic decay. For this table we have used PYTHIA 6.227 to determine the cross-section and branching ratios. The branching ratios (BR) have been summed over the 3 lepton flavours.

two high P_T central jets and two high P_T central leptons[8].

While a purely leptonic decay would give a much cleaner event signature, the branching ratio of the leptonic weak boson decay is small when compared to its hadronic counterpart. Since the cross-section of any given Higgs production process is already quite small, see for example table 1.5, we sacrifice some signal clarity for an increase in cross-section by studying the mixed decay mode.

---

[8]The central region of the detector is the region that lies furthest, in angle, from the beamline.

19

Chapter 2

The Large Hadron Collider and the Atlas Detector

2.1 Large Hadron Collider

The Large Hadron collider (LHC) is being constructed in the Large Electron Positron (LEP) collider tunnel. The LHC ring has a 27 km circumfrence and straddles the French-Swiss border. The LHC, shown in figure 2.1, will collide energetic protons with a center of mass energy (E_{cm}) equal to 14 TeV, roughly 7 times more energetic than the Tevatron at Fermilab.

The LHC injector complex, shown in figure 2.1, is series of progressively more energetic accelerators. The protons are produced and accelerated through a 50 MeV linear accelerator (LINAC). They are then accelerated to 1.4 GeV in the booster (PSB) and further accelerated in the proton synchrotron (PS) to 26 GeV. The super-proton synchrotron (SPS), accelerates the protons to 450 GeV at which point they are fed into the main LHC ring. The proton bunches in the LHC will be accelerated until they reach 7 TeV collision energy.

The LHC will then collide the protons at 5 separate interaction points. There are two general purpose experiments: CMS (Compact Muon Solenoid), and ATLAS (A Toroidal Lhc ApparatuS). LHCb will be focused on b-physics, while ALICE (A Large Ion Collider Experiment) is a heavy ion collision detector. TOTEM will measure the total cross section for elastic scattering and diffractive processes at the LHC.

The LHC can be used to collide heavy ions with a center of mass energy (E_{cm}) of 1150 TeV (5.5 TeV/nucleon), 30 times the energy of Relativistic Heavy Ion Collider(RHIC) at Brookhaven National Labs. This thesis will focus on the proton-proton collision mode of the LHC.

20
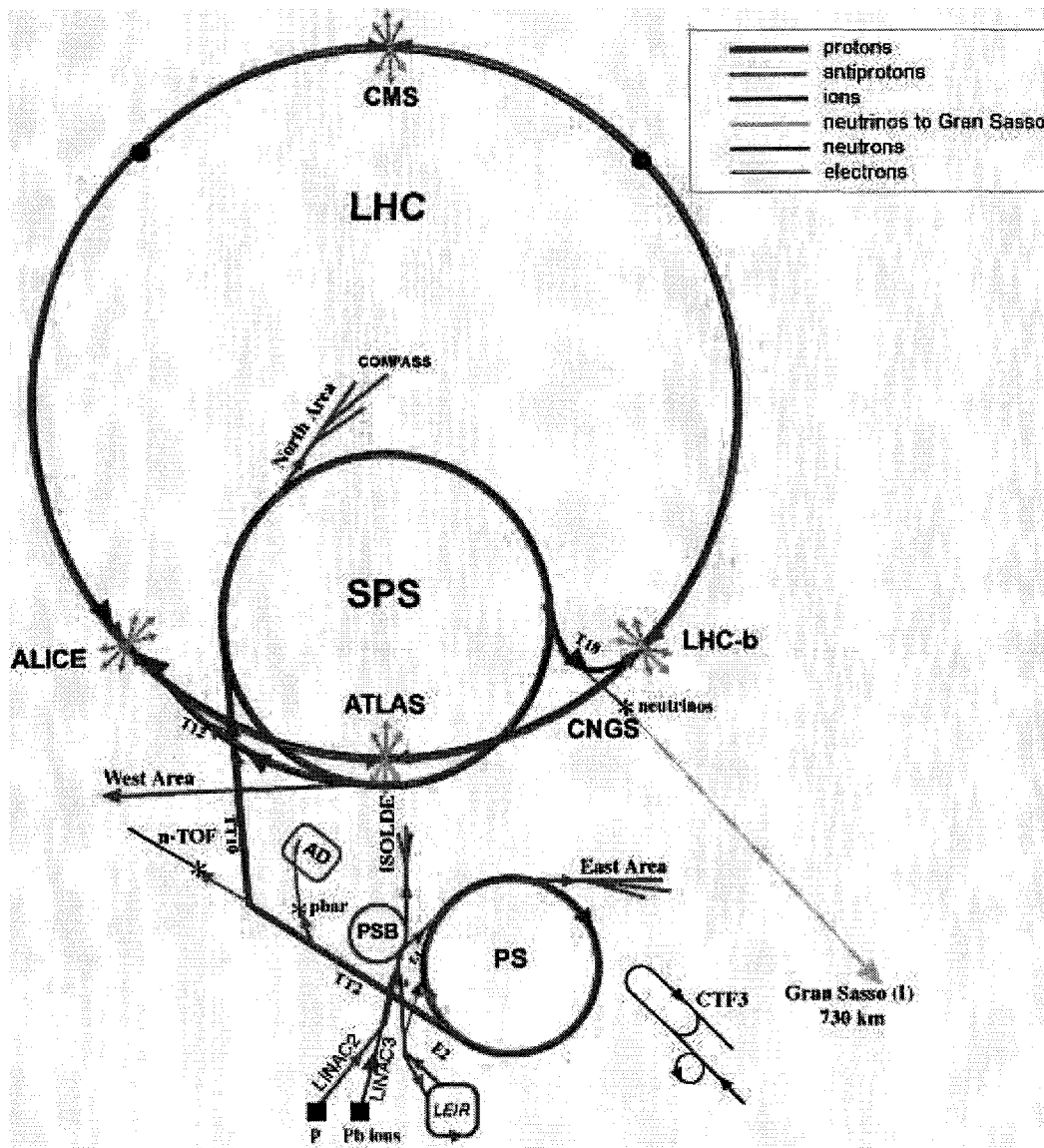
Figure 2.1: The CERN accelerator complex.

21

The luminosity of a symmetric collider is given by:

$$L = \frac{1}{4\pi} \frac{N^2 f}{t A_T} \qquad (2.1)$$

where N is the number of protons in a "bunch", t is the time between the bunches in the ring and A_T is a measure of the spread of the bunch transverse area. At the interaction point the proton bunches have a r.m.s transverse size of approximately 16 μm and a r.m.s length of 7.55 cm. The requirement that there be no additional interactions within the detector outside the interaction point limits the bunch spacing to about 7.5 metres, giving a bunch crossing every 25 nanoseconds. To be able to continuously fill the LHC requires that the proton bunches be organized in bunch trains followed by empty bunches. Only 2808 of the 3564 available bunch spaces are filled giving the value $f = 0.788$. At peak energies the protons will loose on average 7 keV per rotation due to synchrotron radiation. Due to the large mass of the proton synchrotron radiation will only become significant at beam energies approaching 100 TeV. Table 2.1 lists some properties of the Large Hadron Collider.

	units	Low	High	Ultimate
Luminosity	$10^{34} cm^{-2} s^{-1}$	0.12	1.0	2.3
Number of Particles/bunch	10^{11}	0.4	1.15	1.7
RMS bunch length at Collision	cm	7.55		
Transverse Beam size at IP	μm	17.0	16.63	15.9
Luminosity Life time	hours	28	13.9	13

Table 2.1: The LHC design specification for both low, high and ultimate luminosity settings[36],[37].

The ultimate (end goal) luminosity of the LHC is assumed to be roughly $2\times10^{34} cm^{-2} s^{-1}$. During the first three years of operation the accelerator will operate at a lower luminosity taken to be $L_{low}=1.2\times 10^{33} cm^{-2} s^{-1}$ at which point the luminosity will be increased to the high luminosity setting $L_{high}=1\times 10^{34} cm^{-2} s^{-1}$.

The rate (R) at which physics events are detected is given in terms of the Luminosity (L), the physics channel cross-section (σ), and a detection efficiency (ϵ).

$$R(Hz) = L \; \sigma \; \epsilon \qquad (2.2)$$

Figure 2.2 plots the cross section for interesting physics processes at a proton-proton collider as a function of center of mass energy.

As the luminosity is increased the efficiency for event detection and the quality of event reconstruction decreases as extraneous pileup events[1] from other interactions within the

---

[1]The definition of minimum bias/pile-up events will be discussed in more detail in section 3.1.2.
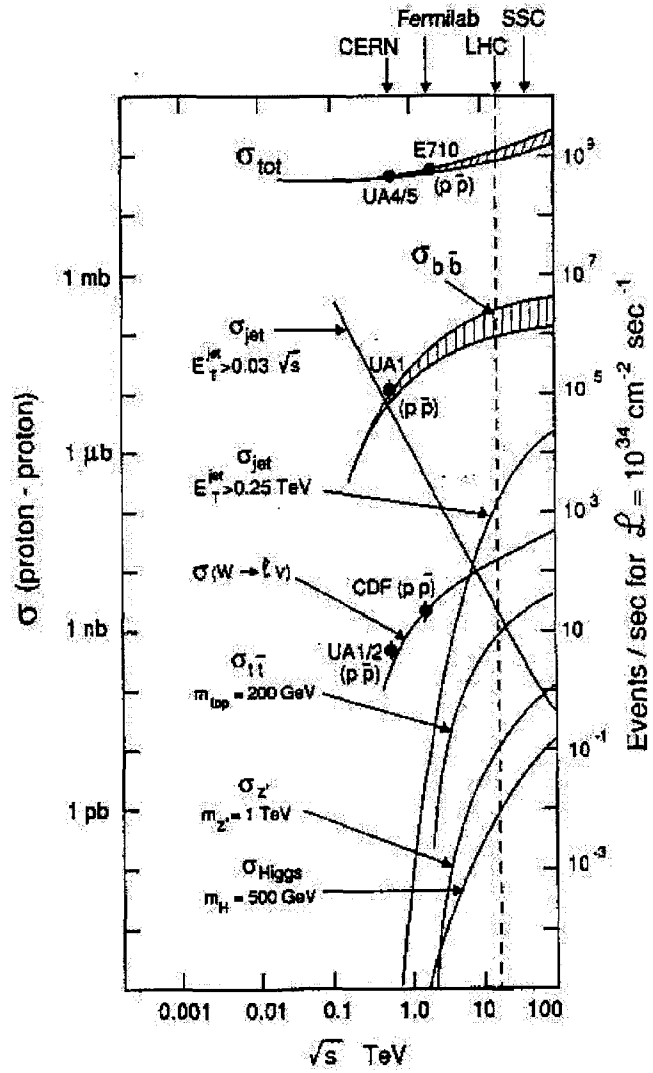
Figure 2.2: The cross section of interesting physics processes as a function of center of mass energy[38]. The LHC energy is marked by the dashed vertical line.
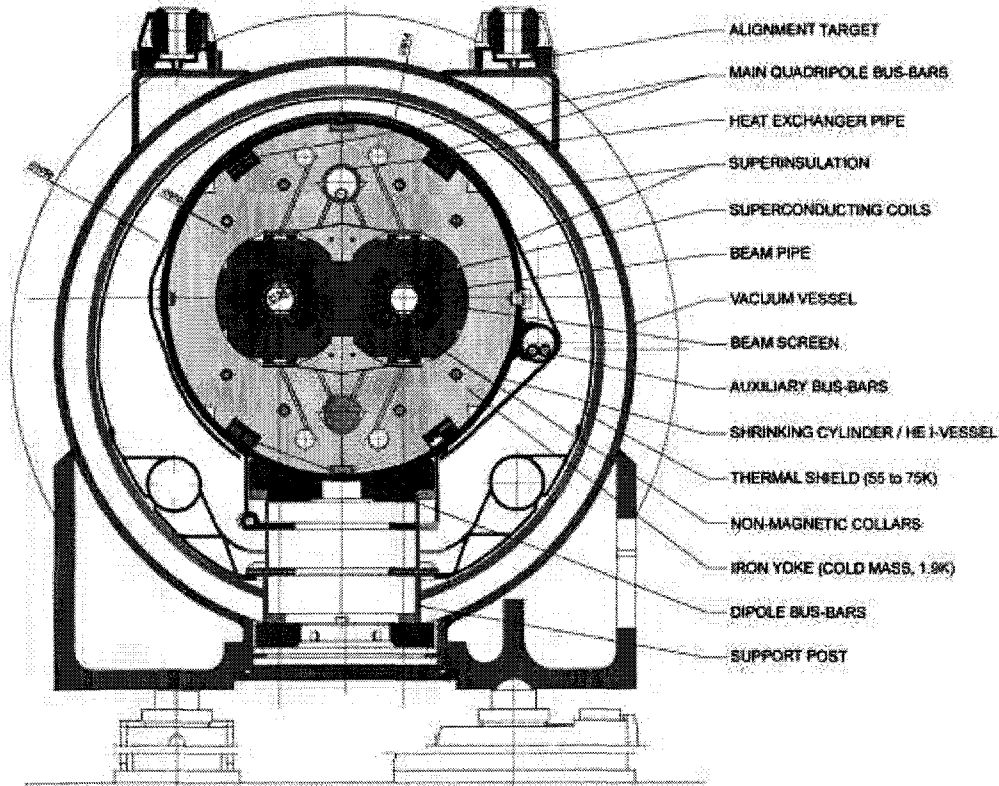
Figure 2.3: The LHC dipole magnet is 14.2 m in length, with an inner diameter of 56 mm. The beam separation is 194 mm.

bunch crossing deposit their energy in the calorimeter and obscure the topology of the signal event. The cross-section for minimum bias events is large, $\sigma_{m.bias} = 101.5$ mb. Taking the high luminosity conditions there will be:

$$R(pileup) = (L_{high})(\sigma_{m.bias}) \times 25 \times 10^{-9}\text{s/bunch} = 25.4 \text{ events/bunch} \qquad (2.3)$$

a Poisson average of 25 pile-up events for every bunch crossing.

2.1.1 LHC Magnet System

Unlike the LEP accelerator which collided oppositely charged electrons and positrons, the LHC collides like charged protons and therefore requires two separate magnetic beam channels. Space limitations and cost concerns do not allow the construction of two separate assemblies so the LHC uses the twin-bore design shown in figure 2.3 which places the two separate beam channels within the same mechanical structure and cryostat.

In addition to the 1296 bending dipole magnets and 474 focusing and defocusing quadrapole magnets there are an additional 6800 superconducting corrector magnets in the LHC [39]. The LHC magnet coils are made of copper-clad niobium-titanium cables. To generate the

24

8.36 Tesla magnetic field necessary to produce the 2.9 km radius of curvature, the super-conducting cables are kept in a 1.9 K bath of superfluid helium. This bath will be cooled by low pressure liquid helium. In total the magnet cryogenics must provide a total cooling power of 144 kW at 4.5 K along the LHC ring. The LHC dipole magnets will be trained to reach a magnetic field strength of 9 Tesla (a value well above the operating specifications).

2.2 The ATLAS detector

The design of the general purpose ATLAS detector has been described in great detail in the ATLAS Technical Proposal (TP)[40], and the Technical Design Report (TDR) [41] [42]. The ATLAS detector consists of four major subsystems. The inner detector which lies within a 2 Tesla magnetic field provided by a superconducting solenoid. The electromagnetic and hadronic calorimetry lie outside the solenoid. The muon spectrometer is the outermost detector system with an outer radius of 11 m and a length of 45 m. The ATLAS detector has a net weight of 7000 tonnes. The basic design requirements for ATLAS can be summarized as :

- Very good electromagnetic calorimetry allowing for electron and photon identification, combined with hermetic hadronic coverage allowing for accurate missing E_T determination.

- Efficient tracking at low and high luminosity allowing for lepton identification and momentum measurement, as well as b-quark tagging, with only a minimal misidentification rate.

- Stand alone high precision muon measurements allowing for triggering on low P_T muons (6 GeV/c) and giving a resolution no worse than 10% at P_T=1 TeV/c.

To maximize its physics capability the ATLAS detector must be hermetic, covering as much of the solid angle of the collision as possible. Regions of the detector are referred to in terms of the standard azimuthal angle ϕ and pseudo-rapidity η which is defined as:

$$\eta = -ln(tan(\theta/2)) \tag{2.4}$$

where θ is the angle measured to beam axis. The ATLAS detector, shown in figure 2.4 has hadronic calorimetry coverage down to a pseudorapidity value (η) of 4.8 ($\theta = 0.94°$). The detector must also have good calorimeter resolution that, among other objectives, allows for an accurate calculation of the missing transverse energy.

25
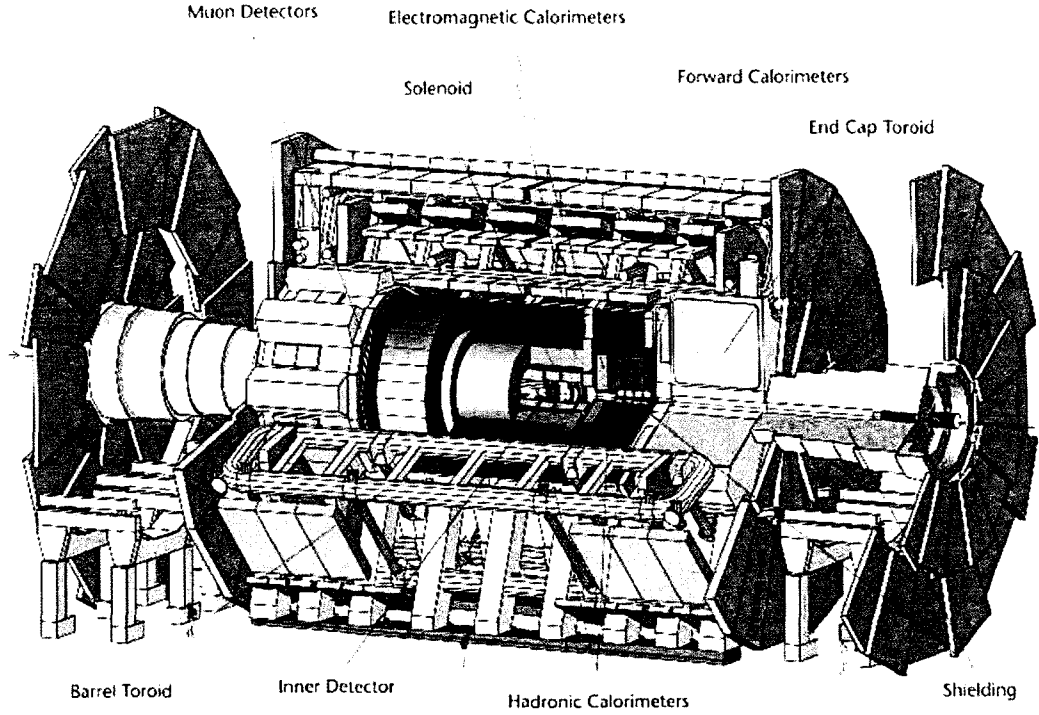
Figure 2.4: A 3-dimensional diagram of the ATLAS detector labeling all its key components.

2.2.1 Inner detector

The inner detector, lies closest to the beam line and is able to reconstruct the path of the charged tracks using the magnetic field of the 2 Tesla superconducting solenoid that lies just before the electromagnetic calorimeter. The inner detector must allow for the identification and momentum measurement of individual particles in very dense jets up to an $|\eta| < 2.5$ with only a small fake rate. It must also give accurate momentum measurement over a very large momentum range. Tracks with P_T less than roughly 0.5 GeV/c cannot be reconstructed since they loop inside the magnetic field. Lastly, in both the low and high luminosity scenarios it must be able to reconstruct primary and secondary vertices to allow τ and b-jet tagging.

The inner detector, shown in figure 2.5, has an outer radius of 115 cm and a half-length of $|Z|$=345 cm. It is composed of three primary components: the silicon-pixel vertex detector and the semi-conductor tracker (SCT), these are surrounded by the transition radiation tracker (TRT). Silicon has a small 3.6 eV band gap allows for many electron-hole pairs to be produced; roughly 80 electron-hole pairs per μm for a minimum ionizing particle. An applied electric field is used to collect the charged particles at their respective electrodes giving rise to a signal that is proportional to the energy deposited.

26
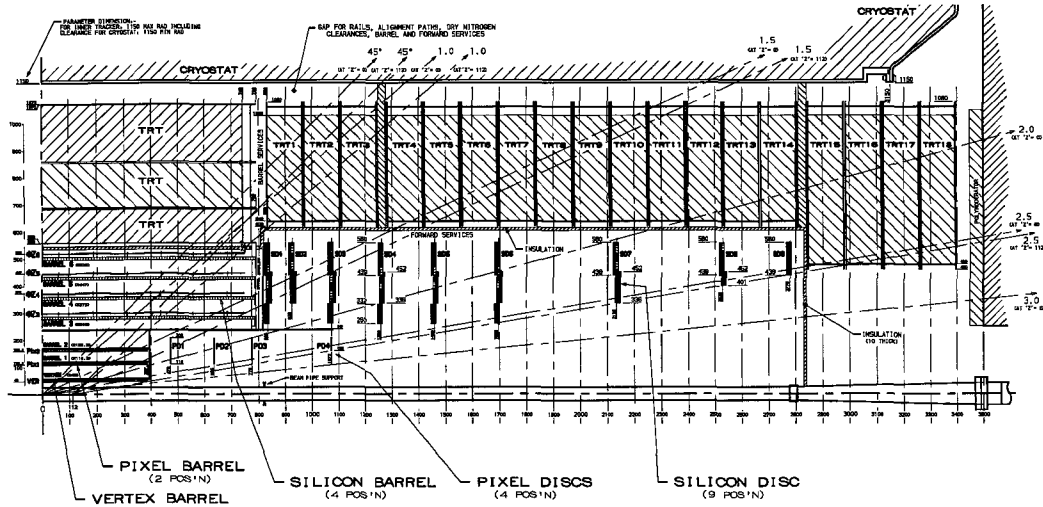
Figure 2.5: A schematic of the inner detector showing the transition from the barrel structure to wheel structure at a pseudo-rapidity of 1.0.

The silicon vertex pixel detector is a high granularity, high precision detector located closest to the beam line with an inner radius of 4 cm and an outer radius of 22 cm. It contains three barrel layers located at 4, 11 and 14 cm; and eight disc layers (4 on each side) at distances from the interaction point(IP) of 473, 635, 776, 1072 mm and covering a radius of 11 cm to 21 cm (the furthest disc from the interaction point has a minimum radius of 15.9 cm). This configuration provides at least 3 spatial points for tracks with an $|\eta|$ <2.5. Each pixel measures 50 μm in rϕ by 300 μm in Z, giving 140 million channels with a spacial resolution of 12 μm by 66 μm. Over the lifetime of the experiment (at least 10 years), at a radius of 11 cm from the IP, there is expected to be over 300 kGy of ionizing radiation and a neutron fluence over 5×10^{14}/cm^2. The b-layer, located 4 cm from the IP, would receive an ionization radiation dose of over 1000 kGy. Current silicon detectors are not capable of surviving doses beyond 200-300 kGy so the innermost pixel layer has been designed to be replaceable.

The semi-conductor tracker (SCT) uses silicon microstrips to provide precision measurements of Rϕ and Z at intermediate radii. A silicon wafer in the barrel region physically measures 6.36×6.40 cm^2 (6.16×6.20 cm^2 active area) with 768 readout strips each with 80 μm pitch. Two wafers are wire bonded to form one 12.8 cm (12.32 cm) long module. Stereoscopic measurements are possible in the SCT by aligning one module layer parallel to the beam-pipe, and having the next immediate layer rotated by 40 mrad. The forward region uses tapered strips with one layer aligned radially and the second layer provides the radial coordinate. The SCT contains 4 barrel layers at radii of 300, 373, 447 and 520 mm, and 9

27

System	Position	Resolution $\sigma(\mu m)$	Channels 10^6	η Coverage
Pixels	1 removable barrel layer	Rϕ=12,Z=66	16	±2.5
	2 barrel layers	Rϕ=12,Z=66	81	±1.7
	4 EndCap disks on each side	Rϕ=12,R=77	43	1.7-2.5
Silicon	4 barrel layers	Rϕ=16,Z=580	3.2	±1.4
Strips	9 EndCap wheels on each side	Rϕ=16,R=580	3.0	1.4-2.5
TRT	Axial barrel Straws	170 (per straw)	0.1	±0.7
	Radial EndCap straws	170 (per straw)	0.32	0.7-2.5

Table 2.2: The spatial resolution values for the various subcomponents of the ATLAS inner detector, as given in the Inner Detector TDR[43][44].

EndCap wheels at distances from the IP between 835 mm and 2788 mm. The three ring radial coverage of each of these wheel layers is chosen to cover the pseudorapidity region up to $|\eta|$=2.5.

The Transition Radiation Tracker (TRT) extends from a radius of about 50 cm to about 110 cm, and covers the full pseudo-rapidity range of the inner detector. The TRT is comprised of approximately 370,000 4 mm diameter proportional drift tubes filled with 70% Xe, 20% CF$_4$ and 10% CO$_2$: 50000 straws in the barrel region and 320000 radial straws in the EndCap; giving a total of 420,000 electronic channels for the TRT. The barrel TRT is comprised of three 32 module cylinders ranging in radius from 56 to 107 cm and covers the region ±75 cm in Z. The tubes are oriented in such a fashion that they are perpendicular to the passage of the relativistic particles. The tubes of the TRT are meant to detect the transition radiation, in the X-ray region, produced when the relativistic particles pass through the radiators which are interspersed throughout the detector. Each module in the inner cylinder contains 329 straws, 520 in the centre cylinder and 793 straws in the outer cylinder. Each EndCap contains 9 wheels; the 7 wheels closest to the interaction point cover a radius of 64 to 104 cm while the final two extend down to 48 cm. The barrel component of the TRT will directly measure the R-ϕ components of the particle, while the EndCap TRT can measure ϕ,Z directly and R indirectly through the particles entrance and exit positions in the detector, providing a spatial resolution of 170 μm.

The pseudo-rapidity coverage and expected spatial resolutions of the ATLAS silicon detector systems and the Transition Radiation Tracker are summarized in table 2.2.

For tracks with transverse momentum greater than 0.5 GeV/c the inner detector will provide six precision space-points and 36 straws over the full pseudorapidity coverage of the Inner Detector. With the addition of the extra b-layer in the pixel detector the inner

28
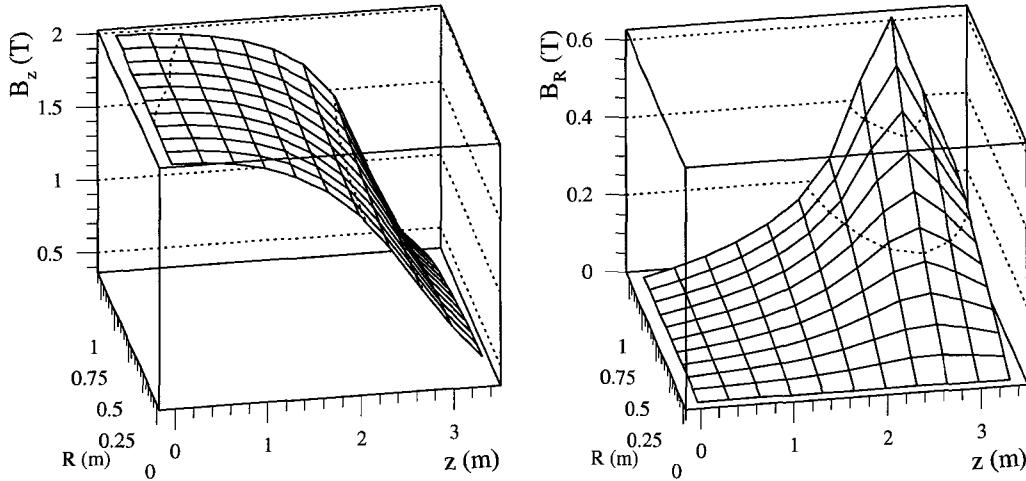
Figure 2.6: The magnetic field strength (a) in the beam direction, (b) in the radial direction as a function of radius and distance along Z.

detector impact parameter[2] resolution is expected to be :

$$R\phi(\mu m) \quad \sigma(d_0) = 11 \oplus \frac{60}{p_T\sqrt{sin(\theta)}} \tag{2.5}$$

$$Z(\mu m) \quad \sigma(z_0) = 70 \oplus \frac{100}{p_T\sqrt{sin^3(\theta)}} \tag{2.6}$$

The magnetic field in the inner detector is provided by a 2 Tesla superconducting solenoid. However, the true magnetic field strength is not uniform across the full length of the inner detector. The magnetic field falls away from its central 2 Tesla value and picks up a large radial component as the distance along the Z axis increases. This variation in strength and direction is shown in figure 2.6. The momentum resolution of the inner detector for 500 GeV/c P_T tracks is given in figure 2.7, and can be approximated (for a uniform field) by the equation :

$$\sigma(\frac{1}{p_T}) = 3.6 \times 10^{-4} \oplus \frac{1.3 \times 10^{-2}}{p_T\sqrt{sin\theta}} (GeV^{-1}c) \tag{2.7}$$

Tracks with a pseudorapidity greater than 1.85 exit the detector before reaching the inner detector's maximum radius. This gives the marked decrease in resolution presented in figure 2.7.

2.2.2 Calorimetry

The ATLAS calorimetry, shown in figure 2.8, is divided into electromagnetic (EM) and hadronic (HAD) sections. To identify important physics processes, the electromagnetic calorimetry must be able to reconstruct electron and photon direction as well as provide

---

[2]The impact parameter is a measure of how far away from the interaction point a track lies, it will be discussed in more detail in section 3.3.2.

29
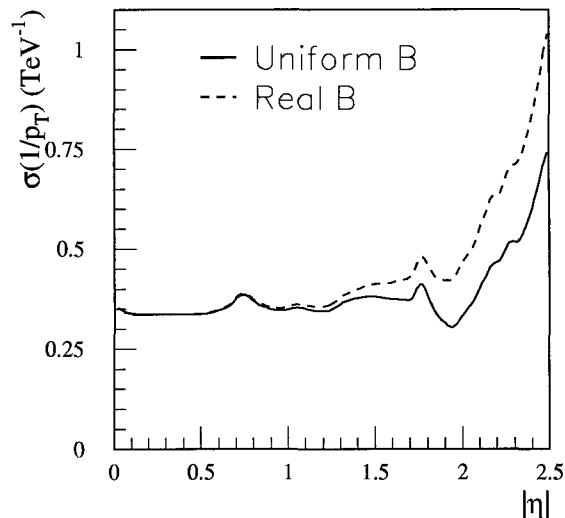
Figure 2.7: The momentum resolution of the inner detector as a function of pseudorapidity for 500 GeV/c P_T tracks. The dashed line gives the momentum resolution when the real magnetic field of figure 2.6 is used.

accurate momentum reconstruction over a large transverse momentum range from 2 GeV/c (for the process H$\rightarrow$ZZ* $\rightarrow$4e) to 5 TeV/c (for the decay Z' $\rightarrow$ee). The major goals for the ATLAS hadronic calorimetry are the identification of hadronic jet energy and direction, and the measurement of missing transverse energy resulting from those particles, such as neutrinos and super-symmetric particles, which escape the detector.

Calorimetry resolution is described by 3 terms, added in quadrature,

$$\frac{\Delta E}{E} = \frac{A}{\sqrt{E}} \oplus \frac{B}{E} \oplus C \tag{2.8}$$

where A is the sampling term that accounts for the fluctuations in the number of particles produced, B is the noise term (for electronic noise and pileup) which is dominant at lower energies and C is the constant term which is dominant at high energies. The constant term is linked to such effects as non-uniformities in the calorimeter response; examples of this would include dead material in the calorimeter, and calibration of the global energy scale. The $\oplus$ symbol indicates that the terms are added in quadrature.

The bulk of the ATLAS calorimetry operates using Liquid Argon (LAr) Ionization chambers. The calorimeter incorporates a material (the absorber) of high atomic material to generate and contain the showers, and an active detector material to sample the shower. Liquid Argon Calorimetry is used because of its radiation hardness. The expected radiation levels in the ATLAS calorimetry are summarized in table 2.3[45]. The high density of LAr allows

30
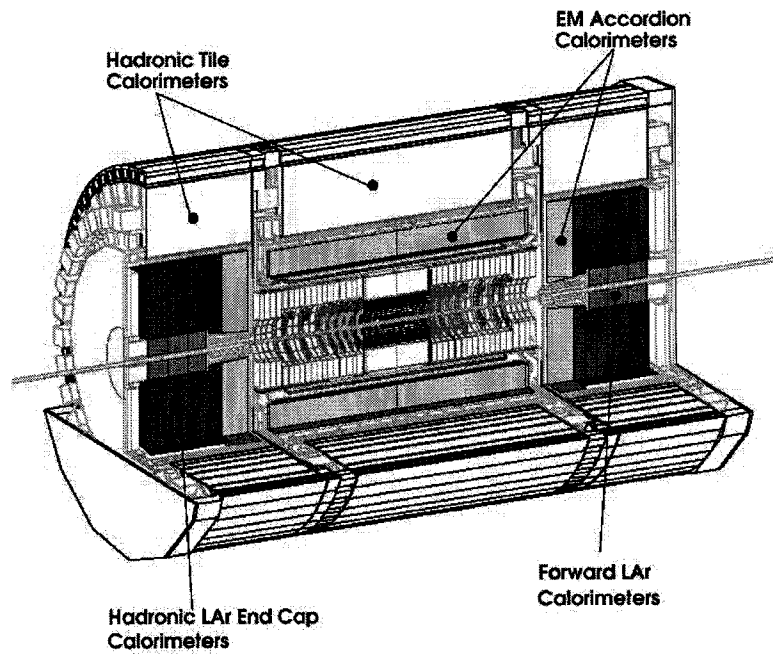
Figure 2.8: Three dimensional representation of the ATLAS calorimeter as produced by GEANT

Detector Component	dose [kGy/yr]	fluence [cm^{-2}/yr]
Barrel EM calo.	0.6	1.5×10^{13}
Barrel Tile calo.	0.02	1.6×10^{12}
Barrel/EB crack	0.036	2.0×10^{12}
EndCap EM calo	53	4.1×10^{14}
EndCap had. calo.	12	6.1×10^{14}
Forward calo.	2300	1.0×10^{16}

Table 2.3: Maximum yearly values for dose and fluence rates in ATLAS.

31

for the production of a large amount of ionization and as a good insulator it allows a high voltage to be applied to maximize electron production and capture at the readout electrodes.

ATLAS LAr calorimetry is cooled by 3 cryostats to an operating temperature of 90 K. The barrel cryostat contains the EM barrel calorimetry and the solenoidal coil which provides the magnetic field for the inner detector. Two EndCap cryostats enclose the EM and hadronic EndCap as well as the integrated forward calorimeter. The hadronic tile calorimeter is located outside the cryostats.

The pseudorapidity coverage and granularity of the electromagnetic and hadronic calorimetry is given in table 2.4.

Electromagnetic calorimetry

When an electron is incident on a volume of matter it may radiate a photon through bremsstrahlung, if this photon possess enough energy it will then produce an e^+e^- pair. This showering process continues until the energy of the secondary particles falls below some critical energy at which stage the remaining energy is lost due to atomic ionization. A 50 GeV electron can produce up to 1000 secondary particles. The length of an electromagnetic shower is proportional to the logarithm of its incident energy, and its transverse spread related to the Moliere radius, R_M.

$$R_M = 0.0265 X_O (Z + 1.2) \qquad (2.9)$$

where X_0 is the radiation length and Z is the atomic number of the detector material. A high energy photon, with energy greater than 1 GeV, will shower in a manner similar to an electron since pair production is the dominant interaction process above this energy. The presence of tracks in the Inner Detector helps distinguish between an electron and photon shower in the EM calorimetry.

The electromagnetic calorimeter is divided into two sections: the barrel and the EndCap both of which are detailed in table 2.4. The barrel lies within a radius of 1500 and 1980 mm from the beamline, and extends to a half length $|Z|$=3150 mm, providing pseudorapidity coverage up to an $|\eta| < 1.4$. It has a minimum depth of 26.5 X_0. In order to obtain a symmetric detector, without any cracks in the azimuthal angle, the 1024 lead absorbers have been given the accordion shape presented in figure 2.9. Shown in figure 2.10 (a) the waves of the accordion in the barrel region extend outward in radius. The stainless steel sheets are 0.2 mm thick (added for stability) and the thickness of the lead is 1.8 mm for an $|\eta| <0.9$ and 1.2 mm for an $|\eta| <2.4$. Located in the middle of any two absorbers there are

32

	Barrel	EndCap
electromagnetic calorimeter		
η coverage	1.4	1.4-3.2
Depth samples		
presampler	1	-
calorimeter	3	3
Granularity $\Delta\eta \times \Delta\phi$		
Presampler	0.025×0.1 ($|\eta| < 0.8$)	-
	0.003×0.1 ($|\eta| > 0.8$)	
calorimeter	0.003×0.100	0.003×0.100 ($|\eta| < 2.4$)
	0.025×0.025	0.025×0.025 ($|\eta| < 2.4$)
	0.025×0.050	0.025×0.050 ($|\eta| < 2.4$)
		0.050×0.050 ($|\eta| > 2.4$)
Read out Channels		
presampler	32000	
calorimeter	100000	82000 (both sides)
LAr hadronic EndCap		
$|\eta|$ coverage	-	1.5-3.2
Depth Samples		4
Granularity $\Delta\eta \times \Delta\phi$		0.1×0.1($|\eta| <$2.4)
		0.2×0.2($|\eta| >$2.4)
Readout Channels		8600 (both sides)
LAr forward calorimeter		
$|\eta|$ coverage	-	3.1-4.9
Depth Samples	-	3
Granularity $\Delta\eta \times \Delta\phi$	-	$\approx$ 0.15×0.15
Readout Channels	-	1500 (both sides)
	Barrel	Extended Barrel
Scintillator tile calorimeter		
$|\eta|$ coverage	<1.0	1.0-1.6
Depth Samples	3	3
Granularity $\Delta\eta \times \Delta\phi$	0.1×0.1	0.1×0.1
	0.2×0.1 (last sample)	0.2×0.1 (last sample)
Readout Channels	6000	4000 (both sides)

Table 2.4: The granularity and coverage for the various ATLAS detector components. The finer granularity in the EM calorimetry allows for better sampling of the higher multiplicity EM jets, and as such EM calorimetry tends to have a better sampling resolution term than its hadronic counterpart.
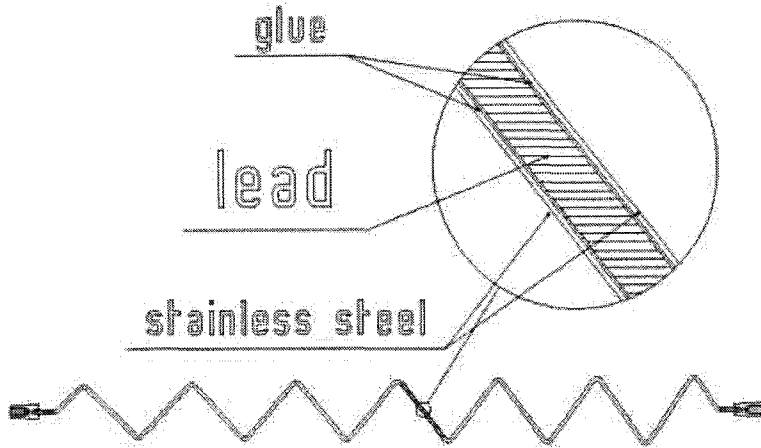
Figure 2.9: A schematic of the absorber plate used in the accordion LAr EM Barrel.
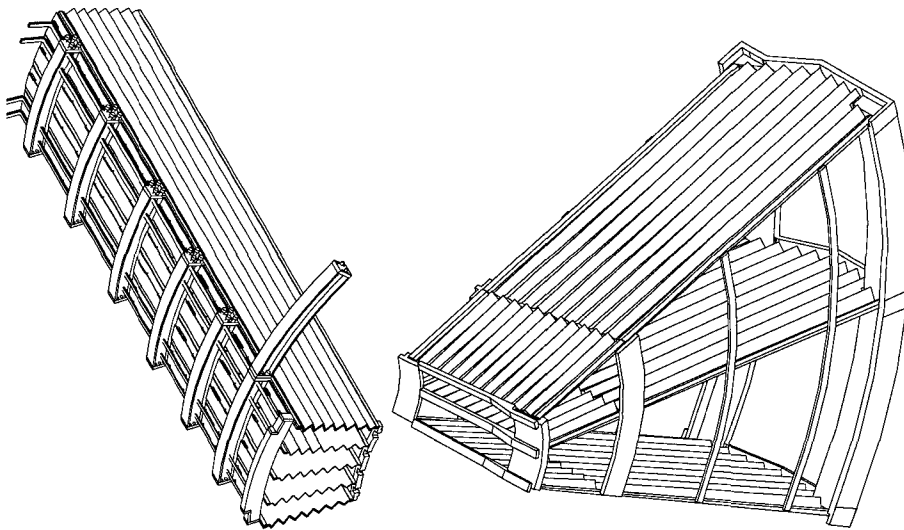
Figure 2.10: (a) In the EM barrel the waves of the accordion extend outward in radius. (b) In the EM endcap the waves of the accordion travel parallel to the beamline.

two gaps for LAr (2 x 1.94 mm). The 300 μm readout electrodes are sandwiched between the two LAr sections. To keep the LAr gap and sampling fraction constant the folding angle of decreases from 90.7° to 67.5° as the radius increases.

The electromagnetic (EM) EndCap covers a pseudo-rapidity range of $1.4 < |\eta| < 3.2$. It has an inner radius of 296 mm and an outer radius of 2030 mm with the front face of the wheel a distance of 3623 mm from the interaction point (IP). The folds in the plates, shown in figure 2.10 (b), are arranged such that they are traveling in a direction parallel to the beamline. To ensure that the amount of absorber and detector that a particle travels through is independent of angle, the EndCap is broken up into an inner and outer wheel each of which possess a different folding angle. The EM EndCap provides a minimum of 28

34
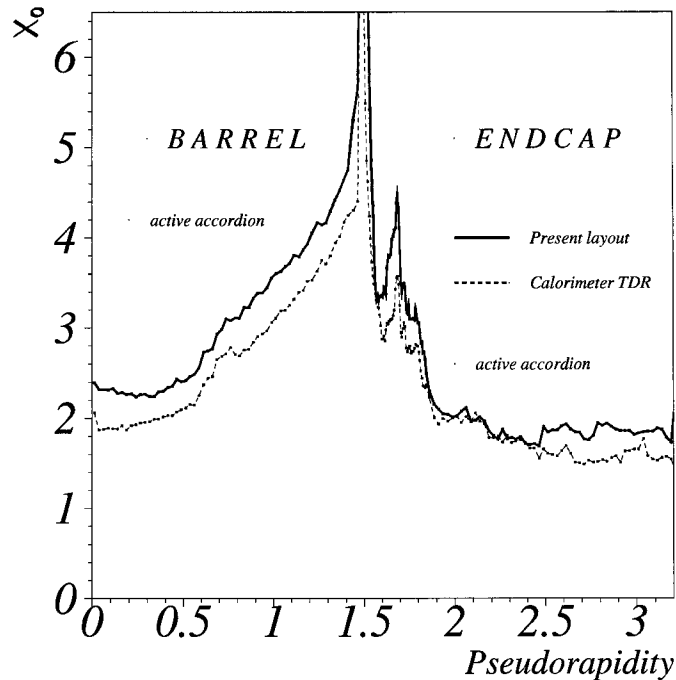
Figure 2.11: The amount of material in front of the EM calorimetry as a function of pseudorapidity.

X_0 for the full pseudorapidity range.

Figure 2.11 shows that there is a large amount of material between the interaction point and the EM calorimeter, namely the inner detector cryostat and the solenoid. An electron may therefore start to shower prior to reaching the calorimeter. The installation of pre-samplers allows the position and energy of the incident particle to be more accurately reconstructed. The barrel presampler covers a pseudorapidity of ± 1.4, the EndCap presampler extends coverage to a maximum value of 1.8.

Test beam results on the EM barrel and EndCap give a combined resolution for electromagnetic showers of:

$$\frac{\Delta E}{E} = \frac{10\%}{\sqrt{E}} \oplus \frac{400\text{MeV}}{E} \oplus 0.7\% \tag{2.10}$$

2.2.3 Hadronic Calorimeter

The hadronic interaction length (λ, the length over which the energy drops by a factor e) characterizing hadronic energy loss is typically greater than the EM radiation length (X_0). Therefore the hadronic calorimetry is thicker and placed farther from the interaction point than the electromagnetic calorimetry.

35

The number of particles in a hadronic shower is typically much smaller than that of an EM shower, only on the order of 50 secondary pions for a 50 GeV incident pion. Furthermore, up to 30% of the incident particle's energy is lost due to non-observable interactions: breakup of nuclei, spallation, evaporation of slow moving nucleons, neutrino production to name a few. The hadronic shower usually has a sizeable electromagnetic component due to the production of neutral pions.

One of the design goals of ATLAS is to provide an accurate measurement of missing energy, and as such we need hadronic calorimetry with as much pseudo-rapidity coverage as possible. The Hadronic calorimetry has 3 detector systems: the Tile barrel, the Hadronic EndCap (HEC) and the Forward Calorimetry (FCAL). The radiation hard Forward Calorimeter provides coverage to within 1° of the beam line.

The Tile Barrel Calorimeter (tilecal) lies outside the EM barrel between a radius of 2.28 m and 4.23 m, and extends to a maximum pseudorapidity of 1.6. As this is a low radiation area, ATLAS has chosen to depart from the standard LAr calorimetry and instead utilize a scintillator-iron sampling calorimeter comprised of scintillating tiles oriented perpendicular to the beamline, within iron absorbers as shown in figure 2.12. The iron absorbers generate showers which produce light in the scintillators. Wavelength shifting fibers are used to transport the signal from the scintillators to the supporting girder which house the electronic readout. Each of the three cylinders in the tile calorimeter, 1 barrel and 2 EndCap, is composed of 64 wedges in the azimuthal direction with a granularity in $\eta \times \phi$ of 0.1×0.1. The tilecal has a radiation depth of 9.5 λ.

Each Hadronic EndCap consists of two separate wheels containing 32 modules, and provides coverage to a pseudorapidity of 3.2. Using copper as an absorber the calorimeter can meet the requirements of a 10 λ depth. The first wheel, located closest to the IP, has flat 25 mm thick copper plates, separated by an 8.5 mm liquid argon gap, while the second wheel implements 50 mm thick plates. This gap increase in the LAr (over the iron absorber used in the EM calorimeter) reduces the individual cell capacitance, and reduces the overall electronic noise.

The granularity of the hadronic EndCaps is 0.1×0.1 up to a pseudorapidity value of 2.5, and then 0.2×0.2 for the remainder of the EndCap and the FCAL. The expected energy
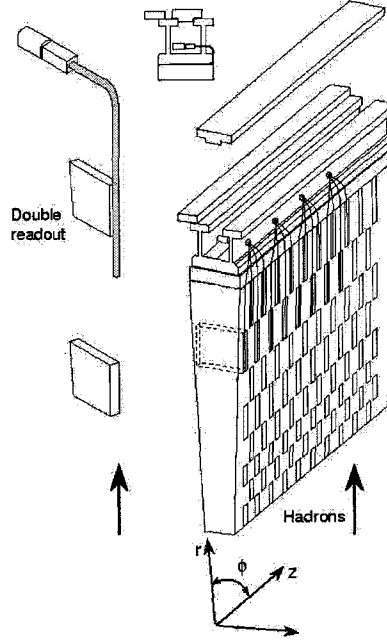
Figure 2.12: One module of the tile calorimeter which is a sampling calorimeter that uses scintillating tiles embedded in iron.

resolution of the hadronic calorimetry is given in equation 2.11.

$$\frac{\Delta E}{E} = \frac{50\%}{\sqrt{E}} \oplus 3\% \quad \text{Central+EndCap Region}$$

$$\frac{\Delta E}{E} = \frac{100\%}{\sqrt{E}} \oplus 10\% \quad \text{Forward Region}$$

(2.11)

2.2.4 Forward Calorimetry

The forward region, covering the pseudorapidity range $3.2 < |\eta| < 4.8$, is subject to extremely high radiation levels (2300 kGy/yr according to table 2.3), which force a change in the calorimeter design.

The forward calorimeter (FCAL) is a metal matrix that is interspersed with hollow tubes (each with 5 mm diameter) as shown in figure 2.13. A nylon/plastic fibre, of thickness 250 μm, is used to separate the hollow tube from a metal rod which measures 4.5 mm in diameter. The remaining space between the tube and the rod is filled with liquid argon. The rods are then set at 250 V, providing a 10 kV/cm electric field. The average separation of neighbouring electrodes is roughly 1.5 times the hollow tube diameter. As in the EndCap the small gap avoids the build up of ions due to the large amount of radiation in this region which could distort the internal electric field.

37
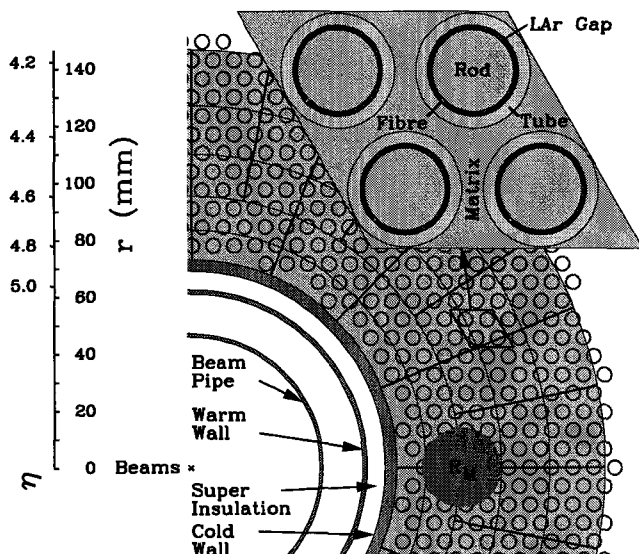
Figure 2.13: The metal matrix design of the forward calorimeter in ATLAS.

The FCAL is built from three different modules. The first module closest to the interaction point is an EM module made with copper absorbers. The next two modules are hadronic, where the matrix and the rods are built out of a tungsten alloy and the tubes are stainless steel. Usually the energy of an event is confined to the first two modules, the third is meant to catch the tail of the shower.

2.2.5 Energy Shapers

When the LHC is running at High Luminosity ($L=10^{34}cm^{-2}s^{-1}$) there will be, in addition to the signal event, approximately 23 extra events which are "piled" on top of the signal[3]. The specific makeup of these pile-up events will be discussed later in section 3.1.2. This increases the measured energy of the event, and worsens the effective overall energy resolution of the ATLAS detectors. Since the ionization chambers have a finite charge collection time we would need to integrate over approximately 400 ns, figure 2.14(a), to include the "tail" of the event. During this time period there have been an additional 16 bunch crossings within the detector.

The addition of the bipolar shaping algorithm reduces the effects of pileup. The shaping function integrates out to zero, so the energy added by the pileup events in 24 bunches also integrates to zero. But because pileup is a random process, we are still left with a poorer effective energy resolution.

---

[3]The number of events added at high luminosity actually follows a Poisson distribution with a mean value of 23.

38
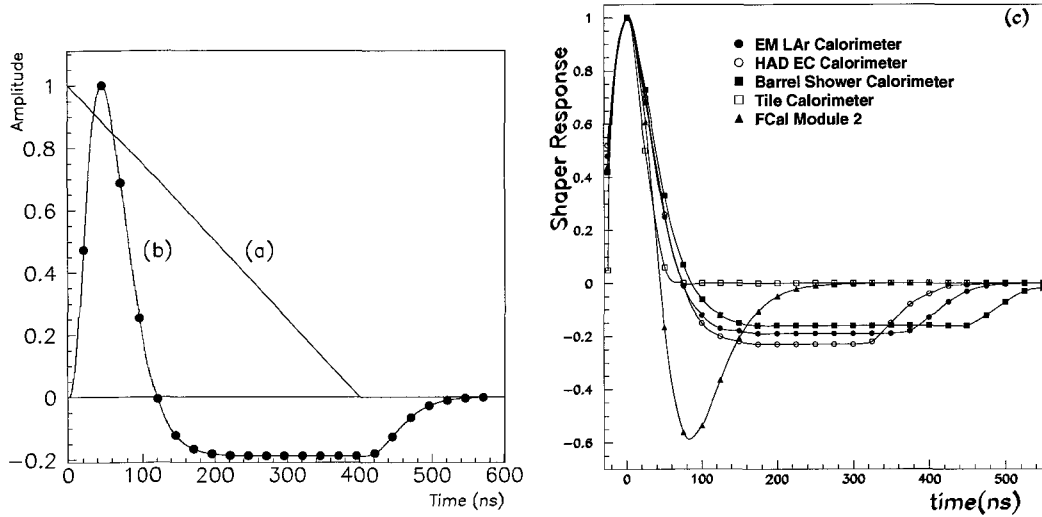
Figure 2.14: (a) For any ionization chamber there is finite drift time for the ions resulting in a drift current versus time plot (the solid line). (b) The bipolar shaping function quickly attenuates the signal and averages away the energy of the pileup events that occur every bunch crossing (the circles on the graph). (c) The shaping functions for a variety of the calorimeters.

Each calorimeter has a slightly different response to the signal due to its mechanical design. We can maximize detector resolution by using shaping functions, figure 2.14(c), tuned to the individual calorimeters [46].

2.2.6 Muon System

Muons interact primarily through their electromagnetic charge, but since they are 200 times more massive than the electrons they are less affected by the electric fields (for energy loss via bremsstrahlung $\frac{dE}{dx} \propto \frac{-1}{m^2}$) of the nuclei they encounter. Muons with an energy of more than a few GeV penetrate the calorimetry and reach the muon spectrometer. The muon system has been constructed to:

- Identify and reconstruct muon tracks, measure their momenta and provide matching to the corresponding inner detector tracks.

- Trigger on single or multi-muon event topologies.

- Conclusively associate the muon with its bunch crossing.

Magnet system

The magnetic field of the muon system is provided by three air toroid super-conducting magnets; one barrel and two EndCaps as shown in figure 2.15. The barrel toroid has a

39
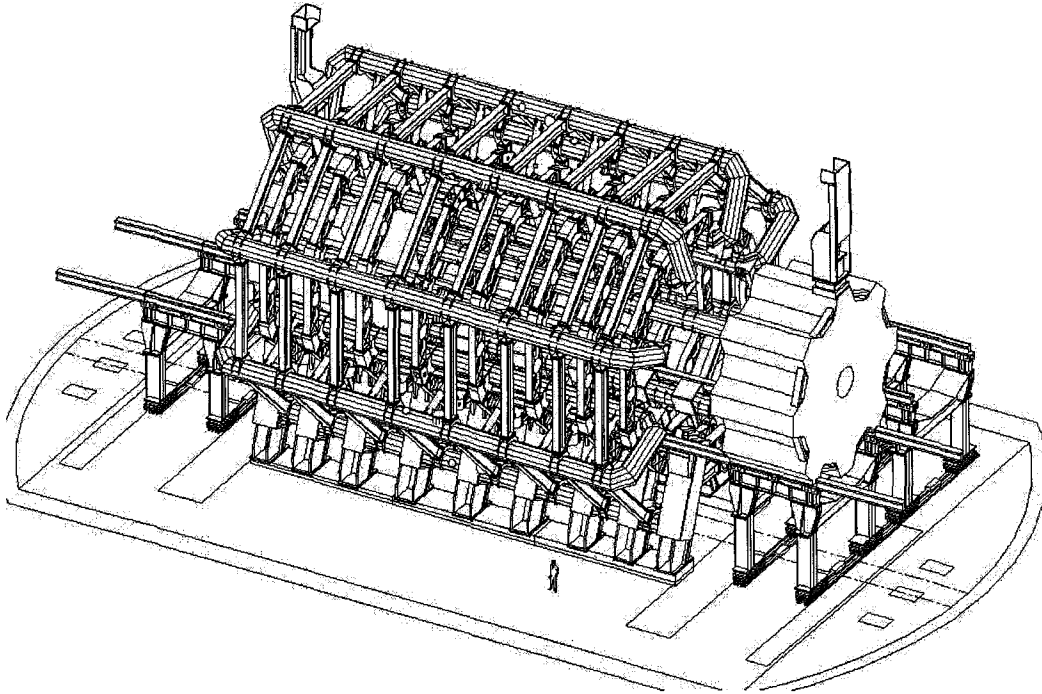
Figure 2.15: A 3-dimensional view of the ATLAS muon superconducting toroidal magnet system. One EndCap toroid is shown removed from its inserted position.

length of 25 m and an inner bore of 9.4 m and an outer diameter of 20.1 m. The two EndCap toroids have an inner bore of 1.65 m and an outer diameter of 10.7 m. Each toroid consists of eight flat coils that are assembled radially and uniformly around the beamline. The toroids provide 3 T·m bending power in the barrel region and 6 T·m in the EndCap region. The uniformity of the magnetic field lines in the transition region between the barrel and the EndCap is shown in figure 2.16.

Muon Spectrometer

A cross-section of one quadrant of the muon spectrometer is shown in figure 2.17. In the barrel region, $|\eta| < 1.0$, the muon system provides 3 measurements at radii of approximately 5, 7.5 and 10 m. In the forward region up to an $\eta = 2.7$, measurements are taken by discs at distances from the interaction point of : 7, 10, 14 and 20 m. These measurements are provided by 4 different chamber technologies: two for precision spatial measurements, Monitored drift tubes and cathode strip chambers; and two for timing/triggering, resistive plate chambers, and thin gap chambers.

In order to obtain precision spatial resolution measurements of 60 μm in the bending

40
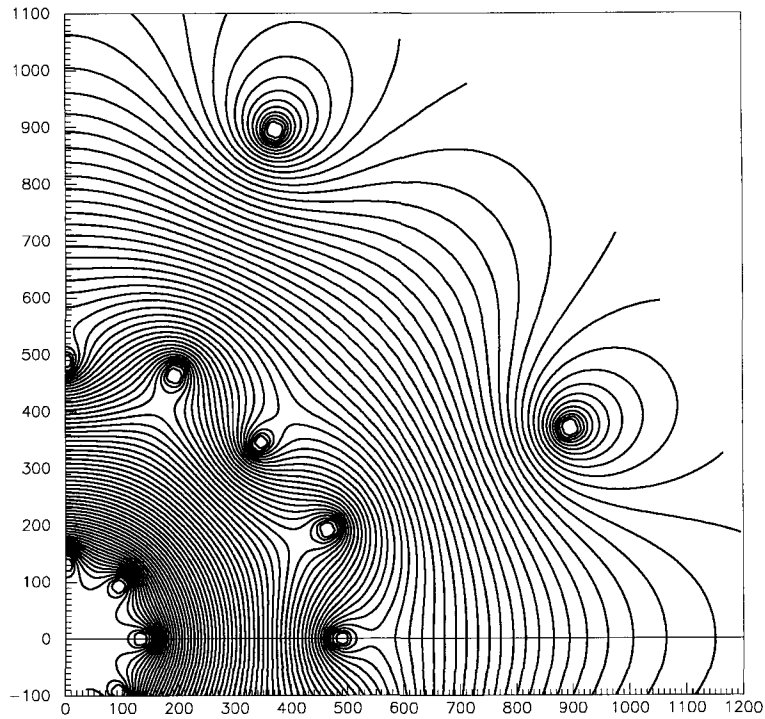
Figure 2.16: Due to the limited number of coils the magnetic field lines are slightly rippled. This field map is for the transition region between the barrel and EndCap toroids.
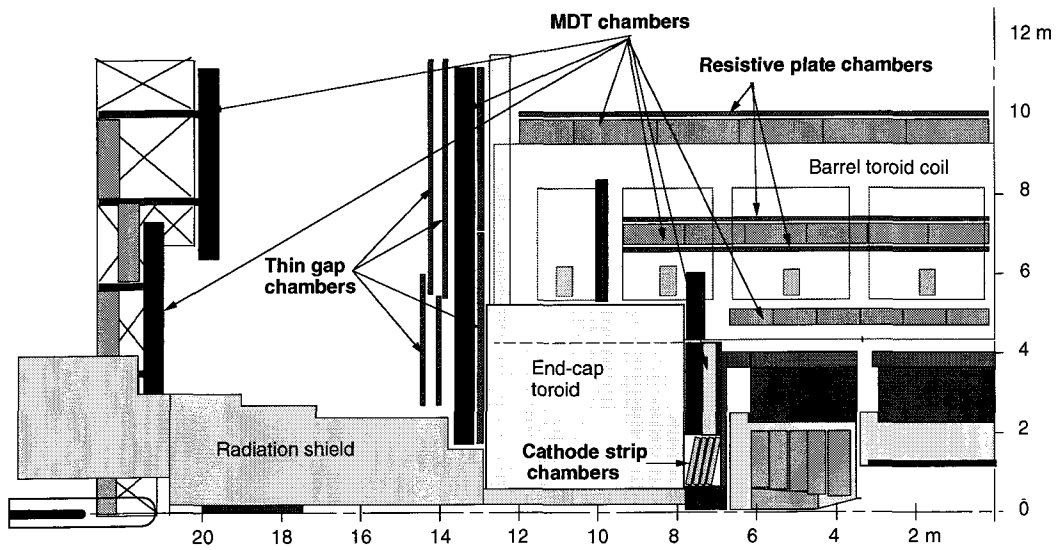
Figure 2.17: A rz (radial:z-coordinate) cross-section of one quadrant of the ATLAS muon system. The third layer of MDTs in the forward region are mounted on the cavern wall.

41

direction of the magnetic field Monitored Drift Tubes (MDT) are used up to a maximum pseudorapidity of 2.0. Such precision is possible because of the inherent precision of the detectors combined with a laser alignment system which is used to determine the precise spatial position of the chamber with respect to other detectors and the detector itself. For larger pseudo-rapidity values ($2.0 < |\eta| < 2.7$), in the inner most region of the EndCap where the particle fluxes are higher, cathode strip chambers (CSC) are used. CSC are fast multi-wire proportional chambers with a symmetric cell in which the anode-cathode distance equals the anode-wire spacing (2.5 mm). Measurement of the center of gravity of the collected charge allows for spatial resolution of 50 μm.

The trigger system provides pseudorapidity coverage over $0 < |\eta| < 2.4$, bunch crossing identification and the measurement of the "second coordinate"[4]. Resistive plate chambers are gaseous parallel plate chambers that allow for both good spatial and timing resolution (1 cm $\times$ 1 ns) to an η=1.6. Each chamber has two orthogonal strips (parallel and orthogonal to the MDT wires) that allow for a two dimensional readout of the particle position. The RPC's are located on either side of the middle MDT station, and on the outside of the outer MDT. In the EndCap, in the pseudo-rapidity range between 1.6 and 2.4, three stations of Thin Gap Chambers (TGC) are used. Thin Gap Chambers are similar to multi-wire proportional chambers. TGC's sandwich 50 μm wires, with 1.8 mm pitch, between two graphite cathodes at a distance of 1.4 mm from the anode plane. The second coordinate is measured by readout strips located behind the cathode planes.

Figure 2.18 gives the muon resolution that is possible when the independent muon measurements from the Inner Detector and the Muon Spectrometer are combined.

2.3 Data Acquisition And Trigger

The LHC has a 40 MHz bunch crossing rate. For average event sizes, approximately 1 MB, data can only be stored at a rate of about 100 Hz. In order to reduce the trigger rate to approximately 100 Hz ATLAS implements the three level trigger system shown in figure 2.19.

The Level 1 trigger uses only the muon system and the calorimetry with a coarse granularity of $\Delta\eta \times \Delta\phi$=0.1$\times$0.1. This trigger looks for high transverse energy muons, high E_T isolated EM clusters, highly E_T hadronic jets or large missing E_T. The Level 1 trigger has approximately 2 μs to accept or reject the event, thus reducing the data rate to about 50 kHz.

---

[4]The second co-ordinate is a position measured along the magnetic field.

42
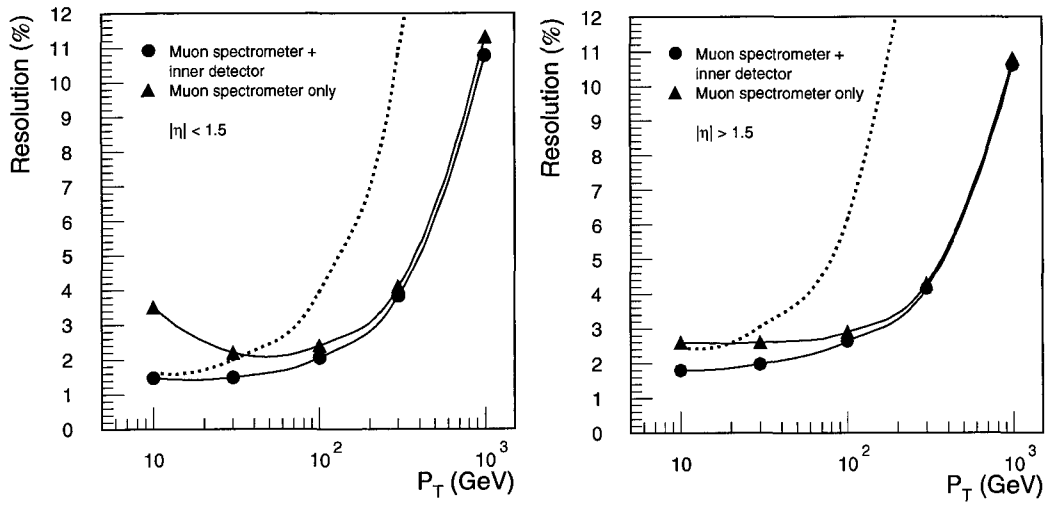
Figure 2.18: The combined muon momentum resolution for $|\eta| < 1.5$ and $1.5 < |\eta| < 2.7$. The dashed curve resolution of the inner detector. The filled circles represent the resolution from the muon spectrometer, and the triangles the combined resolution. The resolutions are averages over the $\eta \times \phi$ space.
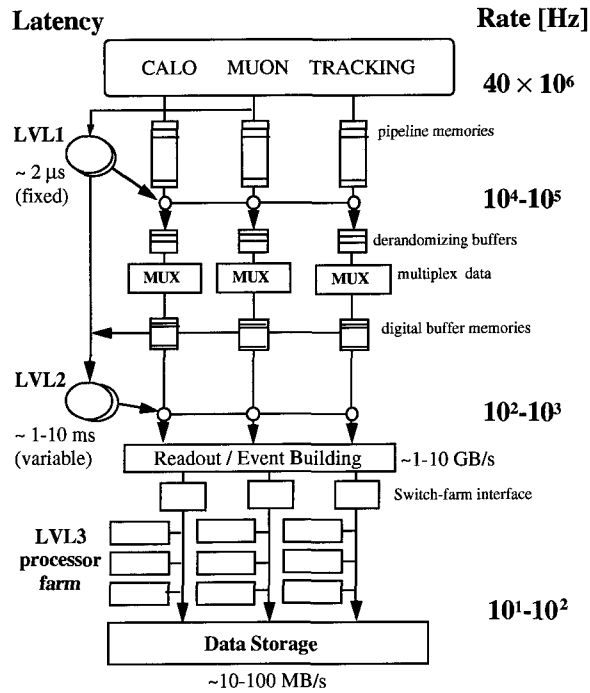
Figure 2.19: Schematic diagram detailing the ATLAS 3 level trigger system.

43

Level 1 Trigger				Level II Trigger			
10^{33} cm^{-2}s^{-1}		10^{34} cm^{-2}s^{-1}		10^{33} cm^{-2}s^{-1}		10^{34} cm^{-2}s^{-1}	
Trigger	Rate (kHz)	Trigger	Rate (kHz)	Trigger	Rate (Hz)	Trigger	Rate (Hz)
MU6	23	MU20	3.9	μ20	200	μ20i	200
		MU6x2	1			μ6x2+m$_B$	10
						μ10x2	80
EM20i	11	EM30i	22	e20i	100	e30i	600
EM15ix2	2	EM20ix2	22	e15ix2	few Hz	e20ix2	20
				γ40i	100	γ60i	400
				γ20ix2	5	γ20ix2	100
J180	0.2	J290	0.2	j180	100	j290	120
J75x3	0.2	J130x3	0.2	j75x3	80	j130x3	80
J55x4	0.2	J90x4	0.2	j55x4	4	j90x4	80
J50+XE50	0.4	J100 +XE100	0.5	j50+xE50	250	j100+xE100	$\approx$ 100
T20+XE30	1	T60 +XE60	1	τ20+xE30	400	τ60+xE60	$\approx$ 100
		MU10 +EM15I	0.4	μ6i+e15i	15	μ10i+e15i	
B-Physics					1150		
other	5		5		100		100
TOTAL	44		40		2400		2000

Table 2.5: ATLAS first and second Level Trigger tables as given in the ATLAS TDR. The first three rows give the trigger conditions for muons(MU,μ). The following four rows are the trigger settings for electrons(e) and photons(γ). The next three rows give the single(j) and multijet(jx3,jx4) trigger requirements. The last section specifies the jet and missing energy trigger, tau lepton and missing energy, and muon+electron trigger respectively.

44

The regions of interest highlighted by the Level 1 trigger constitute the input for the Level 2 trigger. At Level 2 each region of interest is examined, at full resolution, in the detector system in which it was identified to determine if it is confirmed as a valid object. After confirmation, features of the object are then searched for in other detectors; for example an inner detector track corresponding to the electron initiator of an electromagnetic cluster. The information from all systems is then combined to produce candidates for such objects as muons and jets which form the input to the LVL2 global decision. The trigger thresholds presented in table 2.5 and the analysis software written for the Level 2 trigger can be modified as often as necessary during the lifetime of the experiment. This trigger has a latency time of about 1 to 10 ms and reduces the trigger rate to about 1 kHz.

The ATLAS TDR succinctly summarizes the Level 1 and Level 2 trigger values along with their expected rates. These expectations are given in table 2.5. The two different ATLAS luminosities have similar cuts, but differing thresholds. The muon trigger extends to $\eta_{muon} = 2.4$, the EM trigger $\eta_e = 2.5$, the jet trigger $\eta_{jet} = 3.2$ and the $\not{E}_T$ (missing transverse energy) trigger uses the full pseudo-rapidity range of the ATLAS detector. For the analysis performed in this thesis it is essential to ensure that the selected events will also pass the trigger criteria.

The Level 3 trigger, also known as the event filter, will use offline physics and event reconstruction algorithms accessing the full event data. Vertex reconstruction and track fitting are examples of algorithms that can be run at this level. The event filter completes the classification of the event and establishes a catalogue of discovery type events. This trigger utilizes normal PC workstation clusters which may be upgraded when significant processor advancements are made. The Level 3 trigger has a couple seconds to determine wither or not to accept the event producing output at a rate of 10-100 Hz.

The four components of the ATLAS detector: the inner detector, electromagnetic and hadronic calorimetry and the muon spectrometer have been designed to provide excellent spatial, timing and momentum resolution for any subatomic particle. The ATLAS detector is therefore capable of making precision measurements of the Standard Model as well as being prepared for the possibility of new physics.

45

Chapter 3

Monte-Carlo Issues

The simulation phase of this thesis is broken into 3 steps: Monte-Carlo event generation, detector modelling and event reconstruction. The steps are summarized by the flowchart in figure 3.1.

1. The Monte-Carlo program PYTHIA, version 6.227 [47], is used to generate a tree level history of all the outgoing particles from a high energy physics event. The energy and type of incident particles are specified by the user. The PYTHIA program also allows the user to specify a specific channel of interest and restrict the accepted kinematic range of the process. A branch in the tree is produced when a particle decays or a string fragments. A branch is terminated when only stable particles are produced.

2. There are two programs used to model the response of the ATLAS detector: full simulation using DICE (version 3.20) and ATRECON (version 1.41) and fast simulation using ATLFAST (00-00-22) [48]. Full simulation uses GEANT 3.21 [49] to model the interaction of the event particles with the components of the ATLAS detector. The digitization of the GEANT information is performed by DICE. ATRECON interprets
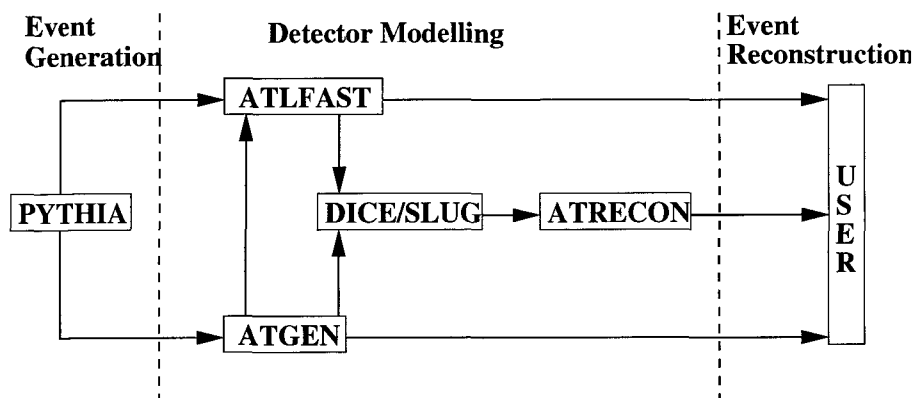
Figure 3.1: A flowchart detailing the progression of an ATLAS analysis.

46

DICE and outputs physical quantities such as cell energy, electromagnetic cluster and muon information to the ATLAS combined ntuple (CBNT). The full simulation interface to PYTHIA is mediated by the GENZ event manager. The conversion from the PYTHIA common block can by completed by either the standard GENZ libraries in FORTRAN or with the ATGEN 2.0 [50] program. The FORTRAN based ATLFAST can link directly the PYTHIA common block or accept input in the GENZ data format.

3. ATLFAST allows the user to add their own analytical FORTRAN subroutines to perform event reconstruction using the ATLFAST common blocks as input. Full simulation implements similarly structured FORTRAN code but uses the ATRECON combined ntuple (CBNT) as its input. At this stage both full and fast simulation output their results to an HBOOK[51] which contain the important variables that describe the event topology. HBOOK is a package that handles statistical distributions in a FORTRAN scientific environment. An hbook file provides a compressed view of a physics event, in the form of histograms and ntuples, and it is from these files that we will extract our final results.

Steps 1 and 3 are virtually identical between the full and fast simulations and take approximately the same amount of time. However due to the complexities of the GEANT program, particularly shower formation in the calorimeter (a process not modelled in ATLFAST), full simulation takes much longer to model the detector response (step 2) to an event. The analysis of 50 events takes approximately 6 hours in full simulation but just under 6 seconds in fast simulation. The cross-section for the dominant backgrounds is on order 10^7 times larger than the signal indicating that any analysis would require a background data set that is 10^7 larger than the signal set. The production of 10^7 events requires approximately 140 CPU years in full simulation but only 0.04 CPU years for fast simulation[1]. While full simulation produces the most accurate results an ATLFAST analysis provides a more manageable time-line. The modifications that were made to the ATLFAST software to bring it into agreement with the full simulation are described as required.

3.1 Calorimeter modifications

Extra energy, not related to the studied event, can be introduced into the ATLAS calorimetry through two processes: electronic noise from the readout and pileup. Electronic noise arises from the inherent noise in the calorimetry electronics. Pileup is due to the presence

---

[1]These numbers have been determined using a Intel Pentium IIIprocessor with a 1.4 GHz CPU.
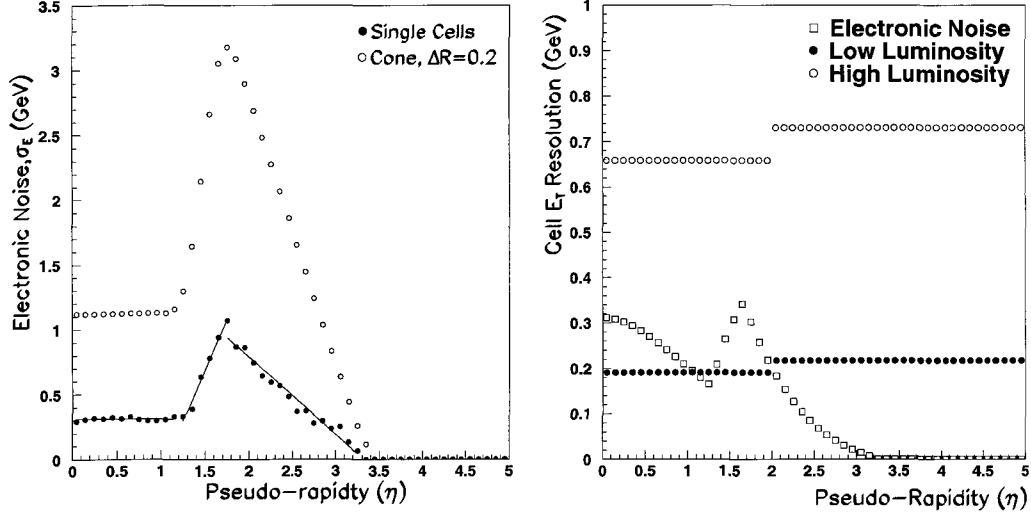
Figure 3.2: (a) Electronic noise in a 0.1×0.1 cell in the ATLAS calorimetry, the unfilled circles represent the noise level present in a cone of radius ΔR=0.2. (b) The width contribution to the cell level E_T measurement due to electronic noise and pileup, averaged over the azimuthal angle, as a function of pseudo-rapidity.

of minimum bias events that overlay the signal event.

3.1.1 Electronic Noise

To introduce the effects of electronic noise in ATLFAST, a parameterization of the noise level must first be obtained from fully simulated data. Electronic Noise is included in full simulation when ATRECON is run with the following flags:

*DETP 'CALO'	'CCAL(1).Inoi=' 1.	'CCAL(2).Inoi=' 1.	'CCAL(3).Inoi=' 1.
	'CCAL(4).Inoi=' 1.	'CCAL(5).Inoi=' 1.	'CCAL(6).Inoi=' 1.
	'CCAL(11).Inoi=' 1.		
	'CCAL(1).calmod=' 1.	'CCAL(2).calmod=' 1.	'CCAL(3).calmod=' 1.
	'CCAL(4).calmod=' 1.	'CCAL(5).calmod=' 1.	'CCAL(6).calmod=' 1.
	'CCAL(11).calmod=' 1.		
	'CCAL(1).ThrNo=' 0.	'CCAL(2).ThrNo=' 0.	'CCAL(3).ThrNo=' 0.
	'CCAL(4).ThrNo=' 0.	'CCAL(5).ThrNo=' 0.	'CCAL(6).ThrNo=' 0.
	'CCAL(11).ThrNo=' 0.		

At any given pseudo-rapidity value electronic noise has a Gaussian distribution about a mean value of zero with a width σ_E. Figure 3.2(a) shows that there are three distinct pseudo-rapidity regions in regards to electronic noise. The solid lines in figure 3.2(a) are the straight line fits to each of these three pseudorapidity regions; the equations of best fit are given in equation 3.1.

$$\sigma_E(GeV) = \begin{cases} 0.031 & |\eta| \leq 1.25 \\ -1.78 + 1.64 \times |\eta| & 1.25 \leq |\eta| \leq 1.75 \\ 1.90 - 0.57 \times |\eta| & 1.75 \leq |\eta| \leq 3.25 \\ 0 & 3.25 \leq |\eta| \end{cases} \quad (3.1)$$

48

ISUB	Process	Cross Section (mb)
0	All included subprocesses	101.5
91	Elastic scattering	22.21
92	Single diffractive (XB)	7.151
93	Single diffractive (AX)	7.151
94	Double diffractive	9.736
95	Low-pT scattering	0.000

Table 3.1: The subprocesses comprising minimum bias events in ATLAS; instituted in PYTHIA under the MSEL=2 flag.

The addition of electronic noise worsens the resolution of any energy measurement performed by the calorimetry. For example, the open circles in figure 3.2(a) give the contribution to the width of this measurement as a function of pseudorapidity when the energy is determined by summing up all the cells within a cone radius of 0.2 ($\Delta R = \sqrt{(\Delta\eta)^2 + (\Delta\phi)^2} < 0.2$).

Electronic noise will be present in the forward calorimetry ($|\eta| > 3.2$) when the ATLAS detector is operating but it was not modelled in the version of ATRECON utilized in this thesis. The effects of electronic noise in this region are expected to be negligible compared to the dominance of pileup in this pseudorapidity region. The electronic noise and pileup contributions to the E_T resolution (σ_E and σ_P respectively) in full simulation as a function of pseudo-rapidity are compared in figure 3.2(b). The total combined resolution of a single calorimeter cell due to these factors would be $\sqrt{\sigma_E^2 + \sigma_P^2}$. The contribution to the resolution due to pileup is prone to large fluctuations over small pseudo-rapidity regions, especially in the forward calorimeter. The open and closed circles in 3.2(b) give the average widths for a single cell E_T measurement for $|\eta| < 2.0$ and $|\eta| > 2.0$. Electronic noise is added to the calorimetry in ATLFAST only after the addition of pileup and the cell level energy smearing effects.

3.1.2 Luminosity Pileup

When running at high (low) luminosity there will be on average 23 (2.3) extra events per bunch crossing. Therefore the bunch crossing (interacting proton bunches travelling in opposite directions) containing the signal will also contain the energy of, on average, 23 extra minimum bias events "piled" on top of the signal event. For this analysis we adopt the pileup prescription used in [52]; table 3.1 lists the subprocesses that contribute to the minimum bias events. The parameters related to the minimum bias prescription used in this thesis are given in table 3.2.

	Switch	Implemented
PDF		CTEQ5L
Multiple Interaction	MSTP(81)	1
Model	MSTP(82)	4
PT min	PARP(82)	2.0
	PARP(89)	1800
	PARP(90)	0.25
Core Radius	PARP(84)	0.4
Gluon Production	PARP(85)	0.9
Mechanism	PARP(86)	0.95
α_s and K-factors	MSTP(2)	1
	MSTP(33)	0
Regulating Initial State Radiation	PARP(67)	1

Table 3.2: Default PYTHIA 6.227 flags pertaining to minimum bias events.

The bipolar shaping function, introduced in section 2.2.5, weights the event energy by a factor corresponding to its bunch crossing. The shape of the weighting function is chosen such that, on average, the amount of energy overlapping the signal event is removed by the negative weighting of later bunches. This ensures that the average energy added to the calorimetry is zero. In full simulation pileup energy is added at the cell level. In our modified version of ATLFAST pileup is added at the particle level. The simulation programs cycle through the 24 bunch crossings covered by the shaping functions; the number of events included in each bunch crossing follows a Poisson distribution with a mean depending on luminosity: 23 and 2.3 events for high and low luminosity respectively. Events are then randomly sampled from a pre-existing reservoir of 5000 minimum bias events. The ATRECON combined Ntuple only provides access to the projected calorimeter matrix[2], so the event weighting was simplified into 3 sections (ATLFAST also uses this segmentation):

- $0.0 < \eta < 1.5$: EM LAr shaping function

- $1.5 < \eta < 3.2$: Hadronic LAr Shaping function

- $3.2 < \eta < 5.0$: FCAL2 shaping function

The particular weightings of these shaping functions are given in figure 2.14. The time required for event production in full simulation precludes the generation of a significantly large minimum bias reservoir. For each data run in ATLFAST a different reservoir of minimum bias events is generated thereby minimizing the systematic errors that would arise from sampling the same minimum bias event repeatedly. Each minimum bias event that is added as pileup event in full simulation has already been subject to the resolution affects of

[2]The projected calorimeter matrix has a granularity of 0.1×0.1 in the barrel region and 0.2×0.2 in the forward region. It contains the combined energies from the EM and hadronic calorimetry.

50
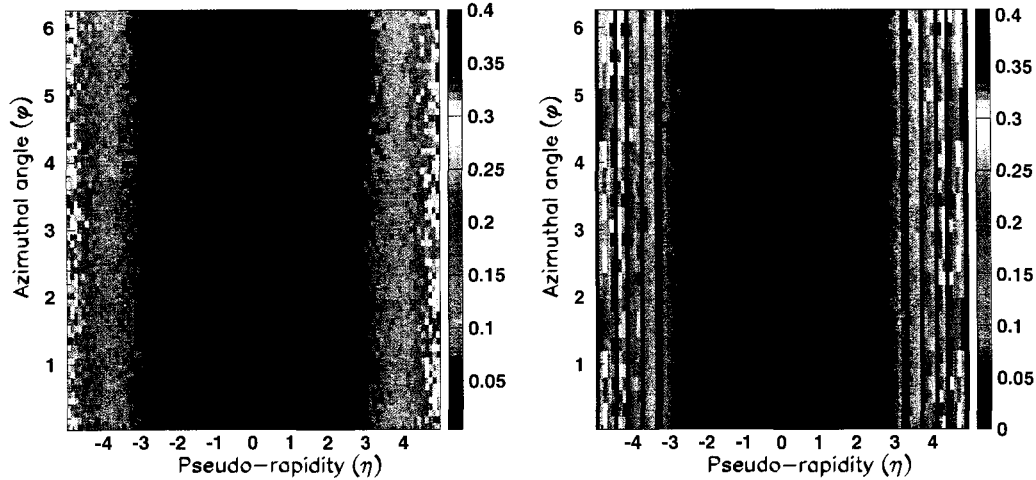
Figure 3.3: (a) The left graph depicts the average energy deposited in ATLFAST(in GeV) by minimum bias events.(b) The average amount of energy deposited by the same minimum bias events in full simulation.

the ATLAS calorimetry. The detector resolution effects are applied to ATLFAST after the pileup energy has been added.

Full and fast simulations were used to generate 5000 minimum bias events, each minimum bias data set was then projected into a single calorimeter matrix. Figure 3.3 compares the average amount of energy deposited by a single full and fast simulated minimum bias event at different $\eta \times \phi$ regions of the ATLAS calorimeter. The vertical dark bands in the full simulation plot are due to the increased granularity in the forward calorimeter: 0.2×0.2 as opposed to barrel 0.1×0.1 cell size. The distribution is roughly constant with azimuthal angle. Taking an average over the azimuthal angle and a larger pseudorapidity binning ($\Delta\eta = 0.5$), figure 3.4 shows good agreement in the average amount of energy deposited by pileup in full and fast simulations.

Tracks due to Pileup

While the effects of pileup are most dominant in the forward region, a sizable component of the energy is deposited in the central region as well. Particles in the central region due to pileup will produce tracks in the inner detector. According to [53] all the tracks that occur in the same bunch as the signal must be considered. In addition at high luminosity an additional 9 events from either side of the signal bunch must also be included. The vertex location of pileup tracks will be displaced from the primary vertex following a Gaussian distribution with full width half-maximum (FWHM): $\sigma_x = \sigma_y$=16 μm, σ_z =7.5 cm. This

51
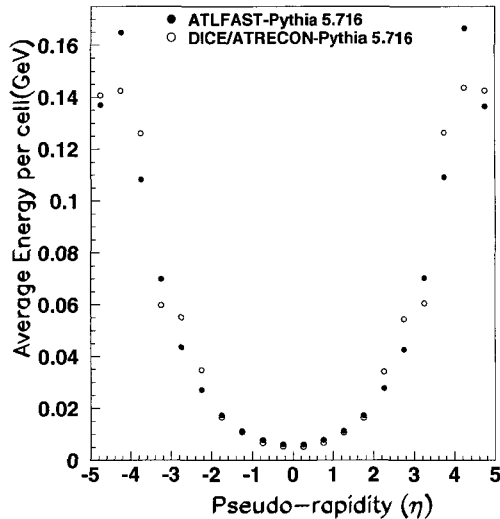
Figure 3.4: When the calorimeter is broken into larger pseudorapidity sections, in this case $\Delta\eta$=0.5, the amount of energy deposited in the two simulation programs is seen to be in reasonable agreement.

displacement of the vertex locations will facilitate in the identification of signal and pileup tracks.

3.2 Jet algorithms

Jet algorithms are routines that are used to identify hadronic jets in the calorimetry. These jets arise from the hadronization of quarks or gluons. Several routines current exist and the most common are outlined in this section.

3.2.1 Cone Algorithm

The cone algorithm is the default jet-finding routine of ATLFAST. It consists of three simple variables: a minimum transverse energy for possible jet initiators (E_T^{init}), a threshold transverse energy for jet acceptance (E_T^{jet}) and a jet radius ($R=\sqrt{\Delta\phi^2 + \Delta\eta^2}$=0.4 by default). Jet finding is an iterative process that follows the basic steps below.

1. The cell with the highest E_T of the unused cells is identified. If the cell E_T is less than E_T^{init} the jet algorithm is terminated.

2. If step 1 is satisfied the energy of the cells in a cone of ΔR=0.4[3], are summed up using equation 3.2 to determine the energy of the jet. If the jet energy is less than E_T^{jet}, the

---

[3]The cut is actually placed at $\Delta R \leq 0.401$ to account for the REAL/DOUBLE precision errors in FORTRAN.

52

cell containing the jet initiator is marked as used and we return to step 1. Otherwise all cells inside the jet are marked as used.

With the addition of each new cell (E_T^{cell},η^{cell}) the direction and transverse energy of the jet are calculated as:

$$E_T^{jet} = E_T^{jet}|_{old} + E_T^{cell}$$
$$\eta_{jet} = \frac{E_T(jet)|_{old} \times \eta_{jet}|_{old} + E_T^{cell} \times \eta^{cell}}{E_T^{jet}}$$
$$\phi_{jet} = TAN^{-1}(\frac{E_Y^{jet}}{E_X^{jet}})$$

$$(3.2)$$

where the subscript "old" refers to the jet information from the previous step. The above algebra assumes that the reconstructed jets are massless. This analysis requires an algorithm that is applicable over a very large range of transverse momentums. If the jet is particularly energetic with a large radial spread the cone algorithm may find one or more jets from originating from the same parton. If there is significant overlap from two jets such that their baricentres are separated by less than the cone radius R=0.4, the cone algorithm may only identify one jet rather than two.

When jets partially overlap the energy of the overlap region is considered as belonging completely to the first jet identified. This incorrectly increases the energy of one jet and decreases the energy of the other. Further this overlap region also pulls the first jet toward the second jet due to the floating baricentre thereby decreasing the jet-jet separation.

3.2.2 K_T Clustering

Another common jet technique is the K_T clustering algorithm. This method starts by identifying proto-jets: calorimeter towers that possess an E_T above a given threshold. The following quantities are then calculated for each calorimeter tower pair :

$$d_{ij} = min(p_{T,i}^2, P_{T,j}^2)\frac{R_{ij}^2}{R^2}$$
$$R_{ij}^2 = (\delta\eta)^2 + (\delta\phi)^2$$
$$d_i^2 = p_{T,i}^2$$

$$(3.3)$$

Once these values are determined for each possible pair the minimum of d_i and d_{ij} is found. If the minimum value is d_{ij} then the two "jets" are combined to form a single jet, otherwise the ith proto-jet is discarded from future consideration. The simplest method to combine the jets is the covariant E-scheme in which the 4-momentum of the new jet is the sum of the 4-momentum of the two initial jets. This is an iterative process, each step reduces the number of proto-jets by one. The K_T algorithm terminates when the number of jets

53

remaining is equal to the number of jets requested by the user.

One of the cuts to be introduced in this analysis is a cut on the number of jets in the event. The K_T clustering technique was not utilized in this analysis since it is topology driven (the number of jets is an input parameter), nor does it allow jet-overlap (every cell is unambiguously assigned to a single jet).

3.2.3 Sliding Window Algorithm

The sliding window algorithm moves a 3x3 $\eta \times \phi$ window along the calorimeter to find regions with a summed transverse energy above some given threshold value. The cell with the maximum transverse energy in this window is identified as the initiator for a possible jet candidate. The jet energy is then determined using a cone of pre-determined radius centered about this cell.

If the minimal distance between the new jet and any previously identified jet is above a given separation (typically defined with respect to the RMS width of the jets) the jet is accepted. However, if the separation is below the threshold the lesser energy jet is dropped and replaced with the new jet. Therefore, like the cone algorithm the sliding window algorithm does not properly reconstruct jets that severely overlap.

3.2.4 Local Maximum Method

The local maximum method was written to overcome the limitations of the previous jet finding algorithms, namely it will be able to properly identify jets whose baricentres occur closer together than the standard cone radius (ΔR=0.4). For this reason the local maximum method will be utilized in this analysis. The basic elements of this approach to jet finding are as follows:

1. All cells with a transverse energy greater than E_T^{init}, that are also the local maximum in a surrounding 3×3 ($\eta \times \phi$) window are identified as possible jet initiators. To remove spurious maxima it is also required that the jet corresponding to this initiator have E_T greater than E_T^{jet}.

2. Cycle through all the local maxima:

   (a) If two cells are within $\Delta R \leq 0.4$ drop the lowest energy cell unless E_{T1}^{init} and E_{T2}^{init} $\geq E_T^{cut1}$, where E_T^{cut1} is some threshold value.

54

Parameter	ATLFAST	ATRECON
E_T^{init}	5(7) GeV	3(4) GeV
E_T^{jet}	5(7) GeV	5(5) GeV
E_T^{cut1}	20 GeV	10 GeV

Table 3.3: Parameters implemented in the local maximum jet finding routine for ATLFAST and ATRECON. The values in brackets correspond to the values at high luminosity. These values are determined in section 4.2.5.

Once the erroneous local maxima have been dropped the energy of the jets can be calculated. The local maximum routine cycles through all the cells in the calorimetry, if a particular cell lies within a distance $\Delta R \leq 0.4$ from a jet initiator it is folded into the jet using the algebra in equation 3.2. If the cell lies near two or more jet initiators the energy is shared between the jets using the weighting function W_i:

$$W_i = \frac{\frac{E_{T,i}}{\Delta R_i}}{\sum_{i=1}^{N} \frac{E_{T,i}}{\Delta R_i}} \tag{3.4}$$

where $E_{T,i}$ is the transverse energy of the ith jet initiator, and ΔR_i is the distance from the cell in question to the jet initiator.

The ATLAS calorimetry is modelled differently in full and fast simulation and therefore the parameters introduced in this section differ between the two. A single particle in ATLFAST deposits all of its energy into a single calorimeter cell. In ATRECON a single particle may share its energy in multiple cells due to the transverse shower spreading. Consequently the default jet finding thresholds, summarized in table 3.3, are lower in full simulation.

3.3 Jet energy Calibration

Jet calibration must take into account energy that is lost from the jet cone as well as energy introduced into the cone that does not belong to the jet[4]. If the transverse spread of the jet is larger than the assigned cone radius then the jet energy contained in the cone must be calibrated to account for this loss. This is the predominant mechanism for jet energy loss in ATLFAST. The greater the energy of the jet the more collimated it becomes and as such this factor becomes less of an issue at high jet energies. Full simulation uses GEANT to model particle interaction within the detector. Not all interactions within the detector, for example nuclear excitation, produce a measurable output signal. Further the GEANT model of the ATLAS detector includes dead space in the calorimetry for electronics, cryogenics and other servicing aspects of the experiment. The jet calibration in full simulation must therefore take into account energy that is lost outside the cone as well as "missing"

---

[4]Electronic noise and pileup are both examples of processes that can add energy into the cone of a jet.

55
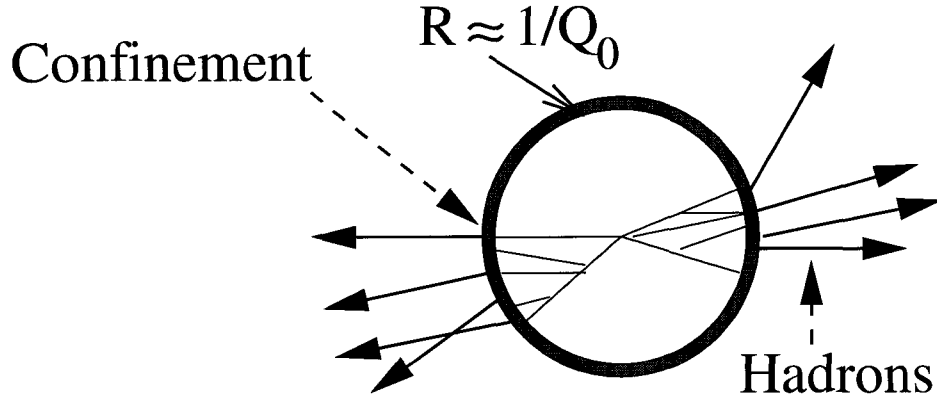
Figure 3.5: The conversion of a string to hadrons is non-perturbative and flavour dependent.

energy[5].

3.3.1 Fragmentation

The notion of calibration is further complicated when it is accepted that different flavour jets fragment differently. Perturbative QCD governs the initial radiation of quarks and gluons. The process of hadronization, converting quarks and gluons to their colourless hadrons depicted in figure 3.5, is non-perturbative and therefore must be modelled.

The Lund symmetric fragmentation model [54] is used to model the fragmentation of light (uds) quarks :

$$f(z) \propto z^{-1}(1-z)^a e^{\frac{-bm_\perp^2}{z}} \tag{3.5}$$

The Peterson fragmentation function[55] is used for the heavier charm and bottom quarks:

$$f(z) \propto \frac{1}{z(1 - \frac{1}{z} - \frac{\epsilon_Q}{1-z})^2} \tag{3.6}$$

The fragmentation function $f(z)$ gives the probability that a produced hadron carries away a specific fraction (z) of the remaining light-cone momentum ($E \pm p_Z$). Table 3.4 lists the default PYTHIA parameters used in the modelling of fragmentation. The fragmentation spectrum is harder for the heavy mass quarks and consequently the hadronization produces fewer particles. Since the topology of a jet is flavour dependent this suggests that the calibration of the jet energy is also flavour dependent. B-tagging is a method that allows physicists to distinguish between light and heavy flavour jets and will facilitate better calibration.

---

[5]This notion of missing jet energy is discussed in more detail in section 5.1.1.

56

Light Quarks-uds (gluon)	Heavy Quarks (cb)	
a	0.3 (0.5)	ϵ_c	-0.05
b	0.58(0.9)	ϵ_b	-0.005

Table 3.4: The default fragmentation parameters in PYTHIA
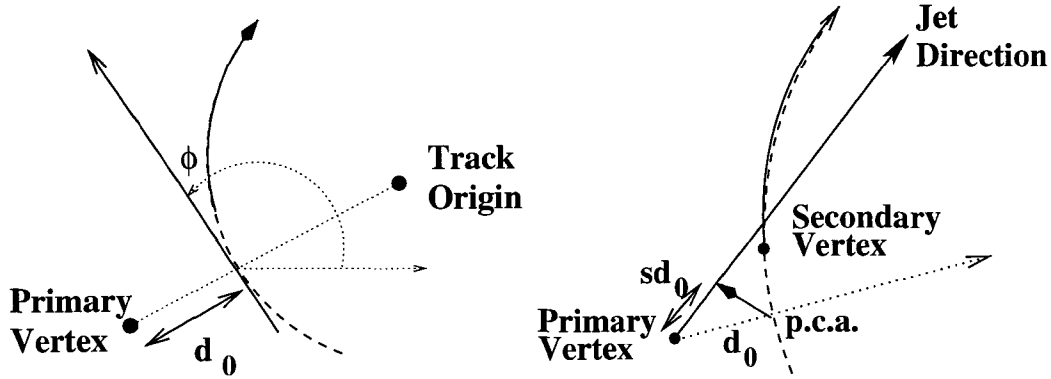
Figure 3.6: (a)A visual definition for the impact parameter. (b) The calculation of signed impact parameter.

3.3.2 B-tagging

If a heavy flavoured meson possesses large enough momentum its subsequent decay will produce a secondary vertex measurably isolated from the primary vertex. Since the precise location of a secondary vertex cannot be determined a track is described by five different variables that all relate to the tracks point of closest approach to the beamline.

d_0 : The impact parameter at the track's point of closest approach (pca). Negative for tracks where the origin lies between the pca and the track origin.

z_0 : Z-position at the point of closest approach.

ϕ_0 : The azimuthal direction of a tangent to the track at the pca.

$\tan(\theta)$: Slope of the track at the pca, where θ is the angle measured from the beamline.

$1/P_T$: Inverse of track transverse momentum (negative for tracks with negative charge).

Figure 3.6(a) visually demonstrates the impact parameters d_0 and ϕ_0. The impact parameter only gives information about how far the track is away from the beamline. To "tag" b-jets the impact parameter must be located a distance away from the origin, in the same direction as the respective jet. The signed impact parameter (sd_0), shown in figure

57
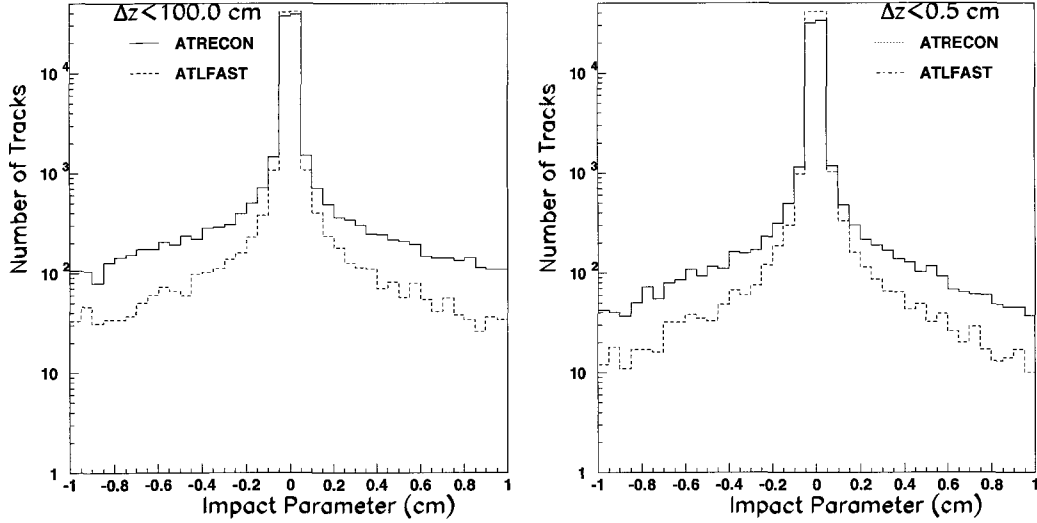
Figure 3.7: A comparison of the impact parameters from a 200 GeV/c^2 Higgs sample, when (a) no cut is applied to the tracks and (b) when the measured z_0 of the track must lie within 5 mm of the primary vertex.

3.6(b), is calculated as:

$$sd_0 = |d_0| \frac{\vec{track} \cdot \vec{jet}}{|\vec{track} \cdot \vec{jet}|} \tag{3.7}$$

where $\vec{track}$ is a 2-dimensional vector identifying the tracks point of closest approach and $\vec{jet}$ is the unit-vector identifying the direction of the jet.

Vertexing

The location of the primary vertex follows a Gaussian distribution with the FWHM: $\sigma_x = \sigma_y = 16$ μm and $\sigma_z = 7.5$ cm. The primary interaction vertex is identified by one of two methods, depending on the physics channel under investigation.

1. H$\rightarrow$ZZ$\rightarrow$ $\mu\mu$(ee)jj : The tracks associated with oppositely charged isolated muons (electrons) are identified. The track pair with the smallest separation (in r,ϕ,z) at their point of closest approach is assumed to originate at the primary vertex. The new vertex is identified as the midpoint between these two tracks.

2. H$\rightarrow$WW$\rightarrow$ $\mu\nu_\mu$(eν_e)jj: The highest P_T isolated muon (electron) is identified. The point of closest approach (in r,ϕ) to the beamline is identified as the primary vertex.

Identifying b-jets

The b-tagging algorithm has been optimized on a 5000 event sample of H$\rightarrow$ZZ$\rightarrow$ $\mu\mu$jj with M_H=200 GeV/c^2. Figure 3.7 compares the impact parameters obtained from using both full and fast simulation. For small values of the impact parameter there is good agreement between the two simulations. ATRECON has a greater rate in the number of tracks giving a

58

large impact parameter. These are caused by multiple scatterings within the inner detector. This process is not modelled in ATLFAST. To remove pileup tracks (not included in figure 3.7), which have unique interaction vertices, we introduce a cut requiring that the z_0 value of the track at its point of closest approach be within 0.5 cm of the primary vertex ($\Delta Z \leq 0.5$ cm). However this cut, shown in figure 3.7(b) also reduces the agreement between the two simulations at low values of the impact parameter. The determination of the primary vertex involves using the curvature of oppositely charged tracks in the 2 Tesla magnetic field to identify their point of closest approach. As previously mentioned in section 2.2.1 and shown in figure 2.6, the magnetic field inside the inner detector (modelled by full simulation) is not uniform, thereby reducing the accuracy with which we identify the primary vertex. However, these discrepancies will not be significant in this analysis as they only affect the resolution of the jets and not the jet-finding efficiency.
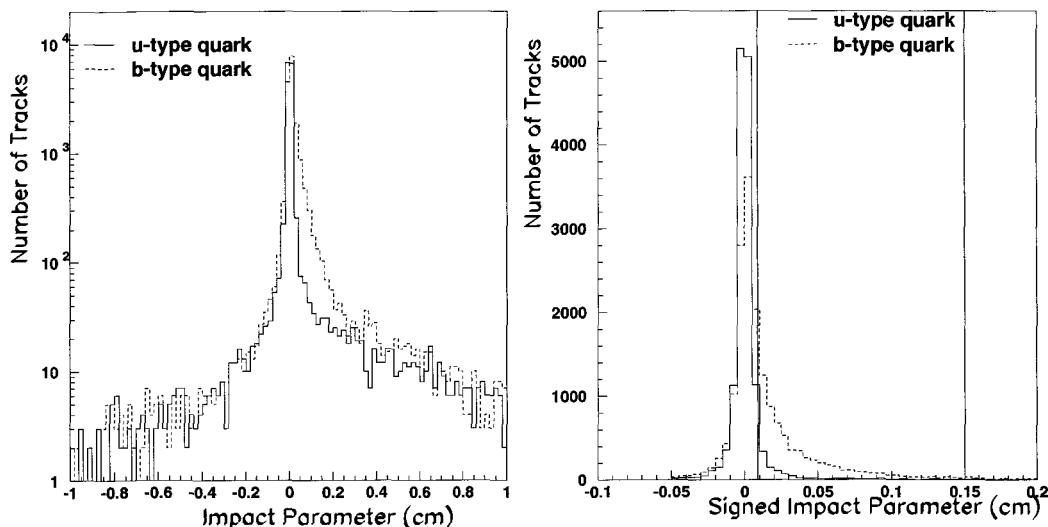
Figure 3.8: A logarithmic and linear comparison of the b-quark and u-quark signed impact parameters using a 5000 event 200 GeV/c^2 Higgs sample.

Figures 3.8 compares the signed impact parameters (in full simulation) of tracks located within a cone of $\Delta R = 0.4$ around both u and b type quarks using the parton direction. The excess of positive entries for the b-type quark can be used to distinguish between the two types of jets. A lower bound (sd0$_{low}$=0.009 cm) removes a significant number of tracks originating from light quark jets. An upper threshold (sd0$_{high}$=0.15 cm) reduces the tracks that come from secondary interactions.

Using this range of allowed impact parameters, we can then count the number of b-tracks around a given quark direction (0.009cm $\leq$ sd0 $\leq$ 0.15 cm). Figure 3.9(a) gives the b-ness of u(ds) and b type quarks in ATLFAST. Requiring that there be greater than or equal to

59

3 b-tracks, with a longitudinal separation $\Delta Z \leq 0.5$ cm from the primary vertex, gives a b-tagging efficiency of 38.6% (30.5%), and a purity of 96% (94%) for ATLFAST (ATRECON), for partons which fall into the pseudo-rapidity (η) range covered by the inner detector.

3.3.3 Calibration

The jet calibration values were determined by analyzing the four quarks originating from a large sample of vector boson fusion events of differing Higgs mass. Jets were found in the calorimetry using the local maximum method outlined in section 3.2.4. A jet was chosen to be associated with a particular quark if it was within a radius $\Delta R \leq 0.2$ of the initial quark direction. To ensure minimal energy contamination from surrounding jets, only those quarks which were a distance $\Delta R \geq 0.8$ from the 3 other quarks in the event were used.

The light quarks (udsc) were grouped under one calibration, the heavy quarks(b) were further divided into hadronic and semi-leptonic (jets containing muons) sectors. Jet calibration in ATLFAST is typically performed using ATLFAST-b which utilizes a 5th order polynomial to calculate the calibration factor. It was found that both ATLFAST and ATRECON, shown in figure 3.9(b), responded well over all energy and pseudorapidity ranges to a simpler calibration of the form:

$$E_{calib} = E_{calo}(A_0 + \frac{A_1}{E_{calo} - A_2})$$ (3.8)

where E_{calo} is the uncalibrated jet energy.
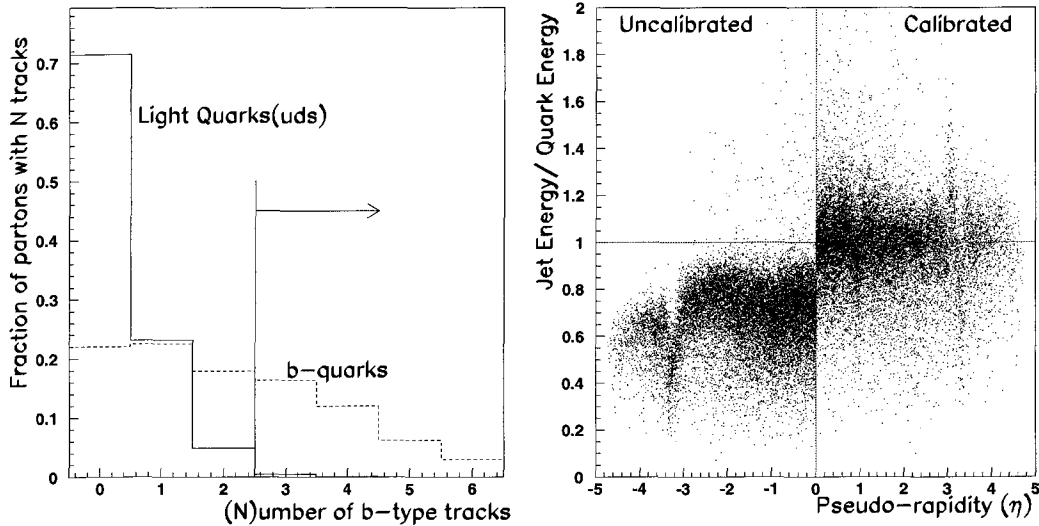
Figure 3.9: (a) There exists a larger number of b-type tracks surrounding the b-quark than there are the lighter uds quarks. (b) Ratio of jet energy to quark energy for ATRECON calibration on jets from the decay of M_H=200 GeV/c^2 .

60

η Range	Light Quarks			Heavy Quarks		
	A_0	A_1	A_2	A_0	A_1	A_2
0.0→0.5	1.140	9.26	-0.66	1.1291	13.086	0.7740
0.5→1.0	1.156	13.35	-4.94	1.1725	14.480	2.942
1.0→1.5	1.134	25.22	-16.74	1.1220	28.32	-0.317
1.5→2.0	1.142	29.15	-15.30	1.1516	30.52	2.924
2.0→2.5	1.146	44.90	-62.8	1.1670	35.23	0.000
2.5→3.0	1.163	187.5	-491			
3.0→4.0	1.273	422.3	-400			
4.0→5.0	1.519	356.9	-920			

Table 3.5: The parameters used for jet calibration in ATRECON.

η Range	Light Quarks			Heavy Quarks					
				Hadronic			Semi-leptonic		
	A_0	A_1	A_2	A_0	A_1	A_2	A_0	A_1	A_2
0.0→1.0	1.001	5.80	3.00	0.983	9.13	2.81	0.93	24.4	-11.03
1.0→2.0	1.007	10.30	3.30	0.981	16.52	4.26	0.78	120.6	-123
2.0→3.0	1.009	31.19	-61.8	0.987	25.748	21.83			
3.0→4.0	1.003	81.37	-169						
4.0→5.0	1.010	146.6	-138						

Table 3.6: The parameters used for jet calibration in ATLFAST.

The calibrations values used in ATRECON (table 3.5) are notably higher than those used in ATLFAST (table 3.6). As the reconstructed jet energy increases the calibration factor approaches a constant value, given by the A_0 parameter of equation 3.8. In ATLFAST this constant has a value of roughly 1 indicating that a cone of radius ΔR =0.4 contains all the jet energy. In ATRECON the A_0 value is greater than 1 over all pseudo-rapidity ranges indicating the a cone of ΔR =0.4 does not contain all the jet energy. This is a combination of two effects. The spread of the jet in the calorimeter is often greater than ΔR =0.4 in full simulation. Secondly, some energy is actually "lost" in the interactions with the calorimetry. Figure 3.10 gives a sample of the jet calibration curves used by the two simulations.

3.3.4 Jet Reconstruction Efficiencies

Due to the different treatments of the ATLAS calorimetry, and the different parameters used to define the jet-finding algorithms, full simulation and fast simulation have different jet finding efficiencies. Since ATLFAST contains no calorimeter dead regions, nor does it accurately model energy loss in the calorimetry it will generally possesses a higher jet finding efficiency than ATRECON. Figure 3.11 gives the relative jet efficiency between ATLFAST and ATRECON, for the default jet-finding parameters given in table 3.3. The relative jet efficiency is defined as the probability of ATRECON finding a jet within a distance ΔR

61
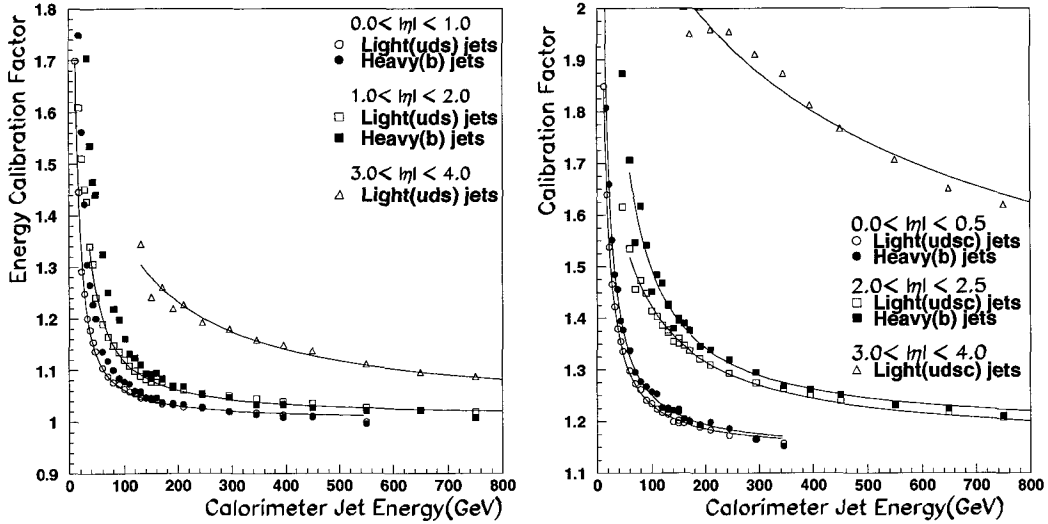
Figure 3.10: The calibration factors for (b) ATRECON are consistently higher than those from a similar detector region in (a) ATLFAST.

≤ 0.2 of the initial quark direction divided by the efficiency with which ATLFAST would identify a jet within $\Delta R \leq 0.2$ of the same quark. The effective pseudorapidity coverage for jets in ATRECON is $\eta \approx 4.8$. ATLFAST provides coverage to a maximum value of $\eta \approx 5.0$. While not shown in figure 3.11 the efficiency for jets found above 4.8 is set to 0%. The relative jet finding efficiency is applied to ATLFAST after all the jets have been identified. The jet reconstruction efficiency in full simulation using a 3 GeV jet initiator and a 5 GeV jet threshold is given in figure 3.12.

3.4 Muon reconstruction

With the full simulation program muons are first identified with the muon spectrometer, a second measurement of the muon momentum is then performed by the identification of the corresponding inner detector track.[6] Combining the muon spectrometer measurement (σ_s) with the inner detector (σ_{id}) gives a net resolution (σ_μ):

$$\frac{1}{\sigma_\mu^2} = \frac{1}{\sigma_s^2} + \frac{1}{\sigma_{id}^2} \tag{3.9}$$

3.4.1 Spectrometer Reconstruction

Due to the large amount of material between the interaction point and the muon spectrometer, the muon will deposit a portion of its energy into the surrounding calorimetry. For muons with a transverse momentum between 50 GeV/c - 100 GeV/c and located $|\eta| <0.5$

---

[6]To avoid associating pileup tracks with the muon, it is required that the track be at least within $\Delta R \leq 0.2$ of the muon direction, $|z - z_0| \leq 0.5$ cm of the primary vertex and have a transverse momentum of at least 30% that of the spectrometer measurement.

62
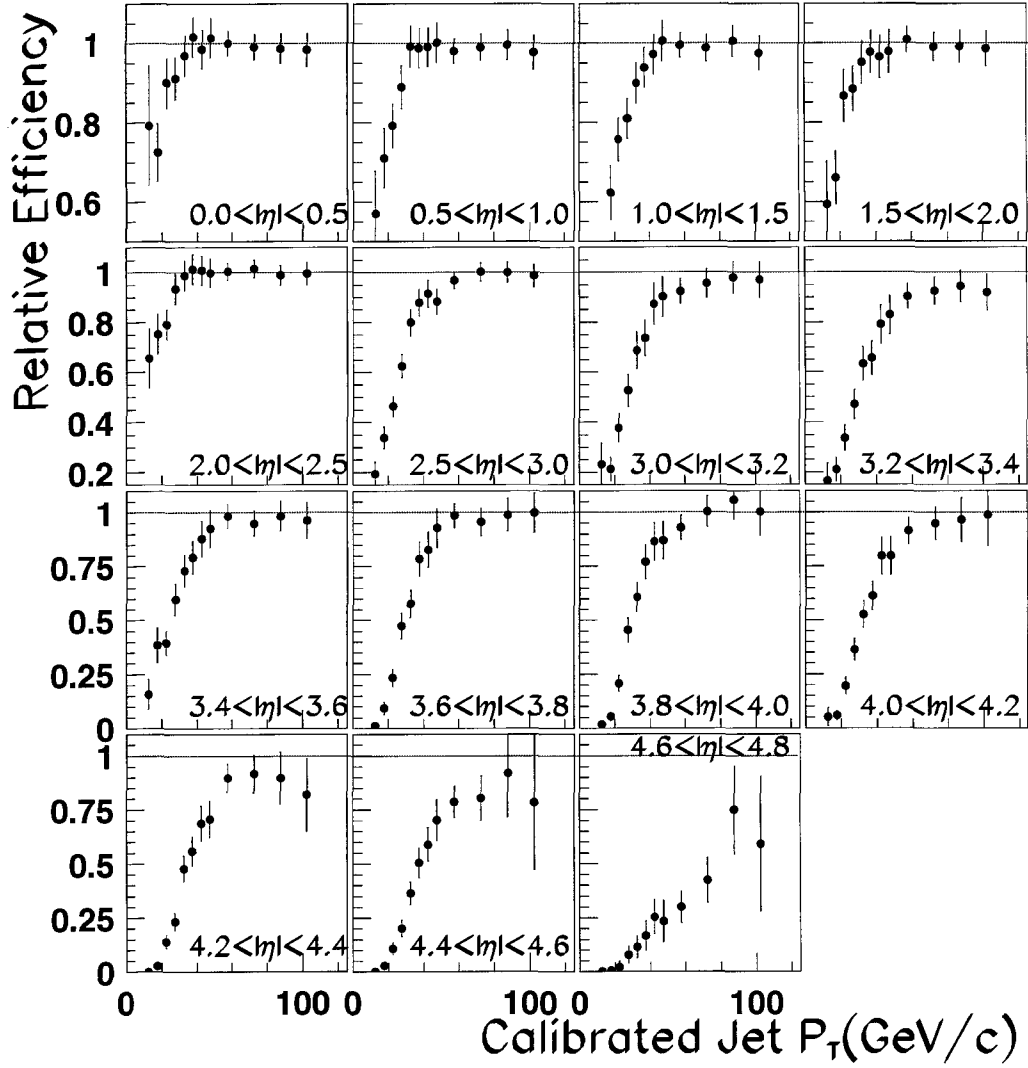
Figure 3.11: The relative jet-finding efficiencies between full and fast simulations.

figure 3.13(a) shows that the muon deposits on average about 5% of its energy into calorimetry. The muon spectrometer measurement (P_x^{spec}, P_y^{spec}) can be corrected by using equation 3.10 to recalculate the muon transverse momentum by including the P_x^{cell}/P_y^{cell} information of cells that lie within a cone of $\Delta R \leq 0.2$ around the muon direction.

$$P_T = \sqrt{(P_x^{spec} + \sum_{\Delta R \leq 0.2} P_x^{cell})^2 + (P_y^{spec} + \sum_{\Delta R \leq 0.2} P_y^{cell})^2} \qquad (3.10)$$

The resolution of the combined muon spectrometer plus calorimeter measurement is written as :

$$\sigma_s = A \oplus \frac{B}{\sqrt{P_T}} \oplus CP_T \oplus \sqrt{\frac{(\sigma_N)^2 + (\sigma_P)^2}{P_T^2}} \qquad (3.11)$$

Averaging over the azimuthal angle, the resolution as a function of transverse momentum and pseudo-rapidity is given in figure 3.13(b). The resulting fits to the resolution curves

63
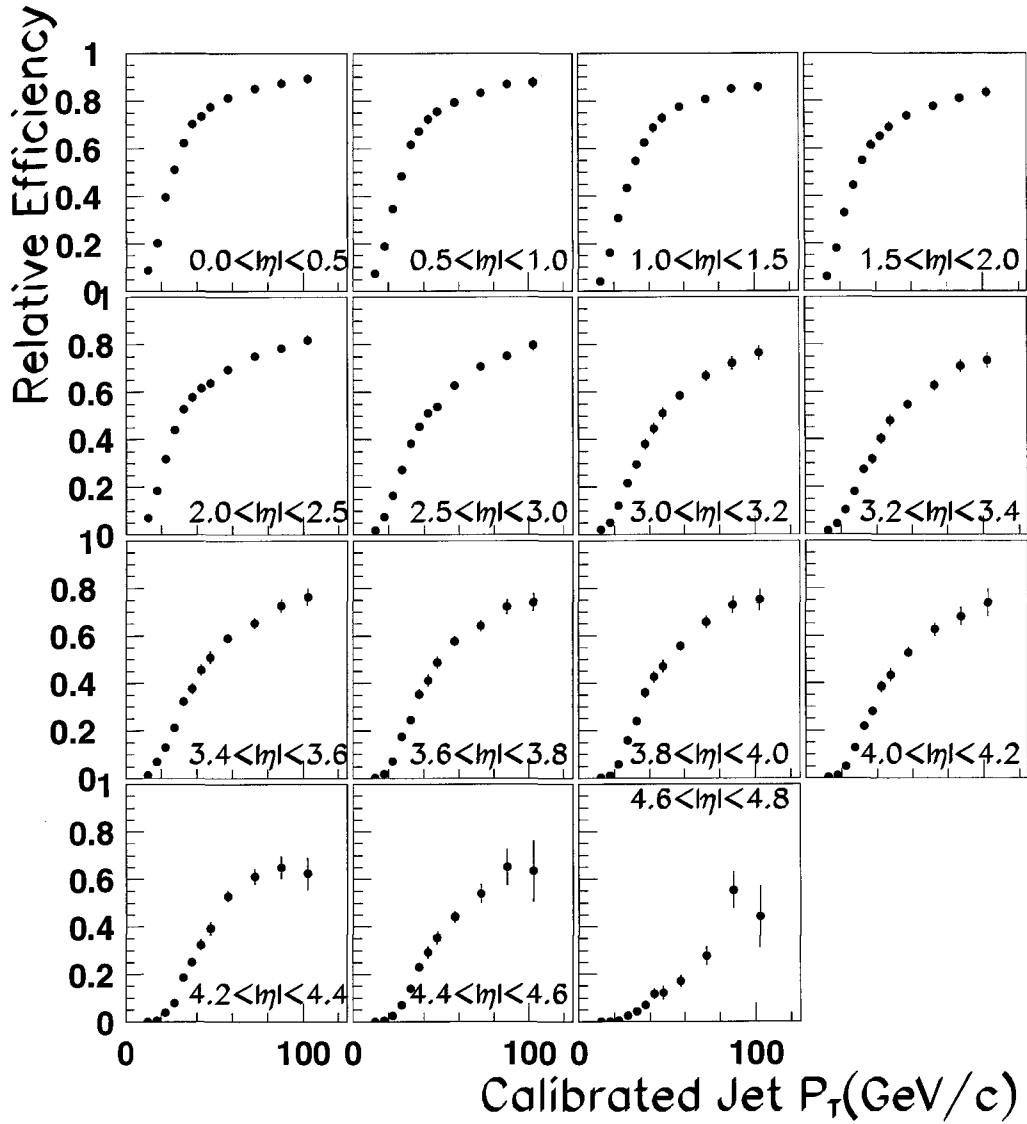
Figure 3.12: The jet reconstruction efficiency in full simulation as a function of calibrated jet P_T and pseudo-rapidity.

in figure 3.13(b) are given in table 3.7. The barrel and endcap muon calorimetry are each divided into 8 azimuthal sections, with the barrel section rotated by 22.5° with respect to the endcap sections. The detector regions between these segmentations are marked by reduced resolution as shown in figure 3.14. Corrections to the muon resolution terms in table 3.7 are presented in table 3.8.

Muon Detection Efficiency

The ATLFAST program assumes a perfect muon detection efficiency. In full simulation muons may not make it through to the muon spectrometer or they may pass through dead regions in the detector and leave no muon signature. In addition, inelastic collisions of high energy muons in the ATLAS calorimetry may produce secondary muons, a process not

64
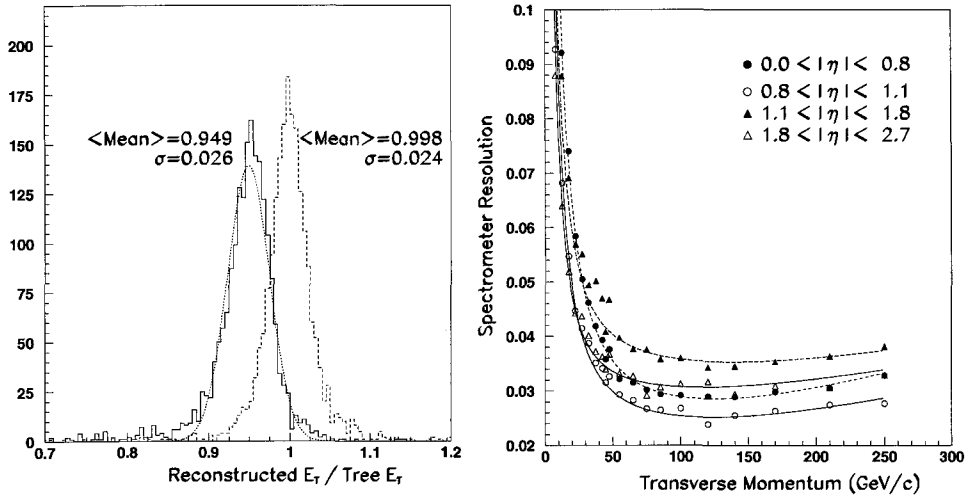
Figure 3.13: (a) The shift in peak location when the energy surrounding a muon is included in the calculation of muon energy. (b) Pseudorapidity and P_T dependence of the muon spectrometer resolution for no electronic noise and no pileup.

η Range	Spectrometer			Noise Terms		
	constant A	sampling $B(\sqrt{\text{GeV}/c})$	linear $C((\text{GeV}/c)^{-1})$	Electronic $\sigma_N(\text{GeV}/c)$	Low Lumi $\sigma_P(\text{GeV}/c)$	High Lumi $\sigma_P(\text{GeV}/c)$
0.0→0.8	0.02236	0.1149	9.2646E-5	1.089	0.5477	1.608
0.8→1.1	0.0205	0.1058	7.472E-5	0.7655	0.5	1.608
1.1→1.8	0.0309	0.1460	7.472E-5	0.7655	0.5477	1.757
1.8→2.7	0.02744	0.0995	7.472E-5	0.637	0.5477	1.675

Table 3.7: Parameterization of the ATLAS muon spectrometer resolutions. Since calculation of the muon energy uses energy deposited in the calorimetry the muon spectrometer is subject to the effects of pileup.

η Range	Phi Location (rads)	Phi Width (rads)	Constant	Linear (GeV^{-1})
$0.0< |\eta| <0.8$	$\frac{\pi}{8}, \frac{3\pi}{8}, \frac{5\pi}{8}, \frac{7\pi}{8}, \frac{9\pi}{8}, \frac{15\pi}{8}$ $\frac{11\pi}{8}, \frac{13\pi}{8}$	0.01	0.03036	-
		0.03	0.05536	30.3×10^{-5}
$0.8< |\eta| <1.1$	$\frac{\pi}{8}, \frac{3\pi}{8}, \frac{5\pi}{8}, \frac{7\pi}{8}, \frac{9\pi}{8}, \frac{15\pi}{8}$ $\frac{11\pi}{8}, \frac{13\pi}{8}$	0.01	0.0305	-
		0.03	0.0705	-
$1.1< |\eta| <1.8$	$\frac{\pi}{8}, \frac{3\pi}{8}, \frac{5\pi}{8}, \frac{7\pi}{8}, \frac{9\pi}{8}, \frac{15\pi}{8}$ $\frac{11\pi}{8}, \frac{13\pi}{8}$	0.01	0.0459	-
		0.01	0.02744	-
	$\frac{0\pi}{8}, \frac{2\pi}{8}, \frac{4\pi}{8}, \frac{6\pi}{8}, \frac{8\pi}{8}, \frac{10\pi}{8}, \frac{12\pi}{8}, \frac{14\pi}{8}$	0.01	0.0329	-
$1.8< |\eta| <2.7$	$\frac{0\pi}{8}, \frac{2\pi}{8}, \frac{4\pi}{8}, \frac{6\pi}{8}, \frac{8\pi}{8}, \frac{10\pi}{8}, \frac{12\pi}{8}, \frac{14\pi}{8}$	0.01	0.05044	-

Table 3.8: Correction to the muon resolution terms based on azimuthal angle.

65
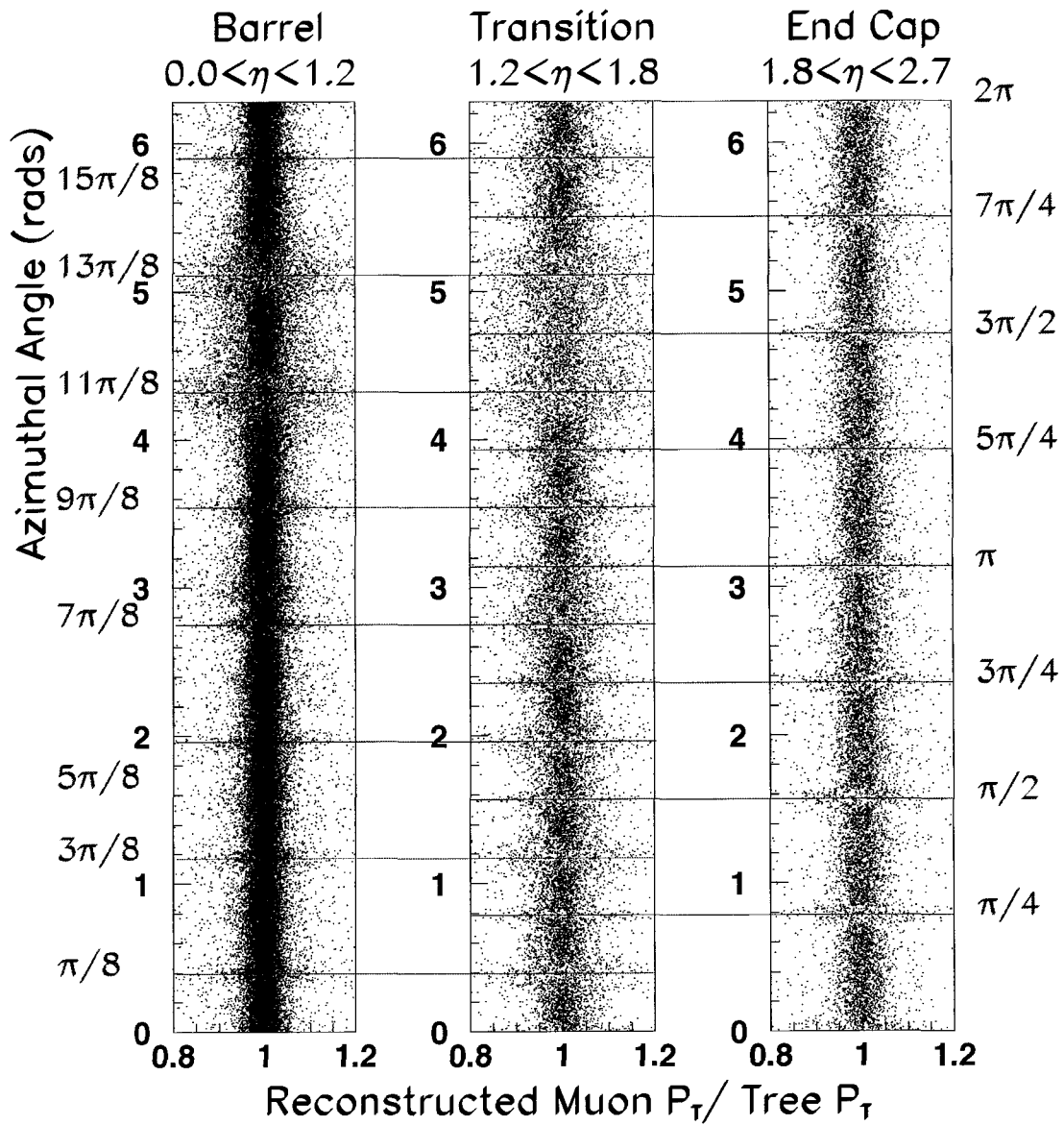
Figure 3.14: The segmentation of the spectrometer produces 8 regions in ϕ that are marked by reduced resolution. The transition region is subject to the reduced resolution of both the barrel and EndCap spectrometers.

66

E_T Range	Pseudorapidity Range							
	0.0	0.95	1.25	2.3	0.0	0.95	1.25	2.3
(GeV)	→0.95	→1.25	→2.3	→2.7	→0.95	→1.25	→2.3	→2.7
5-10	96.2	92.1	95.6	91.4	100	100	99.93	100
10-15	97.5	97.2	96.2	95.5	100	100	100	99.87
15-20	98.0	97.5	97.3	94.9	100	100	99.92	99.78
20-100	98.2	98.1	97.5	96.2	99.96	99.96	99.80	99.70
100-200	98.1	98.2	96.2	93.0	99.85	99.83	99.34	98.63
200-300	97.3	97.1	94.2	88.9	99.71	99.46	98.85	96.51
300-400	96.4	97.1	94.0	.	99.78	99.83	98.49	84.62
>400	91.5	94.8	87.2	.	99.67	100	96.5	

Table 3.9: The left side of the table lists the efficiency for identifying isolated muons with the proper charge determination. The right side of the table gives the charge identification efficiency. This table summarizes regions located outside the support structure.

modelled in ATLFAST. The efficiency of detecting a muon in a specific η-P_T range, where there is no secondary muon and the spectrometer properly identifies the muon charge, is given in table 3.9.

There are also regions in the detector that are not sensitive to the presence of a muon and these are highlighted in figure 3.15(a). The dead regions can be linked to the cable feedthroughs at a pseudo-rapidity of 0, and to the feet and rails of the detector support structure.

3.4.2 Inner Detector Muon Measurement

Once the muon has been identified in the spectrometer, matching spatial positions between the track's exit from the inner detector and the entrance into the spectrometer allows a specific track to be associated with the spectrometer muon. The track located closest to direction of the muon (with a $\Delta R \leq 0.2$ and $\Delta Z \leq 5$ mm), with a transverse momentum greater than 30% that determined by the muon spectrometer, is choosen as the correct track.

Resolution in the inner detector can be parameterized in terms of two variables :

$$\sigma_\mu = A \oplus BP_T \qquad (3.12)$$

where A and B are constants. The inner detector in full simulation was broken down into 7 regions. Typical resolution curves are shown in figure 3.16, with the fits to the curves given in table 3.10.

Figure 3.16(b) shows that for large transverse momentums ($P_T \geq 220$ GeV/c) the mean ($< P_T >$) of the reconstructed track momentum falls away from the tree level (P_T^{tree}) value
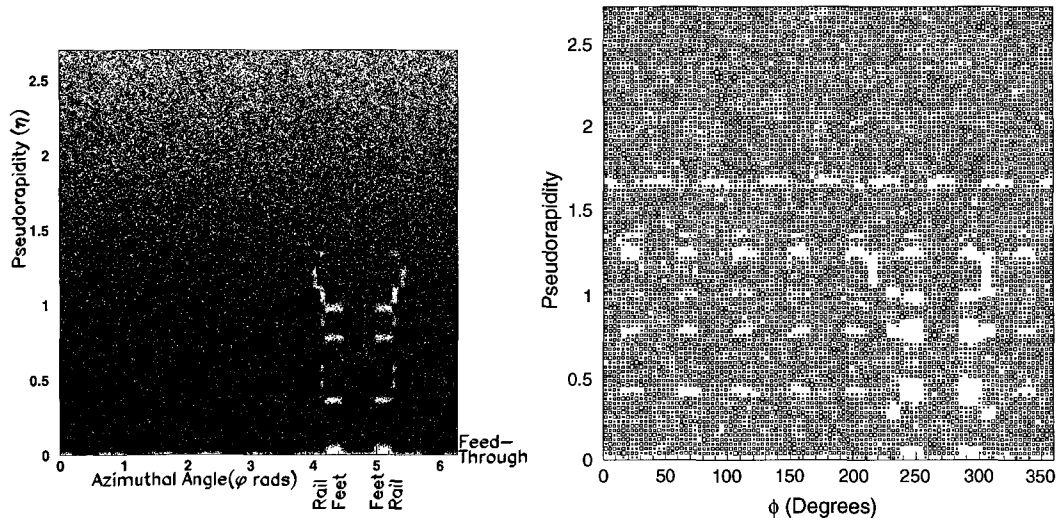
Figure 3.15: Support structures and cable feedthroughs for the ATLAS detector produce dead regions in the Muon spectrometer.(b) A similar plot from the muon TDR featuring infinite energy muons and requiring 3 superpoints per track. A superpoint is a coincidence of at least six hits in six different sensitive planes in one chamber.
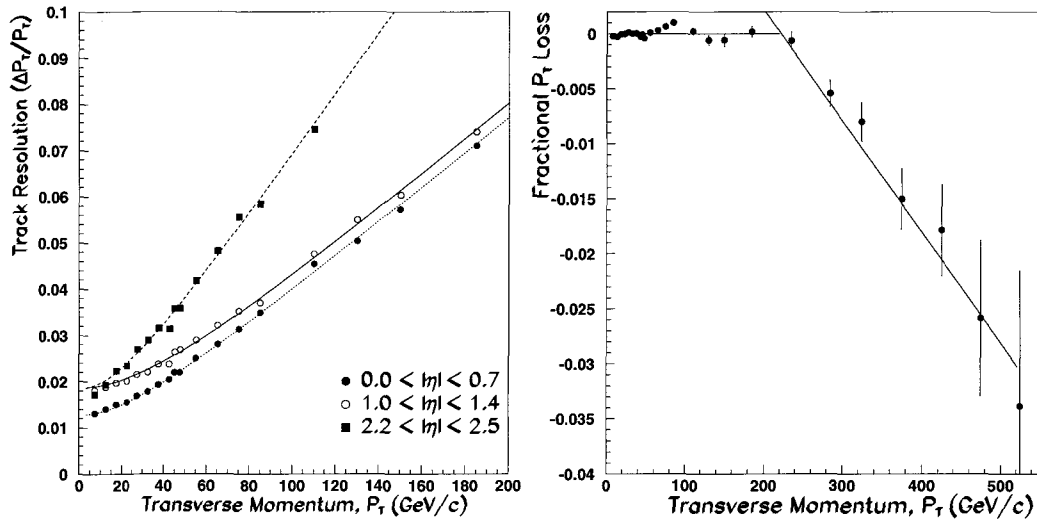
Figure 3.16: (a) Pseudorapidity dependence of the inner detector averaged over all ϕ. (b) The reconstructed track momentum deviates from the tree level value at high P_T.

68

Pseudo-rapidity Range η	Tracking Resolution	
	Constant A	Linear B ((GeV/c)$^{-1}$)
0.0→0.35	0.0128	0.00038
0.35→0.7	0.0135	0.00038
0.7→1.0	0.0155	0.00045
1.0→1.4	0.0187	0.00039
1.4→1.8	0.021	0.00042
1.8→2.2	0.020	0.00040
2.2→2.5	0.195	0.00070

Table 3.10: The parameterization of the muon resolution using the Inner Detector.

as energy is lost in the detector. The mean of the reconstructed energy falls off as :

$$< P_T >^{track} = P_T^{tree} \times (1 + 0.0225 - 0.000101 \cdot P_T^{track}) \tag{3.13}$$

The slight up-turn between 60 and 100 GeV/c is an artifact of the fitting procedure and is small compared to the resolution of the muon transverse momentum measurement. For regions where no suitable track candidate is found, the muon resolution is taken to be that of the spectrometer itself. This is only prevalent between the upper pseudo-rapidity bound of the inner detector (η=2.5) and the end of the spectrometer (η=2.7).

3.5 Electron Reconstruction

Identification of high energy electrons in the ATLAS detector is complicated by the fact that while an electromagnetic shower will deposit a large fraction of its energy into the EM calorimeter they will punch-through the EM calorimetry and deposit a fraction of their energy into the hadronic calorimeter. Also early neutral pion production in a hadronic jet can also leave a sizable contribution of energy in the electromagnetic calorimetry. ATRECON does not specifically identify electrons, it identifies electromagnetic clusters. These clusters are 5 cells wide in ϕ ($\delta\phi$ = 0.5) and 3 cells wide in η ($\delta\eta$ = 0.3). We then need to determine if these clusters correspond to electrons.

A sample of 5000 H→ZZ→eejj (m$_H$=200 GeV/c^2) events were analyzed with full simulation, producing 6348 EM clusters located in close proximity (ΔR≤0.2) to the tree level electrons and isolated (ΔR≥0.8) from the tree level quarks. There were also 7505 EM clusters close to the quarks but isolated from the electrons. As shown in figure 3.17(a), requiring that the EM cluster contain 80% of the transverse momentum recorded in the projected calorimeter matrix[7] accepts 98.8% of the electrons and rejects 94.9% of the hadrons, giving

[7]The projected matrix is the contains the combined energy of both the electromagnetic calorimeter and the hadronic calorimeters.

69
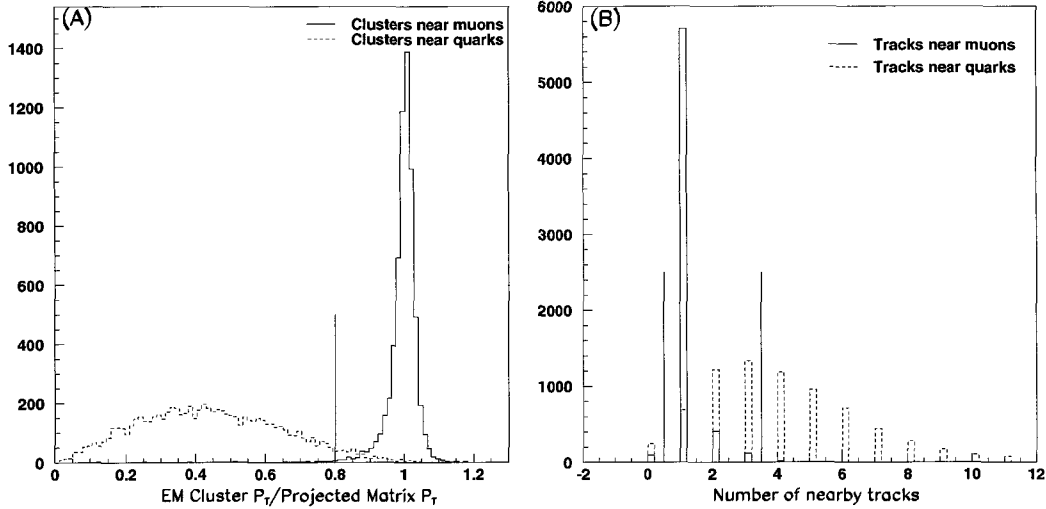
Figure 3.17: (a) In full simulation we can differentiate between an electromagnetic cluster and a hadronic cluster by requiring that 80% of the cluster transverse momentum be EM in nature. (b) Further improvement can be obtained by requiring there to be between at least 1 and 3 tracks associated with the cluster. This cut also distinguishes between photons and electrons.

a total of 6654 clusters as possible electrons, with a fake rate of 5.7%.

The transverse momentum of the projected matrix is determined by summing over the cells in the cluster satisfying

$$P_T = \sqrt{(\sum_{\substack{\Delta\eta \leq 0.1 \\ \Delta\phi \leq 0.2}} P_x)^2 + (\sum_{\substack{\Delta\eta \leq 0.1 \\ \Delta\phi \leq 0.2}} P_y)^2} \tag{3.14}$$

The electric charge of the electromagnetic cluster is determined by identifying the inner detector track located closest to the center (within $\Delta R \leq 0.2$) of the EM cluster with a transverse momentum of at least 30% that of the projected matrix. If the EM cluster is hadronic in nature there will be a substational number of tracks within the EM window. Requiring there be greater than one track allows the calculation of the electric charge. No more than 3 tracks will remove hadrons as well as allow for excess track production from the electron interaction within the detector and extra track production at high luminosity. ATLFAST does not produce extra tracks so the upper limit is set to two tracks, and three tracks at high luminosity. This requirement on the number of tracks returns 6179 electrons (97.3% efficiency) and 230 hadrons (96.9% rejection) giving a final electron purity of 96.4%.

The calculation of the charge of a track in ATLFAST is exact, however in ATRECON there is a incorrect charge identification for approximately 1% of the electrons. ATLFAST was modified to incorporate this effect by randomly flipping the charge on 1% of the elec-

70

	Resolution Terms					
	EM calorimeter			Noise Terms		
η Range	constant A	sampling B ($\sqrt{GeV}$)	noise C (GeV)	Electronic σ_N (GeV)	low σ_P (GeV)	high (GeV)
0.0→0.25	0.592E-02	0.796E-01	0.280	1.240	0.548	1.643
0.25→0.5	0.543E-02	0.756E-01	0.290	1.096	0.547	1.673
0.5→0.75	0.417E-02	0.840E-01	0.445	1.140	0.548	1.852
0.75→1.0	0.157E-02	0.999E-01	0.373	1.140	0.5805	2.049
1.0→1.2	0.431E-07	0.125	0.262	1.140	0.5474	2.435
1.2→1.4	0.369E-02	0.140	0.590	1.502	0.794	2.94
1.4→1.5	0.967E-02	0.418	0.112E-02	1.64	0.794	2.94
1.5→1.6	0.153E-01	0.182	2.48	3.38	0.794	3.88
1.6→2.0	0.802E-02	0.128	1.04	3.250	1.600	4.800
2.0→2.5	0.829E-02	0.111	0.865	2.650	2.226	8.226

Table 3.11: Resolution terms for electron reconstruction us determined in ATRECON and modelled in ATLFAST.

trons.

3.5.1 Resolution

ATRECON provides electromagnetic coverage to a maximum pseudorapidity of 2.7, however the identification of the electromagnetic charge requires the presence of a track in the inner detector limiting the accepted range to 2.5. The resolution of the electron can be written in the form,

$$\frac{\Delta E}{E} = A \oplus \frac{B}{\sqrt{E}} \oplus \frac{\sqrt{C^2 + \sigma_N^2 + \sigma_P^2}}{E} \tag{3.15}$$

where σ_N and σ_P correspond to the electronic and pileup noise terms, respectively.

Figure 3.18 gives typical resolution curves obtained using the full simulation program ATRECON, the fits to which are summarized in table 3.11. The electron reconstruction efficiencies in ATRECON after the cuts discussed in the previous section are given in figure 3.19. The transition regions of the electromagnetic calorimetry shown in figure 3.18 are marked by a notable reduction in efficiency in figure 3.19.

3.6 Tree level EM Radiation off Leptons

The fact that the produced leptons frequently radiate a photon with a large amount of energy presents a problem for the ATLFAST reconstruction program. Lepton reconstruction in ATLFAST is summarized in the following steps:

71
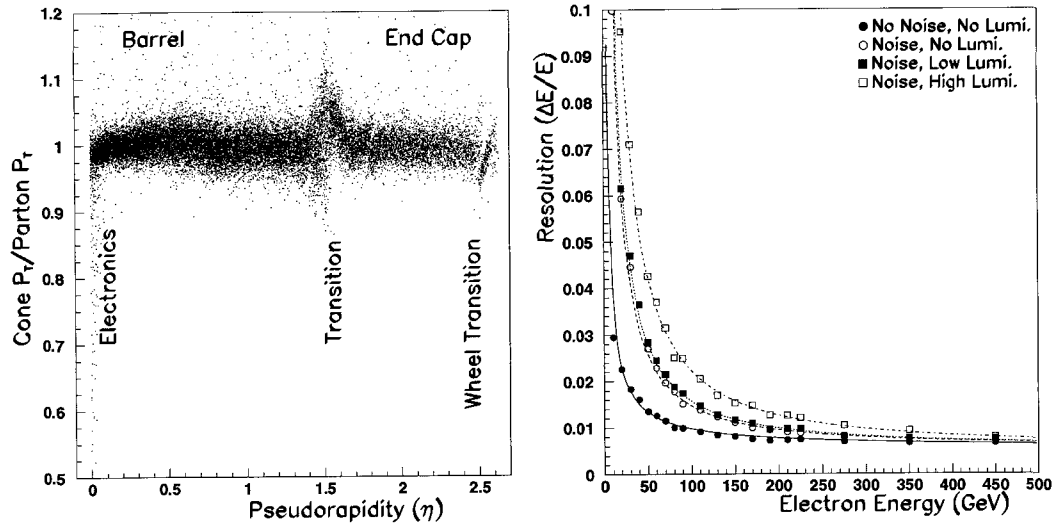
Figure 3.18: Electron resolution as a function of (a) Pseudorapidity for electrons with 40 GeV/c $<P_T < 60$ GeV/c. (b) energy for $0.25< \eta <0.5$ for various noise and luminosity levels.
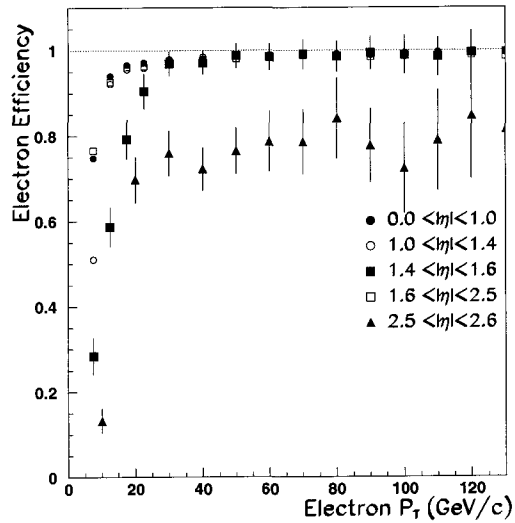
Figure 3.19: The electron efficiency map for ATRECON.

1. The energy of all stable particles in the event tree, including electrons and excluding muons and neutrinos, are deposited into the $\eta \times \phi$ (100×64) calorimeter bins.

2. *Muons* in the tree are identified and marked as isolated if they are separated from jet-clusters and the energy in the surrounding cells ($\Delta R \leq 0.2$) is below a certain threshold.

3. *Electrons* in the tree are identified and marked as isolated if they are separated from jet-clusters, and the energy difference between the electron and the surrounding cells is below a certain energy.

4. *Photons* are identified in a manner similar to the electrons in step 3.

If the radiated photon and the scattered lepton are particularly collimated they will both deposit their energy in the same region of the calorimetry (ATLFAST step 1). If the photon radiated has a large enough energy this will cause the scattered lepton to be marked as non-isolated and removed from further consideration. This does not present an issue for ATRECON. As outlined in section 3.4.1 the muon can deposit a considerable amount of electromagnetic energy into the calorimetry. A cone of $\Delta R = 0.2$ is used to "catch" this energy, which would also include the radiated photon. In section 3.5 we showed that a cut on the fraction of electromagnetic and hadronic energy in a cluster can be used to distinguish between and electron and a hadronic jet. The identification of an electron in full simulation therefore makes no distinction as to whether or not the incident electron radiated a photon before it entered the calorimetry.

A subroutine was added to ATLFAST to be performed after the routines MAKMUO, MAKELE and MAKPHO that corrected this problem. The first step was to cycle through the isolated leptons and determine if a non-isolated photon lay within a distance $\Delta R < 0.15$ from the lepton direction. If so the photon energy was folded into the lepton energy. Second, the non-isolated leptons were cycled through; if a non-isolated photon was located nearby the energy is added to the lepton and the lepton is marked as isolated.

3.7 Monte-Carlo Generation

To perform the final analysis in this thesis we have used PYTHIA 6.227 as our Monte-Carlo generator. We have performed our analysis using a modified version of ATLFAST (00-00-22) in which we have incorporated all the full simulation resolutions and efficiencies that have been discussed in this chapter.

73

Physics Channel	$Z \to \mu^+\mu^-$	$Z \to e^+e^-$	Physics Channel	$Z \to \mu^+\mu^-$	$Z \to e^+e^-$
M_H=180 GeV/c^2	163355	243768	M_H=650 GeV/c^2	211304	215180
M_H=190 GeV/c^2	232476	243062	M_H=700 GeV/c^2	210768	214145
M_H=200 GeV/c^2	219638	240924	M_H=750 GeV/c^2	199755	213453
M_H=210 GeV/c^2	230059	239058	M_H=800 GeV/c^2	199260	213373
M_H=220 GeV/c^2	228836	237622	M_H=850 GeV/c^2	209392	212422
M_H=230 GeV/c^2	182025	236271	M_H=900 GeV/c^2	209197	212315
M_H=240 GeV/c^2	226493	235042	M_H=950 GeV/c^2	209001	212110
M_H=250 GeV/c^2	225262	233778	M_H=1000 GeV/c^2	208963	211737
M_H=300 GeV/c^2	221641	228631	Z^0+jets		
M_H=350 GeV/c^2	218920	225203	CKIN(3)=0	502747396	468983732
M_H=400 GeV/c^2	216768	222039	CKIN(3)=40	63343395	68176904
M_H=450 GeV/c^2	150476	220186	CKIN(3)=100	71785795	76272239
M_H=500 GeV/c^2	214059	218257	ff$\to$ZZ	14393247	15533558
M_H=550 GeV/c^2	202254	216843	$t\bar{t} \to l^+l^- + \not{E}_T$	10975735	11314406
M_H=600 GeV/c^2	212009	215882			

Table 3.12: Total number of PYTHIA events generated for the Neutral Vector Boson study.

The event generation and analysis was performed using the THOR[8] computing cluster at the University of Alberta, and the Glacier[9] cluster provided by the WestGrid collaboration. Separate data sets for each of the 4 processes listed in equation 1.45 were generated along with their corresponding background processes. Table 3.12 gives the total number of PYTHIA events generated for the neutral vector boson channel study which will be discussed in chapter 4. Table 3.13 gives the total number of PYTHIA events generated for the charged vector boson channel study which will be discussed in chapter 5. In total the generation and reconstruction of each of these 4 processes took approximately 5 CPU years, giving a total of 20 CPU years for the complete analysis.

---

[8]The THOR computing cluster consits of 74 dual processors with an average CPU speed of 1.4 GHz[58]

[9]Glacier is a 1680 processor Beowulf cluster hosted by the University of British Columbia. It consists of 840 dual-processor(each CPU is a 3.0 GHz Xeon processor) computing nodes[59]

Physics Channel	$W \to \mu^{\pm}\nu_{\mu}$	$W \to e^{\pm}\nu_e$	Physics Channel	$W \to \mu^{\pm}\nu_{\mu}$	$W \to e^{\pm}\nu_e$
M_H=170 GeV/c^2	436053	335263	M_H=600 GeV/c^2	414197	314210
M_H=180 GeV/c^2	434737	333866	M_H=650 GeV/c^2	413324	313369
M_H=190 GeV/c^2	433380	332599	M_H=700 GeV/c^2	412675	312903
M_H=200 GeV/c^2	432140	331636	M_H=750 GeV/c^2	411989	312448
M_H=210 GeV/c^2	430761	330572	M_H=800 GeV/c^2	411790	301706
M_H=220 GeV/c^2	430058	329663	M_H=850 GeV/c^2	411482	301216
M_H=230 GeV/c^2	429039	317555	M_H=900 GeV/c^2	410845	311269
M_H=240 GeV/c^2	427997	327990	M_H=950 GeV/c^2	410842	300777
M_H=250 GeV/c^2	427017	316278	M_H=1000 GeV/c^2	410658	310805
M_H=300 GeV/c^2	423596	323598	W+jets		
M_H=350 GeV/c^2	421198	321280	CKIN(3)=0	192966138	194645371
M_H=400 GeV/c^2	419031	319119	CKIN(3)=40	65287601	68937703
M_H=450 GeV/c^2	417365	317237	CKIN(3)=100	81710579	73300917
M_H=500 GeV/c^2	415990	316056	ff→WW	25169020	39789738
M_H=550 GeV/c^2	415020	314899	$t\bar{t} \to l\nu$jjbb	35901872	42343477

Table 3.13: Total number of PYTHIA events generated for the Charged Vector Boson study.

75

Chapter 4

H → ZZ Event Reconstruction

A heavy neutral scalar Higgs boson that is produced through vector boson fusion and decaying through the neutral vector boson channel, H→ZZ→lljj, is characterized by:

- Two central high P_T leptons ($l=e,\mu$).

- Two central high P_T hadronic jets.

- Two tagging jets, one in the forward ($\eta > 0$) and one in the backward ($\eta < 0$) direction.

- Apart from the jets arising from the Z^0 decay there is minimal hadronic activity in the central region.

The Feynman diagram describing Higgs production by vector boson fusion is shown in figure 4.1.
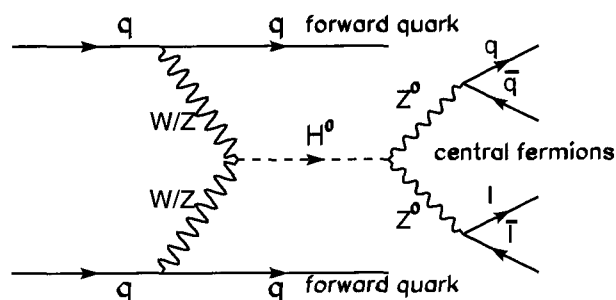
Figure 4.1: The Higgs boson signal is characterized by two high P_T central jets with a combined mass M_Z and two oppositely charged leptons also with mass M_Z. There are also 2 highly energetic forward jets.

The definition of forward and central jets utilized in this thesis is discussed in more detail in section 4.4. The central region is usually defined as $|\eta| \leq 2.0$ and the forward (backward) region as $\eta > 2.0$ ($\eta < -2.0$).

76

Process	Higgs Mass (GeV/c^2)	PYTHIA ISUB Process	Cross Section (mb)
H$\rightarrow$ZZ$\rightarrow$lljj (l=e,μ)	200	123/124	2.98×10^{-11}
	600	123/124	4.59×10^{-12}
	1000	123/124	1.30×10^{-12}
Z+jets$\rightarrow$ll+jets	-	15/30	1.05×10^{-5}
ff$\rightarrow$ZZ$\rightarrow$lljj	-	22	6.01×10^{-10}
t$\bar{t}$ $\rightarrow$WbWb$\rightarrow$(lνb+lν b)	-	81/82	5.66×10^{-9}

Table 4.1: The cross sections for the neutral vector boson signal and its backgrounds as calculated by PYTHIA 6.227.

The Feynman diagrams for the main backgrounds are shown in figure 4.2 and their cross-sections are given in table 4.1. The main background processes are summarized below:

- p+p$\rightarrow$Z^0+jets: This process has the largest cross section, in some cases 10^7 times greater than the signal, but has on average low event P_T and a small number of jets.

- The ZZ continuum, q+$\bar{q}$,g+g$\rightarrow$Z+Z^1: This process has the high P_T nature of the signal but has a small cross section and no tagging jets (at tree level). This is also referred to as the irreducible background since it closely resembles the signal.

- t$\bar{t}$ production: The top quark decays predominantly through the channel t$\rightarrow$Wb, producing two oppositely charged W-bosons. Forcing each W boson to decay W$\rightarrow$ lν gives two b-jets and two oppositely charged leptons. A cut on the invariant mass of the two reconstructed Z^{0}s greatly reduces this background. These events are not accompanied by tagging jets.

There is potential that the large QCD background could mimic the Higgs signature. For this to occur we would need a QCD event with 6 jets; according to [60] 6 jets with P_T >15 GeV/c has a cross-section of roughly 0.4 nb (compared to roughly 10 nb for the Z+jets background). We would then need to misidentify 2 of the hadronic jets as either electrons or muons. Studies from the Tevatron[61] indicate that the fake electron rate is below 1/1000. The probability of 2 jets "fluctuating" to electrons is roughly 15 in 10^6. Secondly, these two fake leptons do not originate from a vector boson therefore a cut on the mass of the leptonically reconstructed Z will also greatly reduce this background. For these reasons we did not consider intrstrumental QCD backgrounds to be significant.

Precuts are cuts that are applied prior to the final event reconstruction. They are meant to limit the number of Monte-Carlo events that need to be generated and fully analyzed. These cuts can be applied at one of two stages: as a switch for the PYTHIA Monte-Carlo program; or, at the particle level prior to the four vectors being processed by the ATLAS

---

[1]This will be referred to as ff$\rightarrow$ZZ where f=g,q
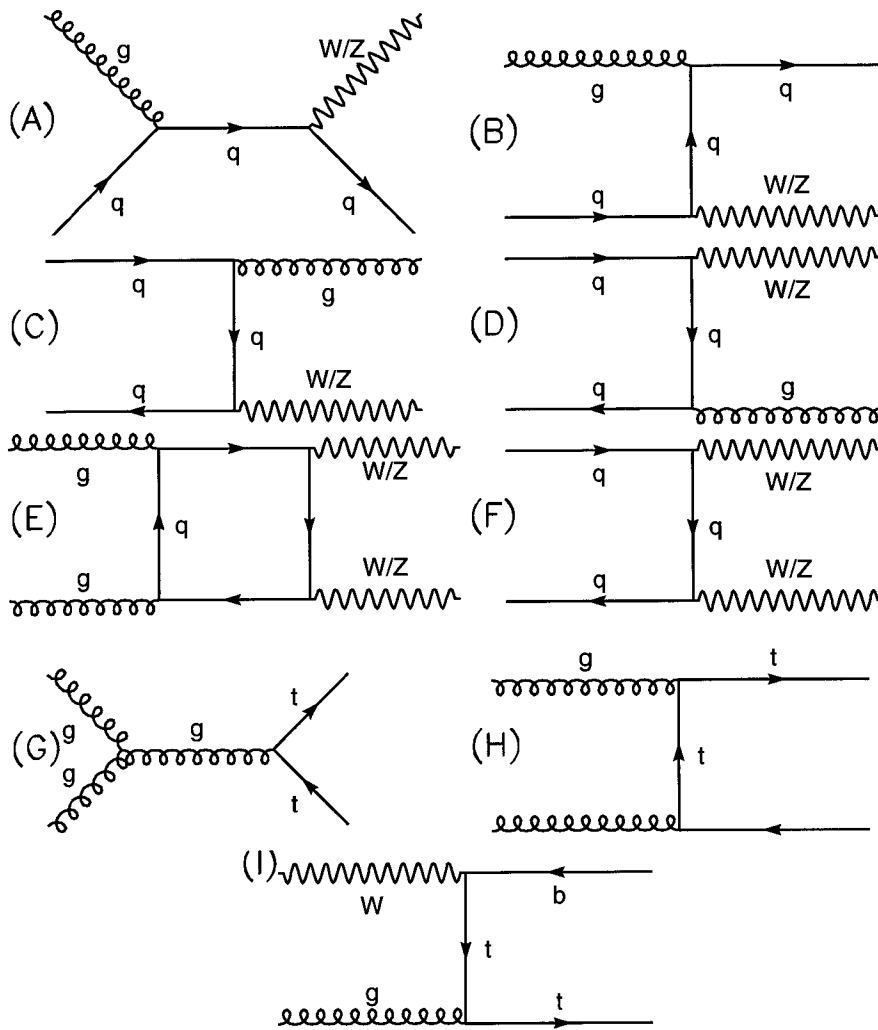
Figure 4.2: Diagrams (A) through (D) are the Z+jets background. (E)+(F) represent the ZZ continuum.(G)+(H) t$\bar{\text{t}}$ →WbWb. (I) Electroweak single top production is a possible background to the WW physics channels.

78
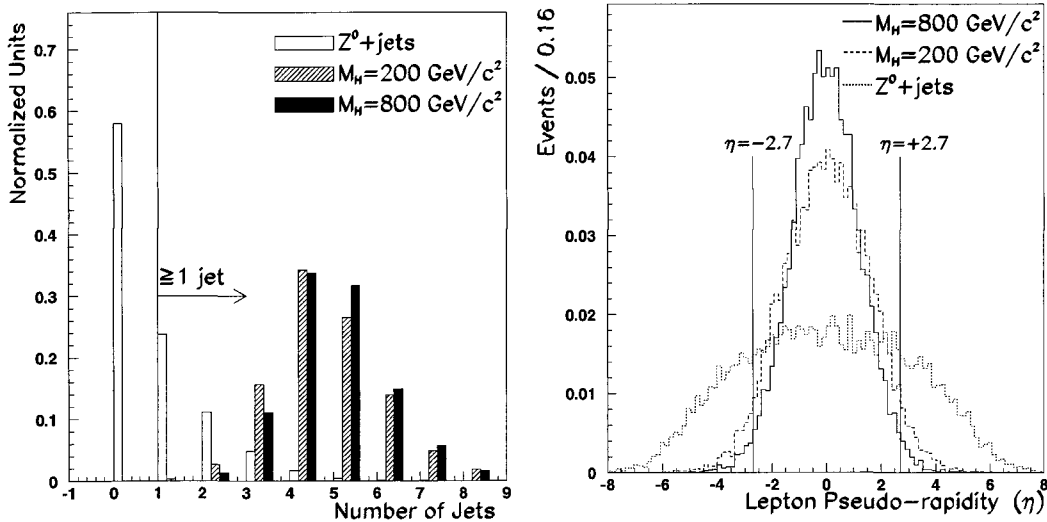
Figure 4.3: (a) The Z+jets background contains fewer jets than the signal. To reduce the background rate we require there to be ≥ 1 jet.(b) The low transverse momentum of the Z-boson in the Z+jets background gives a larger spread in pseudo-rapidity for the lepton. The vertical lines give the bounds of the muon detector.

software. In the former case the switches restrict the phase space available to the requested physics channel reducing the number of events that need to be generated. The latter case uses information from the PYTHIA tree to determine if the event topology resembles that of the Higgs signal. The 4-vectors of muons and electrons in the PYTHIA tree are examined to determine if they track to their respective detectors. The PYTHIA tree, excluding muons and neutrinos[2], is then projected into the calorimetry with a coarse granularity of $\Delta\eta \times \Delta\phi$=0.1×0.1. A cone algorithm (section 3.2.1) implementing a 5 GeV/c jet initiator and 5 GeV/c jet is then used to identify jets.

The main background to the signal H$\rightarrow$ZZ$\rightarrow$ l^+l^-jj, is the Z^0+jets channel. Figure 4.3 compares the number of jets and the distribution of event leptons between a 200 (800) GeV/c^2 Higgs sample and the background. The Feynman diagrams for the Z^0+jets background, figures 4.2(a) to (d), suggest a single final state parton. However this parton may not be energetic enough to produce a jet that can be reconstructed in the detector resulting in a significant number of background events not containing any jets. We may also get more than the expected number (one) of jets due to initial state/final state radiation, as well as secondary collisions within the interacting protons (multiple interactions). It is tempting to place a strong cut on the number of jets but it must be noted that the energy introduced by pileup events may also introduce extra jets. For example, an event which contains 2

---

[2]We have also removed electrons with $|\eta| < 2.5$ arising from the decay Z$\rightarrow$ee. This avoids mistakingly identifying the energy deposited by an isolated electron as a possible hadronic jet.

79
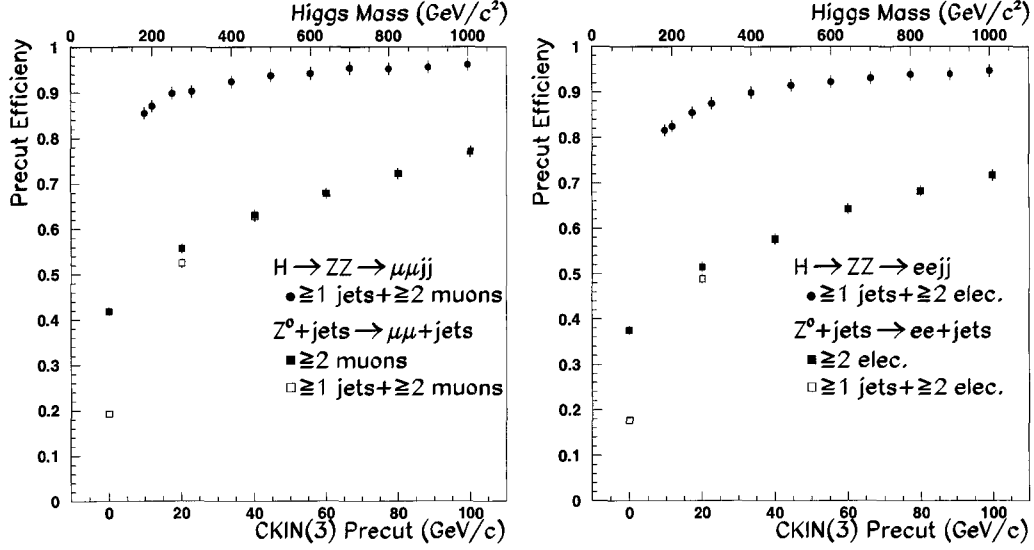
Figure 4.4: Precut efficiency as a function of Higgs mass (for the signal), and the CKIN(3) parameter threshold for the Z+jets; (a) for the muon channel and (b) for the electron channel.

Process	Electron Channel	Muon Channel
M_H=200 GeV/c^2	82.5%	87.0%
M_H=600 GeV/c^2	93.9%	95.2%
ff$\rightarrow$ZZ	63.7%	67.8%
t$\bar{\text{t}}$ $\rightarrow$WbWb	88.6%	91.2%
Z^0+jets,CKIN(3)=0 GeV/c	17.7%	19.2%
Z^0+jets,CKIN(3)=40 GeV/c	57.6%	62.7%

Table 4.2: Precut efficiencies for selected Z^{0}physics processes requiring 2 leptons and 1 jet.

jets in the absence of pileup may contain the required 4 jets in the high luminosity case. Requiring that there be greater than or equal to one jet reduces the background but does not significantly bias the results at high luminosity[3].

For the Z$\rightarrow$ $\mu^+\mu^-$ channel we require that the tree contain 2 muons/anti-muons in the pseudorapidity region $|\eta| < 2.7$. Similarly for the Z$\rightarrow$ e^+e^- channel we require that there be 2 electrons/positrons with a pseudo-rapidity $|\eta| < 2.5$. These two channels require different precut pseudo-rapidity values due to the differences in their respective detector coverage. Select precut efficiencies are shown in figure 4.4 and listed in table 4.2. It should be noted that at this preliminary stage we are assuming 100% efficiency in reconstructing jets and leptons.

---

[3]This is addressed in more detail in section 6.4.3.

The PYTHIA CKIN(3) parameter is a cut, in the center of mass frame, on the three-momentum of the particles responsible for the hard $2\rightarrow 2$ interaction. A value of CKIN(3)=40 GeV/c applied to the process $gq\rightarrow qZ^0$ restricts the momentum of the initial and final particles to be greater than 40 GeV/c. Previous studies have used cuts of 50 GeV/c for a Higgs mass between 300 GeV/c^2 and 600 GeV/c^2 [62], and 100 [14] or 150 [63] GeV/c for a Higgs mass of 1 TeV/c^2. This thesis uses three different CKIN(3) values. Each value is used to evaluate a specific Higgs boson mass region. The CKIN values and the corresponding mass regions[4] are:

$$180 \text{ GeV/c}^2 < \text{M}_H \leq 250 \text{ GeV/c}^2 \quad \text{CKIN(3)=0 GeV/c}$$
$$250 \text{ GeV/c}^2 < \text{M}_H \leq 500 \text{ GeV/c}^2 \quad \text{CKIN(3)=40 GeV/c}$$
$$500 \text{ GeV/c}^2 < \text{M}_H \leq 1000 \text{ GeV/c}^2 \quad \text{CKIN(3)=100 GeV/c}$$

4.1   Lepton Reconstruction

The first stage in the ATLFAST reconstruction of the leptonic decay $Z^0 \rightarrow l^+l^-$ is to identify all the isolated leptons in the event. We previously discussed muon resolution and identification efficiency in section 3.4.1 and electron resolution and identification efficiency in section 3.5. There are two possible origins of leptons in our events: leptons which arise from the decay $Z\rightarrow l^+l^-$ and leptons which originate from particle decay inside a hadronic jet.

4.1.1   Muon Identification

The amount of energy surrounding a muon is calculated as :

$$E_T = \sqrt{(\sum_{\substack{\Delta R \leq 0.2 \\ i=1}}^{N_{cells}} E_x)^2 + (\sum_{\substack{\Delta R \leq 0.2 \\ i=1}}^{N_{cells}} E_y)^2} \tag{4.1}$$

In full simulation this cone will include the underlying activity of the event as well as any energy deposited by the muon as it traversed the calorimetry. A muon is isolated in full simulation when it satisfies the condition:

$$\frac{E_T}{P_T^{spec}} \leq 0.4 \tag{4.2}$$

where E_T^{spec} is the transverse energy of the muon as measured by the muon spectrometer.

In fast simulation we determined the muon transverse energy (E_T^{atlf}) by smearing the tree level value by the appropriate resolution as determined using full simulation (section 3.4.1). In ATLFAST the muon does not deposit any of its energy in the calorimetry so E_T

---

[4]The mass regions given are only approximate.

81

is only a measure of the underlying activity of the event. A muon is isolated in ATLFAST when:

$$\frac{E_T}{E_T^{atlf}} \leq 1.0 \tag{4.3}$$

In the full simulation the muon loses energy in the calorimetry; therefore, the muon transverse energy measured by the muon spectrometer in full simulation (P_T^{spec}) will be less than the energy recorded by ATLFAST (P_T^{atlf}). This accounts for the difference in isolation cuts between the two programs.

4.1.2 Electron Identification

In full simulation, as outlined in section 3.5, we were able to distinguish between electron jets and hadron jets by requiring that a specific fraction of the jet cluster transverse energy be electromagnetic in nature. This cut will also distinguish between isolated electron jets and non-isolated electrons (electrons which originate inside hadronic jets). This is possible in full simulation since the calorimetry measures the hadronic and electromagnetic components separately.

In ATLFAST the electron transverse energy (E_T^{elec}) is determined by applying a resolution factor to the tree level value. An isolation cone surrounding the electron direction will contain both the underlying activity of the event as well as the energy of the electron. We define an isolated electron in ATLFAST as those electrons which satisfy the condition:

$$\frac{E_T}{E_T^{elec}} \leq 2.5 \tag{4.4}$$

4.1.3 Lepton Pair Reconstruction

The $Z^0 \to l^+l^-$ reconstruction algorithm cycles through all possible combinations of oppositely charged isolated leptons and picks the pair with an invariant mass closest to $M_Z = 91.2$ GeV/c^2. The reconstructed Gaussian width of the Z^0 as a function of Higgs boson mass and lepton flavour is shown in figure 4.5.

For a Higgs boson with a mass above 190 GeV/c^2 the Gaussian width of the muonic decay can be parameterized as:

$$\begin{aligned} \text{Low Luminosity} \quad \Gamma(Z^0) &= \quad 2.49 + 0.00182 \, M_H - 0.844 \times 10^{-6} M_H^2 \\ \text{High Luminosity} \quad \Gamma(Z^0) &= \quad 2.60 + 0.00164 \, M_H - 0.735 \times 10^{-6} M_H^2 \end{aligned} \tag{4.5}$$

Similarly for the electronic decay:

$$\begin{aligned} \text{Low Lumi.} \quad \Gamma(Z^0) &= 3.89 - 0.00073 M_H - 0.867 \times 10^{-6} M_H^2 + 0.992 \times 10^{-9} M_H^3 \\ \text{High Lumi.} \quad \Gamma(Z^0) &= 5.70 - 0.00635 M_H + 0.564 \times 10^{-5} M_H^2 - 0.152 \times 10^{-8} M_H^3 \end{aligned} \tag{4.6}$$

82
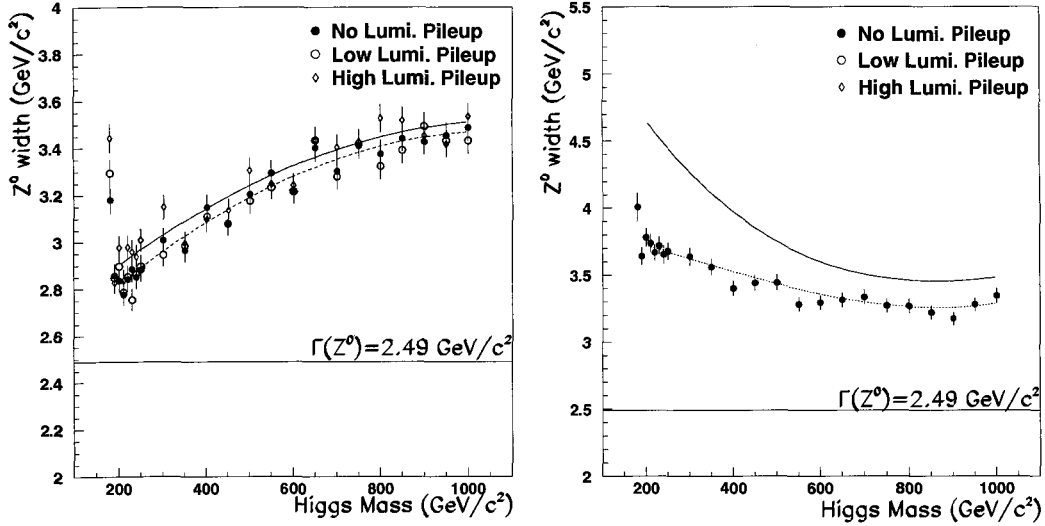
Figure 4.5: The width of the leptonically reconstructed Z^0 boson as a function of Higgs Mass. (a) Muon channel (b) Electron channel. Electronic noise has been turned on. $\Gamma(Z^0)$=2.49 GeV/c^2 is the Z^0 width as stated in the PDG[3].

The resolution of the $Z \to e^+e^-$ decay is measurably worse in the high luminosity scenario due to the pileup energy deposited in the calorimetry. The combination of the muon spectrometer and the tracking measurement from the inner detector reduce the effect of luminosity pileup on the resolution of the $Z \to \mu^+\mu^-$ decay channel.

A comparison of the reconstructed Z^0 invariant mass between the electron and muon channels can be found in figure 4.6. The inner detector allows for accurate measurement of low P_T muons giving a better resolution to the $\mu^+\mu^-$ channel at low Higgs boson masses. When the Higgs mass is increased the average E_T of the leptons increases. Equation 2.10 shows that the electron resolution improves with increasing transverse energy while figure 2.18 shows that the muon measurement worsens. Above approximately M_H=700 GeV/c^2 the electron channel gives the best resolution for reconstructing the leptonic Z decay. Both the electron and muon channels have a non-Gaussian low mass tail that is caused by the radiation of photons off the primary leptons with a photon-lepton separation (ΔR) greater than 0.2.

4.2 Z→jet+jet Reconstruction

To avoid confusing the jet energy deposited in the calorimetry with energy deposited by signal leptons arising from the decay $Z \to l^+l^-$, the cells which lie in a cone of $\Delta R \leq 0.2$ around the selected isolated leptons are marked as "used" and removed from consideration

83
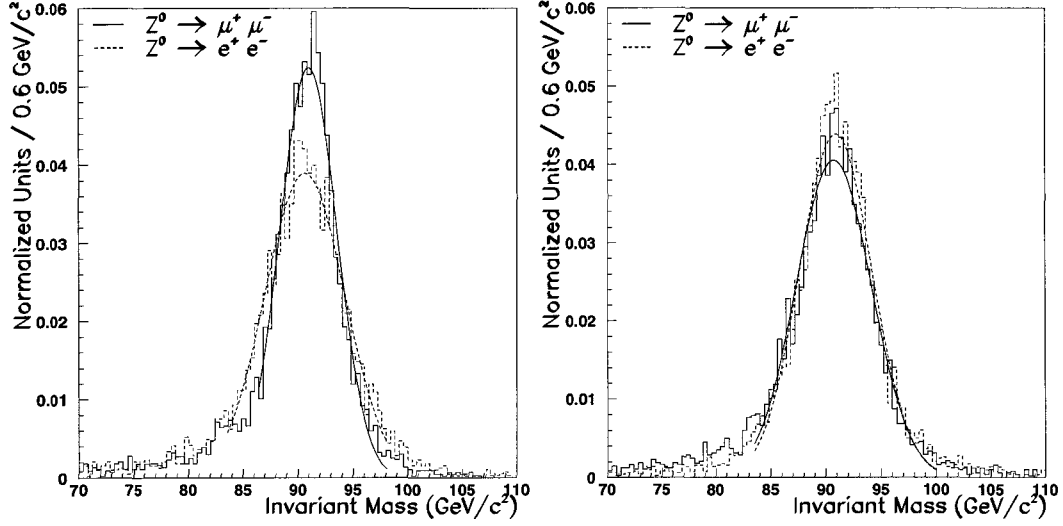
Figure 4.6: The width of the leptonically reconstructed Z^0 boson as a function of Higgs Mass; (a) M_H=200 GeV/c^2, (b) M_H=1000 GeV/c^2. Performed while including electronic noise and in the absence of luminosity pileup.

as possible jet initiators.

There are expected to be four jets in an event with two of the jets arising from quarks in the hadronic decay $Z^0 \rightarrow q\bar{q}$. There are three different approaches [64] to the reconstruction of this decay. However, picking one method (and one cone radius) removes the need for multiple calibration routines.

The first and most flexible of these methods, and the method used for this analysis, is to calculate the invariant mass[5] by summing up the four-momentum (P_μ^{cell}) of all given cells within a distance R_0 around the two jet baricentres.

$$M_Z^2 = (\sum_{\substack{\Delta R_1, \Delta R_2 \leq R_0 \\ i=1}}^{N_{cells}} P_{cell_i}^\mu)^2 \tag{4.7}$$

It was found that in full simulation, at low luminosity, a cone with radius R_0=0.6 optimized the Z→jet+jet mass resolution. A smaller cone looses too much of the jet energy and a larger cone magnifies the effects of electronic noise and luminosity pileup.

Secondly, if the hadronically decaying Z^0 has low transverse momentum the jets are sufficiently isolated ($\Delta R > 0.8$) and the invariant mass can be calculated using the 4-momentum of the calibrated jets.

$$M_Z^2 = (P_{\mu,(j1)} + P_{\mu,(j2)})(P_{(j1)}^\mu + P_{(j2)}^\mu) \tag{4.8}$$

---

[5]The dot product of a contravariant 4-vector P^μ=(E,p_x,p_y,p_z) and a covariant 4-vector P_μ=(E,-p_x,-p_y,-p_z) is a Lorentz invariant. For jets arising from a Z^0 this invariant is M_Z^2.

84
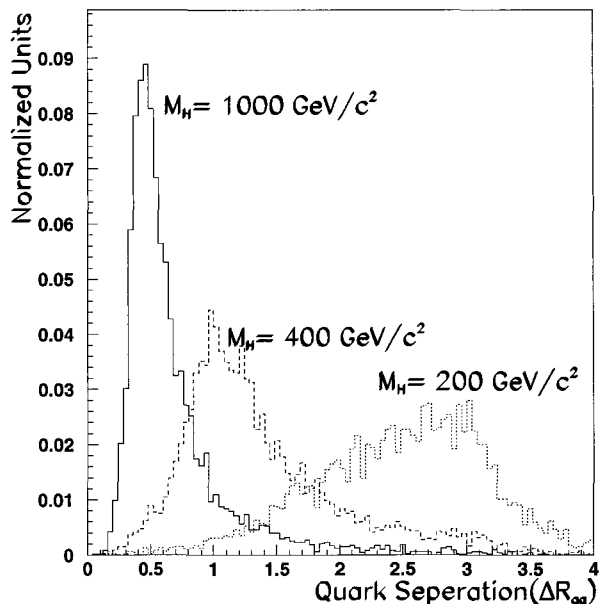
Figure 4.7: As the Higgs boson mass increases the quark-quark separation in $\eta \times \phi$ space decreases.

where $P_{\mu,(j1)}$ is the covariant 4-vector for the first jet and $P_{\mu,(j2)}$ is the covariant 4-vector for the second jet. This method is not appropriate for Higgs boson masses above 400 GeV/c² since a significant number of events will have overlapping jets as shown in figure 4.7.

Lastly, for high vector boson transverse momentums the jets from the Z→jet+jet decay have a substantial overlap. The four-momentum of the vector boson can be determined by summing up the four-momentum of the cells in a single cone with a larger radius, typically between R=0.5-0.8.

$$M_Z^2 = (\sum_{\substack{\Delta R \leq R_0 \\ i=1}}^{N_{cells}} P_{cell_i}^{\mu})^2 \tag{4.9}$$

Figure 4.7 shows that even for a 1 TeV/c² Higgs boson sample the vector bosons are produced with a wide range of transverse momentums giving a wide range of quark-quark separations, producing many events without jet overlap.

The work presented in this thesis covers a very large Higgs boson mass range, approximately 170 GeV/c² to 1 TeV/c² , and consequently a very large transverse momentum range for the vector bosons. Since the first outlined method does not make specific requirements on the jet-jet separation (as do the other two possible methods) it is ideal for this thesis.

The hadronic Z^0 identification proceeds by cycling through all possible jet-initiator pairs,

85
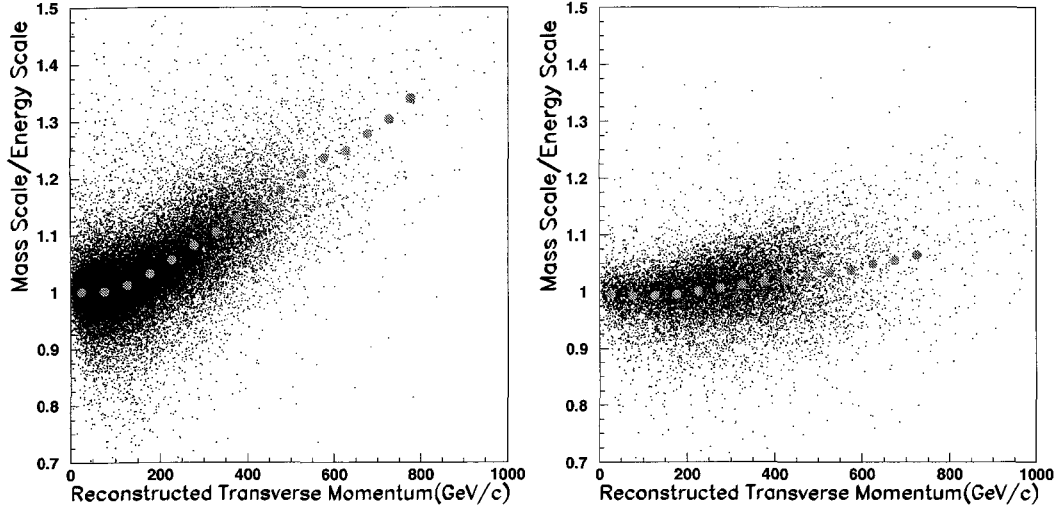
Figure 4.8: The relationship between the mass and energy scales as a function of reconstructed P_T for (a) full and (b) fast simulations. The light circles are the mean values of 50 GeV bins, average over all pseudo-rapidity.

identified using the local maximum method (section 3.2.4), and choosing the pair with the best calibrated invariant mass. The calibration of jet-jet pairs is discussed in the following section.

4.2.1 Calibration

It has been noted in [40] and [64] that there exists a deviation from unity in the mass scale to energy scale ratio at high transverse momentums. Figure 4.8 displays this deviation as a function of the reconstructed (uncalibrated) Z^0 transverse momentum for both full and fast simulations. If the event has been properly reconstructed one would expect the relationship between the mass scale and energy scale to be unity.

$$\frac{M_{Z(recon)}/M_{Z(quarks)}}{E_{Z(recon)}/E_{Z(quarks)}} \equiv 1 \tag{4.10}$$

A particle in ATLFAST deposits all of its energy into a single projected calorimeter cell. Full simulation uses GEANT 3 to model the interaction of the incident particle within the calorimetry. Secondary particles are produced in these interactions and the subsequent transverse spread of the shower deposits energy in the calorimeter cells that surround the seed cell. To reconstruct the four-momentum of the incident particle ($|E| \approx |\vec{P}|$ for an ultra-relativistic particle) the four-momentum of all energetic cells surrounding and including the incident seed cell must be summed. Each cell is assumed to be massless and its four-

86

momentum calculated as:

$$
\begin{aligned}
P^{\mu,cell} &= (E^{cell}, P_x^{cell}, P_y^{cell}, P_z^{cell}) \\
E^{cell} &= E \\
P_x^{cell} &= \frac{E}{cosh(\eta)} cos(\phi) \\
P_y^{cell} &= \frac{E}{cosh(\eta)} sin(\phi) \\
P_z^{cell} &= \frac{E}{cosh(\eta)} sinh(\eta)
\end{aligned}
\tag{4.11}
$$

where η, ϕ are the pseudo-rapidity and azimuthal angle (respectively) of the centre of the seed cell. The transverse spread of the shower reduces the 3-momentum (P_x, P_y, P_z) of the particle while maintaining the energy(E). This produces a massive particle with $|E| > |\vec{P}|$.

This behaviour can be extended to the reconstruction of the massive jet-jet pair originating from the Z^0 decay. If a single calibration factor were applied to both the jet-jet energy and the jet-jet 3-momentum we properly identify the initial energy but underestimate the three-momentum resulting in a calibrated invariant mass that would be greater than M_Z.

While ATLFAST does not have the full showering in the calorimeter that is modeled in ATRECON it still displays the deviation from unity at high transverse momentum. Any process which increases the transverse spread of the jet contributes to this deviation. In ATLFAST this can be attributed to two factors:

- The Inner Detector magnetic field: The applied magnetic field separates oppositely charged particles increasing the azimuthal spread of the jet.

- The granularity of the calorimeter: while most of the jet energy arrives in the portion of the cell nearest to the jet baricentre the summation of the four-momentum uses the center (η,ϕ) of the cell to determine the 3-momentum (P_x, P_y, P_z), effectively increasing the size of the jet.

These effects are over-shadowed in full simulation by the shower spreading inside the calorimeter.

Introducing two calibration constants α and β, where α is the calibration factor of the energy and β the additional correction (applied after α) for the 3-momentum, we expect the relationship:

$$
\beta(\alpha \frac{P_{recon}}{P_{quarks}}) = \alpha \frac{E_{recon}}{E_{quarks}} = 1
\tag{4.12}
$$

where E_{recon} is the reconstructed energy and E_{quarks} is the tree level energy. The energy calibration factor is a function of energy and direction:

$$
\alpha = \alpha(E_{recon}, \eta_{recon}) = \frac{E_{quarks}}{E_{recon}}
\tag{4.13}
$$

87
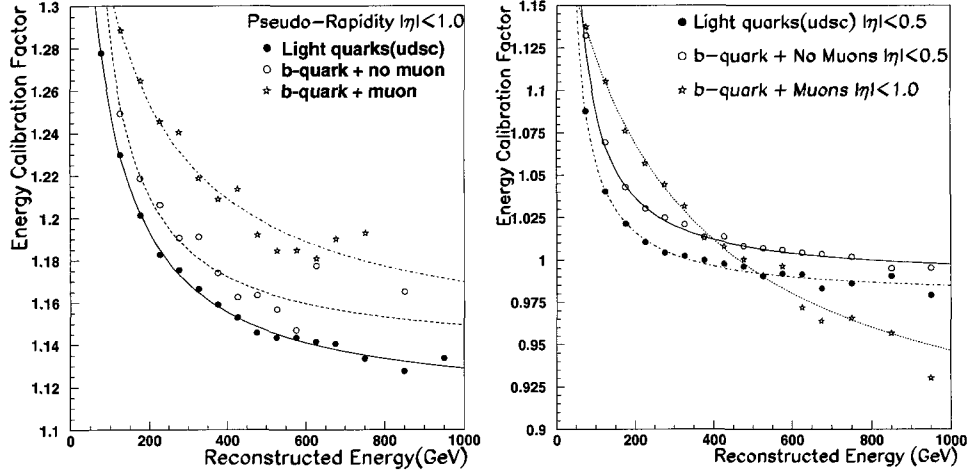
Figure 4.9: Sample energy calibration (α) curves for jet-jet pairs in (a) ATRECON and (b) ATLFAST.

The correction factor for momentum is also a function of energy and position. Solving equation 4.12 for β :

$$\beta(E_{\text{recon}}, \eta_{\text{recon}}) = \frac{E_{\text{recon}}}{E_{\text{quarks}}} \frac{P_{\text{quarks}}}{P_{\text{recon}}} \quad (4.14)$$

Using the jets found from the local maximum method the jet-jet pair with the best invariant mass is identified as a possible Z^0 boson candidate. The invariant mass of the pair is determined by summing up the 4-momentum of all the cells within a distance of ΔR <0.6 from either jet baricentre using equation 4.15 and the algebra from equation 4.11.

$$
\begin{aligned}
E_{recon} &= \sum_{i=1}^{N_{cells}} E_{cell_i} \\
P_{recon} &= \sqrt{\sum_{j=2}^{4} (\sum_{i=1}^{N_{cells}} P_{cell_i}^j)^2}
\end{aligned}
\quad (4.15)
$$

A Z^0 boson candidate is identified as a true Z^0 if the two jet baricentres lie at a distance no greater than ΔR =0.2 from the initial tree level quark directions. As was the case with the jet calibration the light quarks (udsc) and heavy b-quarks are calibrated separately. The heavy b-quarks are further sub-divided into those events with a muon and those without.

The energy calibration factor (α) for the hadronic reconstruction of a jet-jet pair can be parameterized as:

$$\alpha = (A_0 + \frac{A_1}{E_{recon} - A_2}) \quad (4.16)$$

A sample of the calibration curves for both ATLFAST and ATRECON are given in figure 4.13, with the fits to the curves summarized in table 4.3. For the case of the leptonic b-decay the energy of the non-isolated muons within a distance ΔR < 0.6 is included in the reconstructed energy.

88

Full Simulation								
η range	Light quarks			Heavy b quarks				
				Hadronic			Semi-Leptonic		
	A_0	A_1	A_2	A_0	A_1	A_2	A_0	A_1	A_2
0.00→1.0	1.11	20.6	-47.3	1.13	15.4	-4.34	1.14	39.3	-131
1.00→2.0	1.09	54.1	-204.5	1.12	37.1	-86.7	1.14	58.6	-231
η >2.0	1.12	32.2	-99.7	1.15	21.9	-22.3	:	:	:
Fast Simulation								
η range	Light quarks			Heavy b quarks				
				Hadronic			Semi-Leptonic		
0.0→0.5	0.977	7.52	6.72	0.988	9.45	5.33	0.871	97.0	-291
0.5→1.0	0.981	7.64	12.0	0.991	9.98	4.10			
1.0→1.5	0.981	10.4	-16.3	0.991	14.3	-28.8	0.846	57.2	-234
1.5→2.0	0.983	13.4	-62.6	0.993	19.9	-80.7			
2.0→	0.989	22.9	-225	1.005	14.2	-74.0	0.998	102.3	-1425

Table 4.3: The parameters used in the calibration of the Z→jet+jet energy for ATRECON and ATLFAST.

Heavy Flavour identification

The b-ness determination of a jet was previously discussed in section 3.3.2. A jet is identified as a b-jet when it possesses greater than or equal to 3 b-tracks. The b-ness of a jet-jet pair is determined by cycling through all the tracks in the event that fall within a ΔR <0.4 of either jet baricentre and have a Z_0 value at the point of closest approach no further than 0.5 cm from the primary vertex. For each of these tracks the signed impact parameter is calculated. If the track is near both baricentres it is associated with the jet that minimizes the ΔR value. A track is identified as a b-track when the signed impact parameter (sd0) satisfies: 0.009 cm < sd0 < 0.15 cm.

When both quarks fall within the tracking region of the inner detector ($|\eta|$ <2.5), the b-ness of uds and b-type quark pairs originating from a Higgs boson with a mass M_H=200 GeV/c^2, in the absence of pileup, is given in figure 4.10

Jet-pairs with a b-ness greater than or equal to 3 are taken to originate from heavy b-quark pairs and are calibrated accordingly. This condition mistakes uds type events as a b-type event with a frequency of 3.5%. Events which arise from the decay Z→b$\bar{b}$ are improperly identified as a light quark pair approximately 27% of the time.

4.2.2 Momentum Correction

In section 4.2.1 we discussed the motivation for calibrating the energy and momentum separately. This dual-calibration method is required primarily due to the effects of the detector

89
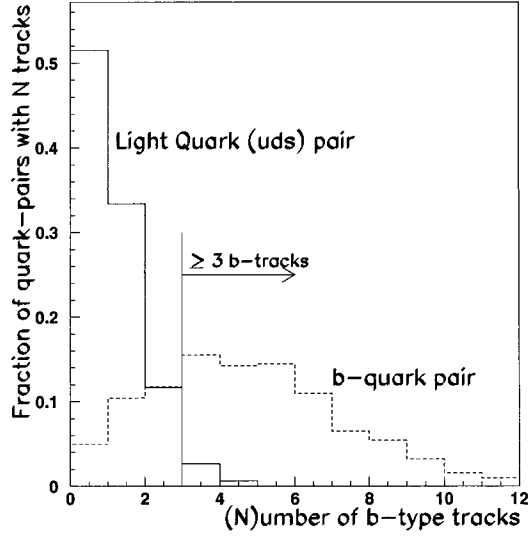
Figure 4.10: The b-ness of uds and b type quark pairs (when both quarks fall in the tracking region) from a Higgs boson with mass 200 GeV/c^2 as determined by ATLFAST.

(showering inside the calorimetry, applied magnetic fields etc.). The momentum correction factor is therefore, to first order, independent of the flavour of the hadronic decay. The correction factor β as a function of energy and pseudo-rapidity is shown in figure 4.11. These curves can be fit with the 5-th order polynomial given in equation 4.17, the values of which are given in table 4.4.

$$\beta - 1 = A_0 + A_1\ M_H^1 + A_2\ M_H^2 + A_3\ M_H^3 + A_4\ M_H^4 + A_5\ M_H^5 \tag{4.17}$$

The reconstructed invariant mass of a properly identified Z$\rightarrow$jj (the reconstructed jets are within $\Delta R \leq 0.2$ of the original quarks) decay originating from the decay of a 600 GeV/c^2 Higgs boson is shown in figure 4.12. Due to the large amount of energy lost in the calorimetry the invariant mass calculated using full simulation falls 12 GeV/c^2 below the nominal mass (4 GeV/c^2 for ATLFAST). Multiplying the reconstructed 4-momentum by the energy calibration factor overcalibrates the invariant mass in full simulation by approximately 5 GeV/c^2. Recalculating the 3-momentum by applying the β-correction factor brings the invariant mass of the reconstructed Z^0 to the nominal value. Figure 4.12(b) shows that for fast simulation there is no significant change in the reconstructed invariant mass when the β-correction factor is introduced.

The invariant mass of the reconstructed hadronic object is now calculated as:

$$M_Z^2 = (\alpha E_{recon})^2 - (\beta(\alpha P_{recon}))^2 \tag{4.18}$$

90
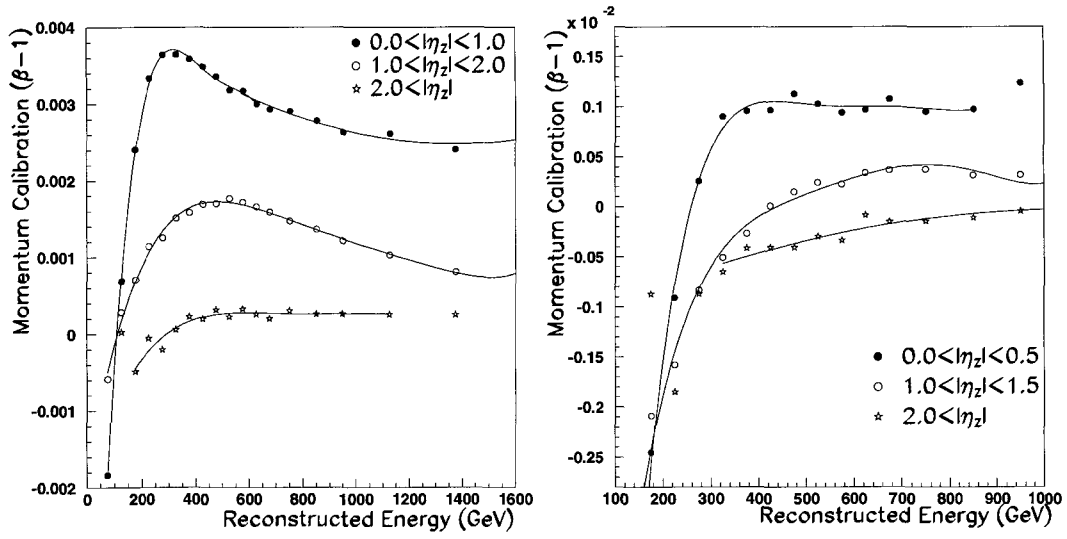
Figure 4.11: The momentum calibration factor β as a function of energy and pseudo-rapidity for (a) full and (b) fast simulations.

Pseudo-Rapidity	Cut-Off Energy (GeV)	ATLFAST					
		A_0 $\times 10^{-1}$	A_1 $\times 10^{-4}$	A_2 $\times 10^{-7}$	A_3 $\times 10^{-9}$	A_4 $\times 10^{-12}$	A_5 $\times 10^{-15}$
0.0→0.5	800	-0.209	1.86	-6.16	0.999	-0.796	0.249
0.5→1.0	800	-0.153	1.12	-3.08	0.417	-0.281	0.0761
1.0→1.5	800	-0.112	0.855	-2.67	0.423	-0.330	0.0999
1.5→2.0	1000	-0.0117	0.0263	-0.0136	0.0	0.0	0.0
2.0→	1000	-0.0116	0.0217	-0.0103	0.0	0.0	0.0
		ATRECON					
0.0→1.0	600	-0.0846	1.13	-3.81	0.545	-0.287	0.0
	1500	0.0439	-0.0278	0.0101	0.0	0.0	0.0
1.0→2.0	1500	-0.0186	0.214	-0.468	0.0473	-0.0235	0.00460
2.0→	1000	-0.0185	0.113	-0.221	0.0186	-0.00571	0.0

Table 4.4: The parameterization fits for the momentum calibration factor β. For calculation purposes events with $E > E_{cutoff}$ we set $E \equiv E_{cutoff}$.

91
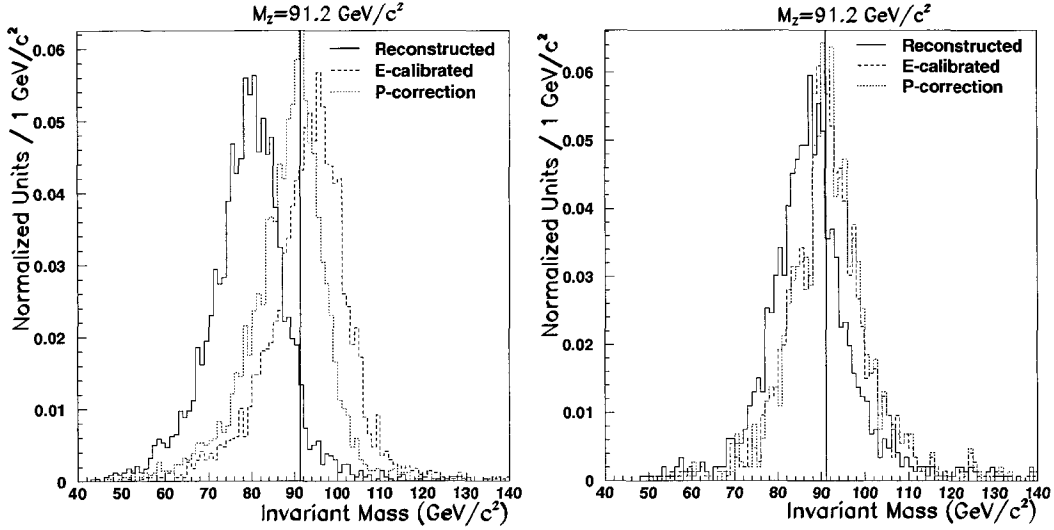
Figure 4.12: (a)The energy-momentum calibration for full simulation properly corrects for the deviation in the mass to energy scale shown in figure 4.8. (b) The correction at ATLFAST is small for this momentum range and therefore not directly obvious. The vertical line corresponds to the mass of the Z^0 boson (M_Z=91.2 GeV/c^2).

4.2.3 Energy Resolution Correction

The different treatment of the calorimetry between full and fast simulation results in a different energy resolution for the reconstructed hadronic Z^0. The resolution of the calibrated energy of the reconstructed Z→jet+jet decay, when the jets have been properly identified, is shown in figure 4.13. The energy resolutions of the two simulations are :

$$\text{Full Simulation} \quad \frac{\Delta E}{E} = \sigma_D = \quad 0.0414 \oplus \frac{0.6442}{\sqrt{E}} \oplus \frac{2.0125}{E}$$

$$\text{Fast Simulation} \quad \frac{\Delta E}{E} = \sigma_A = \quad 0.0404 \oplus \frac{0.5592}{\sqrt{E}} \oplus \frac{0.00212}{E} \tag{4.19}$$

Once the Z→jj event has been reconstructed in ATLFAST an extra Gaussian smearing term is applied to the reconstructed 4-momentum, equivalent in magnitude to $\sqrt{\sigma_D^2 - \sigma_A^2}$, to bring the resolutions (of the jet-jet energy measurement) of the two programs into agreement. This extra term is the same regardless of luminosity or electronic noise settings.

4.2.4 Z→jet+jet mass resolution

Using the local-maximum method, outlined in section 3.2.4, to choose jet-jet pairs and incorporating the energy-momentum calibration from the previous sections, we can use ATLFAST to evaluate the width of the reconstructed hadronic Z^0 decay at different Higgs boson masses. Figure 4.14 shows the Gaussian width, in the presence of electronic noise, for events where the two jet baricentres are properly matched to the tree-level quark direction[6].

---

[6]This avoids the broadening effects that would be introduced by jet mis-identification.

92
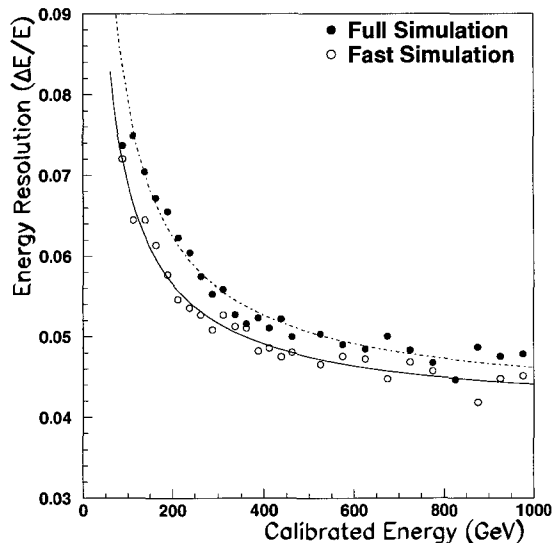
Figure 4.13: The resolution of the calibrated reconstructed jet-jet energy, averaged over all pseudorapidity ranges, as a function of Z^0calibrated energy.

Pileup and electronic noise, on average, add equal amounts of positive and negative energy to jet-jet region thereby maintaining the mean value of the energy and invariant mass, but reducing the resolution.

The Gaussian width of the hadronic decay as a function of Higgs boson mass ($M_H \geq 190$ GeV/c^2) can be estimated using the following parameterizations:

$$
\begin{aligned}
\text{No Pileup} \quad & \Gamma(Z^0) = & 10.1 - 0.580 \times 10^2 M_H + 0.476 \times 10^5 M_H^2 \\
\text{Low Luminosity} \quad & \Gamma(Z^0) = & 11.4 - 0.654 \times 10^2 M_H + 0.510 \times 10^5 M_H^2 \qquad (4.20) \\
\text{High Luminosity} \quad & \Gamma(Z^0) = & 17.6 - 0.105 \times 10^1 M_H + 0.738 \times 10^5 M_H^2
\end{aligned}
$$

A 180 GeV/c^2 Higgs boson lies slightly below the $2M_Z$ threshold causing the Higgs to decay through the channel H→ZZ*, with one Z-boson being produced off mass shell. This results in a low mass tail which increases the width of the Gaussian fit. This increase in width can be seen in the leptonic Z→l$^+$l$^-$ decay widths in figure 4.5 and in the hadronic Z→jj decay widths in figure 4.14.

4.2.5 Hadronic Identification Optimization

The efficiency with which one reconstructs a hadronic jet-jet pair (ie Z→jj) is dependent on the luminosity and the parameters used by the local maximum jet finding algorithm (section 3.2.4). Three different jet-parameterizations were investigated in full simulation: 2 GeV/c jet initiator with a 2 GeV/c jet threshold, a 3 GeV/c jet initiator with a 5 GeV/c jet threshold and finally a 4 GeV/c jet initiator with a 5 GeV/c jet threshold.

93
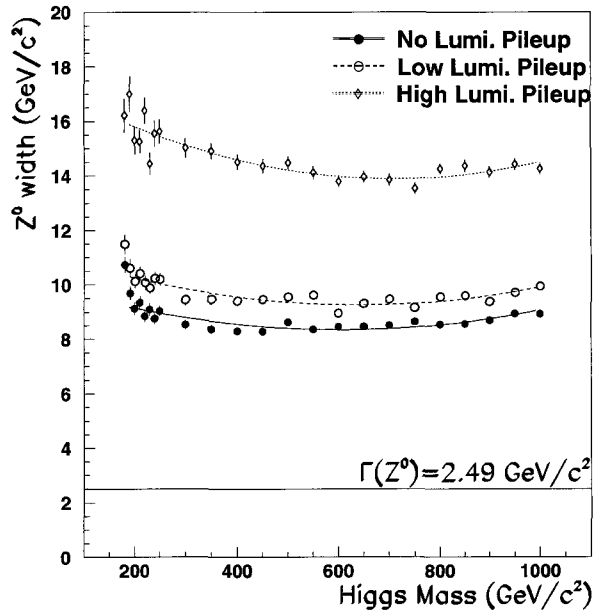
Figure 4.14: The measured ATLFAST width of the reconstructed hadronic Z^0-decays as a function of Higgs mass and luminosity setting. Electronic noise has been included in the calorimeter cells.
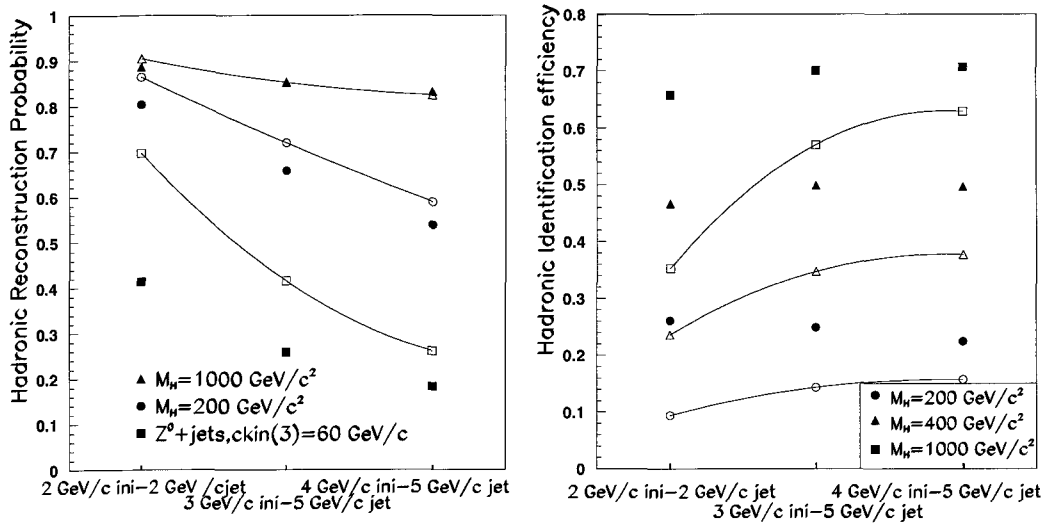
Figure 4.15: (a)The probability of reconstructing a hadronic event in full simulation in both the signal and the Z+jets background.(b) Proper identification of the jets to the original quarks (in the Higgs signal) is dependent on the jet parameters chosen. In both plots the empty markers correspond to the rates at high luminosity, the filled markers are the rates at low luminosity.

94

Figure 4.15(a) shows that as the luminosity is increased, from low luminosity (filled markers) to high luminosity (empty markers plus line), the probability of reconstructing a jet-jet pair, within a mass window of $|M_Z - 91.2| < 25$ GeV/c^2, increases in both the signal and the Z^0+jets background. In the signal we expect two jets corresponding to the two quarks from the $Z \rightarrow q\bar{q}$ decay. Since these jets are energetic with an invariant mass close to M_Z we do not expect a significant increase in the rate when more jets are added due to the increase in luminosity. However, the jets in the Z^0+jets background do not arise from a true Z^0 so the probability of obtaining a jet-jet pair with a mass close to M_Z in this background is small. The addition of extra jets through pileup significantly increases the probability that at least one jet-pair in the event will be close to M_Z.

On average the Z^0+jets background produces jets with low transverse momentum, similarly the jets introduced by pileup also have low transverse momentum. The probability that the Z^0+jets background will contain a jet-pair with a mass near M_Z is greatly reduced by an increase to the jet initiator value used by the jet-finding algorithm. This fake rate decreases by a factor of 2 to 2.5 for low and high luminosity respectively as the jet initiator threshold is increased from 2 to 4 GeV/c. As the Higgs mass increases the average transverse momentum of the jets from the hadronic Z decay increases as well, consequently these jets will possess seed cells with large transverse momentums. When the jet initiator threshold is increased from 2 to 4 GeV/c the reconstruction rate decreases by 30% for a 200 GeV/c^2 Higgs boson, but only by about 5% for a 1 TeV/c^2 Higgs boson.

Figure 4.15(b) shows that the probability of correctly picking the quark jets from the $Z^0 \rightarrow q\bar{q}$ decay in the Higgs signal decreases due to the extra jets introduced by pileup. These pileup jets have low transverse momentum and can be removed from consideration as possible jet initiators by increasing the jet initiator threshold. As the cell threshold is increased the hadron reconstruction efficiency plateaus at low luminosity with a 3 GeV/c initiator and a 5 GeV/c jet threshold. The improvement to this efficiency is most visible at high luminosity and at heavy Higgs masses. The best jet parameters at high luminosity are a 4 GeV/c jet initiator and a 5 GeV/c jet threshold[7].

In section 3.3.4 we discussed that the efficiency with which we reconstruct jets is different in the full and fast simulations. We introduced a jet efficiency term in ATLFAST to better match the jet reconstruction rates in full simulation. These rates were determined using a 3 GeV/c jet initiator and a 5 GeV/c jet threshold in full simulation and a 5 GeV/c jet initiator and a 5 GeV/c jet threshold in ATLFAST. In the previous paragraph we found that

---

[7]Introducing a shorthand; we refer to the condition of a 4 GeV/c jet initiator threshold and a 5 GeV/c jet threshold as 4 GeV/c x 5 GeV/c .

95

increasing the jet initiator threshold to 4 GeV/c in full simulation optimized our Z→ $q\bar{q}$ reconstruction efficiency at high luminosity. Since the jet efficiencies have already been included in ATLFAST any increase in the jet finding parameters in full simulation can be mapped to a new set of jet parameters in ATLFAST. At high luminosity the jet finding algorithm in ATLFAST uses a 7 GeV/c jet initiator and a 7 GeV/c jet threshold.

The local maximum method, described previously, looks for local maximum by identifying seed cells that are separated by at least one cell in $\eta \times \phi$ space (or ΔR >0.18). The local maximum method also assumes that the jet profile is smooth, in that the cell energy falls uniformly away from the jet baricentre. However, a single jet may produce what appears to be a second local maximum near to the true jet baricentre[8]. This secondary seed cell typically possesses much lower energy than the true initiator cell. Since the two seed cells produced from the jets arising from a heavy Higgs decay have comparable transverse energies and fake seed cells typically have lower E_T, we introduce a seed cell threshold.

If two seed cells are close together, $0.18 < \Delta R < 0.4$, and the transverse momentum of the lowest energy cell is below some threshold it will be rejected. We can evaluate the efficiency of this secondary threshold by comparing the jet-pair reconstruction efficiency, that is how frequently our reconstructed jets are correctly associated with the quarks in the decay Z→q$\bar{q}$ and within a mass window $|M_Z - 91.2|$ <20 GeV/c^2. Figure 4.16(a) shows that, for full simulation, introducing a cut of 10 GeV/c on cells that are close together has no effect on the efficiency for a low mass Higgs M_H <400 GeV/c^2. However the efficiency for a Higgs with a mass of 600 (1000) GeV/c^2 displays an improvement of approximately 0.5% and 1.2% respectively.

Since there is no energy sharing between neighbouring cells in ATLFAST, the jets in ATLFAST will tend to produce more fake secondary local maxima. In ATLFAST the jet algorithms, in the absence of luminosity pileup, use a 5 GeV/c jet initiator and a 5 GeV/c jet threshold. Figure 4.16(b) shows setting produces a significant discrepancy in the jet-pair reconstruction efficiency between fast and full simulations. Introducing a threshold cut in ATLFAST of 20 GeV/c on cells with a separation of $0.18 < \Delta R < 0.4$ brings agreement between the jet-pair identification efficiencies determined by full and fast simulations to within 2%.

---

[8]This phenomena is more a problem in ATLFAST since there is no energy sharing between cells.

96
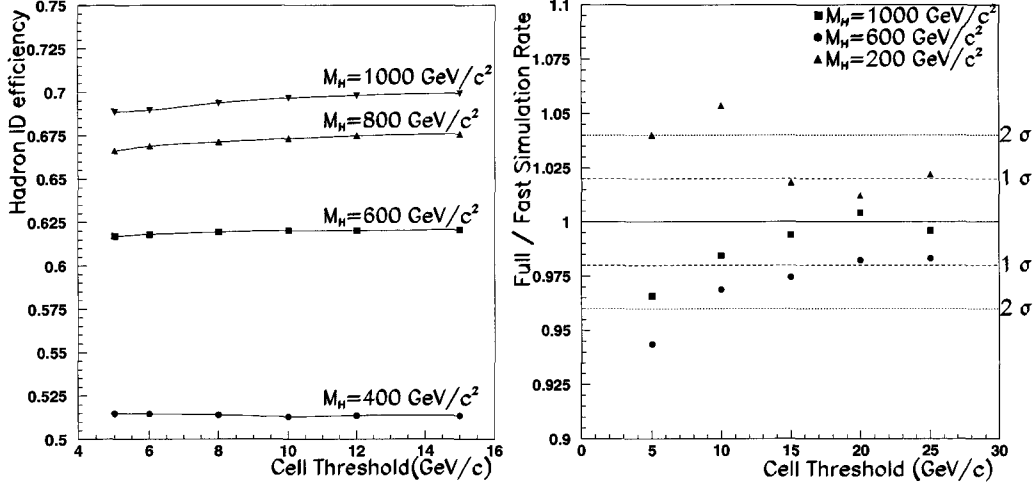
Figure 4.16: The Hadron ID efficiency can be improved in full simulation by applying a 10 GeV/c cell threshold on seed cells which have a separation of 0.18< ΔR < 0.4, (b) The comparable cut in fast simulation is 20 GeV/c.

4.3 Higgs Reconstruction

Once both the hadronic and leptonic Z-decays have been identified the 4-momentum of the Higgs boson can be calculated simply as :

$$P^\mu_{Higgs} = P^\mu_{Z_{hadron}} + P^\mu_{Z_{lepton}} \tag{4.21}$$

For a Higgs that has been properly reconstructed, that is to say the muons and jets have been associated with their corresponding tree level particles to within $\Delta R \leq 0.2$, the width can be approximated by a Gaussian. The Gaussian width, as a function of mass and luminosity (in the presence of electronic noise), is shown in figure 4.17(a). The approximate Gaussian width of the Higgs boson as a function of the Higgs boson mass and the luminosity is parameterized in equation 4.22.

$$
\begin{aligned}
\text{No Pileup} \quad & \Gamma(H^0) = 26.9 - 0.174 M_H + 0.487 \times 10^{-3} M_H^2 - 0.120 \times 10^{-6} M_H^3 \\
\text{Low Lumi.} \quad & \Gamma(H^0) = 30.0 - 0.189 M_H + 0.514 \times 10^{-3} M_H^2 - 0.137 \times 10^{-6} M_H^3 \\
\text{High Lumi.} \quad & \Gamma(H^0) = 33.1 - 0.161 M_H + 0.445 \times 10^{-3} M_H^2 - 0.103 \times 10^{-6} M_H^3
\end{aligned} \tag{4.22}
$$

For Higgs boson masses below 400 GeV/c^2, the width of the reconstructed Higgs is dominated by the resolution of the calorimetry, with the dominant contribution coming from the hadronic reconstruction. The measured width of the Higgs boson is therefore the same for the muon and electron channels. The natural width of the Higgs dominates over calorimeter resolution for Higgs masses above 500 GeV/c^2. A comparison of the tree level Higgs line-shape to the reconstructed line shape for M$_H$=200 GeV/c^2 and 800 GeV/c^2 is shown in figure 4.18. The high mass tail for the "reconstructed" 200 GeV/c^2 Higgs is caused by

97
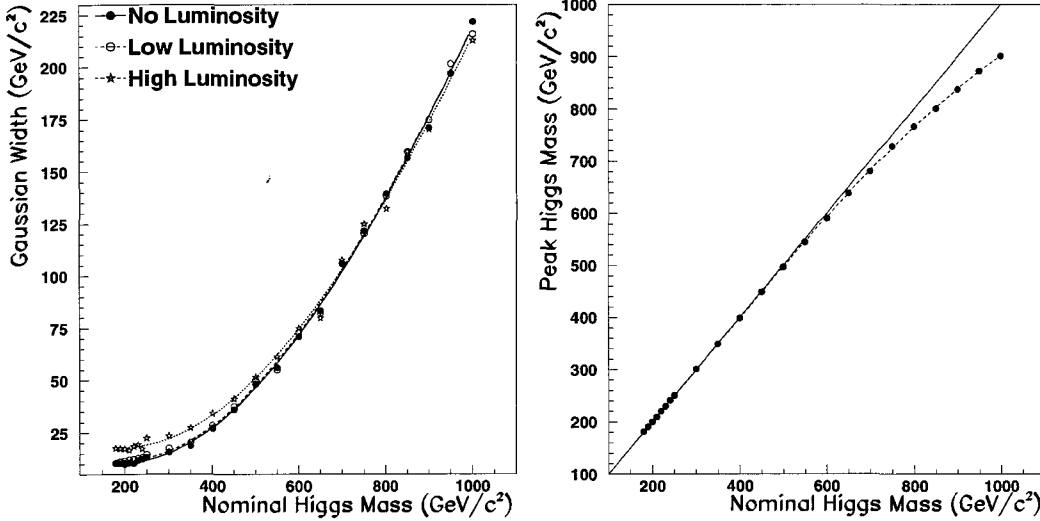
Figure 4.17: (a) The Gaussian width of the Higgs as a function of the Higgs boson mass. (b) Due to the decreased production cross section of a heavy Higgs boson the mass peak falls below the nominal value (given by the solid line).

mistakingly identifying a tagging jet as one component of the hadronic Z-decay.

Figure 4.18(b) shows that the natural line shape for an 800 GeV/c^2 Higgs boson is not centered on 800 GeV/c^2, rather the peak occurs at roughly 750 GeV/c^2. This occurs because the Breit-Wigner curve describing the Higgs Boson resonance is convoluted with the reduced Higgs production cross-section (figure 1.2) of heavier Higgs bosons. This asymmetric weighting causes the mean of the Higgs boson mass curve to shift off the nominal value as shown in figure 4.17(b). The location of the shifted peak can be fit using equation 4.23.

$$M_H|_{peak} = 12.9 + 0.885M_H + 0.333 \times 10^{-3}M_H^2 - 0.329 \times 10^{-6}M_H^3 \qquad (4.23)$$

4.4 Forward Jet Tagging and the Central Jet Veto

The qq→qqH, H→ZZ→l^+l^-jj signal is characterized by two high energy "tagging" jets located in the forward and backward regions of the calorimeter and two high P_T central jets. Figure 4.19 shows that an increase in the Higgs boson mass produces central quarks that are more central and tagging quarks that are more forward.

The standard analysis defines the central region of the detector as $|\eta| \leq 2.0$ with the forward region $|\eta| \geq 2.0$. At low Higgs boson masses a considerable fraction of the tagging jets fall outside the forward region and into the central region. Others [12][68] studying the channel: H→ $W^*W^* \to e^\pm\mu^\pm$+ET$_{miss}$, have suggested a more flexible approach to the
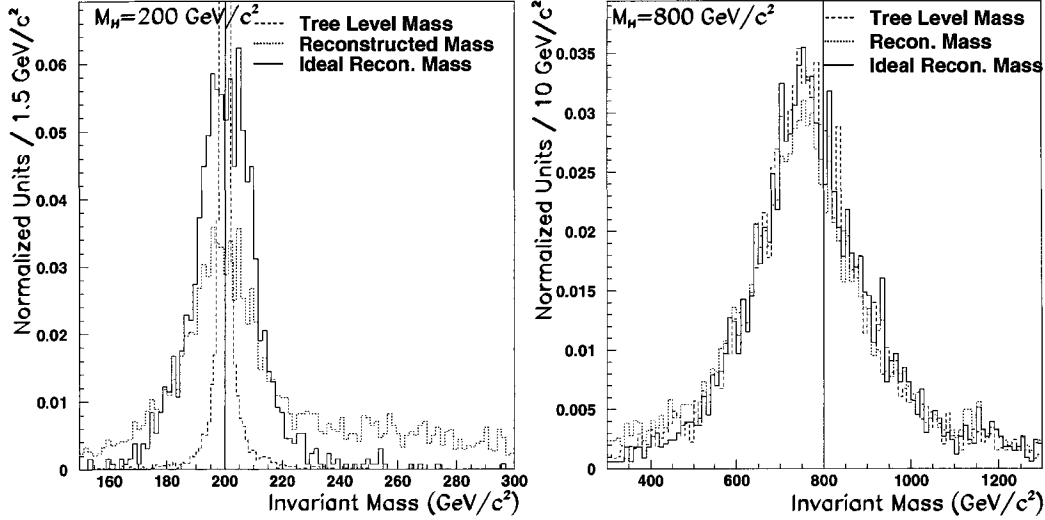
Figure 4.18: (a) At low Higgs masses, $M_H=200$ GeV/c^2, the reconstructed width (dotted line) is dominated by the resolution of the detector; (b) For a heavier Higgs boson, $M_H=800$ GeV/c^2, the natural line shape (dashed line) dominates. The ideal reconstructed masses (solid line) are those events which have been properly reconstructed.

identification of the forward jets (j1,j2) requiring:

$$\eta_{j,min} + 0.6 < \eta_{l(1,2)} < \eta_{j,max} - 0.6$$
$$\eta_{j,1} \cdot \eta_{j,2} < 0.0$$
(4.24)

where $\eta_{l(1,2)}$ are the pseudo-rapidities of the central leptons and $\eta_{j,max}$ ($\eta_{j,min}$) is the pseudo-rapidity of the tagging jet in the forward (backward) direction.

This thesis adopts a similar approach as shown in figure 4.20. The central region is defined as:

$$MIN(\eta_{j1,j2}, \eta_{l1,l2}) - 0.6 \leq \eta_{central} \leq MAX(\eta_{j1,j2}, \eta_{l1,l2}) + 0.6$$
(4.25)

where $MIN(\eta_{j1,j2}, \eta_{l1,l2})$ is the minimum pseudo-rapidity of the 2 central jets and 2 central leptons. The forward region is defined as the region $|\Delta\eta| \geq 0.6$ beyond the highest pseudorapidity of the central particle[9]. Forward and central jet candidates are identified using the local maximum method discussed in section 3.2.4 (excluding those cells included in the Z→jet+jet pair and the cells in a cone of $\Delta R=0.2$ around the isolated leptons). It is also required that these jets have a calibrated transverse momentum above 15 GeV/c. The central jet is taken to be the highest energy jet in the central region. The forward (backward) jet is taken to be the highest energy jet in the forward (backward) region.

---

[9]Conversely the backward region is defined as $|\Delta\eta| \geq 0.6$ below the lowest pseudorapidity.

99
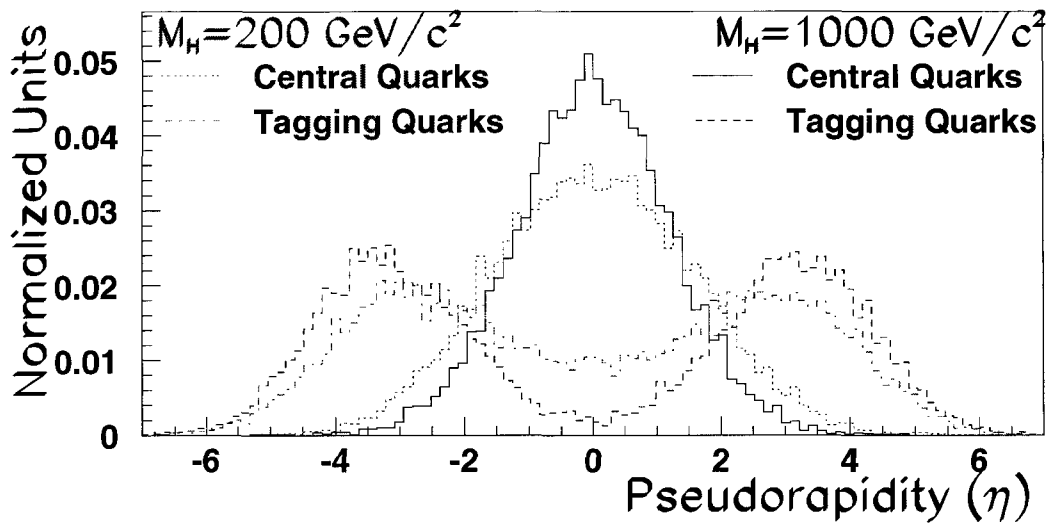
Figure 4.19: Normalized distribution of central and tagging quarks for M_H=200 GeV/c^2, 1000 GeV/c^2.
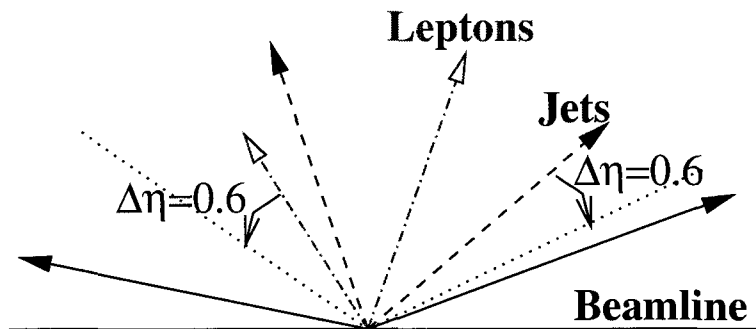
Figure 4.20: Defining the forward and central regions with a less rigid approach. The dashed-dotted lines are the central leptons, the dashed lines are the central jets. The tagging jets are the solid lines. The dotted lines marks the "boundary" between the forward and central regions.

100

4.4.1 Forward Jet Tagging

The identification of the tagging jets is a well established method of reducing the backgrounds (Z^0+jets and ff→ZZ) to Higgs production via vector boson fusion[42]. The tagging jets are expected to be energetic and separated from each-other by a large pseudorapidity gap, in which we find the central activity.

There are four possible cuts that may be applied to these tagging jets. The most common cut is the "double jet tag", requiring that there be two jets each with energy greater than some common threshold value (this will be referred to as the symmetric cut). The "single jet tag" requires that there be a single jet in either the forward or the backward region with energy above a given threshold. In the signal, one tagging jet is typically lower in energy (the trailing jet, E_{trail}) than the other (the leading jet, E_{lead}), therefore an asymmetric cut on the jet energies is more appropriate. The final variable is the invariant mass of the two tagging jets.

$$M_{tag} = (P_{\mu,j1} + P_{\mu,j2})(P_{j1}^{\mu} + P_{j2}^{\mu}) \tag{4.26}$$

In the Higgs signal the two tagging jets are separated by a large pseudo-rapidity gap giving a large invariant mass for the tagging jet pair.

4.4.2 Central Jet Veto

Aside from the jet activity induced by the hadronic decay of the Z^0, from the signal, there is expected to be minimal jet activity in the central region. The jet-jet pair in the Z^0+jets background does not originate from a colour singlet and is therefore more prone to excess gluon bremsstrahlung producing more hadronic activity around the jet-jet pair. A central jet veto (CJV) can be applied to restrict the E_T of any extra jet found in the central region. The central jet veto (CJV) rates are calculated as the probability of an event not having a central jet with an E_T above a given threshold.

Tagging jets can be mistaken for central jets if they fall into the central region as defined in equation 4.25. If this fact is not considered the central jet veto appears ineffective for Higgs boson masses below 400 GeV/c^2. However, if the central jet veto is applied after the two tagging jets have been identified the CJV cut is of benefit even for low mass Higgs bosons.

4.4.3 Fake Central Jet Veto and Fake Forward Tag rates

At low/high luminosity extra jets can be found in the calorimetry through the jets produced by the minimum bias events. In the following section we evaluate the fake central jet veto
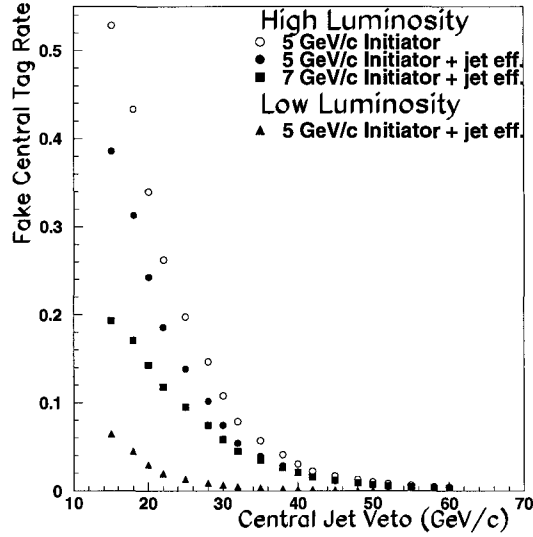
Figure 4.21: The probability of finding a central jet above a given jet veto threshold under the low and high luminosity scenarios.

and forward jet tag rate using only pileup events. Jets were identified using the basic cone-algorithm with a 5 GeV/c jet initiator and a 5 GeV/c jet cut. Further, we required that the jets have a transverse momentum of 15 GeV/c after jet calibration. Since there is no central "event" for this study we define the central region as $|\eta|$ <2.0, the forward region is defined as η >+2.5 and the backward region η <-2.5.

Fake Central Jet Veto

The jet with the highest energy in the central region, $|\eta| < 2.0$, is taken to be the central jet. The fake central jet veto rate as a function of jet transverse momentum for both low and high luminosity is given in figure 4.21. The solid line in figure 4.21 are the rates determined when no jet efficiency is applied and a 5 GeV/c jet initiator is required. The filled and unfilled markers indicate the veto rates when jet efficiencies have been included. The filled markers indicate the veto rate using a 5 GeV/c jet initiator and the unfilled markers correspond to a 7 GeV/c initiator.

Fake Forward Jet Tagging

The single and double fake tag rates are summarized in figure 4.22. The solid lines without markers in figure 4.22(a),(b) are the fake tag efficiencies when no jet reconstruction efficiency is applied. The filled markers indicate the tag rate using a 5 GeV/c jet initiator and the unfilled markers correspond to a 7 GeV/c initiator. Requiring a double tag at high luminosity with a jet initiator of 7 GeV/c reduces the fake rate to be below 1% for all jet energies. Similarly requiring a double tag at low luminosity the rate falls below 0.1%.

102
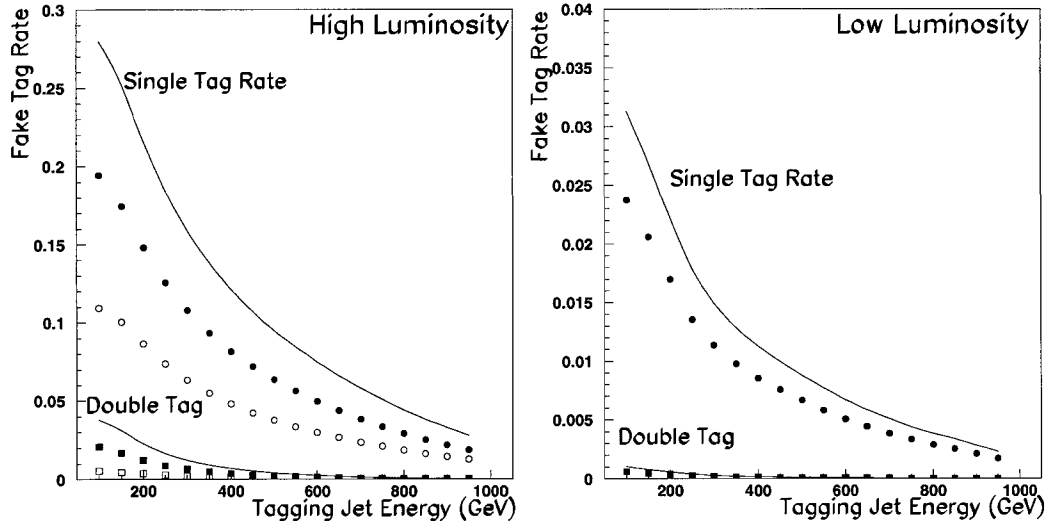
Figure 4.22: The probability of a double or single jet tag at (a) High Luminosity and (b) Low luminosity. The solid line are the efficiencies when no jet efficiency is applied. The filled markers indicate the tag rate determined using a 5 GeV/c jet initiator and the unfilled markers correspond to a 7 GeV/c initiator. The circles correspond to the single tag rates and the squares to the double tag rates.

4.5 Optimization of Cuts

Each cut in this analysis has been optimized for every Higgs boson mass being studied. Since we do not have access to the tree level data in the final analysis, optimization is performed using information from the reconstructed event ntuple. The optimization procedure that led to the final analytical cuts is performed in five steps, each step will be discussed below. Optimization is a sequential process, once one variable has been optimized that particular cut is included when optimizing the variables of the next step. During the optimization of the first three steps there is a loose cut on the invariant mass of the Z→ll(jj) decay of 10(20) GeV/c^2 respectively. This loose cut is replaced with a 2σ mass window cut on the reconstructed Z→ll(jj) decays for the remaining steps. With the exception of the cut on the width of the Z→ l^+l^- decay the kinematic cuts for the two decay channels $Z \rightarrow \mu^+\mu^- (e^+e^-)$ are identical.

Unless otherwise stated the optimization procedure has been performed by comparing the Higgs signal to the Z^0+jets channel in the absence of pileup. The optimal cuts are those values which maximize the significance[10] value.

---

[10]The significance is calculated as the number of signal events passing the given cut divided by the square root of the number of background events passing the same cut.

103
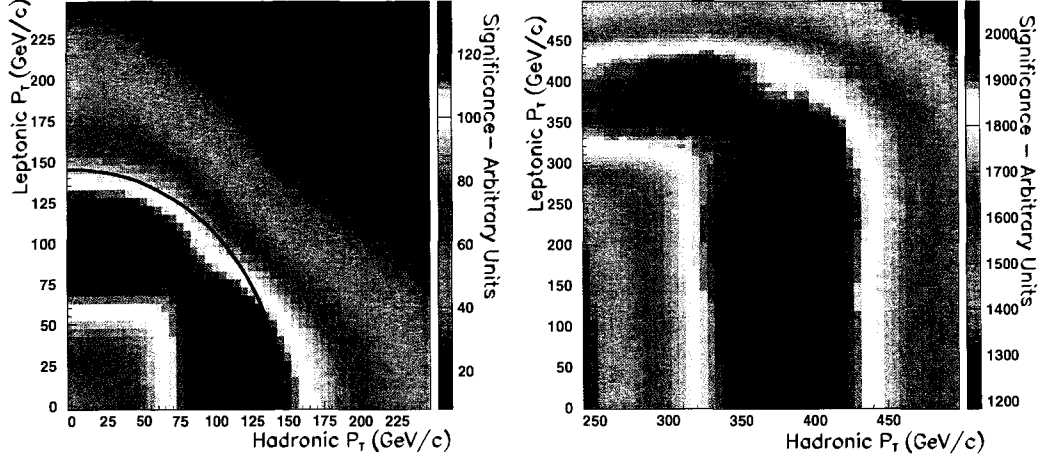
Figure 4.23: Significance as a function of $P_T^{Z \to ll}$ and $P_T^{Z \to jj}$ for a Higgs mass of (a) 300 GeV/c^2 and (b) 1000 GeV/c^2.

4.5.1 Step 1

For a heavy Higgs boson it is standard[15] to apply a kinematic cut on the transverse momentum of both the leptonically ($P_T^{Z \to ll}$) and hadronically ($P_T^{Z \to jj}$) decaying vector bosons. Figure 4.23(a) shows that for a low mass Higgs, M_H=300 GeV/c^2, there is no one optimal value in $P_T^{Z \to ll} \times P_T^{Z \to jj}$ space at which to place individual cuts on the Z-bosons in the event. In the case of low Higgs masses a more effective variable, represented by the arc in figure 4.23(a), would be :

$$P_T^{pair} = \sqrt{(P_T^{Z \to jj})^2 + (P_T^{Z \to ll})^2} \qquad (4.27)$$

This P_T^{pair} cut is not as restrictive on the acceptable phase space as cuts on the individual P_T^Z values.

Figure 4.23(b) shows that the individual cuts are better defined for a heavier Higgs, M_H=1000 GeV/c^2 : $P_T^{Z \to ll} > 240$ GeV/c and $P_T^{Z \to jj} > 390$ GeV/c. The ratio of the significances obtained by the two different step 1 cuts, the values of which are listed in table 4.5, is plotted as a function of Higgs mass in figure 4.24. The individual P_T cuts become more effective than the P_T^{pair} cut for $M_H \geq 700$ GeV/c^2. This transition is included in all subsequent cuts. Figure 4.25 compares the P_T distribution of the signal and background events for a variety of Higgs boson masses in the absence of pileup.

104
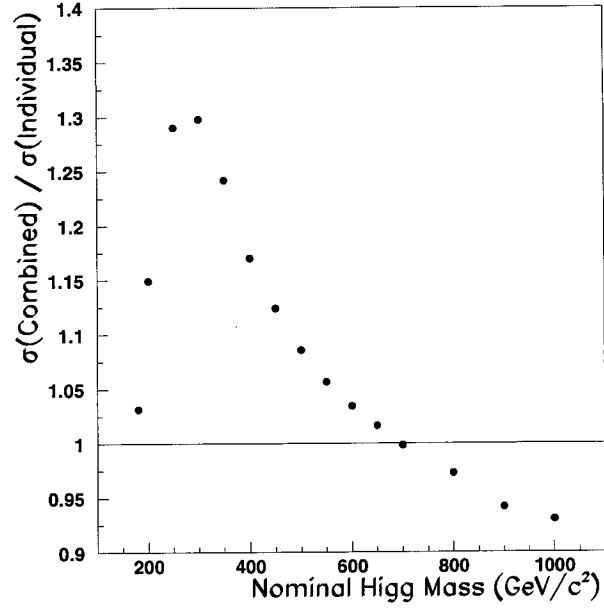
Figure 4.24: An analysis cut on the combination of the Z-transverse momentums(P_T^{pair}) is a more effective cut than individual cuts ($P_T^{Z \to jj}$, $P_T^{Z \to ll}$) on the Z-bosons for Higgs boson masses below 650 GeV/c^2 .

Higgs Mass (GeV/c^2)	P_T^{pair}	$P_T^{Z \to jj}$	$P_T^{Z \to ll}$	Higgs Mass (GeV/c^2)	P_T^{pair}	$P_T^{Z \to jj}$	$P_T^{Z \to ll}$
		(GeV/c)				(GeV/c)	
180	45	10	15	500	270	195	25
190	45	10	15	550	305	220	25
200	55	5	25	600	335	240	50
210	70	5	35	650	355	255	100
220	80	60	0	700	390	280	135
230	90	5	55	750	410	300	145
240	100	5	65	800	445	320	145
250	110	5	75	850	460	335	185
300	150	110	5	900	480	360	205
350	180	135	5	950	530	360	240
400	215	155	10	1000	530	390	240
450	245	175	10				

Table 4.5: The optimal values, as determined by maximizing the significance, for the step 1 transverse momentum cuts on the reconstructed Z^0 bosons.

105
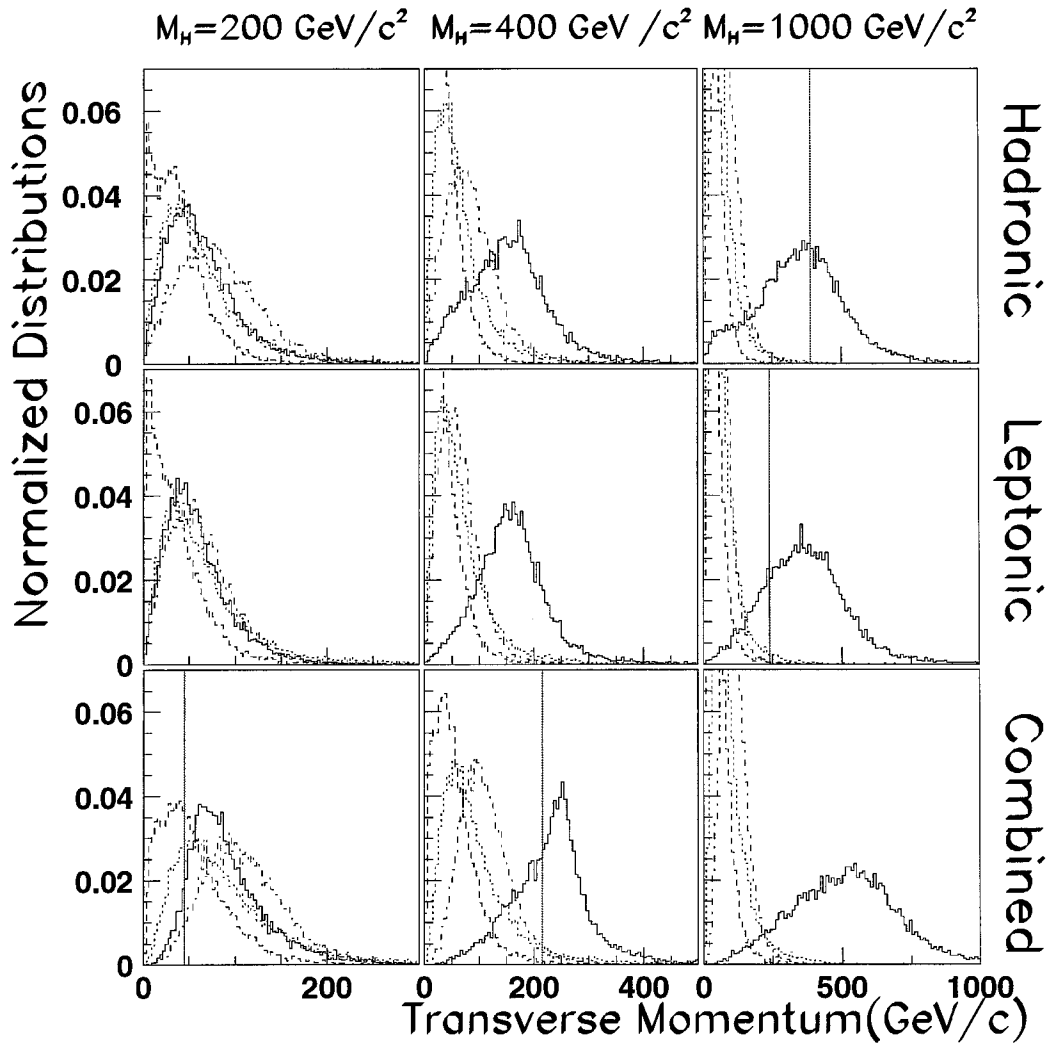
Figure 4.25: The distribution of $P_T^{Z \to jj}$, $P_T^{Z \to ll}$ and P_T^{pair} for 3 different Higgs masses in the absence of pileup. The solid line is the shape of the signal, dashed line of Z^0+jets, dotted line ff$\to$ZZ and the dashed-dotted line t$\bar{t}$. The vertical lines correspond to the cuts applied in the final analysis.

106

Higgs Mass (GeV/c^2)	ΔR_{ll}	ΔR_{jj}	Higgs Mass (GeV/c^2)	ΔR_{ll}	ΔR_{jj}
180-250	-	-	650	1.30	0.75
300	-	2.2	700	1.30	0.75
350	-	1.75	750	1.00	0.75
400	4.05	1.35	800	0.95	0.70
450	2.35	1.25	850	0.85	0.70
500	1.65	1.10	900	0.75	0.65
550	1.40	1.00	950	0.75	0.55
600	1.40	0.95	1000	0.75	0.55

Table 4.6: The optimal values for the level 2 ΔR central object separation cut.

4.5.2 Step 2

Increasing the Higgs boson mass increases the transverse momentum of the Z^0 bosons. This increase in transverse momentum reduces the angle between the Z^0 decay products. Taking the two baricentres found by the local maximum method two jets can be reconstructed around these baricentres using the algebra introduced in section 3.2.1 and the cell weighting formula in equation 3.4. The hadronic and leptonic separation of signal and background event types are compared in figure 4.26. A hadronic and leptonic separation cut is introduced:

$$\begin{aligned} \Delta R_{ll} &= \sqrt{\Delta\phi_{ll}^2 + \Delta\eta_{ll}^2} \\ \Delta R_{jj} &= \sqrt{\Delta\phi_{jj}^2 + \Delta\eta_{jj}^2} \end{aligned} \tag{4.28}$$

The optimization is performed using data that has already passed the cuts from the first step. The optimal cut values for step 2 are given in table 4.6.

For low Higgs masses, $M_H \leq 250$ GeV/c^2, the shape of the Z^0+jets background is very similar to that of the Higgs signal. In these cases there is no significant improvement to the significance value through the addition of a cut on the central object separations.

4.5.3 Step 3

Using only the events that have passed the step 1 and step 2 cuts, we introduce cuts on the individual transverse momentum of the central leptons and central jets. The two jets that comprise the hadronic Z decay in the event are arranged in falling E_T giving a leading ($P_{T,j-big}$) and trailing jet ($P_{T,j-small}$). Likewise the leptons are similarly organized as $P_{T,l-big}$ and $P_{T,l-small}$. The normalized distribution of the trailing E_T jets and leptons for signal and background events are shown in figure 4.27. The optimal cuts are summarized in table 4.7. For all but the lowest Higgs boson masses the significance of the cut is optimized by placing a single cut on the transverse momentum of the trailing jet/lepton.

107
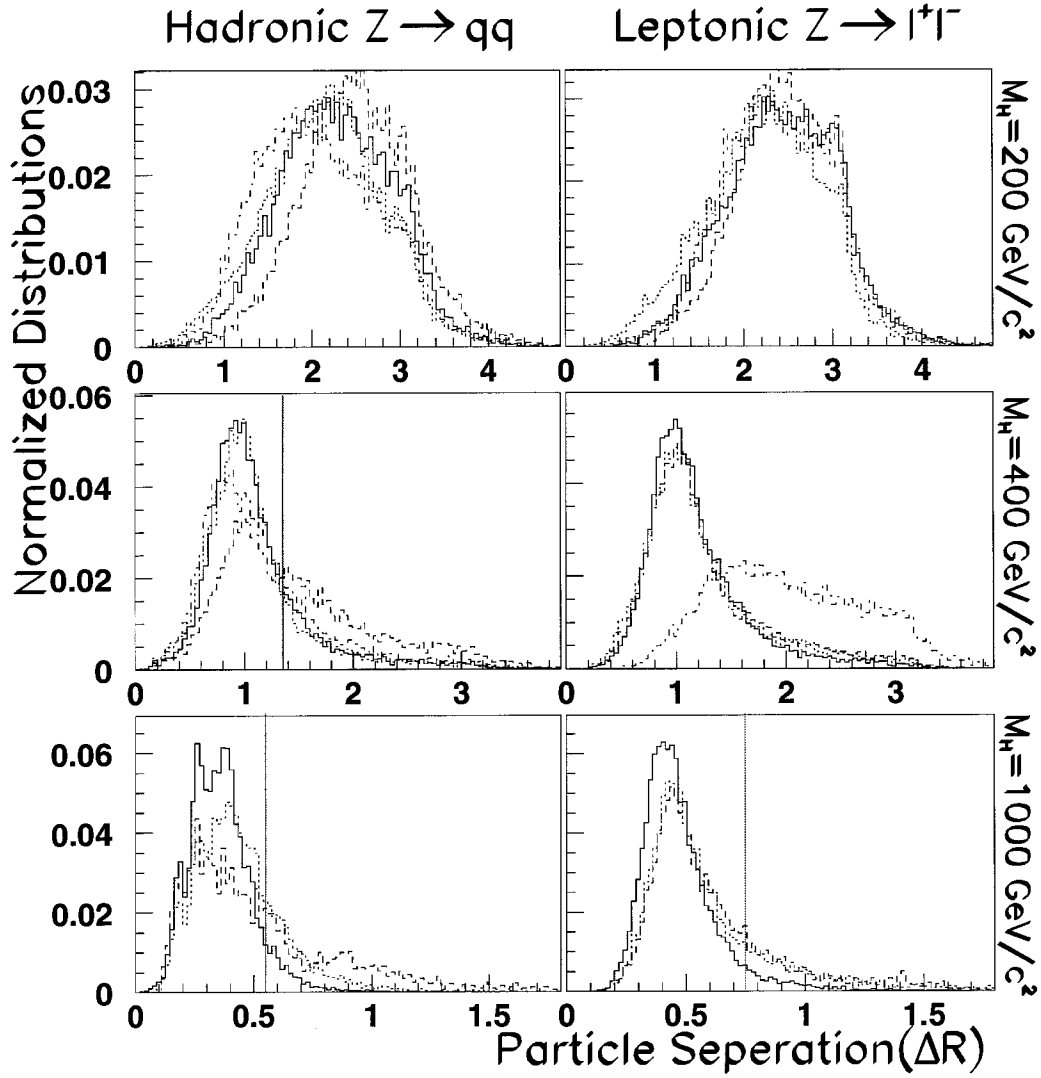
Figure 4.26: The distribution of ΔR_{jj} and ΔR_{ll} for 3 different Higgs masses in the absence of pileup. The solid line is the shape of the signal, dashed line of Z^0+jets, dotted line ff$\rightarrow$ZZ and the dashed-dotted line $t\bar{t}$. The $t\bar{t}$ spectrum is not included in the bottom graphs as it has been sufficiently removed by the first 2 levels of cuts. The vertical lines correspond to the cuts applied in the final analysis.

108
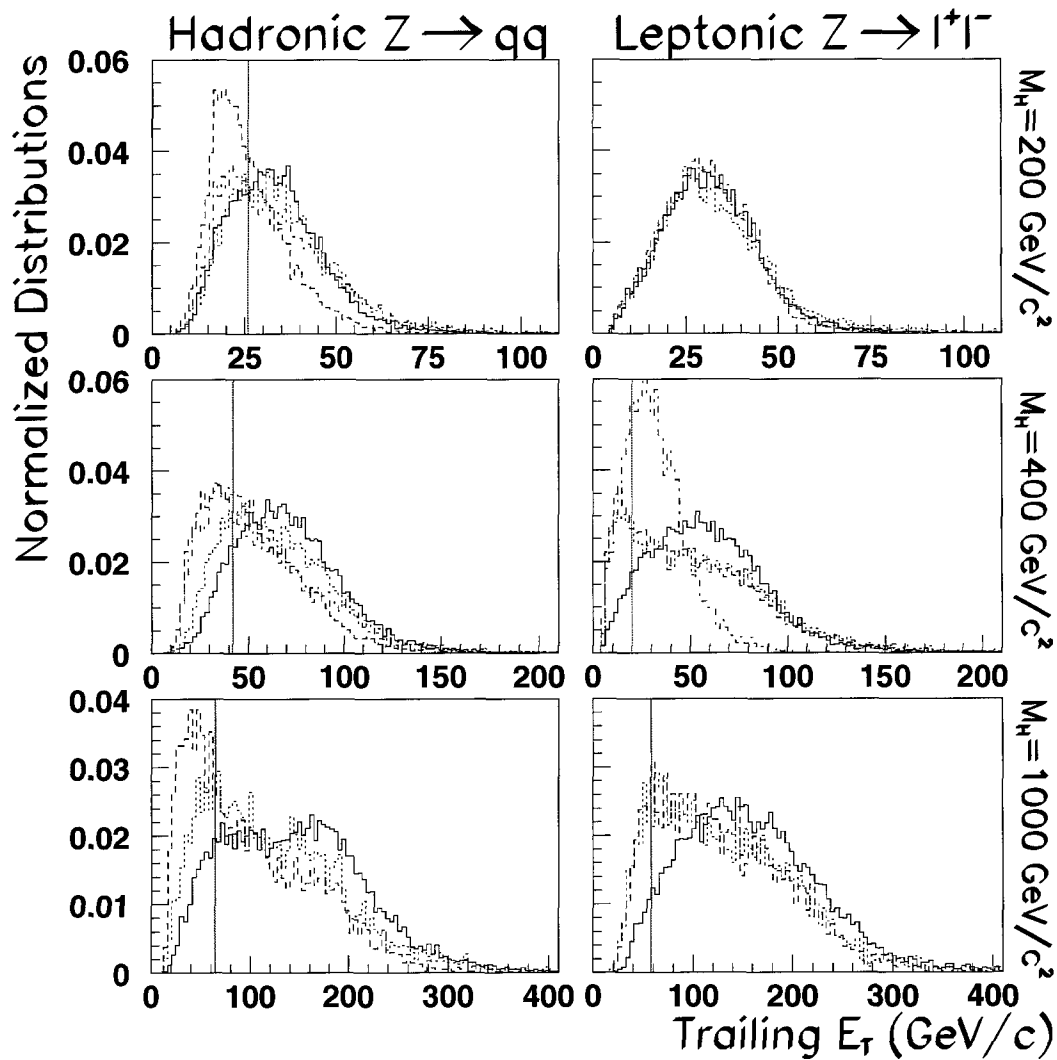
Figure 4.27: The distribution of trailing P_T(lepton and jet) for 3 different Higgs masses in the absence of pileup. The solid line is the shape of the signal, dashed line of Z^0+jets, dotted line ff→ZZ and the dashed-dotted line $t\bar{t}$. The vertical lines correspond to the cuts applied in the final analysis.

109

Higgs Mass (GeV/c²)	Hadronic (GeV/c) Lead	Trail	Leptonic (GeV/c) Lead	Trail	Higgs Mass (GeV/c²)	Hadronic (GeV/c) Lead	Trail	Leptonic (GeV/c) Lead	Trail
180	38.0	20.0	-	-	500	-	50.0	-	32.0
190	40.0	24.0	-	-	550	-	58.0	-	36.0
200	40.0	26.0	-	-	600	-	64.0	-	38.0
210	-	28.0	-	-	650	-	64.0	-	44.0
220	-	28.0	-	-	700	-	64.0	-	44.0
230	-	28.0	-	-	750	-	64.0	-	44.0
240	-	28.0	-	-	800	-	64.0	-	44.0
250	-	28.0	-	-	850	-	64.0	-	50.0
300	-	32.0	-	18.0	900	-	64.0	-	54.0
350	-	40.0	-	20.0	950	-	64.0	-	54.0
400	-	42.0	-	20.0	1000	-	64.0	-	58.0
450	-	46.0	-	24.0					

Table 4.7: The optimal values for the step 3 central object transverse momentum cuts.

Higgs Mass(GeV/c²)	No tagging jets No Pile	Low Lumi	High Lumi	With tagging jets No Pile	Low Lumi	High Lumi
180	0.659	0.628	1.005	0.471	0.471	0.471
190	0.973	1.068	1.35	0.785	0.879	0.942
200	1.57	1.539	1.821	1.35	1.413	1.444
210	1.758	1.915	2.104	1.601	1.664	1.79
220	2.041	2.041	2.324	1.79	1.978	2.198
230	2.292	2.198	2.386	2.198	2.01	2.324
240	2.449	2.418	2.512	2.386	2.198	2.355
250	2.481	2.543	2.606	2.481	2.292	2.543
300	2.826	2.857	2.889	2.952	2.92	2.92
350	2.952	2.920	2.952	2.952	3.014	3.046
400	2.952	2.983	3.014	3.014	3.014	3.046

Table 4.8: The maximum azimuthal angle(in radians) as a function of Higgs mass.

4.5.4 Step 4

Azimuthal Angle

The effectiveness of the first 3 sets of cuts increases greatly with increasing Higgs boson mass. However, at low Higgs masses there still remains a considerable fraction of the main Z^0+jets background.

Figure 4.28(a) shows that the transverse momentum spectrum of the Higgs boson maintains the same shape over the full Higgs boson mass range. This spectrum peaks at around 75 GeV/c. In the case of a heavy Higgs boson this P_T is small when compared to the overall Higgs energy and the two vector bosons are emitted back-to-back. As the Higgs boson mass is decreased the azimuthal angle between the emitted bosons decreases due to the larger fractional P_T.

The azimuthal angle distributions shown in figure 4.29 are those distributions obtained
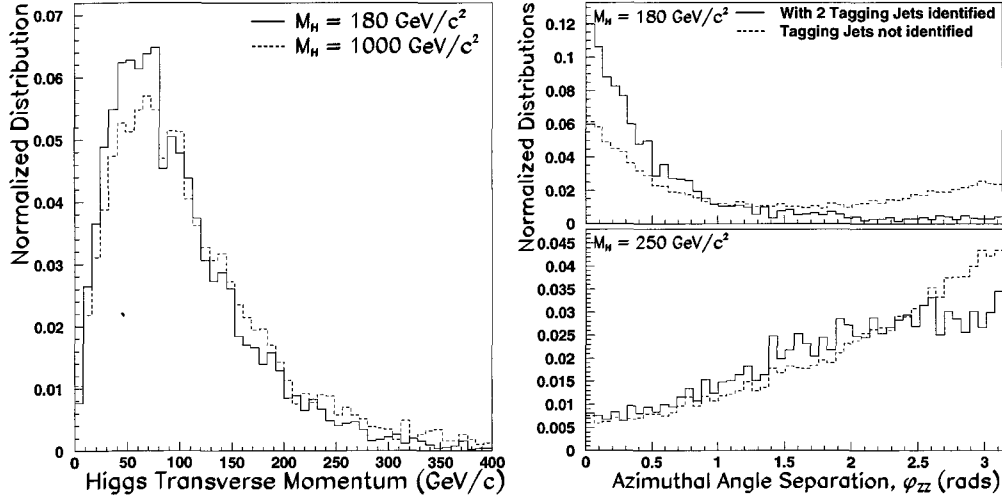
Figure 4.28: (a) The tree level transverse momentum of a Higgs boson produced by VBF. (b) The reconstructed azimuthal angle, in the absence of pileup, when 2 tagging jets have/have not been identified.

once the central event has been reconstructed, ie the first three steps. The optimal cuts are listed in the first 3 columns of table 4.8. Incorrectly using a tagging jet or a pileup jet to reconstruct the Z→jj component of the event will pull the ϕ_{ZZ} distribution of the signal to a larger value as shown in figure 4.28(b). When we ensure that tagging jets are present in the event and have been identified as such, the flattening effect is removed. The optimal azimuthal angle cuts are therefore larger when pileup is included and smaller when tagging jets are identified (last 3 columns of table 4.8) in the event.

Missing ET

The first three steps have made no specific effort to reduce the $t\bar{t}$ background. Due to its large cross-section it remains a considerable background for low Higgs boson mass settings. A cut on $P_T^{Z \to ll}$ significantly reduces the contribution from this channel at M_H >250 GeV/c^2. The missing transverse energy cut is therefore not applied for Higgs boson masses above 250 GeV/c^2.

The $t\bar{t}$ background possesses a large missing E_T ($\not{E}_T$) signature:

$$t\bar{t} \to W^+bW^-b \to l^+l^-b\bar{b}\not{E}_T \tag{4.29}$$

While the signal and the other background events characteristically don't produce high energy neutrinos they do possess a finite $\not{E}_T$ due to the resolution of the calorimetry. The inclusion of high luminosity pileup further reduces the energy resolution of the calorimetry[11]

---

[11]This is discussed in detail in section 5.1.4.

111
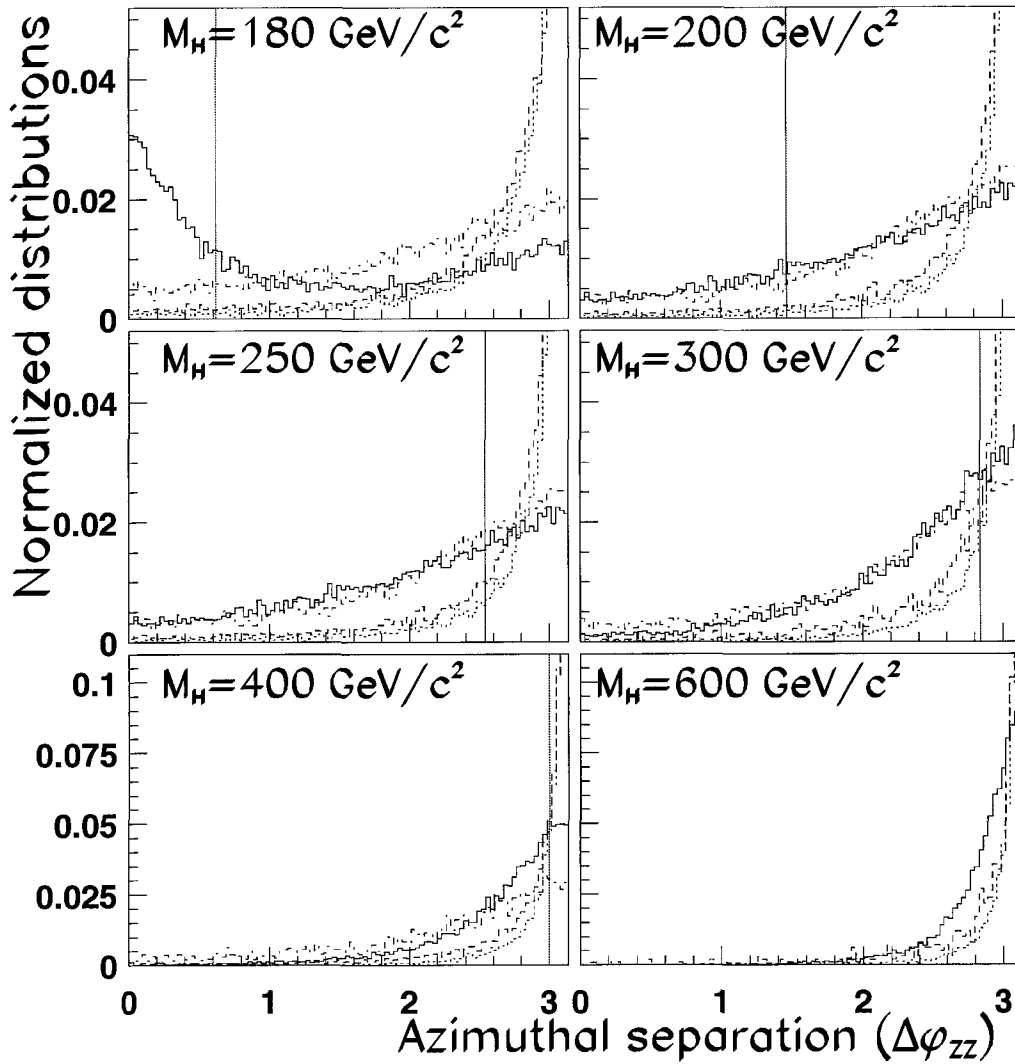
Figure 4.29: The azimuthal separation of the reconstruction Z bosons. The solid line is the shape of the signal, dashed line of Z^0+jets, dotted line ff→ZZ and the dashed-dotted line $t\bar{t}$. The vertical lines correspond to the cuts applied in the final analysis.

112
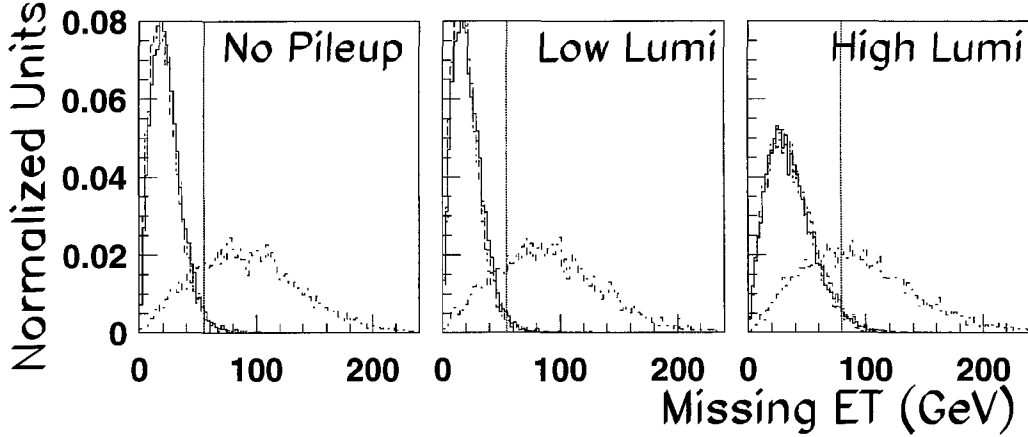
Figure 4.30: Missing energy distribution of the signal and backgrounds after the M_H=200 GeV/c^2 step 3 cuts. The vertical lines are the cuts applied in the final analysis.

increasing the average $\not{E}_T$ of the event. Figure 4.30 shows the $\not{E}_T$ distribution for all physics channels and the three different luminosity settings after the 200 GeV/c^2 step 3 cuts have been applied.

The cuts from the first three steps select events with similar amounts of energy. When coupled with the addition of electronic noise and luminosity pileup the $\not{E}_T$ distribution is roughly the same for the signal and Z^0+jets, ZZ continuum backgrounds. In the no pileup and the low luminosity scenario restricting the $\not{E}_T$ to be no greater than 55 GeV reduces the $t\bar{t}$ channel by 68% and only reduces the signal by 2%. The cut is increased to 80 GeV for the high luminosity running reducing the $t\bar{t}$ by roughly 48% and the signal by only 3%.

The efficiencies of the first four steps of cuts with respect to the signal and background are given in table 4.9. The results in this table have been calculated in the absence of pileup. The mass cuts mentioned in this table are $\pm 2\sigma$ windows around M_Z where σ_{lep} and σ_{had} are defined in equation 4.5 and 4.20 respectively. The column labeled $\frac{S}{\sqrt{B}}$ is calculated as number of signal events passing the cut divided by the square root of the total number of background events passing the same cut.

4.5.5   Step 5

The previously discussed cuts, steps 1 through 4, are placed on the main central activity of the event and will be referred to as the "central cuts". The remaining cuts fall into one of 2 types:

- **Central Jet Veto**: restriction on the hadronic activity in the central region.

113

Cut Description	Signal	ff→ZZ	$t\bar{t}$	Z^0+jets	$\frac{S}{\sqrt{B}}$
$M_H = 200$ GeV/c^2					
Expected	293.10	5996	56580	106240000	
Passing Precuts	86.4 %	68.7 %	91.0 %	18.8 %	.0566
Mass Cuts	32.1 %	20.9 %	2.07 %	0.693 %	0.110
Step 1	26.9 %	14.5 %	1.89 %	0.291 %	0.141
Step 2	26.9 %	14.5 %	1.89 %	0.291 %	0.141
Step 3	17.8 %	9.71 %	1.14 %	0.109 %	0.153
Remaining	52.3	582.	644.	115281.	
Azimuthal Angle	8.78 %	0.375 %	0.272 %	.00778 %	0.280
Missing ET	8.60 %	0.368 %	.0569 %	.00764 %	0.279
Remaining	25.2	22.1	32.2	8121.	
$M_H = 400$ GeV/c^2					
Expected	111.80	5996	56580	106240000	
Passing Precuts	92.2 %	68.7 %	91.0 %	18.8 %	.0230
Mass Cuts	45.8 %	20.8 %	2.17 %	0.674 %	.0604
Step 1	28.8 %	1.28 %	.0762 %	.00690 %	0.373
Step 2	23.0 %	1.04 %	.0558 %	.00365 %	0.408
Step 3	18.5 %	0.651 %	.0273 %	.00181 %	0.464
Remaining	20.7	39.0	15.5	1924.	
Azimuthal Angle	14.8 %	0.181 %	.0241 %	0.00078340 %	0.567
Missing ET	14.8 %	0.181 %	.0241 %	0.00078340 %	0.567
Remaining	16.6	10.9	13.7	832.	
$M_H = 1000$ GeV/c^2					
Expected	12.95	5996	56580	106240000	
Passing Precuts	95.8 %	68.7 %	91.0 %	18.8 %	.0028
Mass Cuts	53.3 %	21.9 %	2.52 %	0.721 %	.0079
Step 1	21.2 %	.0512 %	0.00009110 %	0.00010460 %	0.257
Step 2	18.5 %	.0327 %	0.00001820 %	0.00005450 %	0.310
Step 3	15.4 %	.0221 %	0.00001820 %	0.00002880 %	0.354
Remaining	2.00	1.32	.0103	30.6	
Azimuthal Angle	15.4 %	.0221 %	0.00001820 %	0.00002880 %	0.354
Missing ET	15.4 %	.0221 %	0.00001820 %	0.00002880 %	0.354
Remaining	2.00	1.32	.0103	30.6	

Table 4.9: The efficiencies of the central cuts for three different Higgs boson mass values. Determined after collecting 10 fb^{-1} at low luminosity, in the absence of pileup.

- Cuts on the **Forward Tagging Jets.**[66]

These cuts were discussed previously in section 4.4.

All the plots and tables in this section have been produced using data that has passed the central and the 2σ M_Z mass cuts.

Central Jet Veto

Figure 4.31 shows that for a Higgs data set with mass M_H=600 GeV/c^2 placing the veto for jets at $P_T \leq 15$ GeV/c and restricting the bound on the central region to be $|\eta| <2.0$ is

114

optimal in the low luminosity approach. In the high luminosity scenario the veto threshold is increased to 25 GeV/c due to the extra energy introduced by pileup. The signal significance in figure 4.31 is calculated as the number of signal events passing the veto divided by the root of the number of Z^0+jets events passing the same veto.
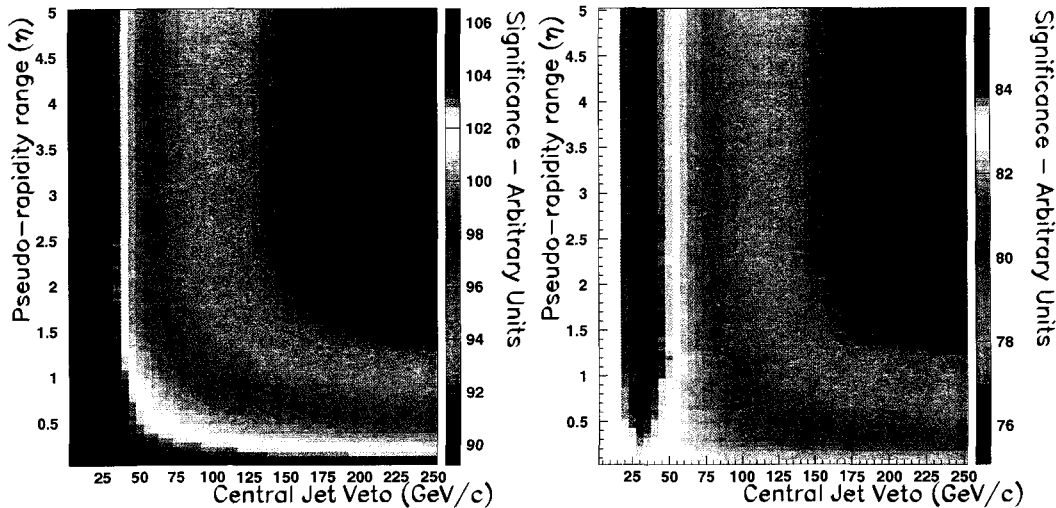
Figure 4.31: Signal significance as a function of the defined pseudo-rapidity range and jet veto value for (a) Low luminosity and (b) High luminosity.

The central jet veto rate, using events that has passed the central cuts, at three different luminosity settings and two different Higgs boson masses, is given in table 4.10.

Tagging Jet Cuts

The symmetric double jet tag rates for events passing the central cuts using the 200 and 600 GeV/c^2 Higgs boson mass settings is given in table 4.11. A heavier mass Higgs boson produces higher P_T events decreasing the effective central region and increasing the size of the forward region improving the forward jet tagging rate. There is also a corresponding increase in the rate for the background processes as well. In the high luminosity scenario, after an increase in the jet initiator threshold from 5 GeV/c to 7 GeV/c, the tag rates for all the background processes increase while the rate for the signal decreases.

Figure 4.32 compares the distribution of three tagging jet variables, leading and trailing jet energies and the tagging jet invariant mass, for the Z^0+jets background with that of the signal at low luminosity and for 3 different Higgs boson mass settings. The distributions do not change significantly in the presence of high luminosity pileup.

Jet Veto (GeV/c)	M_H= 200 GeV/c²					M_H= 600 GeV/c²			
	H→ZZ	ff→ZZ	t$\bar{\text{t}}$	Z+jets	$\frac{S}{\sqrt{B}}$	H→ZZ	ff→ZZ	Z+jets	$\frac{S}{\sqrt{B}}$
No Pileup (10^{33} cm^{-2}s^{-1})									
15.	82.6	42.9	33.9	58.5	1.08	91.3	61.9	53.6	1.25
20.	86.7	49.1	37.2	62.6	1.10	94.5	64.2	57.4	1.25
25.	89.7	51.6	38.7	65.6	1.11	96.1	67.3	61.7	1.22
30.	91.4	57.1	42.0	67.2	1.12	96.9	70.8	63.8	1.21
40.	93.3	63.4	47.4	72.8	1.09	97.7	77.7	67.4	1.19
50.	94.5	70.2	51.4	77.4	1.07	98.0	83.1	69.9	1.17
60.	95.1	72.7	54.1	82.1	1.05	98.3	86.2	73.4	1.15
Low Luminosity (10^{33} cm^{-2}s^{-1})									
15.	77.2	41.3	30.1	43.3	1.17	87.7	57.6	53.9	1.20
20.	82.9	47.9	34.5	49.4	1.18	92.6	61.8	58.2	1.22
25.	86.8	51.6	39.3	55.6	1.16	95.2	65.9	62.3	1.21
30.	89.2	55.9	43.3	60.1	1.15	96.5	68.4	65.5	1.19
40.	92.0	63.8	46.6	66.9	1.12	97.4	73.4	70.2	1.16
50.	93.6	68.3	49.5	71.4	1.11	97.8	78.1	73.7	1.14
60.	94.3	73.7	52.7	75.4	1.09	98.0	82.5	76.5	1.12
High Luminosity (10^{34} cm^{-2}s^{-1})									
15.	71.0	34.7	32.4	43.7	1.07	83.3	61.0	56.7	1.11
20.	73.7	36.8	34.4	47.8	1.07	86.3	63.2	58.7	1.13
25.	76.8	40.5	37.0	51.2	1.07	89.9	66.9	62.4	1.14
30.	80.1	43.6	39.8	57.4	1.06	92.8	70.1	65.2	1.15
40.	84.3	48.0	45.1	67.0	1.03	95.3	75.1	69.4	1.14
50.	87.6	57.4	48.7	73.2	1.02	96.6	79.5	72.2	1.14
60.	89.8	62.6	53.3	77.4	1.02	97.1	81.7	75.4	1.12

Table 4.10: Central jet veto efficiencies (in %) at 3 luminosities and two different Higgs masses. The value $S/\sqrt{B}$ is defined in terms of the fractional values of signal and Z⁰+jets events passing the veto. The t$\bar{\text{t}}$ background is not included for 600 GeV/c² as sufficient statistics do not remain after the application of the first four levels of cuts.

116

Jet Energy	M_H= 200 GeV/c²					M_H= 600 GeV/c²			
(GeV)	H→ZZ	ZZ	t̄t	Z+jets	$\frac{S}{\sqrt{B}}$	H→ZZ	ZZ	Z+jets	$\frac{S}{\sqrt{B}}$
	No Pileup (10^{33} cm⁻²s⁻¹)								
100.	38.4	3.20	6.66	3.90	1.94	49.1	3.48	5.48	2.10
200.	33.7	1.65	4.34	2.54	2.12	43.7	1.69	3.11	2.48
300.	25.5	0.660	2.30	1.44	2.12	34.9	0.680	1.60	2.77
400.	19.0	0.380	1.40	0.860	2.05	27.3	0.290	0.790	3.07
500.	14.0	0.200	0.920	0.600	1.80	21.5	0.170	0.550	2.90
600.	10.9	.0800	0.660	0.380	1.76	16.3	0.170	0.320	2.88
	Low Luminosity (10^{33} cm⁻²s⁻¹)								
100.	38.7	4.24	7.20	5.04	1.72	49.7	3.61	6.04	2.02
200.	32.9	2.22	4.76	3.03	1.89	44.0	1.67	3.22	2.45
300.	24.4	0.950	2.63	1.36	2.09	34.7	0.600	1.47	2.86
400.	18.2	0.460	1.73	0.720	2.15	27.0	0.250	0.800	3.02
500.	13.6	0.250	1.08	0.460	2.00	21.0	0.110	0.530	2.89
600.	10.4	0.160	0.780	0.300	1.89	16.3	.0600	0.330	2.85
	high Luminosity (10^{34} cm⁻²s⁻¹)								
100.	34.1	6.15	7.54	6.25	1.37	48.3	4.38	6.63	1.88
200.	30.0	3.95	5.49	4.38	1.43	43.0	2.13	3.86	2.19
300.	23.0	2.09	2.92	2.40	1.48	33.8	0.750	1.83	2.50
400.	17.2	1.01	1.72	1.38	1.46	26.8	0.430	0.980	2.71
500.	13.0	0.650	1.10	0.830	1.43	21.1	0.260	0.630	2.66
600.	9.80	0.340	0.700	0.500	1.39	16.2	0.160	0.380	2.63

Table 4.11: Double jet tagging efficiencies (in %) on events that have passed the central cuts.

Description	Cut Value
Invariant Mass Cut	M_{tag} >1000 GeV/c²
Symmetric Energy Cut	E_{lead}, E_{trail} > 300 GeV
Asymmetric Energy Cut	E_{lead} >700 GeV, E_{trail} >200 GeV

Table 4.12: Optimal values for the step 5 tagging jet cuts.

The relative significances for the three strongest tagging jets cuts (symmetric, asymmetric and the invariant mass) for a 200 (600) GeV/c² Higgs produced at low luminosity, using events that have passed the central cuts, is shown in figure 4.33(4.34). From these figures we see that the optimal cut values for each of the possible tagging jet cuts of this analysis are those values given in table 4.12. The improvements obtained by changing these parameters with Higgs mass is minimal at best (due to broad peaks in the optimization plots). Figure 4.33 and 4.34 show that of the 3 types of tagging jet cuts studied the most effective is the cut of $\geq$ 1 TeV/c² on the tagging jet invariant mass. It is this cut that is used in the final analysis.
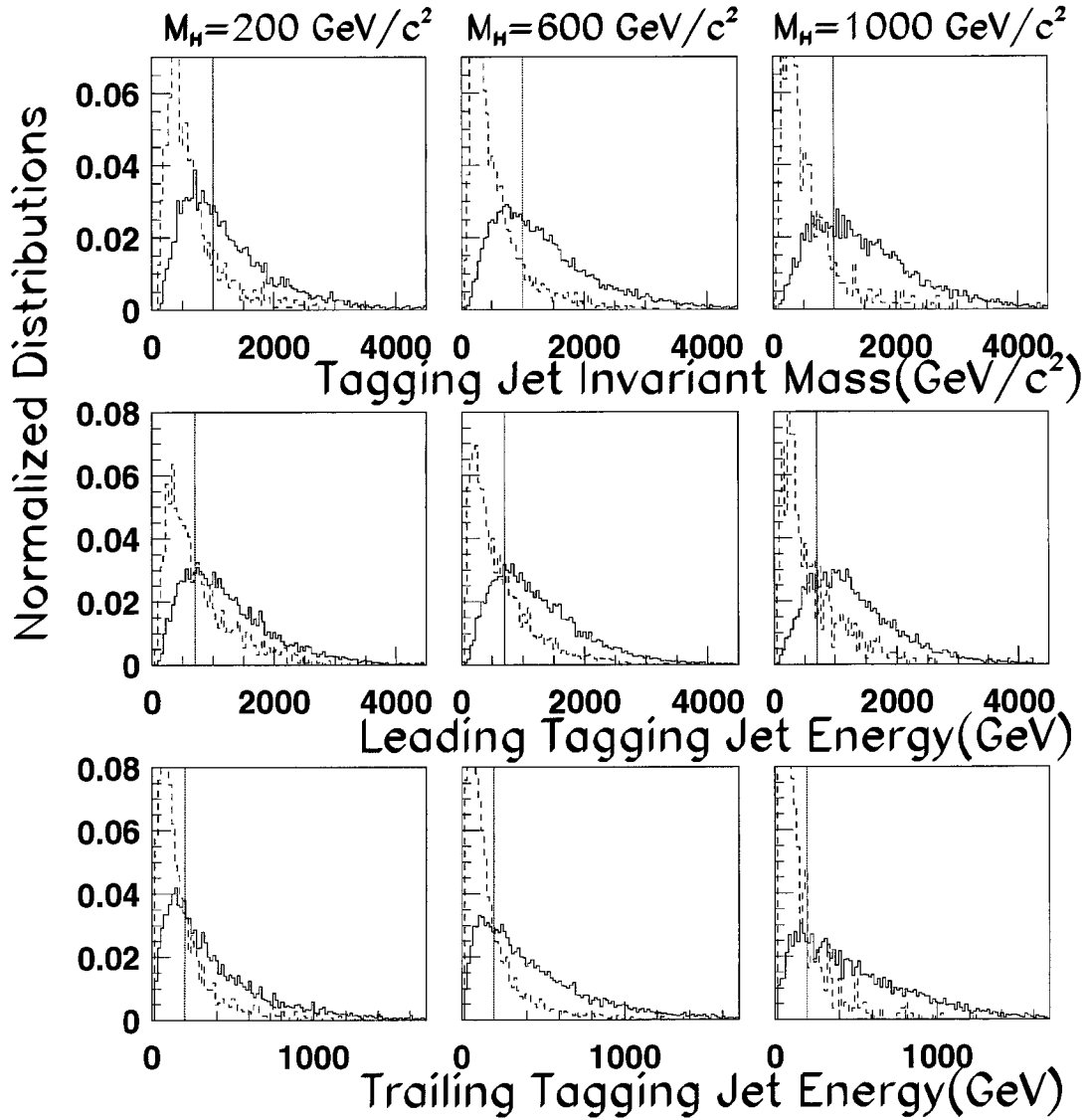
Figure 4.32: The forward tagging variable distribution for the signal and Z^0+jets backgrounds at low luminosity.

118
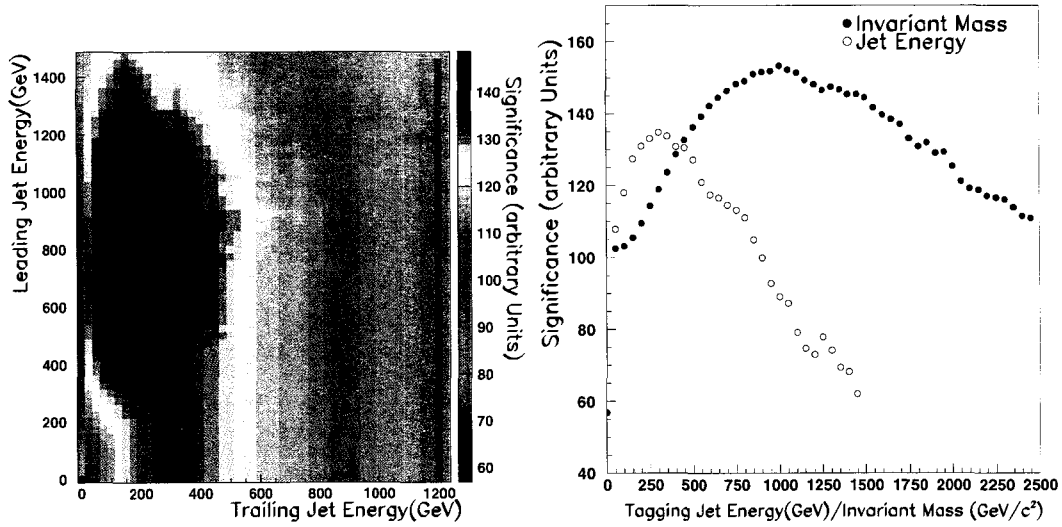
Figure 4.33: Comparing the significances of the (a) asymmetric energy cut to (b) a symmetric energy cut(open circles) and a cut on the tagging jet invariant mass(filled circles).M_H=200 GeV/c^2, low luminosity.
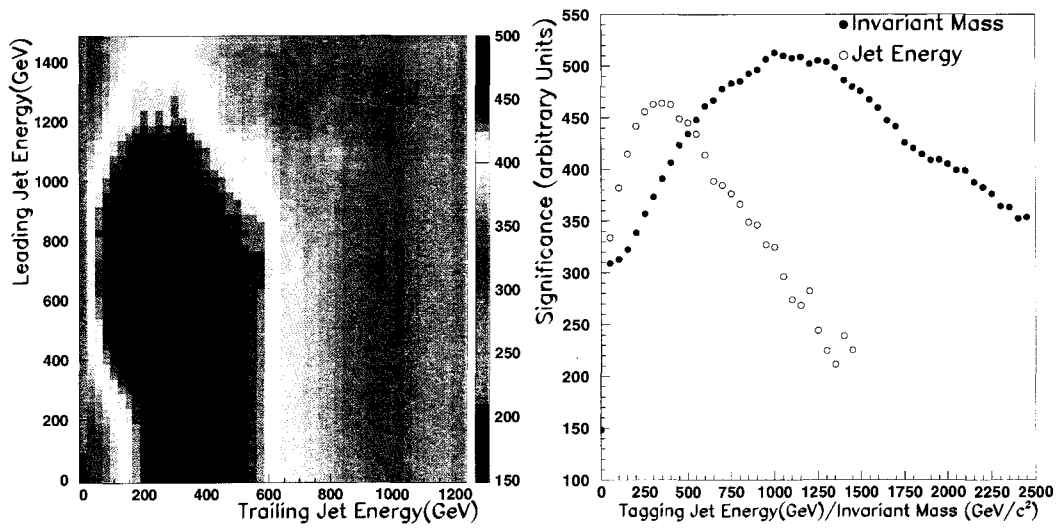
Figure 4.34: Comparing the significances of the (a) asymmetric energy cut to (b) a symmetric energy cut(open circles) and a cut on the tagging jet invariant mass(filled circles).M_H=600 GeV/c^2, low luminosity.

119

Tagging Jet transverse momentum

Table 4.11 showed that when the luminosity is increased from the low luminosity setting (10^{33} cm^{-2}s^{-1}) to the high luminosity setting (10^{34} cm^{-2}s^{-1}) the double jet tag rate for the Higgs signal decreases but the Z^0+jets background rate increases. The decrease in signal rate is caused by the increase to the jet initiator value (from 5 GeV/c to 7 GeV/c) in the local maximum jet finding algorithm. The Z^0+jets rate increases due to the jets introduced by pileup.

Figure 4.35 shows the P_T distribution, after the central cuts, of the leading (tagging jet with the largest transverse momentum) and trailing (tagging jet with the lowest transverse momentum) tagging jets, for no pileup and low and high luminosity running at two different Higgs boson masses. The line shape for the signal tagging jets (solid line) does not appreciably change when the luminosity setting is changed. As we increase the luminosity we see an increased prevalence of low P_T jets in the leading jet plot for the Z+jets background. Minimum bias events have low event P_T and as such the jets introduced by pileup have low P_T as well.

For figure 4.36 a 1 TeV/c^2 cut on the tagging jet invariant mass has been introduced and the prevalence of low P_T jets (in the Z^0+jets background) is still visible in the M_H=200 GeV/c^2 data set, but greatly reduced in the M_H=600 GeV/c^2 data set. As the Higgs mass is increased the central cuts select progressively higher E_T events thereby removing the low E_T Z^0+jets background. The optimal cut values, listed in table 4.13, for the tagging jet transverse momentums have been determined when a 1 TeV/c^2 tagging jet invariant mass cut has been applied to events passing the central cuts.

Higgs Mass (GeV/c^2)	No Pileup (10^{33} cm^{-2}s^{-1})		Low Luminosity (10^{33} cm^{-2}s^{-1})		High Luminosity (10^{34} cm^{-2}s^{-1})	
	Leading	Trailing	Leading	Trailing	Leading	Trailing
170-250	90.0	50.0	90.0	50.0	110.0	60
300	40.0	30.0	60.0	40.0	60.0	40
350	40.0	30.0	40.0	25.0	50.0	30
400	-	-	40.0	25.0	50.0	30
500	-	-	40.0	25.0	50.0	30
600	-	-	-	-	50.0	30

Table 4.13: The optimal P_T cuts (in GeV/c) on the leading and trailing tagging jets as a function of Higgs Mass and luminosity setting.

120
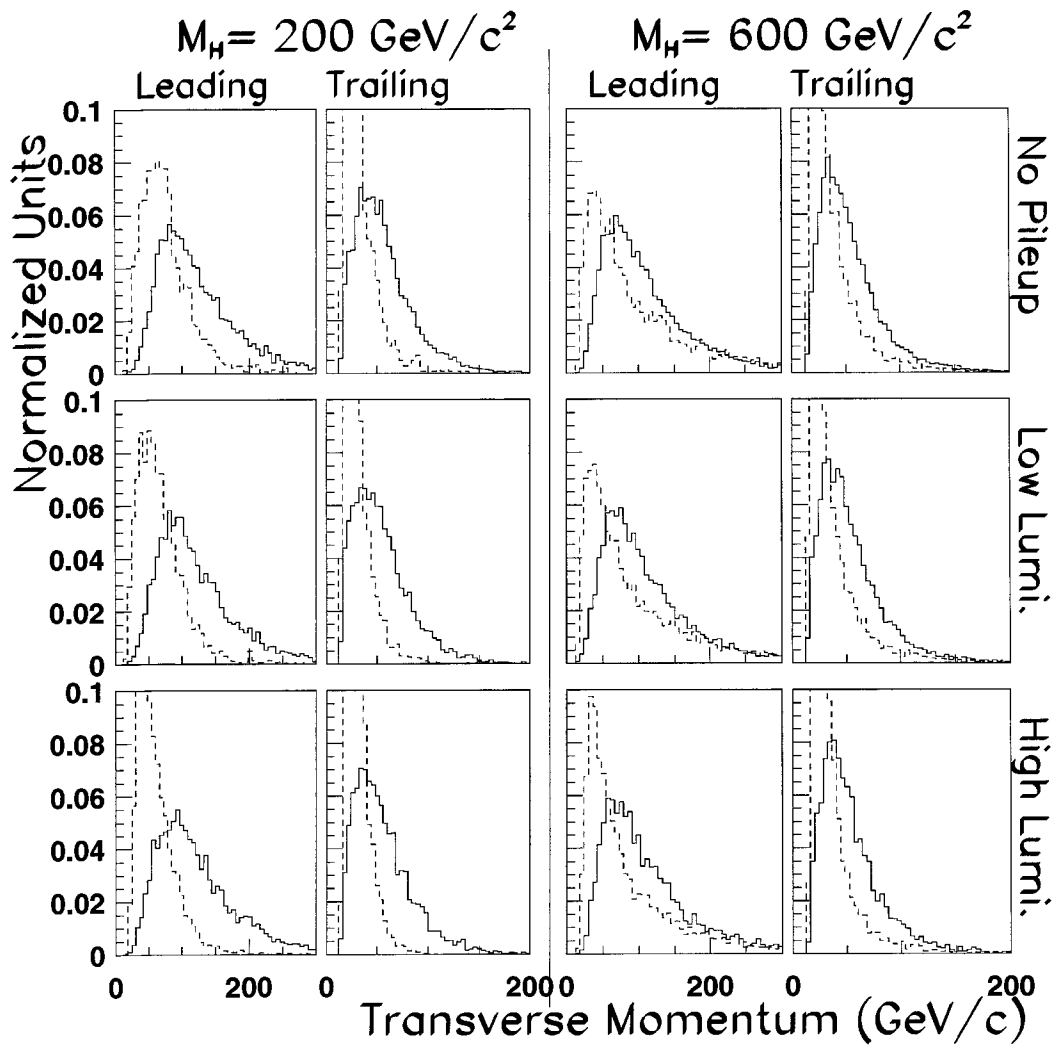
Figure 4.35: The line shape of the leading and trailing tagging jets, after the central cuts, for the three luminosity settings and M_H=200, 600 GeV/c^2. The solid line is the signal, the dashed line the Z^0+jets distribution.

121
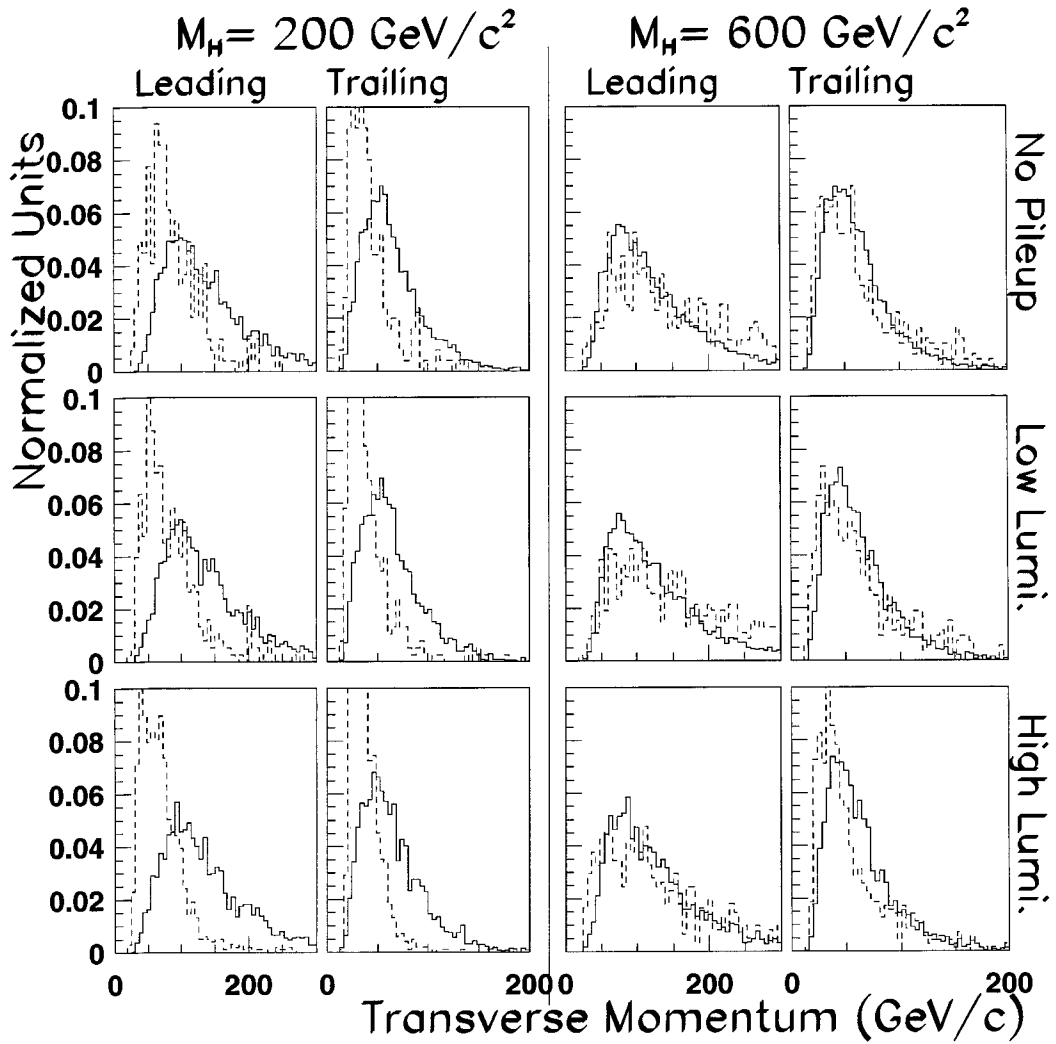
Figure 4.36: The line shape of the leading and trailing tagging jets, after the central cuts and a 1 TeV/c^2 tagging jet invariant mass cut, for the three luminosity settings and M_H=200, 600 GeV/c^2. The solid line is the signal, the dashed line the Z^0+jets distribution.

122
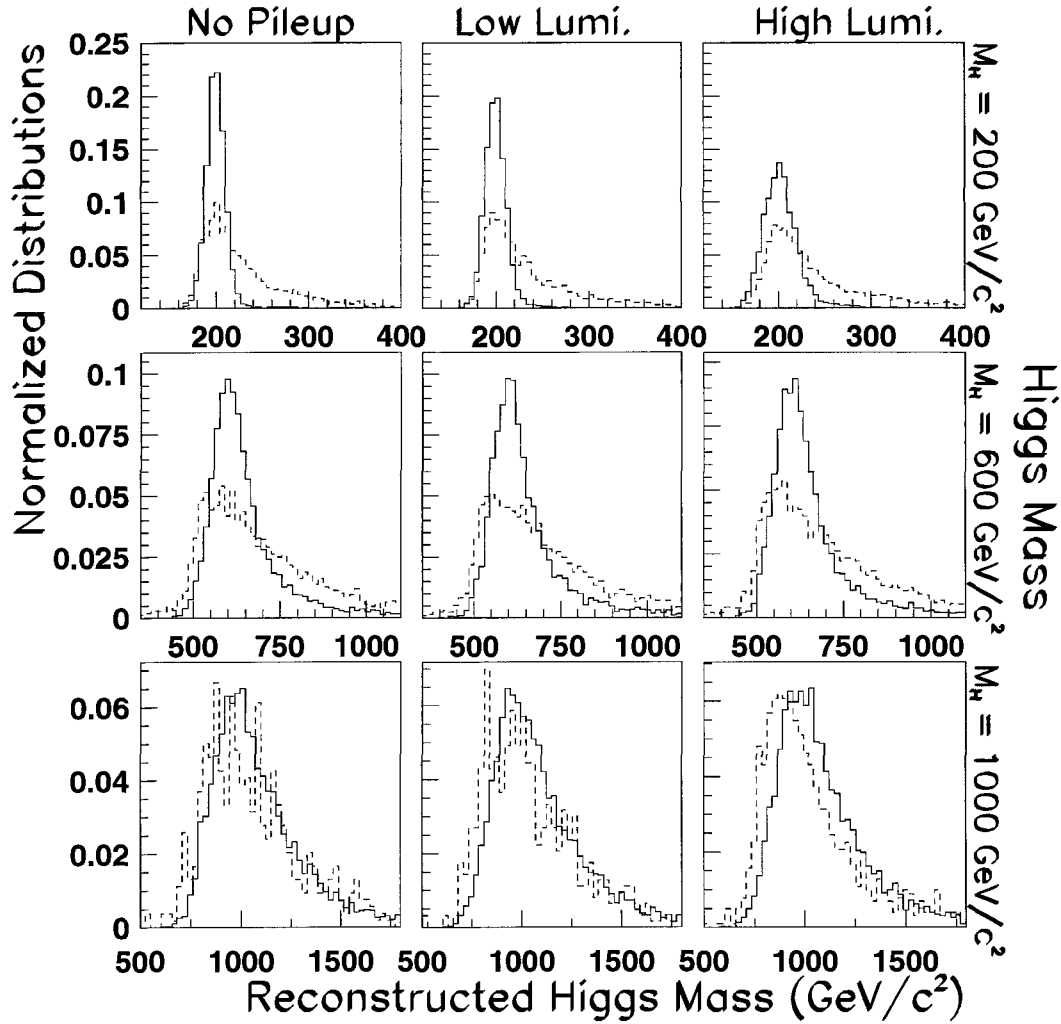
Figure 4.37: The reconstructed Higgs mass spectrum for the Higgs Signal (solid line), and the Z+jets background (dashed line) at 3 different Higgs mass settings and the 3 different luminosities.

Higgs Mass Spectrum

To avoid any analytical bias the central cuts and the tagging jet cuts have been applied without any restriction being placed on the Higgs mass. But we have shown in section 4.3 that the reconstructed mass spectrum of a low mass Higgs can be quite narrow, on the order of 10 GeV/c^2 at low luminosity for a Higgs Mass of 200 GeV/c^2. Figure 4.37 shows the reconstructed Higgs mass spectrum, after the application of the central cuts and the identification of two tagging jets, for the Higgs signal and the Z^0+jets background for a 200, 600 and 1000 GeV/c^2 Higgs at different luminosity settings.

We can see that for the low Higgs mass case (M_H=200 GeV/c^2) there is a clear difference between the Higgs mass resonance peak, and the reconstructed mass spectrum from the

123

Z+jets background. Previous studies[13][74] have shown that for a low mass Higgs boson applying a $\pm 2\sigma$ cut around the resonance peak [12] [13] can greatly improve the expected significance. As the nominal Higgs mass increases, the line shape of the Z^0+jets background becomes very similar to the signal removing the effectiveness of this cut. In this thesis we found that a $\pm 2\sigma$ cut on the reconstructed Higgs invariant mass is beneficial up to a Higgs mass of 600 GeV/c^2.

Summary of the Step 5 cuts

The expected number of events remaining after the central and step 5 cuts are given in table 4.14. The rates have been determined using 10 fb^{-1} for low luminosity and 100 fb^{-1} at high luminosity. The "tagging mass" cut is the 1 TeV/c^2 cut on the invariant mass of the tagging jets, "Veto" is the central jet veto, "Tagging P_T" is the additional cut on the transverse momentum of the tagging jets and ΔM_H is the application of a $\pm 2\sigma$ cut on the invariant mass of the reconstructed Higgs boson.

4.6   H→ZZ Results

Before final results can be calculated using the optimal cut values that were discussed in the previous section we must briefly revisit the ATLAS Trigger. An event must past the ATLAS trigger system before it can be included in the final data set. The triggers enforced for the neutral vector boson channel are given in table 4.15.

Tables 4.17 and 4.18 summarize the significances obtained for a Higgs mass of 300 GeV/c^2 at low (using a integrated luminosity of 30 fb^{-1}) and high luminosity (100 fb^{-1}) pileup. It is common to perform fast simulation studies without pileup, so we have included table 4.16 summarizing the results using an integrated luminosity of 30 fb^{-1} in the absence of pileup. Similar tables have been produced for Higgs masses of 200 GeV/c^2, 600 GeV/c^2 and 1 TeV/c^2 and can be found in appendix A.

Table 4.19 summarizes the total number of signal and background events expected, for a Higgs boson with a mass between 180 GeV/c^2 and 1 TeV/c^2, after the application of all the cuts discussed in this chapter. The results have been summed over both the electron and muon channels.

Figure 4.38 plots the expected significance as a function of Higgs mass when we include

---

[12] Where σ is defined in equation 4.22.
[13] The mean value of this peak is given in equation 4.23.

124

Cut Description	Signal	ff→ZZ	$t\bar{t}$	Z^0+jets	$\frac{S}{\sqrt{B}}$
M_H = 200 GeV/c^2 No Pileup					
Central Cuts	25.2	22.1	32.2	8164.	0.28
Tagging Mass	5.09	0.07	0.45	54.9	0.68
+Veto	4.38	0.03	0.15	28.3	0.82
+Veto+ΔM_H	4.21	0.01	0.09	12.5	1.19
+Veto+Tagging P_T	2.33	0.009	0.06	3.74	1.19
+Veto+Tagging P_T+ΔM_H	2.24	0.003	0.04	1.54	1.78
M_H = 200 GeV/c^2 Low Luminosity Pileup					
Central Cuts	24.6	24.5	39.0	10623.	0.24
Tagging Mass	4.92	0.10	0.63	79.4	0.55
+Veto	4.00	0.04	0.20	37.5	0.65
+Veto+ΔM_H	3.75	0.02	0.10	15.9	0.94
+Veto+Tagging P_T	2.14	0.01	0.07	5.03	0.95
+Veto+Tagging P_T+ΔM_H	2.01	0.004	0.03	1.89	1.45
M_H = 200 GeV/c^2 High Luminosity Pileup					
Central Cuts	245.	401.	1145.	340300.	0.42
Tagging Mass	45.0	3.82	19.8	4229.	0.69
+Veto	33.7	1.19	6.05	1855.	0.78
+Veto+ΔM_H	25.9	0.45	2.79	740.	0.95
+Veto+Tagging P_T	18.1	0.18	1.74	162.	1.41
+Veto+Tagging P_T+ΔM_H	13.9	0.06	0.84	46.8	2.01
M_H = 1000 GeV/c^2 No Pileup					
Central Cuts	2.00	1.32	0.01	30.6	0.35
Tagging Mass	0.66	0.002	0.000	0.24	1.35
+Veto	0.62	0.000	0.000	0.12	1.80
+Veto+ΔM_H	0.52	0.000	0.000	0.10	1.63
+Veto+Tagging P_T	0.62	0.000	0.000	0.12	1.80
+Veto+Tagging P_T+ΔM_H	0.52	0.000	0.000	0.10	1.63
M_H = 1000 GeV/c^2 Low Luminosity Pileup					
Central Cuts	1.99	1.31	0.02	31.6	0.35
Tagging Mass	0.66	0.002	0.000	0.25	1.32
+Veto	0.59	0.001	0.000	0.14	1.60
+Veto+ΔM_H	0.50	0.000	0.000	0.11	1.49
+Veto+Tagging P_T	0.59	0.001	0.000	0.14	1.60
+Veto+Tagging P_T+ΔM_H	0.50	0.000	0.000	0.11	1.49
M_H = 1000 GeV/c^2 High Luminosity Pileup					
Central Cuts	18.7	12.9	0.36	430.	0.89
Tagging Mass	6.09	0.05	0.000	4.86	2.75
+Veto	5.14	0.04	0.000	2.29	3.37
+Veto+ΔM_H	4.37	0.03	0.000	2.05	3.03
+Veto+Tagging P_T	5.14	0.04	0.000	2.29	3.37
+Veto+Tagging P_T+ΔM_H	4.37	0.03	0.000	2.05	3.03

Table 4.14: Number of events and significances($\frac{S}{\sqrt{B}}$) of the step 5 cuts. For a 200 GeV/c^2 and 1 TeV/c^2 Higgs boson. The rates for the No pileup and low luminosity pileup sections are calculated using 10 fb^{-1} of data, high luminosity is calculated using 100 fb^{-1}.

Physics Channel	Luminosity	Single Lepton Trigger	Double Lepton Trigger
Z→ $\mu^+\mu^-$	Low	20 GeV/c	-
($\eta \leq 2.4$)	High	20 GeV/c	10 GeV/c
Z→ e^+e^-	Low	20 GeV/c	15 GeV/c
($\eta \leq 2.5$)	High	30 GeV/c	20 GeV/c

Table 4.15: Trigger conditions for the Z→ $\mu^+\mu^-$ and Z→ e^+e^- physics channels at low and high luminosity.

all the cuts with the exception of the tagging jet P_T cuts. We see that there is no appreciable difference between the expected significances from the electron and muon channels. There is a noticeable reduction in signal significance for a low mass Higgs at high luminosity due to the increase in Z^0+jets background rate. The increase in background is due to the increase in the fake forward jet tag rate which is caused by the jets introduced by pileup. Figure 4.39 shows the improvement to the significances over figure 4.38 when the transverse momentum cut on the tagging jets is applied. For a Higgs mass below 300 GeV/c^2 the tagging jet transverse momentum cut improves our significance by approximately 50% in the absence of pileup and by a factor of 2 when high luminosity pileup is present. A neutral scalar Higgs boson can be observed in the this channel after 3 years at low luminosity if its mass is between 250 GeV/$c^2 \leq M_H \leq$ 700 GeV/c^2 and for $M_H \geq$ 300 GeV/c^2 after 1 year of high luminosity running.

The results presented thus far have been optimized for a counting experiment, that is searching for an excess in signal events over an expected number of background events. Identifying this excess as originating from the existence of a Higgs boson would require observing a Higgs mass peak above a continuous background spectrum. The reconstructed Higgs mass for 3 years of running at low luminosity($30fb^{-1}$at $10^{33}cm^{-2}s^{-1}$) without pileup, for varying Higgs boson masses, is presented in figure 4.40. Figure 4.41 shows the reconstructed mass spectrum when low luminosity pileup has been added. In both these cases a mass peak should be clearly visible for a Higgs boson with a mass above 200 GeV/c^2. After gathering 100 fb^{-1}at the High luminosity setting ($10^{34}cm^{-2}s^{-1}$) figure 4.42 shows that it is more difficult to observe the low Higgs mass resonances. At the high luminosity setting the Higgs resonance peak will be visible for Higgs boson masses above 400 GeV/c^2.

In this chapter we have outlined a method to search for a neutral scalar Higgs boson produced through vector boson fusion and decays through the mixed leptonic/hadronic decays of the neutral vector bosons(H→ZZ→l$^+$l$^-$jj). It has been shown that a neutral scalar Higgs boson can be observed after 3 years of low luminosity running if its mass is

126

	Signal	Z^0+jets	ff→ ZZ	$t\bar{t}$	δ Back	$\frac{S}{\sqrt{B}}$
			$Z\to \mu^+\mu^-$ channel			
Expected	598.50±1.270	6492000.	17988.	169740.	731.29	0.230±0.000
Precuts	540.06±1.210	4090246.	12360.	154496.	581.10	0.260±0.001
Trigger	470.98±1.130	1814010.	7799.0	116402.	387.95	0.340±0.001
Central Cut	84.56±0.480	9557.41	78.1	299.31	28.07	0.850±0.005
M_H Window	69.42±0.430	2816.86	24.0	124.79	15.26	1.270±0.009
Jet Veto	43.83±0.340	1139.12	8.35	41.15	9.700	1.270±0.011
Tagging Mass	14.85±0.200	10.41	0.03	0.850	0.930	4.420±0.192
+Tagging P_T	11.31±0.170	5.740	0.02	0.590	0.690	4.490±0.255
			$Z\to e^+e^-$ channel			
Expected	598.50±1.250	6492000.	17988.	169740.	706.36	0.230±0.000
Precuts	523.55±1.170	3795484.	11580.	150021.	540.80	0.260±0.001
Trigger	455.22±1.090	1651274.	7136.6	108128.	357.61	0.340±0.001
Central Cut	88.07±0.480	9588.64	78.5	337.68	27.17	0.880±0.005
M_H Window	72.13±0.430	2818.93	23.7	143.57	14.76	1.320±0.009
Jet Veto	45.76±0.350	1150.88	8.04	46.93	9.420	1.320±0.011
Tagging Mass	15.64±0.200	11.93	0.03	0.840	0.960	4.370±0.174
+Tagging P_T	11.94±0.180	7.110	0.02	0.480	0.740	4.330±0.221
			Combined Results			
Expected	1197.00±2.520	12984000.	35976.	339480.	1437.65	0.327±0.001
Precuts	1063.61±2.380	7885730.	23940.	304517.	1121.90	0.371±0.001
Trigger	926.20±2.220	3465284.	14935.	224530.	745.56	0.481±0.001
Central Cut	172.63±0.960	19146.1	156.6	636.99	55.24	1.223±0.008
M_H Window	141.55±0.860	5635.79	47.7	268.36	30.02	1.835±0.016
Jet Veto	89.59±0.690	2290.00	16.3	88.08	19.12	1.831±0.021
Tagging Mass	30.49±0.400	22.34	0.06	1.690	1.890	6.212±0.325
+Tagging P_T	23.25±0.350	12.85	0.04	1.070	1.430	6.223±0.412

Table 4.16: M_H=300 GeV/c^2. H→ZZ→lljj. Number of events expected after 3 years of running at the low luminosity setting (L=30 fb^{-1}). Pileup has not been included.

between 250 GeV/c^2 ≤M_H ≤700 GeV/c^2 and for M_H ≥ 300 GeV/c^2 after 1 year of high luminosity running.

	Signal	Z^0+jets	ff→ ZZ	t$\bar{\text{t}}$	δ Back	$\frac{S}{\sqrt{B}}$
			$Z \to \mu^+\mu^-$ channel			
Expected	598.50±1.270	6492000.	17988.	169740.	731.29	0.230±0.000
Precuts	540.06±1.210	4090246.	12360.	154496.	581.10	0.260±0.001
Trigger	471.58±1.130	1990443.	7982.5	117611.	406.18	0.320±0.001
Central Cut	80.73±0.470	10240.8	77.5	313.83	29.06	0.780±0.005
M_H Window	66.34±0.420	3166.29	25.1	138.69	16.18	1.150±0.008
Jet Veto	40.25±0.330	1253.30	8.24	44.29	10.17	1.110±0.010
Tagging Mass	13.63±0.190	13.20	0.05	0.900	1.050	3.620±0.144
+Tagging P_T	10.36±0.170	6.560	0.02	0.650	0.740	3.850±0.207
			$Z \to e^+e^-$ channel			
Expected	598.50±1.250	6492000.	17988.	169740.	706.36	0.230±0.000
Precuts	523.55±1.170	3795484.	11580.	150021.	540.80	0.260±0.001
Trigger	455.62±1.090	1809655.	7294.5	109158.	374.18	0.330±0.001
Central Cut	84.30±0.470	10305.8	78.1	355.45	28.17	0.810±0.005
M_H Window	68.19±0.420	3164.92	24.6	157.73	15.63	1.180±0.008
Jet Veto	41.87±0.330	1244.24	8.06	50.44	9.790	1.160±0.010
Tagging Mass	14.28±0.190	12.85	0.03	0.680	1.000	3.880±0.152
+Tagging P_T	10.90±0.170	7.030	0.02	0.300	0.740	4.020±0.211
			Combined Results			
Expected	1197.00±2.520	12984000.	35976.	339480.	1437.65	0.327±0.001
Precuts	1063.61±2.380	7885730.	23940.	304517.	1121.90	0.371±0.001
Trigger	927.20±2.220	3800098.	15277.	226769.	780.36	0.461±0.001
Central Cut	165.03±0.940	20546.6	155.7	669.28	57.23	1.129±0.008
M_H Window	134.53±0.840	6331.21	49.8	296.42	31.81	1.646±0.014
Jet Veto	82.12±0.660	2497.54	16.3	94.73	19.96	1.608±0.019
Tagging Mass	27.91±0.380	26.05	0.08	1.580	2.050	5.302±0.268
+Tagging P_T	21.26±0.340	13.59	0.04	0.950	1.480	5.568±0.372

Table 4.17: M_H=300 GeV/c². H→ZZ→lljj. Number of events expected in 3 years of running at the low luminosity setting (L=30 fb^{-1}). Pileup has been included.

128

	Signal	Z^0+jets	ff$\to$ ZZ	$t\bar{t}$	δ Back	$\frac{S}{\sqrt{B}}$
			$Z\to\mu^+\mu^-$ channel			
Expected	1995.00±4.240	21640000.	59960.	565800.	2437.64	0.420±0.001
Precuts	1800.21±4.030	13634154.	41200.	514985.	1937.00	0.480±0.001
Trigger	1563.21±3.750	6412748.	24501.	379089.	1331.09	0.600±0.001
Central Cut	268.36±1.550	62576.1	329.2	1586.87	131.08	1.060±0.006
M_H Window	213.41±1.390	25406.0	137.3	889.86	83.59	1.310±0.009
Jet Veto	135.22±1.100	12261.7	53.5	326.16	58.03	1.200±0.010
Tagging Mass	43.57±0.630	175.14	0.50	8.870	6.950	3.210±0.076
+Tagging P_T	34.54±0.560	84.15	0.21	5.830	4.830	3.640±0.114
			$Z\to e^+e^-$ channel			
Expected	1995.00±4.170	21640000.	59960.	565800.	2354.54	0.420±0.001
Precuts	1745.17±3.900	12651614.	38600.	500070.	1802.68	0.480±0.001
Trigger	1520.44±3.640	5776854.	21774.	337327.	1220.36	0.610±0.001
Central Cut	283.83±1.570	64313.2	342.9	2104.95	128.44	1.100±0.006
M_H Window	223.31±1.400	25910.1	140.9	1163.11	81.62	1.350±0.009
Jet Veto	143.60±1.120	12498.2	55.4	421.46	56.63	1.260±0.010
Tagging Mass	46.52±0.640	203.13	0.42	9.350	7.230	3.190±0.070
+Tagging P_T	37.01±0.570	92.26	0.15	5.500	4.880	3.740±0.109
			Combined Results			
Expected	3990.00±8.410	43280000.	119920	1131600.	4792.18	0.598±0.001
Precuts	3545.38±7.930	26285768.	79800.	1015056.	3739.68	0.678±0.002
Trigger	3083.65±7.390	12189602.	46276.	716416.	2551.45	0.857±0.002
Central Cut	552.19±3.120	126889.	672.1	3691.82	259.52	1.524±0.010
M_H Window	436.72±2.790	51316.0	278.2	2052.97	165.21	1.886±0.015
Jet Veto	278.82±2.220	24759.9	108.9	747.62	114.66	1.742±0.018
Tagging Mass	90.09±1.270	378.27	0.92	18.22	14.18	4.519±0.144
+Tagging P_T	71.55±1.130	176.41	0.36	11.33	9.710	5.217±0.217

Table 4.18: M_H=300 GeV/c^2. H$\to$ZZ$\to$lljj. Number of events expected in 1 year of high luminosity running (L=100 fb^{-1}). High luminosity pileup has been included.

129
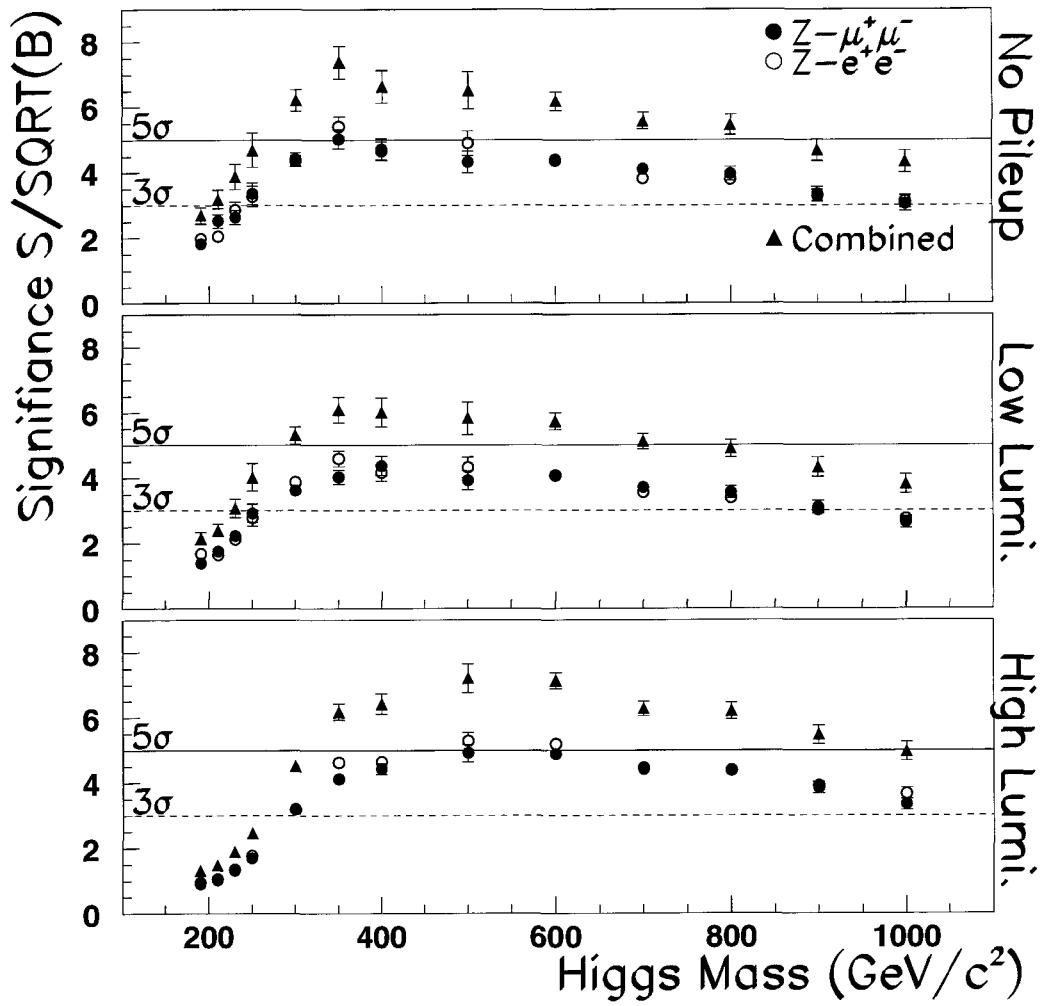
Figure 4.38: Significance (after all cuts except the tagging jet transverse momentum) as a function of Higgs mass (H→ZZ channel) for no luminosity pileup, low luminosity running and an integrated luminosity of 30 fb^{-1}, and for high luminosity pileup with 100 fb^{-1}.

130

| Higgs Mass $(\frac{GeV}{c^2})$ | Low Luminosity $10^{33} cm^{-2} s^{-1}$ | | | | | | High Luminosity $10^{34} cm^{-2} s^{-1}$ | | |
| | w/o Pileup | | | w/ Pileup | | | w/ Pileup | | |
	Signal	Back.	$\frac{S}{\sqrt{B}}$	Signal	Back.	$\frac{S}{\sqrt{B}}$	Signal	Back.	$\frac{S}{\sqrt{B}}$
180	1.62 ± 0.06	4.71 ± 2.43	0.75 ± 0.22	1.51 ± 0.06	1.42 ± 0.99	1.27 ± 0.49	3.15 ± 0.16	22.73 ± 9.84	0.66 ± 0.18
190	10.39 ± 0.26	6.71 ± 2.96	4.01 ± 0.99	9.66 ± 0.25	7.97 ± 3.22	3.42 ± 0.78	19.50 ± 0.66	32.01 ± 11.59	3.45 ± 0.74
200	13.53 ± 0.32	10.14 ± 3.62	4.25 ± 0.86	12.16 ± 0.31	14.12 ± 4.28	3.24 ± 0.57	25.22 ± 0.80	49.98 ± 14.50	3.57 ± 0.63
210	13.95 ± 0.32	7.65 ± 3.10	5.04 ± 1.14	12.30 ± 0.30	13.53 ± 4.17	3.34 ± 0.60	26.87 ± 0.81	72.90 ± 17.61	3.15 ± 0.47
220	15.28 ± 0.34	6.95 ± 2.95	5.80 ± 1.36	13.45 ± 0.32	13.05 ± 4.06	3.72 ± 0.67	31.14 ± 0.87	86.07 ± 19.17	3.36 ± 0.47
230	15.40 ± 0.35	4.95 ± 2.46	6.92 ± 1.88	14.01 ± 0.34	12.33 ± 3.96	3.99 ± 0.74	31.88 ± 0.92	90.34 ± 19.67	3.35 ± 0.46
240	16.19 ± 0.34	3.68 ± 2.08	8.44 ± 2.56	14.84 ± 0.32	9.56 ± 3.50	4.80 ± 0.98	33.84 ± 0.88	81.53 ± 18.68	3.75 ± 0.53
250	16.20 ± 0.32	3.62 ± 2.07	8.51 ± 2.60	14.98 ± 0.32	9.48 ± 3.44	4.87 ± 0.99	35.14 ± 0.88	96.73 ± 20.34	3.57 ± 0.47
300	23.25 ± 0.35	13.96 ± 1.43	6.22 ± 0.41	21.26 ± 0.34	14.58 ± 1.48	5.57 ± 0.37	71.55 ± 1.13	188.10 ± 9.71	5.22 ± 0.22
350	25.55 ± 0.32	10.97 ± 1.30	7.71 ± 0.55	22.90 ± 0.31	12.45 ± 1.39	6.49 ± 0.45	73.54 ± 1.01	113.91 ± 7.66	6.89 ± 0.33
400	19.67 ± 0.24	8.51 ± 1.15	6.74 ± 0.54	18.43 ± 0.24	9.06 ± 1.18	6.12 ± 0.48	58.31 ± 0.77	68.64 ± 5.98	7.04 ± 0.40
450	19.29 ± 0.24	8.52 ± 1.15	6.61 ± 0.53	18.06 ± 0.22	8.23 ± 1.13	6.30 ± 0.51	54.45 ± 0.72	55.99 ± 5.41	7.28 ± 0.45
500	16.19 ± 0.18	6.27 ± 1.00	6.47 ± 0.59	14.95 ± 0.17	6.55 ± 1.02	5.84 ± 0.52	45.64 ± 0.53	33.71 ± 4.20	7.86 ± 0.58
550	13.61 ± 0.14	4.63 ± 0.28	6.33 ± 0.26	12.53 ± 0.14	4.62 ± 0.28	5.83 ± 0.24	36.44 ± 0.44	22.76 ± 1.14	7.64 ± 0.28
600	11.67 ± 0.12	3.56 ± 0.25	6.19 ± 0.28	10.92 ± 0.12	3.62 ± 0.25	5.74 ± 0.26	31.94 ± 0.37	18.00 ± 1.01	7.53 ± 0.30
650	12.21 ± 0.12	4.56 ± 0.28	5.72 ± 0.23	11.42 ± 0.11	4.64 ± 0.28	5.30 ± 0.21	36.79 ± 0.37	31.27 ± 1.33	6.58 ± 0.21
700	10.02 ± 0.10	3.22 ± 0.23	5.58 ± 0.26	9.33 ± 0.10	3.32 ± 0.23	5.12 ± 0.23	29.77 ± 0.30	22.51 ± 1.13	6.27 ± 0.22
750	8.75 ± 0.08	2.45 ± 0.21	5.59 ± 0.29	8.24 ± 0.08	2.59 ± 0.21	5.12 ± 0.26	26.24 ± 0.26	16.69 ± 0.97	6.42 ± 0.25
800	7.57 ± 0.08	1.92 ± 0.18	5.46 ± 0.31	7.07 ± 0.07	2.09 ± 0.19	4.89 ± 0.27	22.71 ± 0.23	13.41 ± 0.87	6.20 ± 0.26
850	6.56 ± 0.06	1.58 ± 0.17	5.22 ± 0.33	6.08 ± 0.06	1.69 ± 0.17	4.68 ± 0.28	19.70 ± 0.19	10.85 ± 0.78	5.98 ± 0.27
900	5.26 ± 0.05	1.26 ± 0.15	4.69 ± 0.32	4.93 ± 0.05	1.30 ± 0.15	4.32 ± 0.29	15.68 ± 0.16	8.19 ± 0.68	5.48 ± 0.28
950	5.00 ± 0.04	1.18 ± 0.14	4.60 ± 0.31	4.65 ± 0.04	1.20 ± 0.15	4.24 ± 0.30	14.78 ± 0.14	7.71 ± 0.65	5.32 ± 0.27
1000	4.10 ± 0.04	0.89 ± 0.12	4.35 ± 0.34	3.80 ± 0.04	0.99 ± 0.13	3.82 ± 0.29	12.04 ± 0.12	5.89 ± 0.58	4.96 ± 0.29

Table 4.19: Signal and background rates for the neutral vector boson channels after the application of all the cuts.

131
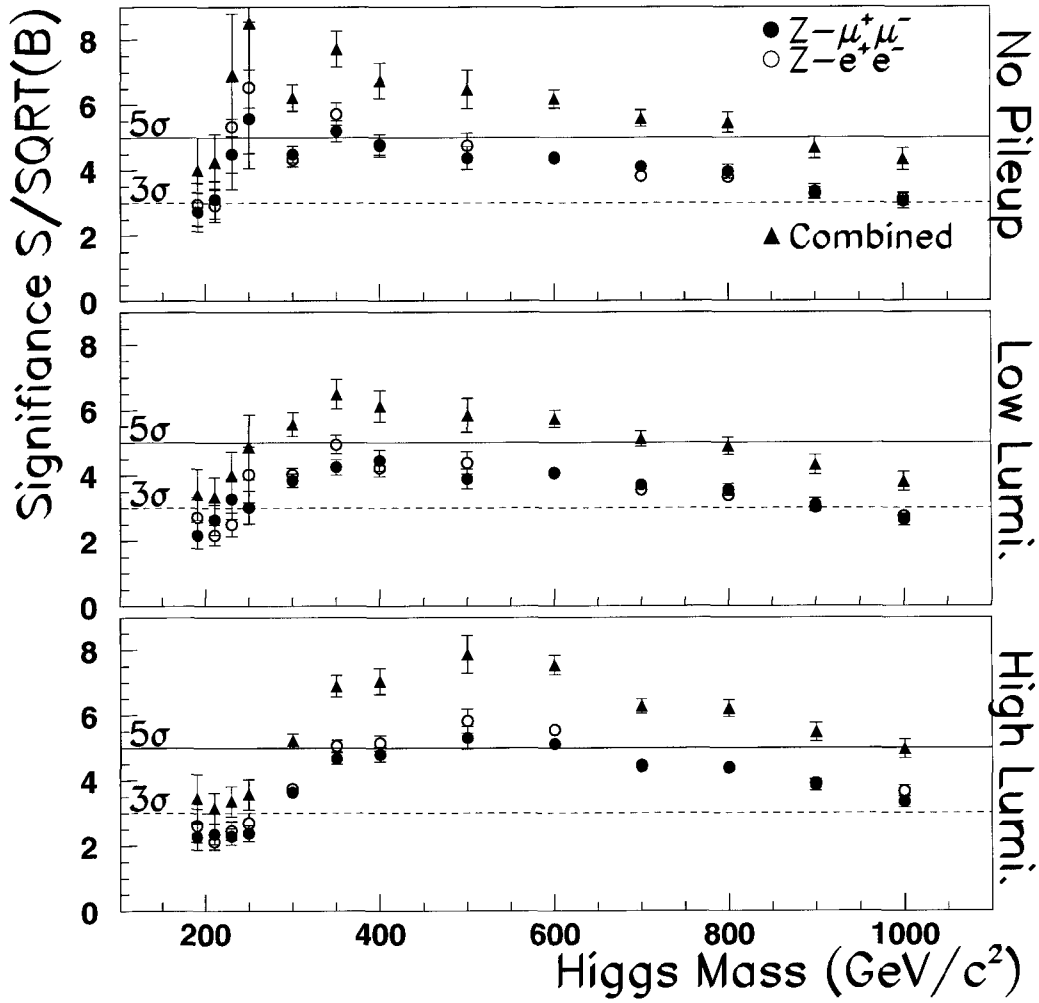
Figure 4.39: Significance (after all the cuts) as a function of Higgs mass (H→ZZ channel) for no luminosity pileup, low luminosity running and an integrated luminosity of 30 fb^{-1}, and for high luminosity pileup with 100 fb^{-1}.

132
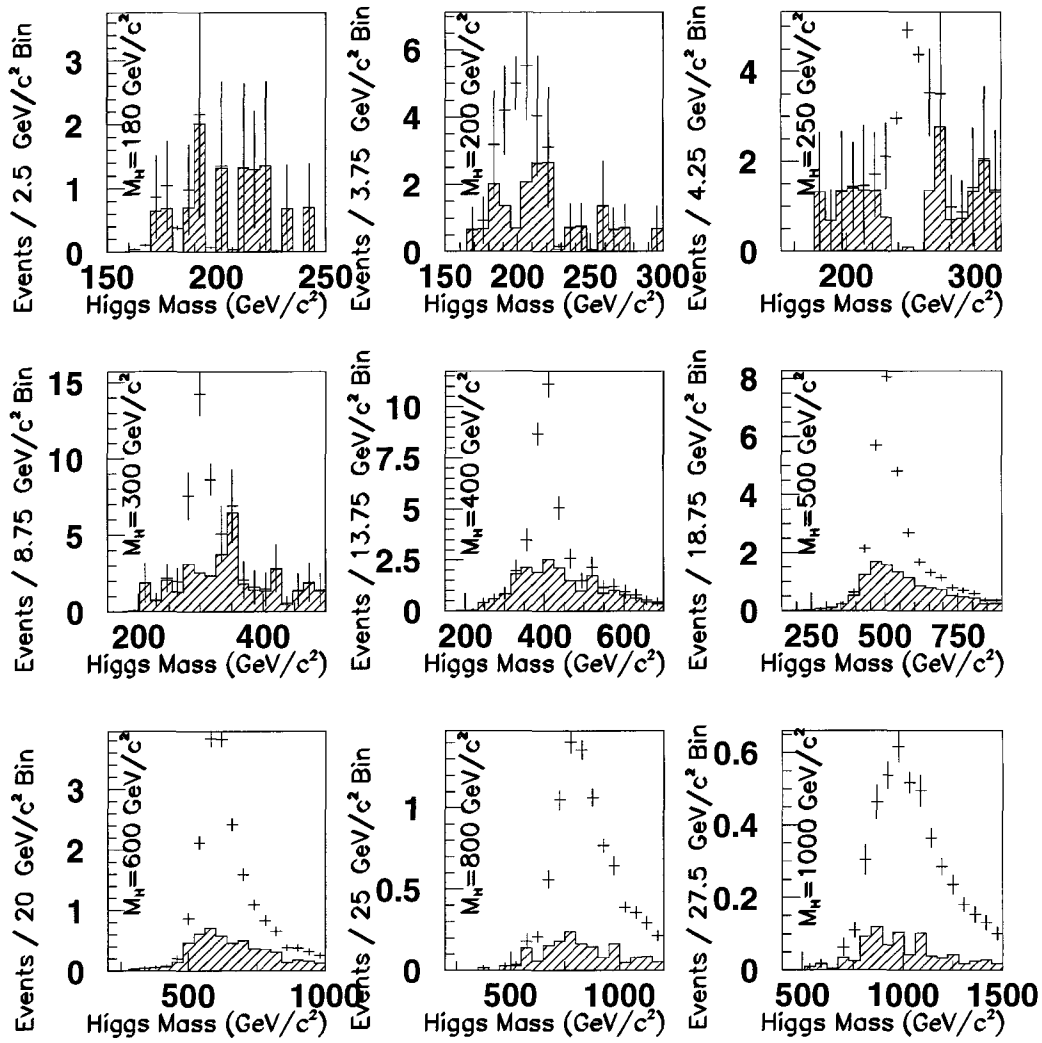
Figure 4.40: Higgs Reconstructed Mass peaks for the channel H→ZZ→lljj with an integrated luminosity of 30 fb^{-1}. Pileup has not been included. The histogram gives the expected number of background events, the data points are the expected number of signal and background events.

133
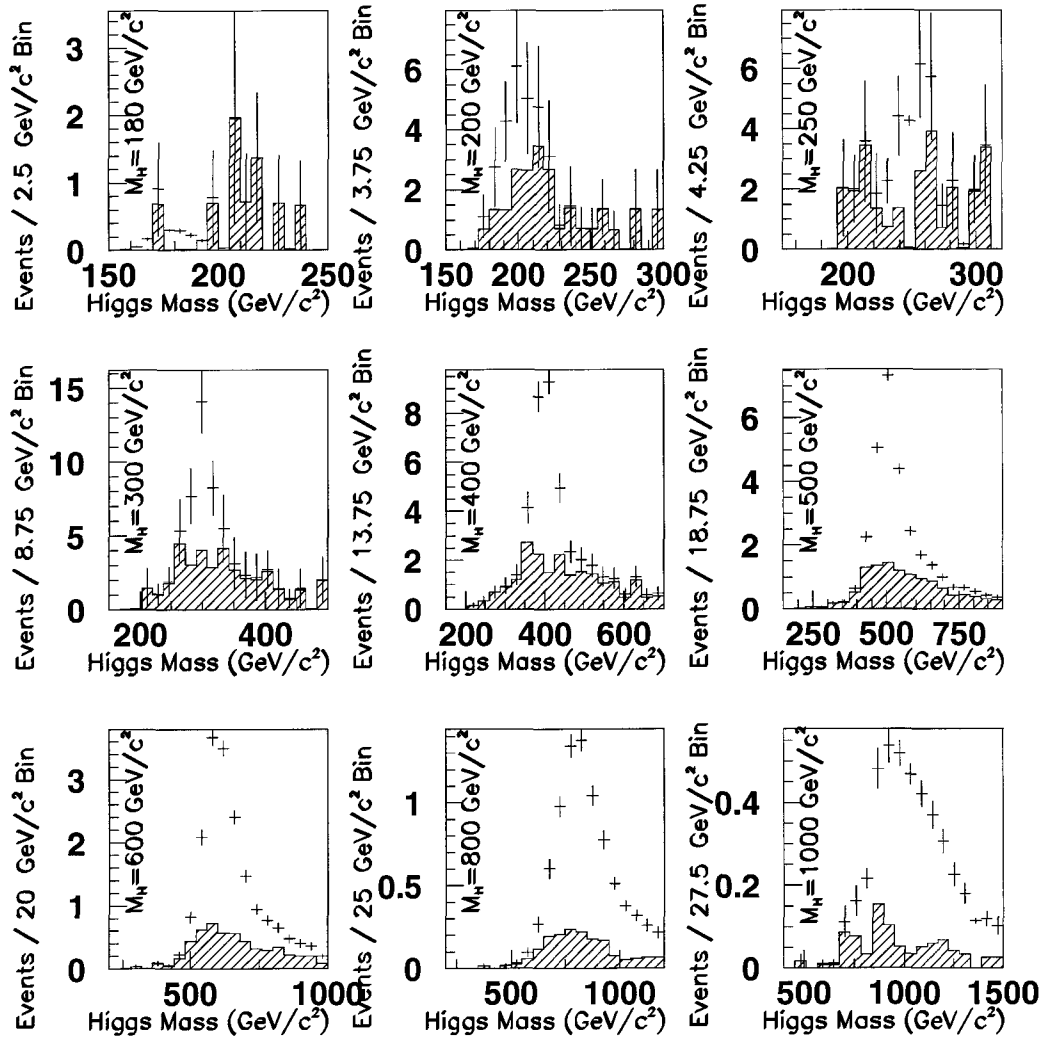
Figure 4.41: Higgs Reconstructed Mass peaks for the channel H→ZZ→lljj with an integrated luminosity of 30 fb⁻¹. Low luminosity pileup has been included. The histogram gives the expected number of background events, the data points are the expected number of signal and background events.

134
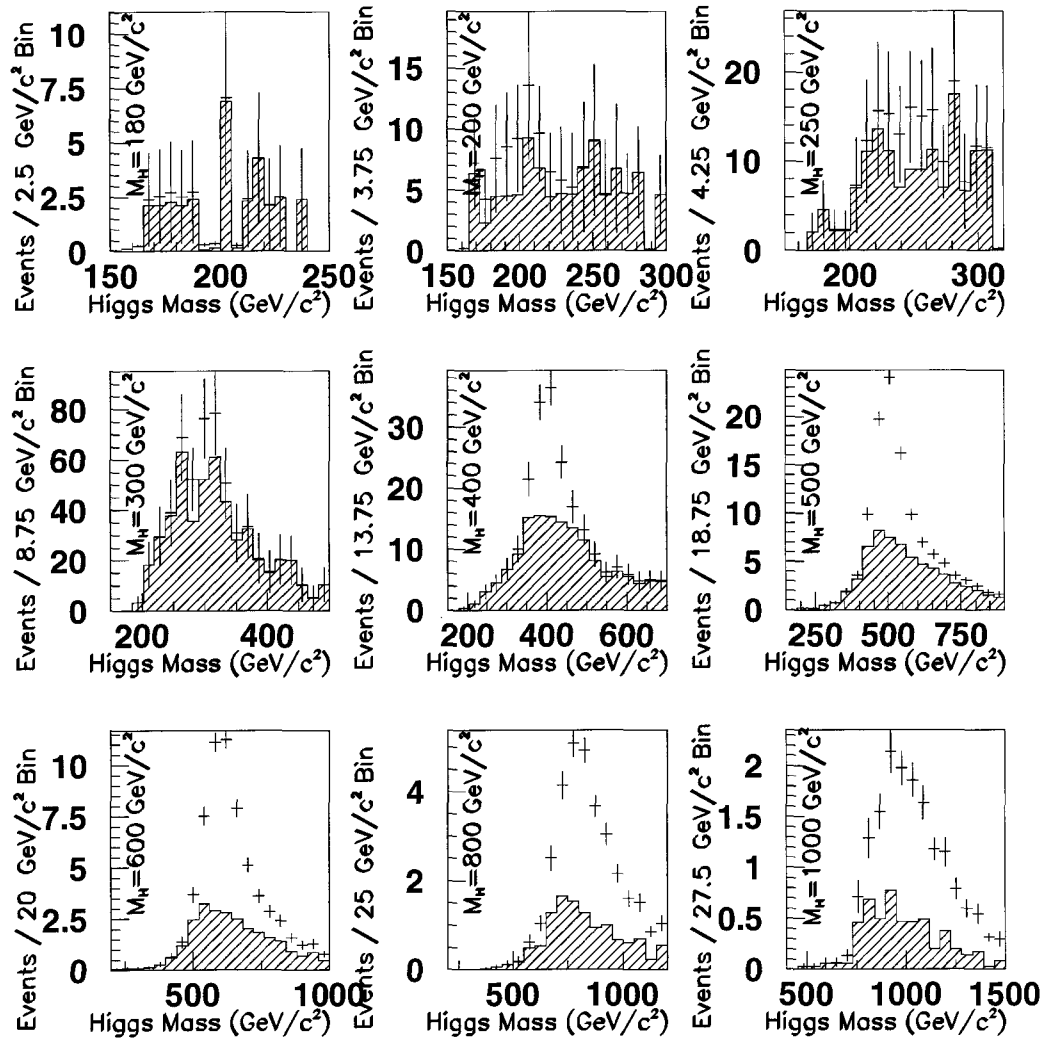
Figure 4.42: Higgs Reconstructed Mass peaks for the channel H→ZZ→lljj with an integrated luminosity of 100 fb^{-1}. High luminosity pileup has been included. The histogram gives the expected number of background events, the data points are the expected number of signal and background events.

135

Chapter 5

H→WW Event Reconstruction

This chapter will discuss the reconstruction of a Higgs boson produced by vector boson fusion and decaying through the charged vector boson channels:

$$H \to W^+W^- \begin{cases} W^+W^- \to & e^{\pm}\nu_e jj \\ W^+W^- \to & \mu^{\pm}\nu_\mu jj \end{cases} \tag{5.1}$$

The signal, whose Feynman diagram is given in figure 5.1, is characterized by:

- 1 central high P_T charged lepton.

- Large missing E_T ($\not{E}_T$).

- Two central high P_T hadronic jets.

- Two highly energetic tagging jets (typically $|\eta| \geq 2$), one in the forward and one in the backward direction.

- Minimal hadronic activity in the central region (typically $|\eta| \leq 2$).
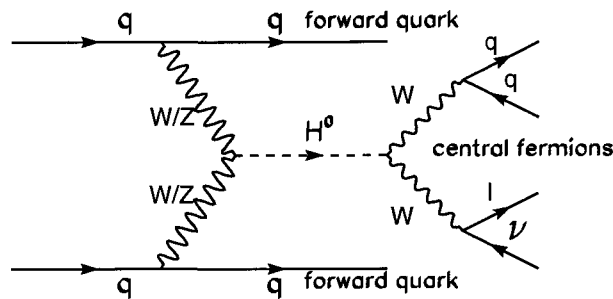
Figure 5.1: The Higgs signal is characterized by two high P_T central jets with a combined mass M_Z, a high P_T charged lepton and large missing E_T. It also has 2 energetic tagging jets.

The predominant backgrounds for the H→WW→lνjj signal are :

136

- p+p→$W^{\pm}$ + jets. This process has the largest cross section, in some cases 10^7 times greater than the signal, but has on average low event P_T and a small number of jets.

- The irreducible background, q+q̄, g+g→W^++W^-. This process has the high P_T nature of the signal but with a small cross section and no tagging jets (at tree level) these events can easily be reduced.

- tt̄ production: The top quarks decays via t→Wb. One W boson decays hadronically and the other leptonically. The central topology of this background is usually more active than the signal since the b-jets from the top decays are emitted centrally. Limiting the number of jets in the central region will reduce this background.

- Electroweak(EW) single top production[70]: t-channel fusion of a W boson coming from one proton and a gluon coming from the other produces a top/bottom quark pair.

The Feynman diagrams for these background processes are given in figure 4.2.

EW single top production has a cross section which is a factor of 2.5 below that of the tt̄ process. Single top production also has fewer jets than the tt̄ channel and a lower P_T event signature. Using the cuts that are outlined later in this chapter we found that the rate at which single top events passed the analysis cuts (at M_H=170 GeV/c^2) was an additional factor of 4 below the tt̄ events, for a net reduction factor of[1] 10. As the Higgs mass is increased the discrepancy increased as well, to a net reduction of 20 by M_H=500 GeV/c^2. Electroweak single top production is not considered a significant background and therefore not evaluated further. The Z+jets process could also be a background to the H→WW channel provided one lepton escapes detection. The Z+jets cross-section is roughly 4 times lower than the W+jets cross-section. Secondly, only one-quarter of these events loose a lepton outside the detection region, giving a reduction by a factor of 16 versus the dominant W+jets background. Therefore instrumental Z+jets is not considered as a background for this physics channel.

The decay widths of the Higgs to the vector bosons are:

$$
\begin{aligned}
\Gamma_{H \to ZZ} &= \frac{g^2}{128\pi} \frac{m_H^3}{m_W^2} \sqrt{1 - x_Z}(1 - x_Z + \frac{3}{4}x_Z^2) \\
\Gamma_{H \to WW} &= \frac{g^2}{64\pi} \frac{m_H^3}{m_W^2} \sqrt{1 - x_W}(1 - x_W + \frac{3}{4}x_W^2)
\end{aligned}
\tag{5.2}
$$

where x_Z=4$\frac{m_Z^2}{m_H^2}$ and x_W=4$\frac{m_W^2}{m_H^2}$. The widths for H→Z^0Z^0 and H→W^+W^- have similar form but the WW width is larger by a factor of two due to the degeneracy of the final decay

---

[1]At low Higgs boson masses, the W+jets background is dominant over the tt̄ background so a factor of 10 is significant.

Process	Higgs Mass (GeV/c^2)	PYTHIA ISUB Process	Cross Section (mb)
H→WW→lνjj (l=e,μ)	200	123/124	2.618×10^{-10}
	600	123/124	2.978×10^{-11}
	1000	123/124	8.163×10^{-12}
W+jets→lν+jets	-	16/31	3.845×10^{-5}
ff→WW→lνjj	-	25	1.027×10^{-8}
t$\bar{\text{t}}$ →WbWb→(jj b+lν b)	-	81/82	5.932×10^{-8}
EW single top production(gW→tb)		83	2.261×10^{-8}

Table 5.1: The cross section for the charged vector boson channel, calculated using PYTHIA 6.227. For this analysis the top mass was set to 175 GeV/c^2.

products in the H→Z^{0}Z^0 decay. Further, the branching fraction of W→ $l^{\pm}\nu$ is 3 times larger than Z→ ll. These factors give a larger cross-section for the H→WW physics channel versus the equivalent mass H→ZZ channel. The cross-sections for the important physics processes are given in table 5.1.

To reduce the number of events that need to be generated precuts were applied. The number of jets and and leptonic pseudorapidity distribution for two different signal masses are compared to the W+jets and the t$\bar{\text{t}}$ backgrounds in figure 5.2. Figure 5.2(b) shows that the lepton from the t$\bar{\text{t}}$ background process is emitted centrally, similar to a Higgs event with mass M$_H$=200 GeV/c^2. The number of jets present in this background is greater than either the Higgs signal or the W+jets background.

For the W→ $\mu^{\pm}\nu_{\mu}$ channels we require one muon/anti-muon in the pseudorapidity region $|\eta|$ <2.7 and one reconstructed jet (5 GeV/c initiator and 5 GeV/c jet E$_T$ cut). Similarly for the W→ $e^{\pm}\nu_e$ channels we require one electron/positron with pseudo-rapidity $|\eta|$ <2.5 and one jet. The precut efficiency as a function of Higgs boson mass and the CKIN(3) cut is given in figure 5.3. These precut rates are notably higher than the case for ZZ (figure 4.4) since we are requiring only one lepton in the central region. Important precut efficiencies are given in table 5.2. The pseudorapidity cut on the electron is more restrictive than the cut on the muon, due to the respective calorimetry coverage, and therefore the precut efficiencies are higher in the muon channel.

The Higgs mass range for the WW channel was broken into the three CKIN(3) parameter regions listed below :

170 GeV/c^2 < M$_H$ ≤250 GeV/c^2 CKIN(3)=0 GeV/c
250 GeV/c^2 < M$_H$ ≤500 GeV/c^2 CKIN(3)=40 GeV/c
500 GeV/c^2 < M$_H$ ≤1000 GeV/c^2 CKIN(3)=100 GeV/c

138
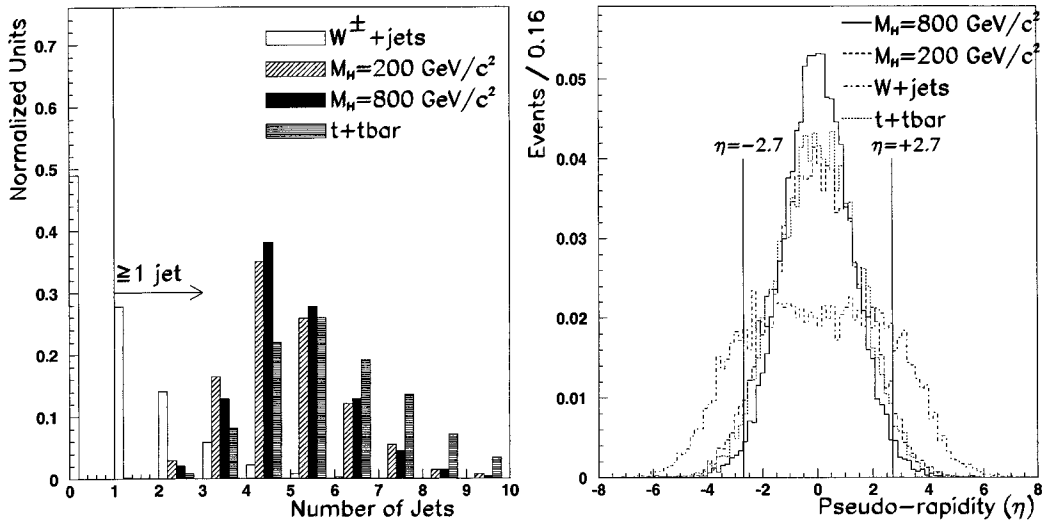
Figure 5.2: (a) The W+jets background contains fewer jets than the signal. The $t\bar{t}$ background contains more jets than the signal. To reduce the dominant background rate we require there to be ≥ 1 jet.(b) The low transverse momentum of the W-boson in the W+jets background gives a larger spread in pseudo-rapidity for the lepton. The vertical lines give the bounds of the muon detector.
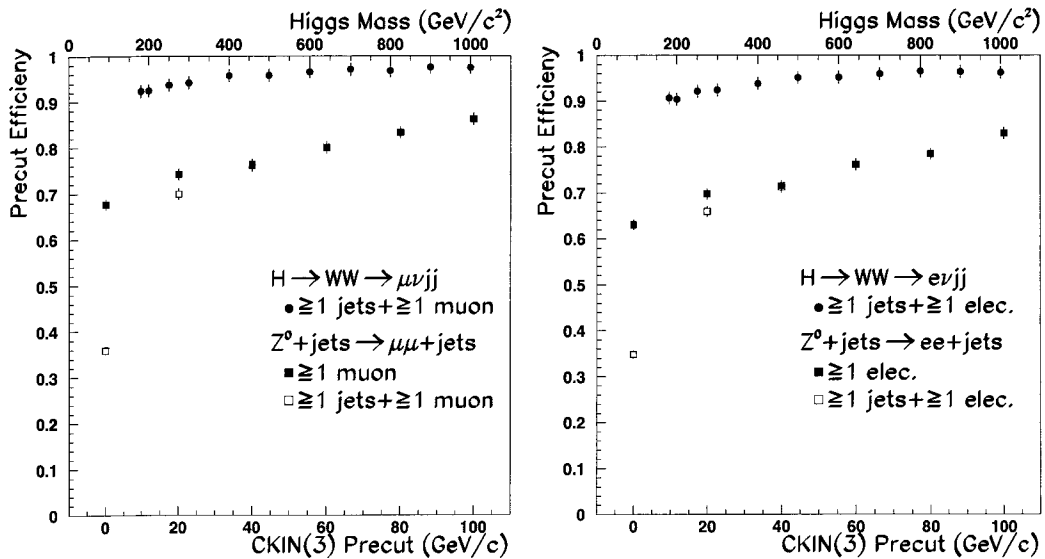
Figure 5.3: Precut efficiency as a function of Higgs boson mass (for the signal), and the CKIN(3) parameter for the W+jets channel. (a) For the muon and (b) the electron sectors.

139

Process	Electron Channel	Muon Channel
M_H=200 GeV/c^2	90.4%	92.5%
M_H=600 GeV/c^2	95.2%	96.6%
ff→WW	74.9%	79.0%
t$\bar{\text{t}}$ →WbWb	94.2%	94.8%
W$^\pm$+jets, CKIN(3)=0 GeV/c	34.8%	35.9%
W$^\pm$+jets,CKIN(3)=40 GeV/c	71.3%	76.1%

Table 5.2: Precut efficiencies for selected WW physics processes requiring 1 lepton and 1 jet.
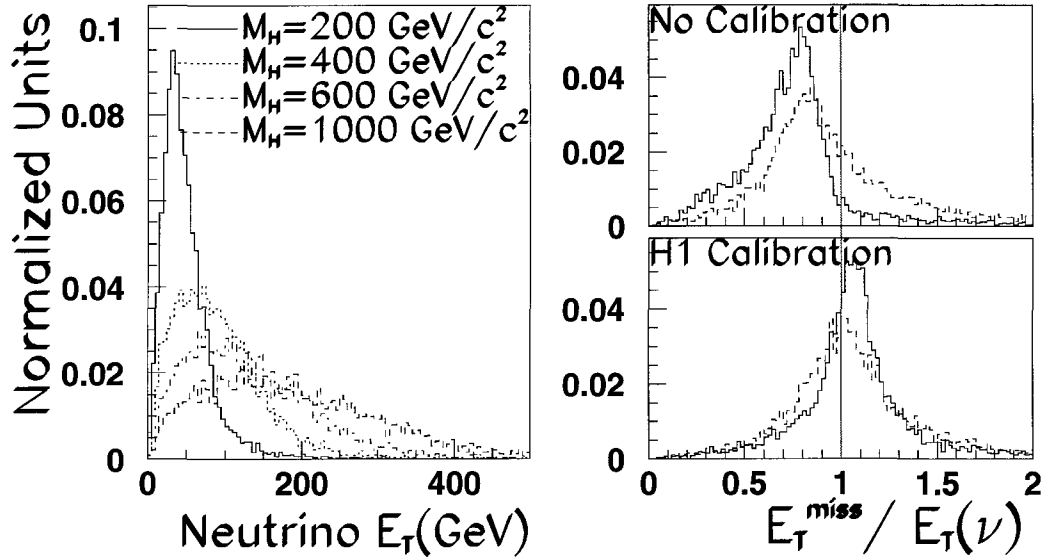
Figure 5.4: (a) The average P_T distribution of a signal neutrino. (b) The ratio of reconstructed $\not{E}_T$ to the tree level neutrino E_T value for an uncalibrated calorimeter and (c) the H1 calibrated calorimeter. The solid line is for a 1 TeV/c^2 Higgs while the dashed line is for a 200 GeV/c^2 Higgs boson.

5.1 W→ $l^\pm \nu_\mu$ Reconstruction

Reconstruction of the leptonic decay W→ $l\nu_l$ involves the identification of an isolated muon/electron, previously discussed in section 4.1, and the measurement of the event's missing transverse energy ($\not{E}_T$). The highest P_T isolated muon/electron is taken to be the signal lepton.

5.1.1 Calculation of Missing E_T

The simplest calculation of E_x^{miss}, E_y^{miss} sums up the energy measured by the calorimetry and the muon spectrometer. Conservation of momentum states that the neutrino was

140

Calorimeter	Calibration
Barrel Presampler	1.16
EM Barrel	1.16
EM Endcap	1.16
Tile Barrel	1.33
Hadronic Endcap	1.35
Forward Calorimeter	1.4
Endcap presampler	1.16

Table 5.3: H1 calibration values for ATLAS.[71]

produced in the opposite direction:

$$E_x^{miss} = \not{E}_x = -(\sum_{i=1}^{N_{cells}} E_{x,i}^{cell} + \sum_{j=1}^{N_{muons}} E_{x,j}^{spec})$$

$$E_y^{miss} = \not{E}_y = -(\sum_{i=1}^{N_{cells}} E_{y,i}^{cell} + \sum_{j=1}^{N_{muons}} E_{y,j}^{spec}) \qquad (5.3)$$

Figure 5.4(a) shows the tree level distribution of the neutrino transverse momentum as a function of Higgs boson mass. The top portion of figure 5.4(b) shows that the calculation of $\not{E}_T$ in full simulation using equation 5.3 underestimates the neutrino energy at all Higgs boson masses, indicating that neutrino production does not account for all the missing energy of the event.

The H1 weighting scheme [71] scales the energy in each calorimeter section independently in order to optimize the missing energy resolution. The default H1 calibration values are given in table 5.3. The missing transverse energy is calculated to be:

$$E_x^{miss} = -(\sum_{i=1}^{7} E_{x,i} \cdot C_i + \sum_{j=1}^{N} P_{x,j}^{spec})$$

$$E_y^{miss} = -(\sum_{i=1}^{7} E_{y,i} \cdot C_i + \sum_{j=1}^{N} P_{y,j}^{spec}) \qquad (5.4)$$

where $E_{x,i}$ is the x component of the energy in the ith calorimeter and C_i is the appropriate H1 calibration factor from table 5.3. This approximation assumes that the energy loss is independent of the event energy scale. The bottom portion of figure 5.4(c) shows that the H1 calibration method can improve the reconstruction of the transverse momentum of a neutrino arising from the Higgs boson decay.

While the H1 method is the accepted calibration scheme it is not used in this thesis since it deals strictly with calorimeter sections. However, the addition of electronic noise and pileup is done at the cell level. Reducing the noise due to these effects requires cuts that are placed at the cell level. The goal of the next section is to outline a cellular level

141

reconstruction method that provides a neutrino resolution equivalent to or better than the accepted H1 method.

5.1.2 Cell level $\not{E}_T$ Reconstruction

When we determined the jet calibration factors in section 3.3 we had to consider two sources of energy loss: jet energy that falls outside the specified radius (R_0) of the jet cone ($P_T^{recon}(R>R_0)$) and energy that is lost (P_T^{miss}, also known as missing energy) in the ATLAS calorimetry due to such processes as nuclear excitation.

The true energy of a jet (P_T^{calib}) can be written as:

$$P_T^{calib} = P_T^{recon}(R < R_0) + P_T^{recon}(R > R_0) + P_T^{miss} \tag{5.5}$$

where $P_T^{recon}(R < R_0)$ is the reconstructed transverse momentum of the jet with a radius $R=R_0$.

We expect the amount of energy missing from a jet (P_T^{miss}) to be a function of the reconstructed jet energy (E_{jet}^{recon}) and pseudo-rapidity (η_{jet}):

$$P_T^{calib} = P_T^{recon} + P_T^{miss}(E_{jet}^{recon}, \eta_{jet}) \tag{5.6}$$

where P_T^{recon} is the total transverse momentum of the jet deposited in the calorimeter. We sum over all the energetic calorimeter cells in an event to obtain a measurement of E_x and E_y. However, since we've identified that there is a missing transverse energy (P_T^{miss}) component to a jet this missing energy must also be accounted for in our sum. The components of E_x and E_y not included in our original sum because of the $\not{E}_T$ components of the jets are:

$$E_x = \sum_{i=1}^{N_{jets}} P_{T,i}^{miss} cos(\phi_i)$$

$$E_y = \sum_{i=1}^{N_{jets}} P_{T,i}^{miss} sin(\phi_i) \tag{5.7}$$

where ϕ_i is the azimuthal angle of the ith jet.

The first correction to the missing energy calculation of equation 5.3 is then:

$$E_x^{miss} = -(\sum_{i=1}^{N_{cells}} E_{x,i} + \sum_{j=1}^{N_{muons}} E_{x,j}^{spec} + \sum_{k=1}^{N_{jets}} P_{T,k}^{miss} cos(\phi_k))$$

$$E_y^{miss} = -(\sum_{i=1}^{N_{cells}} E_{y,i} + \sum_{j=1}^{N_{muons}} E_{y,j}^{spec} + \sum_{k=1}^{N_{jets}} P_{T,k}^{miss} sin(\phi_k)) \tag{5.8}$$

142
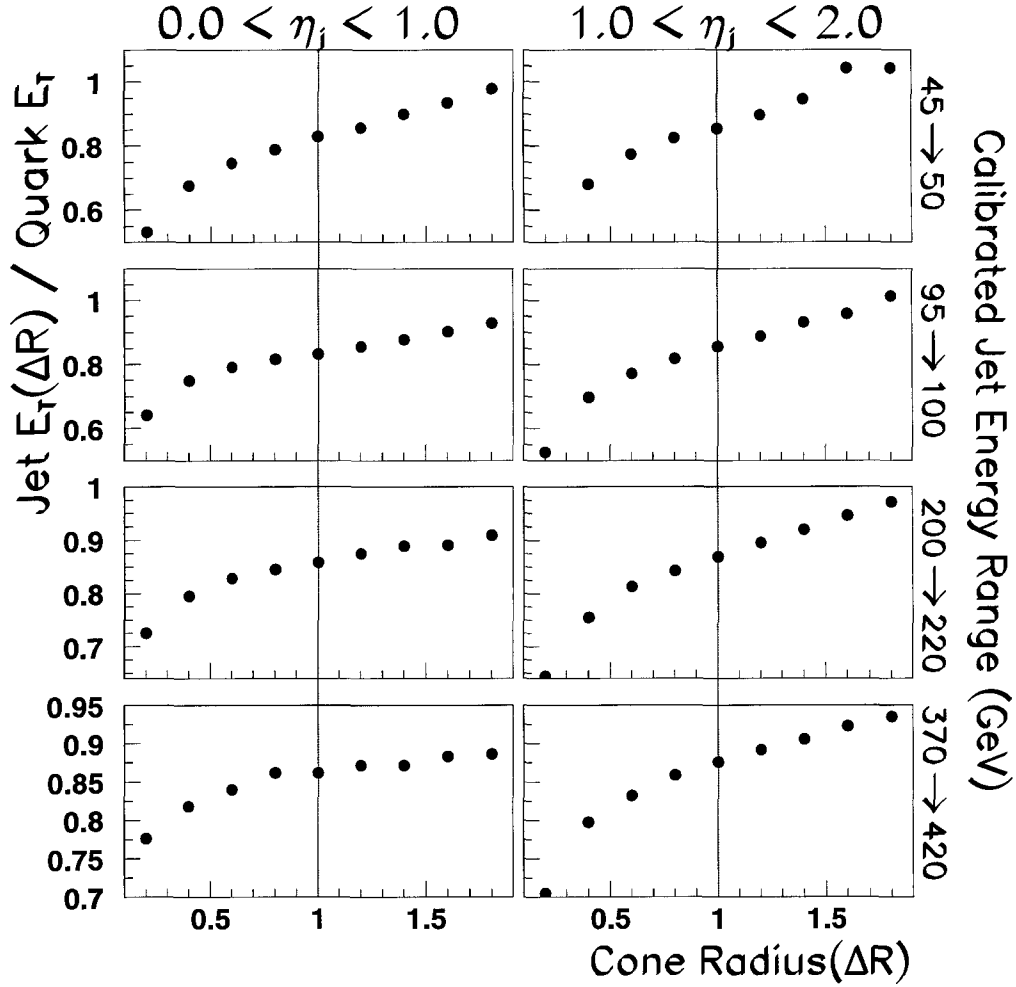
Figure 5.5: The ratio of jet energy to quark energy as a function of increasing jet radius for select calibrated jet energy ranges and pseudorapidity values.

It is important to be able to properly determine the total energy deposited in the calorimeter by a given jet and therefore accurately determine the missing energy component. As we increase the jet radius we expect the quantity $\frac{\text{Jet energy}}{\text{Quark Energy}}$ to increase and eventually plateau at some radius R_{max} that contains all the jet energy. Figure 5.5 shows the fraction of transverse energy contained in a jet of increasing radius as a function of jet energy and pseudorapidity. The transverse energy of the cones were determined using the weighting method presented in section 3.2.1. We can see that the fraction of E_T contained in the cones constantly increases with increasing radius but that at a radius of R=1.0 there is a point of inflection indicating that extra energy being added does not belong to the true jet. We choose the maximum jet radius to be R_{max}=1.0 and assume this cone contains all the measurable energy of the jet.

143
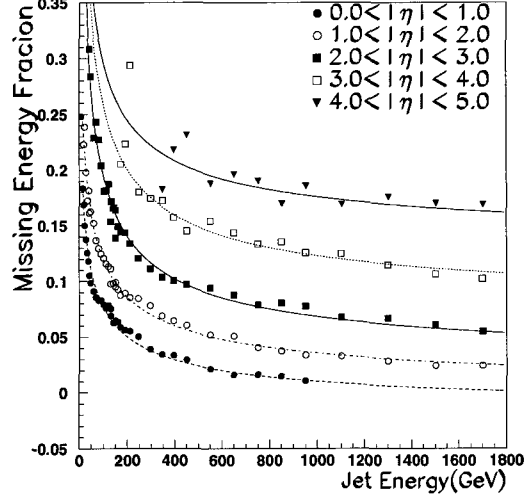
Figure 5.6: The correction to the jet calibration to find the fraction of the jet energy that is missing.

The calibrated jet transverse momentum (P_T^{calib}) is determined by a measurement[2] of $P_T^{R=0.4}$ and a calibration factor C.

$$P_T^{calib} = C \cdot P_T^{R=0.4} \tag{5.9}$$

Introducing a second calibration C_1 to determine the actual energy deposited in the calorimeter :

$$P_T^{R=1.0} = P_T^{recon} = C_1 \cdot P_T^{R=0.4} \tag{5.10}$$

Solving for the missing transverse energy

$$P_T^{miss} = (C - C_1) \cdot P_T^{R=0.4} \tag{5.11}$$

We can redefine the C_1 calibration as a correction term (X) for the jet calibration such that:

$$P_T^{miss} = (\frac{C}{X} - 1) \cdot P_T^{R=0.4} \tag{5.12}$$

where X and C are related

$$X = \frac{C}{C - \frac{P_T^{R=1.0}}{P_T^{R=0.4}} + 1} \tag{5.13}$$

Figure 5.6 plots the calibration correction (X-1) as a function of pseudo-rapidity and uncalibrated jet energy $E_{jet}^{R=0.4}$.

These curves can be fit using an equation of the form:

$$X(\eta_{jet}, E_{jet}^{R=0.4}) = A_0 + \frac{A_1}{\sqrt{E_{jet}^{R=0.4}}} + \frac{A_2}{E_{jet}^{R=0.4}} \tag{5.14}$$

---

[2]We define $P_T^{R=R_0}$ as the reconstructed transverse momentum of a jet with radius $R=R_0$.

144
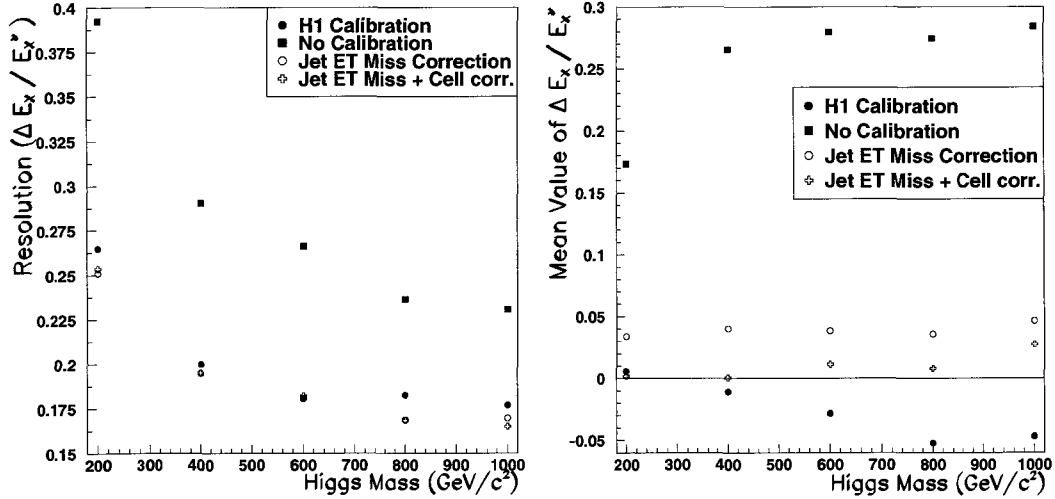
Figure 5.7: (a) The resolution, as a function of Higgs mass, of the E_x^{miss} measurement in full simulation when using different $\not{E}_T$ reconstruction methods.(b) The mean value of $\Delta E_x / E_x^\nu$ in full simulation as a function of Higgs Mass. We expect this to have a mean value of zero.

The fit parameters for this function are given in table 5.4.

Pseudo-Rapidity	A_0	A_1 $(\sqrt{GeV})$	A_2 (GeV)
0.0→1.0	0.975	1.175	-1.536
1.0→2.0	0.991	1.484	-2.016
2.0→3.0	1.010	1.832	0.00
3.0→4.0	1.061	1.965	0.00
4.0→5.0	1.120	1.751	0.00

Table 5.4: Parameterization for the correction term X in the calculation of P_T^{miss}.

To evaluate the validity of these corrections we calculated the quantity:

$$\frac{\Delta E_x}{E_x^\nu} = \frac{E_x^\nu - E_x^{miss}}{E_x^\nu} \tag{5.15}$$

where E_x^ν is the tree level neutrino value and E_x^{miss} is the reconstructed value. If the reconstruction method is correct this quantity will have a mean of 0 and a small width.

Figure 5.7(a) shows that this first order correction (equation 5.8) and the H1 calibration method (equation 5.4) have similar resolutions when measuring E_x^{miss} and that both of these methods give resolutions significantly better than the uncalibrated results (equation 5.3). Figure 5.7(b) shows that this new method tends to under-correct ($|E_x^{miss}| < |E_x^\nu|$), by about 4% at all Higgs boson masses, for the actual mean of the ratio $\Delta E_x / E_x$. The H1 Calibration method tends to increasingly over correct ($|E_x^{miss}| > |E_x^\nu|$) at heavier Higgs masses.

145

	Pseudo-Rapidity Range		
	0.0→1.5	1.5→3.2	3.2→5.0
C_η	1.2	1.15	1.3

Table 5.5: The calibration factor applied, in ATRECON, to cells that lie outside jets when calculating $\not{E}_T$.

This first correction does not change the energy deposited in the calorimeter regions that lie outside the jets. We do expect these regions to have missing energy as well. Defining two regions to the calorimeter: cells that lie inside (E^{in}, $\Delta R < 0.4$) jets and cells that lie outside (E^{out}, $\Delta R > 0.4$) we can write:

$$E_x^{miss} = -(\sum_{i=1}^{N_{cells}} E_{x,i}^{in} + \sum_{i=1}^{N_{cells}} E_{x,i}^{out} C_\eta + \sum_{j=1}^{N_{muons}} E_{x,j}^{spec} + \sum_{k=1}^{N_{jets}} P_{T,k}^{diss} cos(\phi_{jet,k}))$$

$$E_y^{miss} = -(\sum_{i=1}^{N_{cells}} E_{y,i}^{in} + \sum_{i=1}^{N_{cells}} E_{y,i}^{out} C_\eta + \sum_{j=1}^{N_{muons}} E_{y,j}^{spec} + \sum_{k=1}^{N_{jets}} P_{T,k}^{diss} sin(\phi_{jet,k})) \qquad (5.16)$$

the calibration values C_η take the values listed in table 5.5. These calibration values are *not* applied to the cells lying inside jets or around isolated muons. Figure 5.7(a) shows that this second correction improves the E_x^{miss} resolution slightly and figure 5.7(b) shows that it improves the determination of the mean value of $\Delta E_x / E_x^\nu$.

5.1.3 Resolutions in ATLFAST

In ATLFAST the missing energy is calculated as :

$$E_x^{miss} = -(\sum_{i=1}^{N_{cells}} E_{x,i} + \sum_{j=1}^{N_{muons}} E_{x,j})$$

$$E_y^{miss} = -(\sum_{i=1}^{N_{cells}} E_{y,i} + \sum_{j=1}^{N_{muons}} E_{y,j}) \qquad (5.17)$$

In ATLFAST the energy of a muon is determined by identifying and smearing the tree level value with a resolution that is dependent on the muon's transverse momentum and direction. This resolution is also dependent on electronic noise and luminosity pileup. When electronic noise and luminosity pileup are included in the simulation they are added to every cell in the ATLFAST detector, including those cells which surround the identified muon. In the determination of E_x^{miss} and E_y^{miss} (equation 5.17) we include both a cell and a muon summation. To avoid double counting we exclude cells that fall within a distance $\Delta R < 0.2$ of isolated muons from the cell level summation in equation 5.17.

In ATLFAST the mean value of $\frac{\Delta E_x}{E_x^\nu}$ is 0. Figure 5.8 compares the resolution on the measurement of E_x^{miss} between full and fast simulations. The ATLFAST calculation con-

146
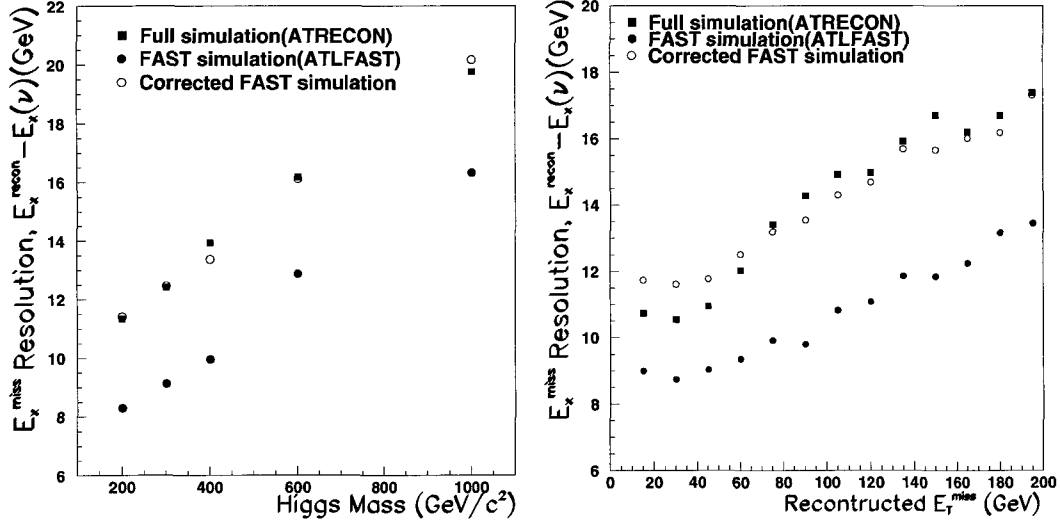
Figure 5.8: A comparison of the resolution of the E_x^{miss} parameter in full and fast simulations, in the absence of electronic noise and luminosity pileup.

Condition	ATLFAST	ATRECON
Electronic Noise	11.5 GeV	11.5 GeV
Low Luminosity Pileup	8.6 GeV	7.7 GeV
High Luminosity Pileup	24.3 GeV	22.9 GeV

Table 5.6: The full and fast simulation contributions to the width of $E_{X,Y}^{miss}$ due to electronic noise and luminosity pileup.

stantly gives a better resolution measurement to the E_x^{miss} value. A resolution correction term (σ_{corr} in GeV), is introduced to the ATLFAST measurements of E_x^{miss} and E_y^{miss}. This correction term can be written in terms of the reconstructed missing transverse energy ($E_{T,\nu}^{recon} = \sqrt{(E_x^{miss})^2 + (E_y^{miss})^2}$).

$$\sigma_{corr} = 5.88 + 0.0202 \times E_{T,\nu}^{recon} \tag{5.18}$$

This correction gives agreement between the two simulations at all Higgs boson masses and all but the very lowest neutrino transverse momentum values.

5.1.4 The effects of Electronic Noise and Pileup

The resolutions discussed in the previous section have been determined in the absence of electronic noise (section 3.1.1) and luminosity pileup (section 3.1.2). However, each of these processes make a significant contribution to the resolution of the $E_x^{miss}(\not{E}_x)/E_y^{miss}(\not{E}_y)$ measurements. The contribution to the width of $\not{E}_x$ from the addition of electronic noise and luminosity pileup in full and fast simulations are compared in table 5.6. The values quoted

147
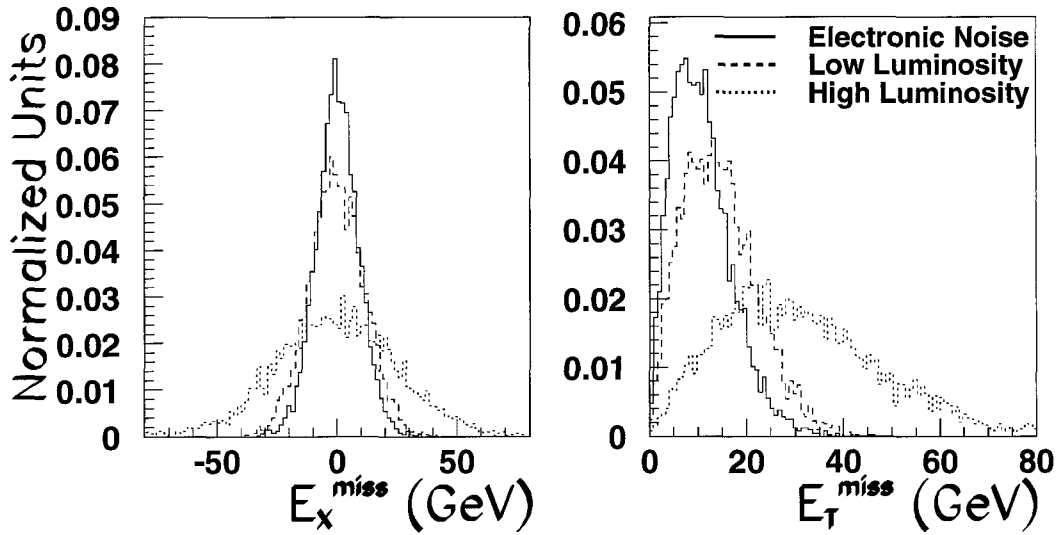
Figure 5.9: (a) The value of E_X^{miss} when only electronic noise or luminosity pileup is added to the calorimetry. (b) Finite widths to E_X^{miss} and E_Y^{miss} from just electronic noise and just luminosity pileup can produce a large $\not{E}_T$ measurement.

for full simulation include the correction factors introduced in section 5.1.2. The fast simulation resolutions have not been adjusted. We have agreement to within 1.5 GeV between both simulation programs.

Figure 5.9(b) plots the calculated $\not{E}_T$ introduced by pileup alone and by electronic noise alone. To optimize the resolution of E_x^{miss} and E_y^{miss} we introduce an asymmetric transverse energy cut on the calorimeter cells. Electronic noise is assumed to be Gaussian introducing equal amounts of positive and negative energy in any given cell with a full width half maximum (FWHM) following the distribution in figure 3.2. Assuming that the minimum bias energy is uniformly distributed around the calorimeter the average amount of energy in a positive cell is going to be larger than the average amount of energy in a negative cell due to the different maximum and minimum weightings of the bipolar shaping functions; originally shown in figure 2.14 their exact values are found in appendix B. The three different shaping functions used for this analysis and their corresponding pseudo-rapidity regions are :

- $0.0 < |\eta| < 1.5$ Hadronic LAr (HADLAR) calorimeter weighting.

- $1.5 < |\eta| < 3.2$ EM LAr calorimeter weighting.

- $3.2 < |\eta| < 5.0$ FCAL2 weighting function.

The weighting function for the HADLAR calorimeter has a maximum positive weight (W_p) of +1.00 and a maximum negative weight (W_n) of -0.23. The EM LAr is similar with a positive weight of 1.00 and a negative weight -0.19. The FCAL2 shaping function has a

148

maximum value of +1.0 and a minimum value of -0.56. Cell cuts introduced to reduce the pileup therefore need to be weighted asymmetrically. We define a positive transverse energy cut (E_T^+) and a negative transverse energy cut (E_T^-):

$$E_T^+(\eta) = \sqrt{(N_P|W_p|\sigma_P)^2 + (N_E\sigma_E)^2}$$
$$E_T^-(\eta) = \sqrt{(N_P|W_n|\sigma_P)^2 + (N_E\sigma_E)^2} \qquad (5.19)$$

where σ_E is the width of the electronic noise term σ_P is a measure on the average amount of energy deposited by a minimum bias event. N_P and N_E are positive numbers that minimize the effects of the electronic noise and luminosity pileup. For a cell to be included in the determination of $\not{E}_T$ it must either possess an E_T greater than E_T^+ or less than E_T^-.

On average, in ATLFAST, a single minimum bias event deposits approximately 0.47 GeV of transverse energy into any one cell. Due to the shower spreading in the calorimetry full simulation only deposits about 0.22 GeV E_T per cell. These numbers correspond to the σ_P values in equation 5.19. The σ_E quantity is the Gaussian width of the electronic noise in figure 3.2 and equation 3.1. The choices of N_P, N_E are optimized in full simulation and the values used for the ATLFAST analysis are chosen to give similar $\not{E}_x$ resolutions.

To determine which values of N_E and N_P optimize the $\not{E}_x$ measurement two different running conditions were investigated. First electronic noise was turned on (pileup was off) and the value of N_E was changed. Secondly, electronic noise was turned off and pileup was investigated. As the Higgs boson mass is increased the natural width of the Higgs is going to limit the benefits of these cell level cuts. Therefore the optimal cut values were chosen such that they optimized the $\not{E}_x$ measurement for a Higgs boson of mass 200 GeV/c^2. Figure 5.10(a) shows that setting N_E=3 is optimal for reducing the contributions to the width from electronic noise. The top portion of figure 5.10(b) shows that there is no improvement when introducing an asymmetric cell cut during low luminosity running (N_P=0), but N_P=3 is best at high luminosity.

For the full simulation component of this analysis we choose a 3 σ_E and 0 σ_P at low luminosity (N_E=3, N_P=0), and a 3 σ_E and 3 σ_P at high luminosity. The corresponding values in ATLFAST are : $3\sigma_E$ and 0 σ_P at low luminosity, and a 3 σ_E and 5 σ_P at high luminosity. In the final analysis no cell level cuts were applied when calculating $\not{E}_T$ in the absence of pileup.

Table 5.7 compares the $\not{E}_x$ resolutions obtained using full and fast simulations at different Higgs boson masses and different luminosity settings. The values in table 5.7 are the FWHM of a Gaussian fit to the value $E_x^{miss}(recon) - E_x^\nu$, where $E_x^{miss}(recon)$ is the reconstructed

149
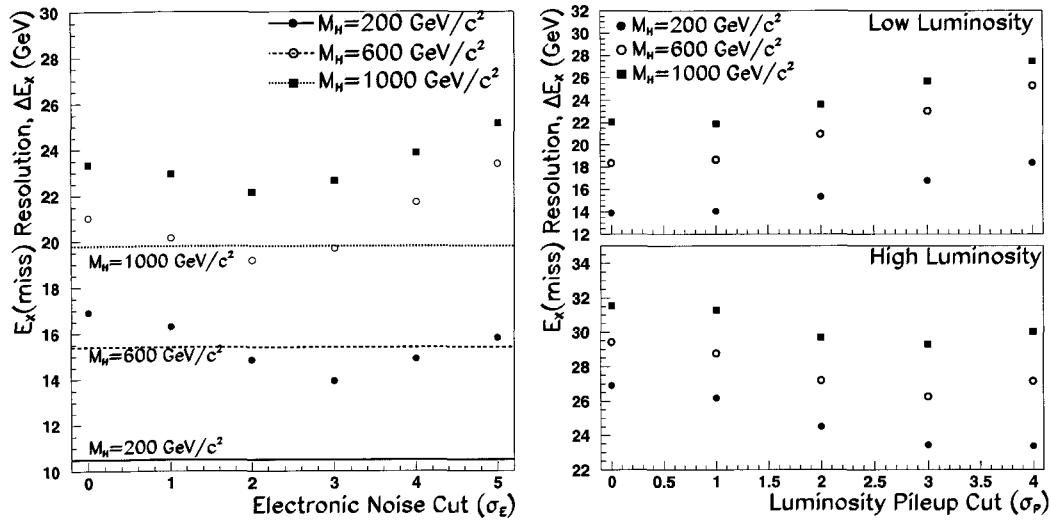
Figure 5.10: The missing energy measurement of $\not{E}_x$ can be improved in the presence of (a) both electronic noise and (b) low and (c) high luminosity by placing cell level cuts. The horizontal lines in (a) give the inherent resolution without electronic noise or pileup.

Pileup	Setting	ATRECON			ATLFAST		
		200	600	1000	200	600	1000
		(GeV/c^2)			(GeV/c^2)		
None	No e-Noise	10.5	15.3	19.8	11.3	16.0	19.9
Low	No e-Noise	13.9	18.4	22.1	14.8	18.5	21.4
	w/ e-Noise	18.7	22.5	25.4	19.3	22.2	25.6
	Cell Cuts	16.2	19.6	24.0	15.8	19.0	22.5
High	No e-Noise	26.9	29.4	31.6	27.3	29.8	31.5
	w/ e-Noise	28.6	30.7	33.6	29.1	31.5	33.4
	Cell Cuts	23.0	28.4	30.0	25.2	28.3	30.6

Table 5.7: A comparison of $\not{E}_x$ resolution between the full and fast simulations.

150

value and E_x^ν is the tree level neutrino value. We have agreement between the full and fast simulations to within approximately 2 GeV at the luminosity and mass settings investigated.

5.1.5 Determination of E_Z^{miss}

A neutrino passes through the ATLAS detector without interacting and in doing so produces the recognizable "missing energy" signature. The missing transverse energy can be determined using the methods discussed in the previous section. The longitudinal momentum is not known and must be calculated. Given that the 4-momentum of the leptons are:

$$
\begin{aligned}
P_\mu(l) &= (E_l, P_{lx}, P_{ly}, P_{lz}) \\
P_\mu(\nu) &= (\sqrt{E_{\nu x}^2 + E_{\nu y}^2 + E_{\nu z}^2}, E_{\nu x}, E_{\nu y}, E_{\nu z})
\end{aligned}
\tag{5.20}
$$

The 4-momentum of the original W boson is calculated as:

$$
W_\mu = P_\mu(l) + P_\mu(\nu)
\tag{5.21}
$$

with the invariant mass being

$$
M_W^2 = (P_\mu(l) + P_\mu(\nu))(P^\mu(l) + P^\mu(\nu))
\tag{5.22}
$$

Assuming that the neutrino comes from a W-boson with a mass M_W=80.41 GeV/c^2, the solution for the longitudinal neutrino momentum ($E_{\nu z}$) is a quadratic:

$$
\begin{aligned}
0 = \ & 4(E_l^2 - P_{lz}^2)E_{\nu z}^2 \\
& -(4P_{lz})((M_W^2 - M_l^2 - M_\nu^2) + 2(P_{lx}E_{\nu x} + P_{ly}E_{\nu y}))E_{\nu z} \\
& +(4(E_l^2)(E_{\nu x}^2 + E_{\nu y}^2) - ((M_W^2 - M_l^2 - M_\nu^2) + 2(P_{lx}E_{\nu x} + P_{ly}E_{\nu y}))^2)
\end{aligned}
\tag{5.23}
$$

The quadratic gives two solutions to the longitudinal momentum ($E_{\nu z}$),

$$
E_{\nu z} = \frac{1}{2P_{t,l}^2}[P_{z,l}(M_W^2 - M_l^2 + 2\vec{P}_{t,l} \cdot \vec{P}_{t,\nu}) \pm E_l\sqrt{(M_W^2 - M_l^2 + 2\vec{P}_{t,l} \cdot \vec{P}_{t,\nu})^2 - 4P_{t,\nu}^2 P_{t,l}^2}]
\tag{5.24}
$$

where M_l is the mass of the charged lepton. The neutrino is expected to be produced centrally, so the $E_{\nu z}$ solution with the minimum absolute value has been chosen. It also more closely recreates the P_Z distribution of the tree level neutrino as shown in figure 5.11.

We cannot use this method to reconstruct Higgs decays of the form H→WW* since the W* is produced off mass shell and our assumption of M_W=80.41 GeV/c^2 is invalid. The WW channel in this analysis only extends to a minimum Higgs mass of 170 GeV/c^2, 10 GeV/c^2 about the 2 M_W threshold. Figure 5.12 shows the tree level invariant mass (determined using PYTHIA 6.227) of the leptonically decaying W at Higgs boson masses near the 2 M_W threshold.
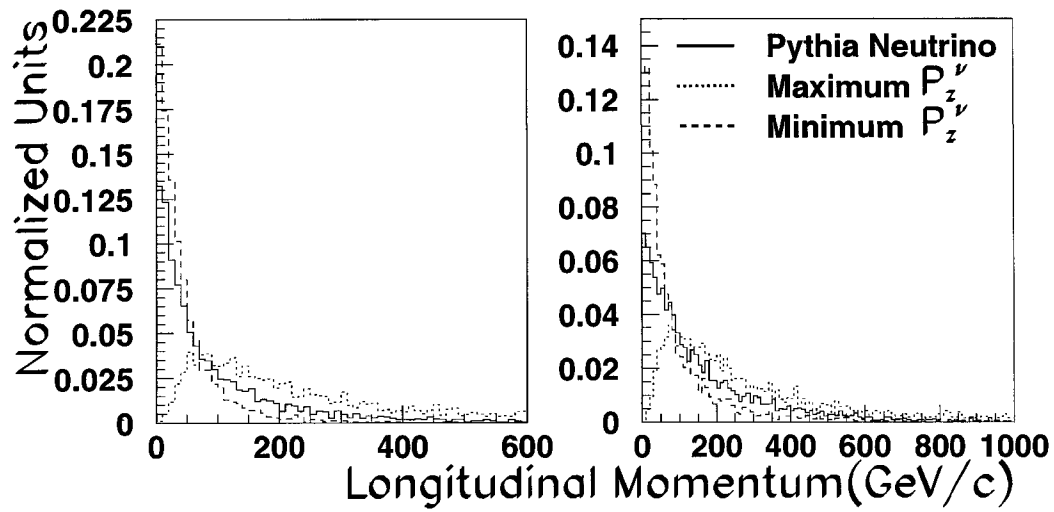
Figure 5.11: The solution to the quadratic with the minimum value of P_z is shown to provide better agreement with the true neutrino value (a) M_H=200 GeV/c^2 (b) M_H=600 GeV/c^2 .
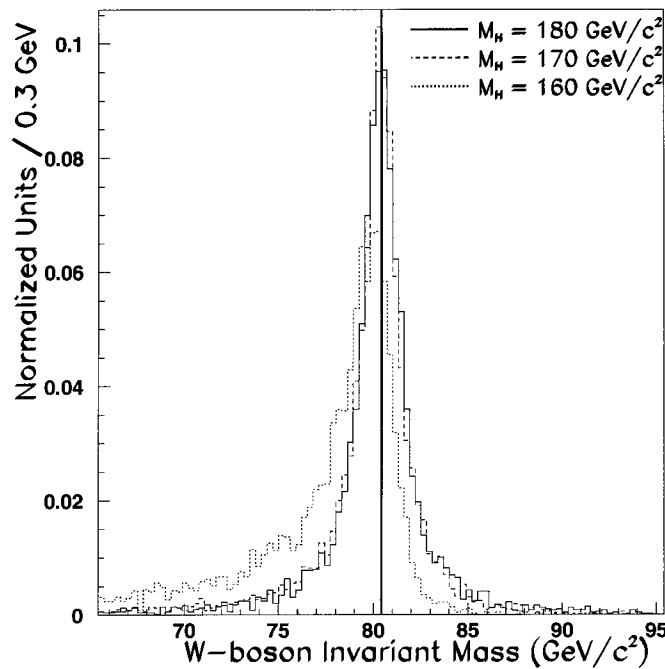
Figure 5.12: For a Higgs boson mass below the $2M_W$ mass threshold the invariant mass of the W shifts off the M_W peak and a low mass tail becomes emphasized.

152
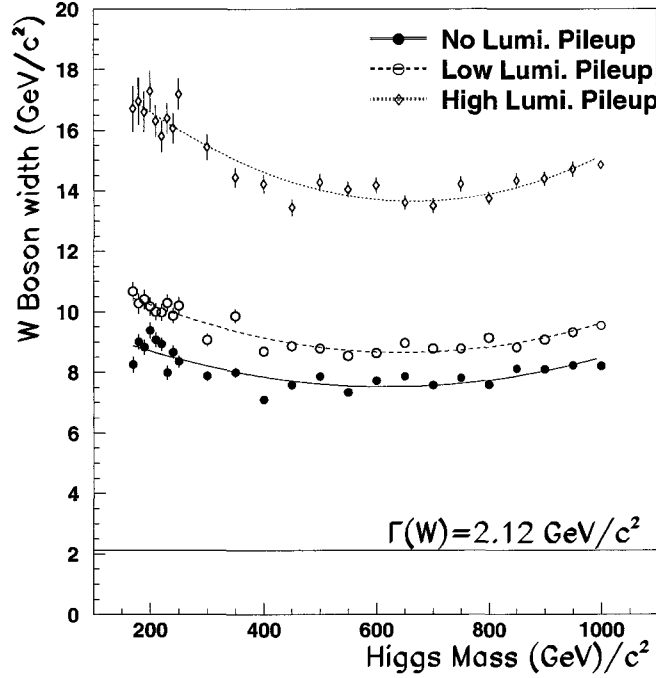
Figure 5.13: The width of the reconstructed hadronic W as a function of Higgs mass and luminosity. Electronic noise has been included.

5.2 W→ jet+jet reconstruction

Using the same reconstruction method outlined in section 4.2 but instead choosing the pair with mass closest to M_W=80.41 GeV/c² we can reconstruct the hadronic decay W→jj. Ensuring that the jets can be matched to the initial quarks the resolution of the reconstructed hadronic W is shown in figure 5.13 and parameterized in equation 5.25.

$$
\begin{aligned}
\text{No Pileup} \quad & \Gamma(M_W) && = 10.1 - 0.834 \times 10^{-2} M_H + 0.672 \times 10^{-5} M_H^2 \\
\text{Low Luminosity} \quad & \Gamma(M_W) && = 11.9 - 0.101 \times 10^{-1} M_H + 0.781 \times 10^{-5} M_H^2 \qquad (5.25)\\
\text{High Luminosity} \quad & \Gamma(M_W) && = 19.7 - 0.180 \times 10^{-1} M_H + 0.135 \times 10^{-4} M_H^2
\end{aligned}
$$

5.3 Higgs Reconstruction

Once both the hadronic and leptonic W-decays have been identified the 4-momentum of the Higgs boson can be calculated simply as :

$$
P^\mu_{Higgs} = P^\mu_{W_{hadron}} + P^\mu_{W_{lepton}} \qquad (5.26)
$$

For a Higgs boson that has been properly identified, that is to say the charged lepton and jets can be associated with their tree level particles (within a separation $\Delta R \leq 0.2$) the width of the Higgs can be approximated by a Gaussian. We don't force the direction of the

153
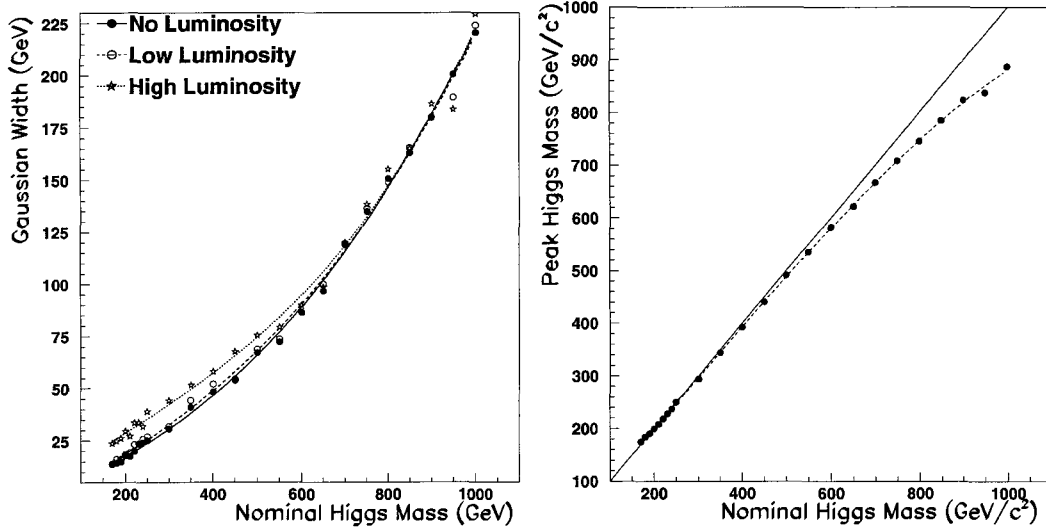
Figure 5.14: (a)The Gaussian width of the Higgs (WW channel, without cell cuts applied) as a function of the nominal Higgs boson mass.(b) As the Higgs mass increases the Higgs mass peak shifts of the nominal value.

neutrino to correspond with the tree level direction as the reconstructed direction of the neutrino is not cleanly defined. The Gaussian width as a function of mass and luminosity is shown in figure 5.14(a).

No Pileup $\quad \Gamma(H^0) = 1.47 + 0.537 \times 10^{-1} M_H + 0.134 \times 10^{-3} M_H^2 + 0.315 \times 10^{-7} M_H^3$

Low Lumi. $\quad \Gamma(H^0) = -2.172 + 0.876 \times 10^{-1} M_H + 0.768 \times 10^{-4} M_H^2 + 0.570 \times 10^{-7} M_H^3$

High Lumi. $\quad \Gamma(H^0) = 1.53 + 0.143 M_H - 0.664 \times 10^{-4} M_H^2 + 0.144 \times 10^{-6} M_H^3$

$$(5.27)$$

The values given in equation 5.27 are for events without the cell level cuts. We saw in section 5.1.4 that placing a cut on the transverse momentum of the cells improves the neutrino energy resolution. This improvement in neutrino energy resolution also improves the resolution on the Higgs mass. This improvement is shown in figure 5.15 with the new Higgs width parameterizations given in equation 5.28.

Low Lumi. $\quad \Gamma(H^0) = 2.95 + 0.449 \times 10^{-1} M_H + 0.153 \times 10^{-3} M_H^2 + 0.140 \times 10^{-7} M_H^3$

High Lumi. $\quad \Gamma(H^0) = 8.33 + 0.827 \times 10^{-1} M_H + 0.562 \times 10^{-4} M_H^2 + 0.684 \times 10^{-7} M_H^3$

$$(5.28)$$

The Breit-Wigner curve describing the Higgs Boson resonance is convoluted with the reduced Higgs production cross-section (figure 1.2) at heavier Higgs boson masses. This asymmetric weighting causes the mean of the Higgs boson mass curve to shift off the nominal value (M_H) as shown in figure 5.14(b). The location of the shifted peak can be fit using equation 5.29.

$$M_H^{peak} = 16.8 + 0.873 M_H + 0.289 \times 10^{-3} M_H^2 - 0.299 \times 10^{-6} M_H^3 \qquad (5.29)$$

154
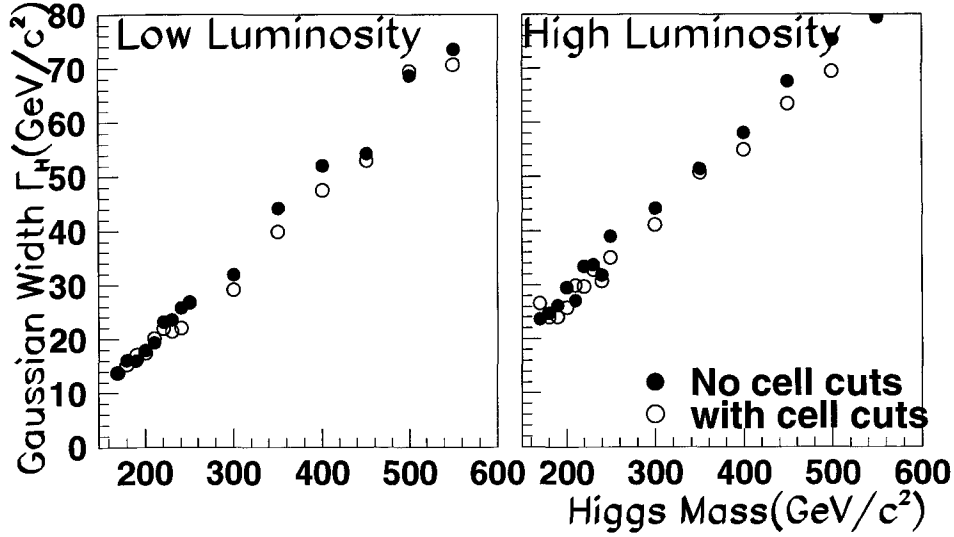
Figure 5.15: The improvement in the measured Higgs width for (a) Low Luminosity and (b) High luminosity. The closed circles indicate the Gaussian width without applying any cuts. The open circles give the measured width after applying the asymmetric cell level transverse energy cuts.

5.4 Optimization of Cuts

This section will address the cuts that are applied to our H$\rightarrow$ W^+W^- analysis. The optimal cuts on the first three steps have been determined in the absence of pileup and with a cut on the mass window of the W$\rightarrow$jj decay of ±15 GeV/c^2 .

5.4.1 Central Cuts

Step 1: The first variable optimized in the H$\rightarrow$ W^+W^- analysis is the cut on the transverse momentum of the reconstructed W-bosons. Two different types of cuts were investigated. The first approach placed separate cuts on $P_T^{W\rightarrow jj}$ and $P_T^{W\rightarrow l\nu}$. As was the case in section 4.5.1 we also investigated a cut on $P_T^{pair}=\sqrt{(P_T^{W\rightarrow jj})^2 + (P_T^{W\rightarrow l\nu})^2}$. The normalized distributions of these quantities are plotted in figure 5.16 and the optimal values for these cuts are given in table 5.8. Figure 5.17 shows that for Higgs boson masses equal to or below 600 GeV/c^2 the cut on P_T^{pair}, versus the separate cuts on $P_T^{W\rightarrow jj}$ and $P_T^{W\rightarrow l\nu}$, gives the greatest improvement in significance.

Step 2: The background can be further reduced by placing a cut on the angular separation (ΔR_{jj}) of the two jets from the decay W$\rightarrow$jj, and the azimuthal angle ($\Delta\phi_{l\nu}$) between the lepton and the reconstructed neutrino direction. These hadronic and leptonic separations are graphed in fig 5.18 with the optimal cut values listed in table 5.9. Figure 5.18

155

M_H=200 GeV/c² M_H=400 GeV/c² M_H=1000 GeV/c²
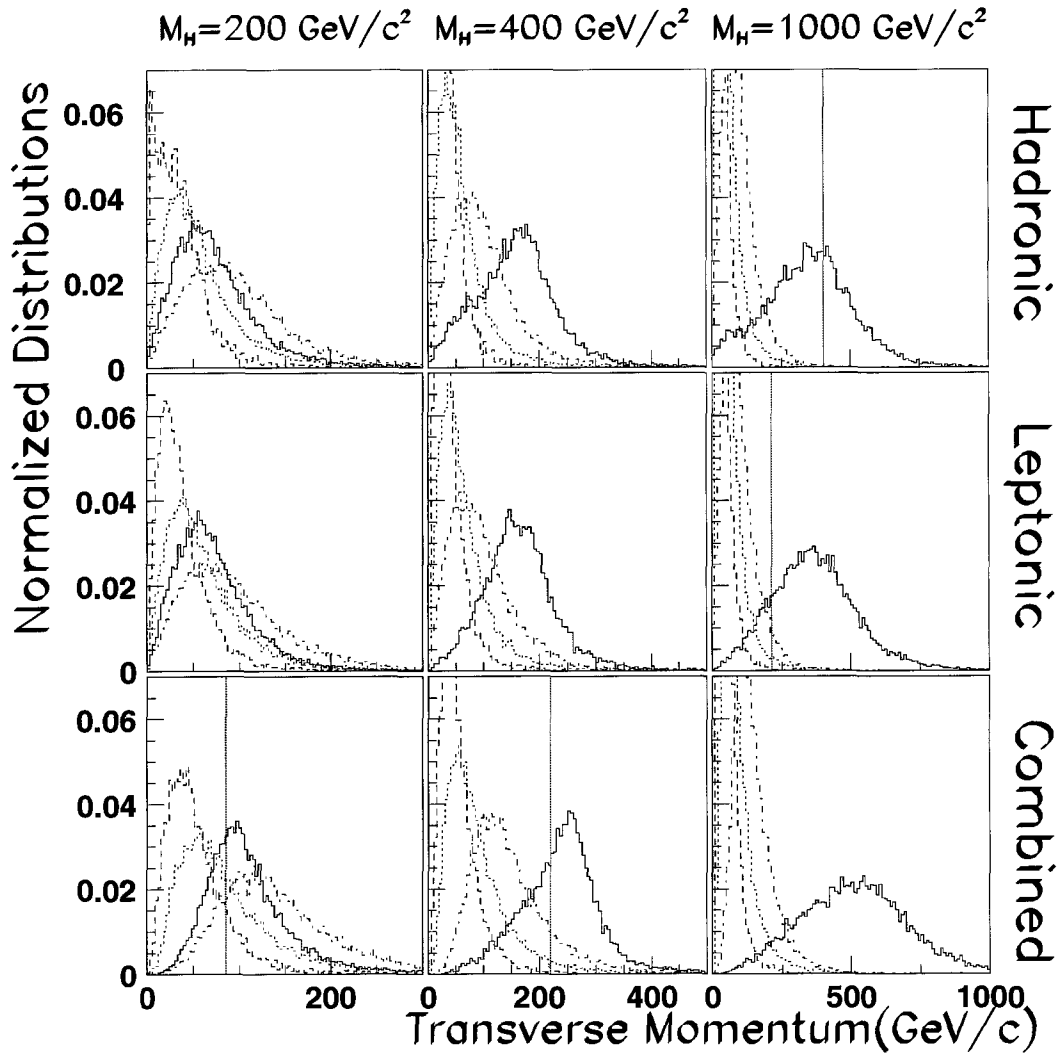
Figure 5.16: The distribution of $P_T^{W \to jj}$, $P_T^{W \to l\nu}$ and P_T^{pair} for 3 different Higgs masses in the absence of pileup. The solid line is the shape of the signal, dashed line of $W^{\pm}$+jets, dotted line ff→WW and the dashed-dotted line tt̄. The vertical lines correspond to the applied cuts in the final analysis.

Higgs Mass (GeV/c^2)	P_T^{pair}	$P_T^{W\to jj}$	$P_T^{W\to l\nu}$	Higgs Mass (GeV/c^2)	P_T^{pair}	$P_T^{W\to jj}$	$P_T^{W\to l\nu}$
		(GeV/c)				(GeV/c)	
170	60	50	0	450	250	180	30
180	70	60	0	500	280	205	40
190	80	65	0	550	305	220	40
200	85	70	0	600	330	240	100
210	95	80	0	650	370	265	100
220	105	85	0	700	390	275	100
230	110	90	0	750	415	290	135
240	115	95	0	800	440	315	170
250	125	100	0	850	470	345	170
300	160	120	0	900	500	350	215
350	190	140	0	950	500	350	215
400	220	160	20	1000	540	400	215

Table 5.8: The optimal values for the step 1 transverse momentum cuts on the reconstructed W bosons.
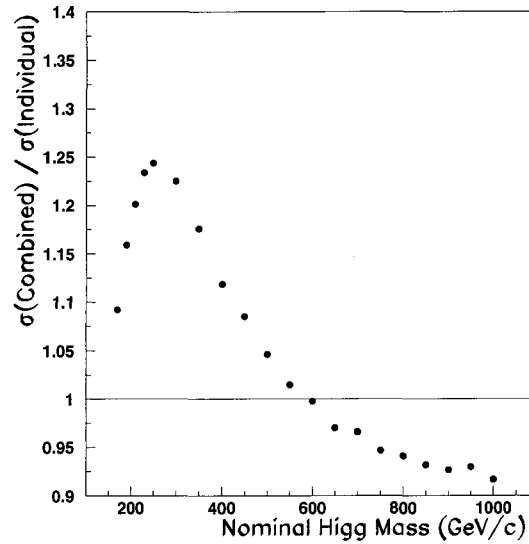
Figure 5.17: A comparison of the ratio of significances between a cut on the combined P_T^{pair} versus individual cuts on $P_T^{W\to l\nu}$ and $P_T^{W\to jj}$. For a Higgs mass equal to or below 600 GeV/c² a cut on P_T^{pair} gives the biggest improvement in significance.

157

Higgs Mass (GeV/c²)	$\Delta\phi_{l\nu}$	ΔR_{jj}	Higgs Mass (GeV/c²)	$\Delta\phi_{l\nu}$	ΔR_{jj}
170-240	-	-	650	1.005	0.75
250	-	3.2	700	0.816	0.70
300	-	2.0	750	0.785	0.7
350	-	1.5	800	0.754	0.6
400	2.95	1.25	850	0.565	0.5
450	2.041	1.10	900	0.534	0.5
500	1.507	0.95	950	0.534	0.5
550	1.068	0.90	1000	0.408	0.45
600	0.942	0.65			

Table 5.9: The optimal values for the step 2 angular separation cuts on the reconstructed W bosons. There is no benefit to applying these cuts for a Higgs boson with a mass between 170-240 GeV/c².

Higgs Mass (GeV/c²)	Hadronic		Leptonic	Higgs Mass (GeV/c²)	Hadronic		Leptonic
	Lead	Trail	$P_T^{l,\nu}$		Lead	Trail	$P_T^{l,\nu}$
	(GeV/c)				(GeV/c)		
170	38	24	-	450	-	48	20
180	34	26	-	500	-	48	25
190	34	26	-	550	-	52	28
200	32	26	-	600	-	52	32
210	32	26	-	650	-	50	32
220	32	26	-	700	-	50	40
230	-	28	-	750	-	50	48
240	-	28	-	800	-	50	57
250	-	28	-	850	-	60	60
300	-	32	10	900	-	60	70
350	-	44	11	950	-	60	80
400	-	44	16	1000	-	60	80

Table 5.10: The optimal values for the step 3 transverse momentum cuts on the individual particles.

shows that these separation cuts do not greatly reduce the backgrounds.

Step 3: We can also place a threshold cut on the transverse momentum of the $W^\pm$ boson decay products. The hadronic component, $W \rightarrow jj$, is broken into leading ($P_{T,J-big}$) and trailing ($P_{T,J-small}$) jets. A single P_T cut is placed on both the neutrino (P_T^ν) and charged lepton (P_T^l) transverse momentums. Figure 5.19 plots the distributions for the trailing jet and charged lepton transverse momentums for signal and background event types. The optimal cut values are summarized in table 5.10.

Step 4: As the Higgs mass is decreased the azimuthal angle between the W-pairs will also decrease. Figure 5.20 compares the azimuthal angle distributions in the absence of pileup for select Higgs boson masses. When comparing the azimuthal angular separation
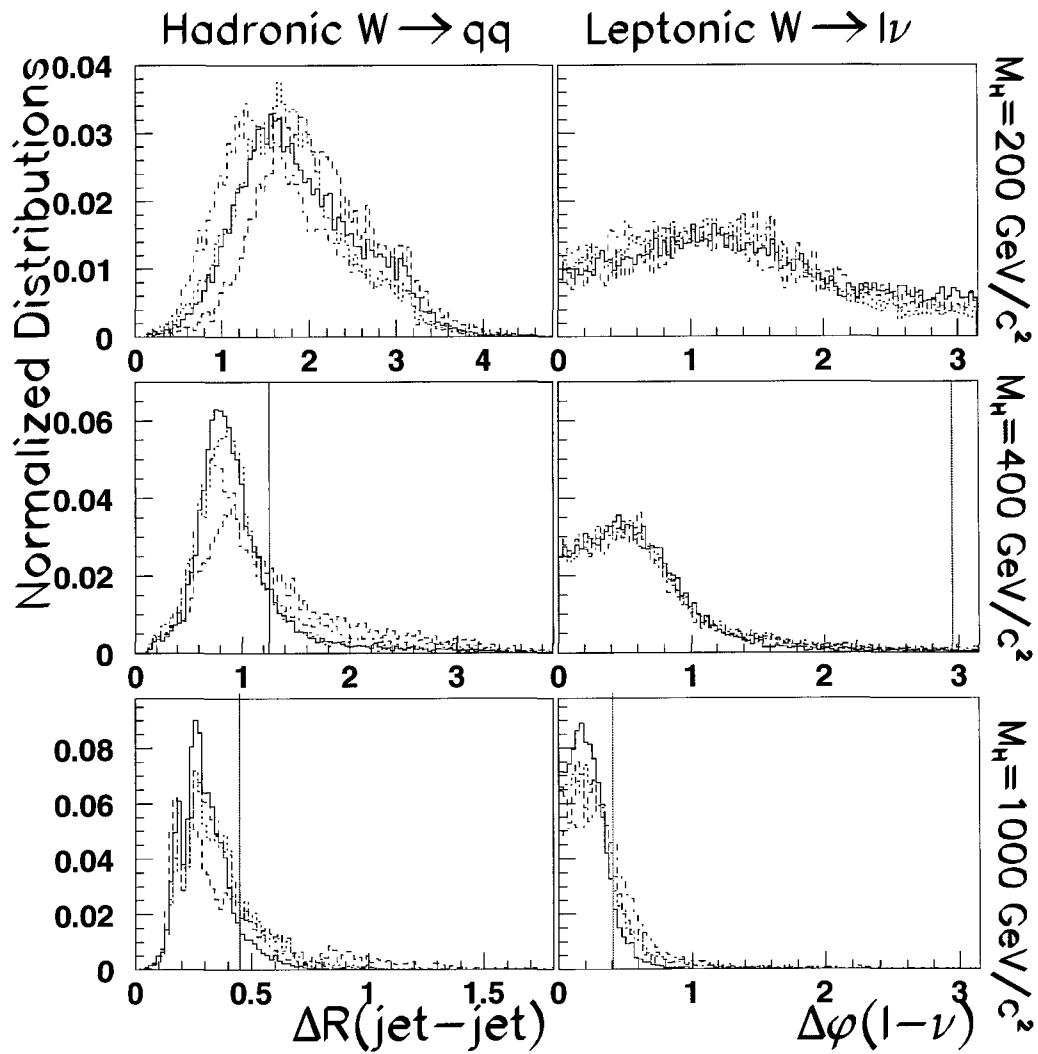
Figure 5.18: The distribution of ΔR_{jj}, $\Delta \phi_{l\nu}$ for 3 different Higgs masses in the absence of pileup. The solid line is the shape of the signal, dashed line of $W^{\pm}$+jets, dotted line ff→WW and the dashed-dotted line $t\bar{t}$. The vertical lines correspond to the applied cuts in the final analysis.

159
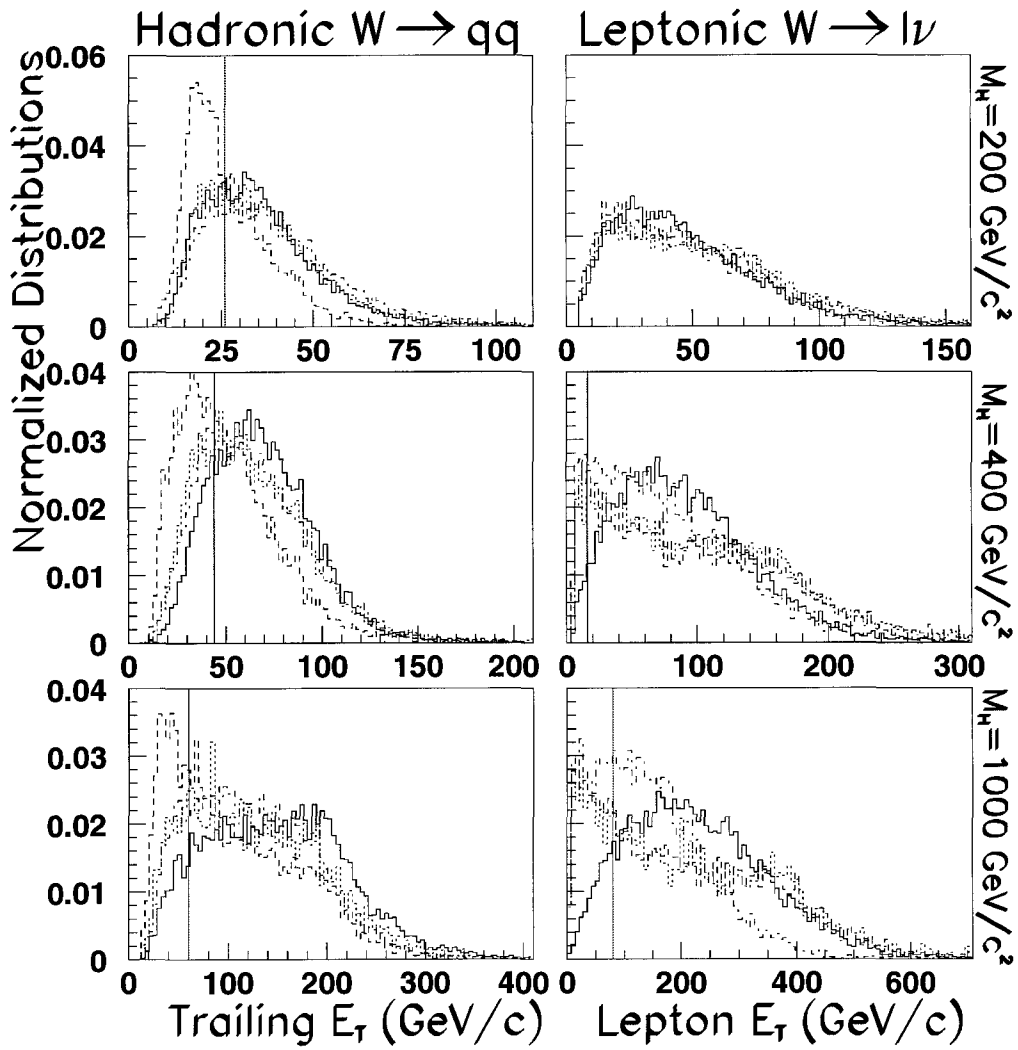
Figure 5.19: The distribution of the trailing jet E_T and the charged lepton E_T for 3 different Higgs masses in the absence of pileup. The solid line is the shape of the signal, dashed line of $W^\pm$+jets, dotted line ff→WW and the dashed-dotted line $t\bar{t}$. The vertical lines correspond to the applied cuts in the final analysis.

Higgs Mass	No tagging jets			With tagging jets		
(GeV/c²)	No Lumi	Low Lumi	High Lumi	No Lumi	Low Lumi	High Lumi
170	0.942	1.005	1.162	0.785	0.879	0.942
180	1.287	1.350	1.601	1.130	1.256	1.382
190	1.696	1.664	2.104	1.663	1.413	1.664
200	1.884	1.947	2.418	1.821	1.790	2.198
210	2.104	2.072	2.418	1.947	2.041	2.386
220	2.229	2.292	2.543	2.198	2.292	2.638
230	2.386	2.386	2.638	2.229	2.355	2.857
240	2.481	2.543	2.763	2.606	2.669	2.952
250	2.575	2.606	2.763	2.606	2.669	2.952
300	2.826	2.857	2.857	2.952	3.014	3.077
350	2.889	2.889	2.857	3.014	3.014	3.109
400	2.983	2.983	2.952	3.109	3.109	3.109
450	2.983	2.983	2.983	-	-	-
500	3.014	3.014	3.077	-	-	-

Table 5.11: The maximum azimuthal angle (in radians) as a function of Higgs Mass in the charge vector boson channel.

in figure 5.20 with the corresponding mass in figure 4.29 we can see that the separation is flatter at low Higgs masses in the WW channel. The accuracy at which we can reconstruct the neutrino direction decreases at lower Higgs mass due to the increase in error in the measurement of E_x^{miss} and E_y^{miss}. These considerations lead to a poorer determination for $\phi(W \to l\nu)$ and as such a less clean WW-azimuthal angle separation. Despite this there is still an improvement in the significance when we apply the cut values listed in table 5.11. Table 5.11 gives the optimal cut values when tagging jets have been identified and reconstructed and when they have not been reconstructed (prior to the cut). The $\Delta\phi_{WW}$ cuts applied in this chapter are those belonging to the cases where we have identified tagging jets.

Taking a two sigma cut on the width of the hadronic W→jet+jet decay, equation 5.25, the efficiencies and expected number of events after the central cuts are given in table 5.12.

5.4.2   Step 5

We can see from table 5.12 that the $t\bar{t}$ background remains significant after the application of the central cuts. The $t\bar{t}$ background is comparable in magnitude with the W+jets background and in some cases, $M_H \approx 400$ GeV/c² , greater in magnitude.

The decay chain for the $t\bar{t}$ and W+jets background is:

$$t\bar{t} \to WbWb \to l\nu b + jjb$$
$$W + jets \to l\nu + jets \tag{5.30}$$

161
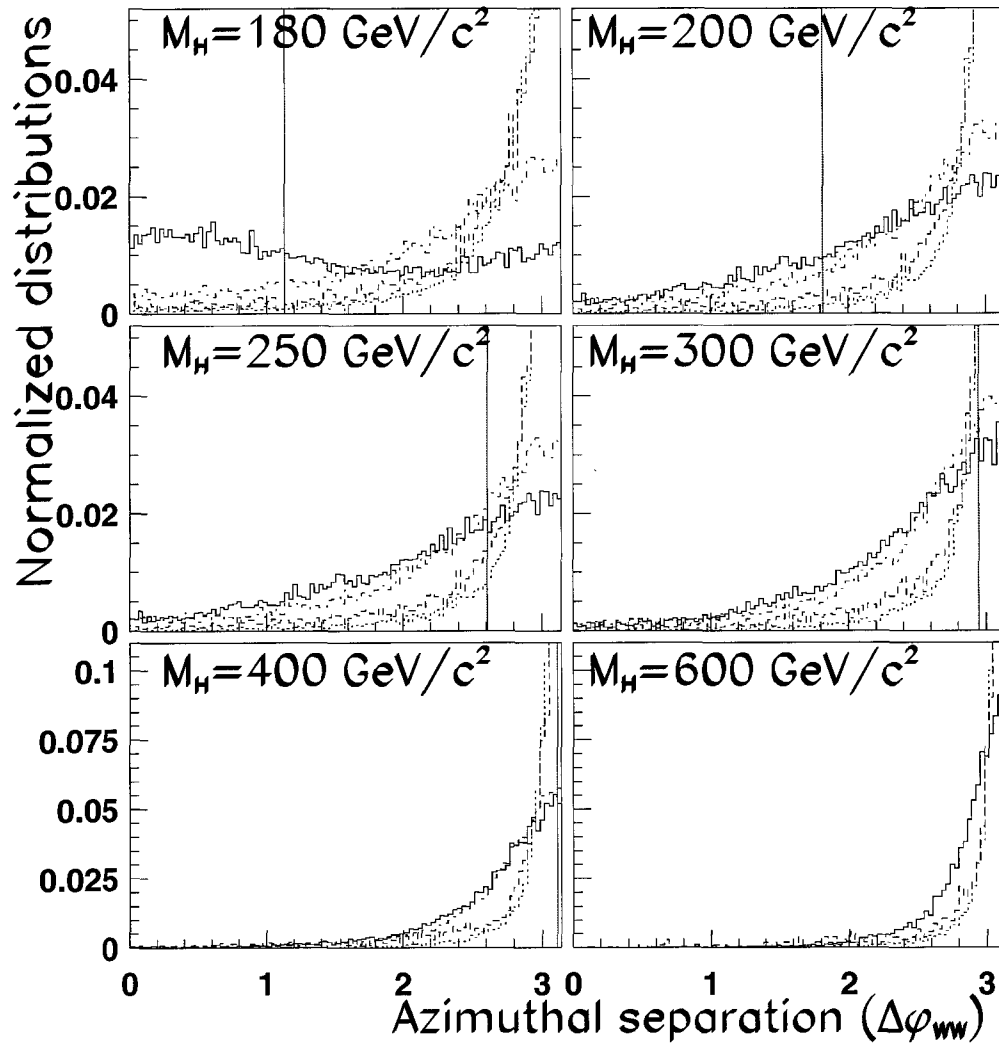
Figure 5.20: The azimuthal separation of the reconstruction W bosons. The solid line is the shape of the signal, dashed line of $W^\pm$+jets, dotted line ff$\rightarrow$WW and the dashed-dotted line t$\bar{t}$. The vertical lines correspond to the applied cuts in the final analysis. There is a strong peak in W+jets background for $\phi_{WW}=\pi$ that cannot be shown on these graphs as it would greatly reduce the visibility of the other processes.

162

Cut Description	Signal	ff→ZZ	$t\bar{t}$	Z^0+jets	$\frac{S}{\sqrt{B}}$
$M_H = 200$ GeV/c²					
Expected	2617.50	102070	713680	384400000	
Passing Precuts	92.5 %	78.9 %	95.6 %	36.2 %	0.205
Mass Cuts	38.6 %	28.6 %	44.0 %	2.75 %	0.306
Step 1	26.7 %	11.6 %	36.3 %	0.416 %	0.512
Step 2	26.7 %	11.6 %	36.3 %	0.416 %	0.512
Step 3	18.3 %	7.91 %	27.0 %	0.178 %	0.510
Remaining	479.	8070.	192894.	683604.	
Azimuthal Angle	9.17 %	0.413 %	7.10 %	.0178 %	0.695
Remaining	240.	421.	50665.	68397.	
$M_H = 400$ GeV/c²					
Expected	761.70	102070	713680	384400000	
Passing Precuts	95.4 %	78.9 %	95.6 %	36.2 %	.0615
Mass Cuts	51.9 %	27.2 %	42.4 %	2.52 %	0.125
Step 1	32.3 %	1.22 %	5.58 %	.0148 %	0.786
Step 2	27.2 %	1.03 %	4.10 %	.00862 %	0.821
Step 3	21.0 %	0.672 %	2.66 %	.00398 %	0.855
Remaining	160.	686.	18976.	15288.	
Azimuthal Angle	19.8 %	0.530 %	2.49 %	.00342 %	0.850
Remaining	151.	541.	17775.	13151.	
$M_H = 1000$ GeV/c²					
Expected	81.63	102070	713680	384400000	
Passing Precuts	97.4 %	78.9 %	95.6 %	36.2 %	.00672
Mass Cuts	58.0 %	28.2 %	43.5 %	2.70 %	.0145
Step 1	21.5 %	.0416 %	.0474 %	0.000200 %	0.517
Step 2	19.6 %	.0321 %	.0393 %	0.000137 %	0.552
Step 3	14.5 %	.0173 %	.0199 %	0.000055 %	0.615
Remaining	11.9	17.7	142.	213.	
Azimuthal Angle	14.5 %	.0173 %	.0199 %	0.000055 %	0.615
Remaining	11.9	17.7	142.	213.	

Table 5.12: The number of signal and background events remaining after the application of the central cuts. Results are calculated for an integrated luminosity of 10 fb^{-1} of data at low luminosity in the absence of pileup.

163

The tt̄ background has a four jet final state which easily mimics the topology of the signal. The W+jets has only 1 tree level jet, with extra jets coming from initial/final state radiation, multiple interactions, and pileup jets. The W+jets background will be reduced by the tagging jet cuts, the tt̄ background will be reduced with the central jet veto.

Central Jet veto

Studies [62] have shown that a central jet veto will greatly reduce the contribution from the tt̄ background. Since the pseudo-rapidity value of the neutrino is not well defined we redefine the central and forward regions in our WW analysis to be :

$$MIN(\eta_{j1,j2}, \eta_l) - 0.6 \leq \eta_{central} \leq MAX(\eta_{j1,j2}, \eta_l) + 0.6 \qquad (5.31)$$

where $MIN(\eta_{j1,j2}, \eta_l)(MAX(\eta_{j1,j2}, \eta_l))$ is the minimum (maximum) pseudorapidity of the central jets and the charged central lepton. The highest energy jet in this region is taken as the central jet. In section 4.5.5 we showed that central jet veto cut is optimized when we limit the central jet to possess a pseudo-rapidity less than 2.0 ($|\eta| < 2.0$), and an E_T no greater than 15 (25) GeV/c at low (high) luminosity.

In some cases a forward jet may fall into the central region and would be mistaken as a central jet. We get different veto rates if we perform the *tagging jet cut after the forward jets are identified*. Table 5.13 gives the veto rate when two tagging jets *have* been identified and reconstructed. The central jet veto strongly reduces the tt̄ background.

Tagging Jets

The forward/backward region is defined as the region $|\Delta\eta| > 0.6$ beyond the highest/lowest pseudorapidity central particle, which in this case are the two jets and the charged lepton. The rate at which the various event types are double tagged after applying the central cuts at the 3 different luminosity settings are given in table 5.14. The tagging jet requirement greatly reduces the dominant W+jets background.

The behaviour of the tagging jets is similar when interchanging the $Z^0/W^\pm$ physics channels. As such the optimal cuts derived from the ZZ physics channels in section 4.5.5 are applied to the WW channel as well. These cuts are listed in table 5.15. Recall that M_{tag} is the invariant mass of the tagging jet pair and that one tagging jet is typically at lower energy (E_{trail}) than the other (E_{lead}).

The distribution of these variables for the H→WW signal and the W+jets and tt̄ backgrounds are given in figure 5.21. The W+jets and tt̄ distributions are very similar.

164

Veto ($\frac{\text{GeV}}{c}$)	M_H= 200 GeV/c^2					M_H= 600 GeV/c^2				
	H→WW	WW	$t\bar{t}$	W+jets	$\frac{S}{\sqrt{B}}$	H→WW	WW	$t\bar{t}$	W+jets	$\frac{S}{\sqrt{B}}$
No Pileup (10^{33} cm^{-2}s^{-1})										
15.	84.7	48.8	17.1	55.8	1.13	91.4	62.8	19.5	58.4	1.20
20.	88.6	52.7	18.5	61.7	1.13	94.5	64.8	21.3	61.7	1.20
25.	91.0	56.9	20.0	65.1	1.13	95.9	68.4	23.6	64.5	1.19
30.	92.3	59.8	22.0	68.6	1.12	96.7	72.5	26.1	67.2	1.18
40.	93.6	64.9	26.7	73.9	1.09	97.5	77.8	31.9	72.1	1.15
50.	94.6	69.2	32.6	77.2	1.08	97.9	81.5	37.1	75.1	1.13
60.	95.1	73.1	38.7	79.7	1.07	98.2	84.1	42.2	77.7	1.11
Low luminosity (10^{33} cm^{-2}s^{-1})										
15.	81.0	42.6	16.6	49.5	1.15	88.9	60.2	19.1	55.9	1.19
20.	86.1	47.5	18.7	55.5	1.15	93.0	64.3	21.1	59.9	1.20
25.	89.0	51.7	20.8	61.0	1.14	95.5	68.8	23.6	63.9	1.19
30.	90.7	54.7	22.8	65.0	1.12	96.5	70.9	26.2	66.5	1.18
40.	92.6	60.6	27.3	70.1	1.11	97.4	76.7	31.8	71.5	1.15
50.	93.6	65.6	32.8	74.6	1.08	97.8	80.7	36.7	74.4	1.13
60.	94.3	70.1	38.8	78.2	1.07	98.1	83.5	41.8	77.2	1.12
High luminosity (10^{34} cm^{-2}s^{-1})										
15.	72.3	44.1	19.7	53.3	0.99	84.9	62.5	20.4	57.0	1.12
20.	75.3	46.6	20.9	56.2	1.00	87.7	64.4	21.3	59.0	1.14
25.	78.6	49.8	22.3	60.2	1.01	90.5	67.0	22.5	61.9	1.15
30.	81.0	53.4	24.1	64.6	1.01	92.7	70.2	24.2	64.7	1.15
40.	84.8	60.9	28.6	72.6	1.00	95.4	75.7	28.6	70.2	1.14
50.	87.4	67.5	34.4	78.7	0.99	96.8	79.8	33.7	74.2	1.12
60.	89.3	73.1	40.5	83.2	0.98	97.3	82.9	38.5	77.2	1.11

Table 5.13: The central jet veto efficiencies using events that have passed the central cuts and have two reconstructed tagging jets with P_T >15 GeV/c . The CJV efficiency is defined as the probability that an event will have a jet below the requested threshold, 15 GeV/c for low luminosity and 25 GeV/c for high luminosity, and $|\eta_{jet}| \leq 2.0$. Significance is calculated as the efficiency of the signal divided by the root of the efficiency of the W+jets process.

165

Energy	$M_H = 200$ GeV/c²					$M_H = 600$ GeV/c²				
(GeV)	H→WW	WW	$t\bar{t}$	W+jets	$\frac{S}{\sqrt{B}}$	H→WW	WW	$t\bar{t}$	W+jets	$\frac{S}{\sqrt{B}}$
No Pileup (10^{33} cm^{-2}s^{-1})										
100.	42.1	5.02	11.0	5.97	1.72	49.8	4.05	16.5	6.51	1.95
200.	36.4	2.63	6.42	3.53	1.94	43.4	1.75	8.92	3.49	2.33
300.	27.4	1.05	2.98	1.56	2.20	34.5	0.65	4.58	1.81	2.56
400.	20.3	0.64	1.50	1.01	2.02	27.2	0.37	2.49	1.07	2.63
500.	15.3	0.29	0.94	0.66	1.88	21.3	0.23	1.54	0.66	2.63
600.	11.7	0.15	0.55	0.33	2.04	16.3	0.12	0.98	0.47	2.38
Low Luminosity (10^{33} cm^{-2}s^{-1})										
100.	42.1	6.06	12.1	7.25	1.56	51.0	4.36	17.7	6.72	1.97
200.	36.5	2.98	6.93	4.21	1.78	44.9	1.66	9.12	3.49	2.41
300.	27.6	1.20	3.54	2.02	1.94	35.5	0.68	4.61	1.87	2.60
400.	20.6	0.59	1.75	1.16	1.92	27.8	0.33	2.54	1.17	2.57
500.	15.6	0.24	1.10	0.66	1.93	21.7	0.18	1.39	0.66	2.67
600.	11.9	0.16	0.68	0.38	1.93	16.8	0.11	0.94	0.43	2.57
High Luminosity (10^{34} cm^{-2}s^{-1})										
100.	33.5	6.70	12.2	7.53	1.22	49.9	4.91	17.4	7.63	1.81
200.	28.7	3.80	7.51	4.79	1.31	43.9	2.16	10.1	4.11	2.16
300.	21.1	1.74	3.59	2.22	1.42	34.8	0.83	5.09	1.96	2.48
400.	15.9	0.86	1.87	1.22	1.44	27.3	0.41	3.13	1.06	2.65
500.	12.0	0.47	1.13	0.79	1.35	21.3	0.26	2.04	0.66	2.62
600.	9.20	0.22	0.73	0.39	1.47	16.6	0.21	1.41	0.39	2.65

Table 5.14: The double jet tag rate for signal and background events passing the central cuts. Significance is calculated as the efficiency of the signal divided by the root of the efficiency of the W+jets process.

Description	Cut Value
Invariant Mass Cut	$M_{tag} > 1000$ GeV/c²
Symmetric Energy Cut	$E_{lead}, E_{trail} > 300$ GeV
Asymmetric Energy Cut	$E_{lead} > 700$ GeV, $E_{trail} > 200$ GeV

Table 5.15: Optimal values for step 5 tagging jet cuts implemented in the WW physics analysis.

5.4.3 Tagging Jet Transverse Momentum

We found in section 4.5.5, that placing a cut on the transverse momentum of the tagging jets after the central cuts and a 1 TeV/c² tagging jet invariant mass cut can greatly improve our signal significance. The distribution of the leading and trailing tagging jet transverse momentum, after applying the central cuts and the invariant mass cut, is shown in figure 5.22 for two different Higgs masses and the three different luminosity settings. In the absence of pileup, the tagging jet transverse momentum is very similar between the W+jets and the $t\bar{t}$ background. This similarity is expected considering the tagging jet energy distributions in figure 5.21. However, when pileup is added the W+jets transverse momentum spectrum peaks at lower values due to the presence of low P_T pileup jets. The $t\bar{t}$ tagging jet P_T spectrum is relatively unaffected by the addition of pileup jets. As shown on the right side of figure 5.22 the addition of P_T cuts on the tagging jets will not be useful at higher Higgs mass values. The optimal cuts on the tagging jet transverse momentum, taken from table 4.13 in section 4.5.5, are given in table 5.16.

Higgs Mass	No Pileup 10^{33} cm^{-2}s^{-1}		Low Luminosity 10^{33} cm^{-2}s^{-1}		High Luminosity 10^{34} cm^{-2}s^{-1}	
(GeV/c²)	Leading	Trailing	Leading	Trailing	Leading	Trailing
170-250	90.0	50.0	90.0	50.0	110.0	60
300	40.0	30.0	60.0	40.0	60.0	40
350	40.0	30.0	40.0	25.0	50.0	30
400	-	-	40.0	25.0	50.0	30
500	-	-	40.0	25.0	50.0	30
600	-	-	-	-	50.0	30

Table 5.16: The optimal P_T cuts (in GeV/c) on the leading and trailing tagging jets as a function of Higgs mass and luminosity setting.

The expected number of events remaining after the application of the central cuts, the central jet veto and tagging jet cuts are given in table 5.17. The cut listed as "tagging mass" is a cut of 1 TeV/c² on the invariant mass of the tagging jet. "Tagging P_T" refers to the cut on the transverse momentum of the tagging jets. ΔM_H is a $\pm 2\sigma$ mass window around the Higgs mass peak, using the width as given in equation 5.28. The motivation for this mass cut was discussed in section 4.5.5. The rates have been calculated using 10 fb^{-1} of data at low luminosity and 100 fb^{-1} at High luminosity.
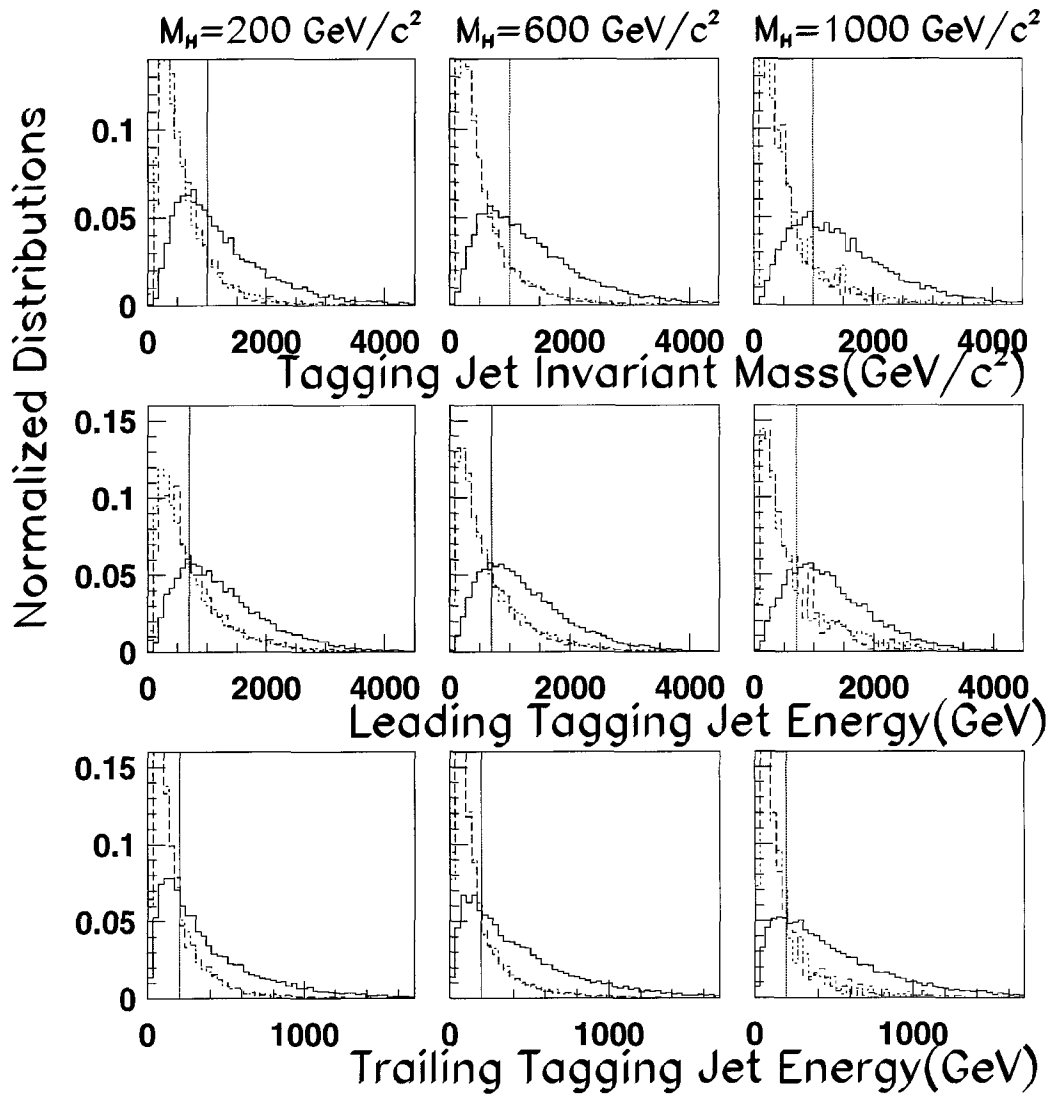
Figure 5.21: Tagging jet variable distribution for three different Higgs masses in the absence of pileup. The solid line is the Higgs signal, the dashed line is W+jets and the dotted line is the t$\bar{\text{t}}$ background. The ff→WW background is not included as it has been greatly reduced by the central cuts. The vertical lines correspond to the optimal cuts on that particular variable.

168
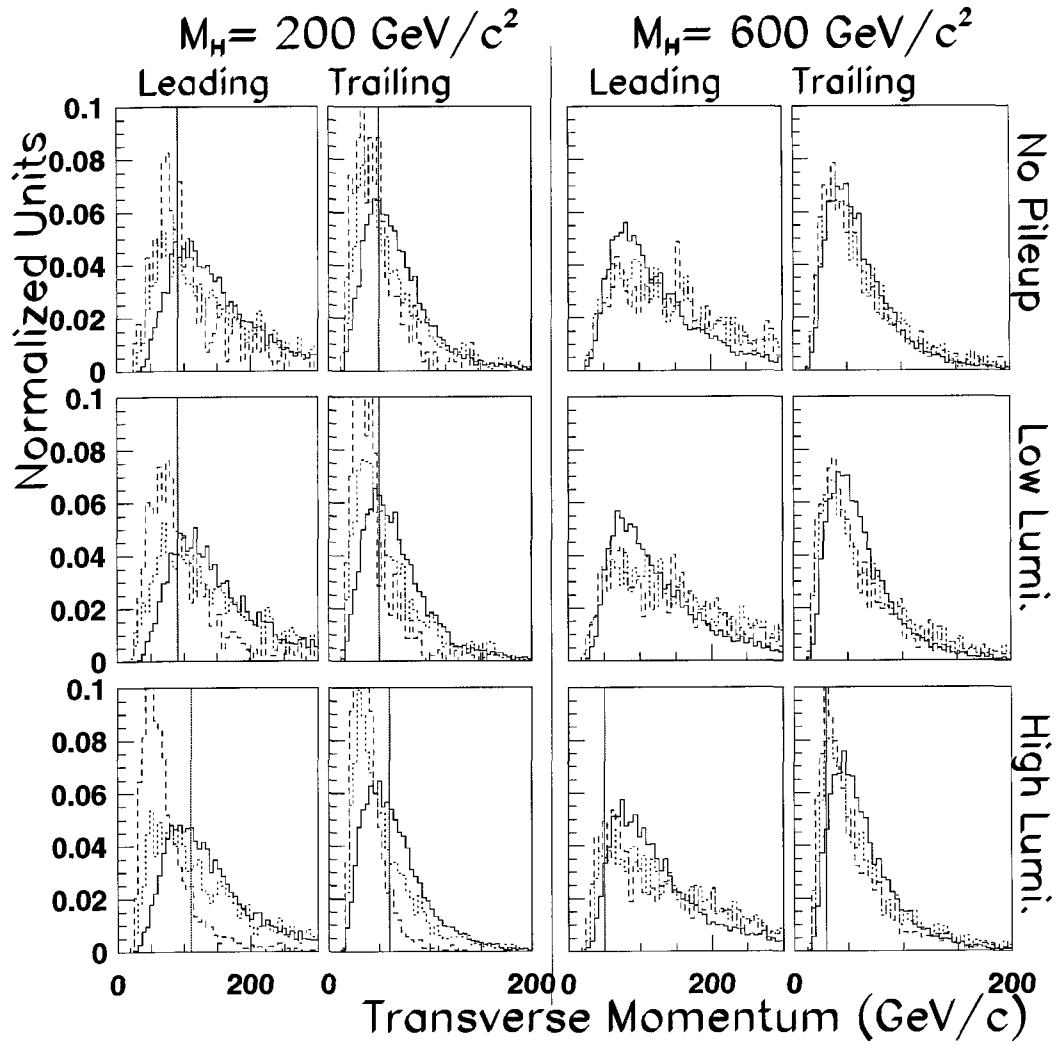
Figure 5.22: Transverse momentum of leading and trailing tagging jets at the three luminosity settings and two Higgs masses. The solid line is the Higgs signal, the dashed line is W+jets and the dotted line is the $t\bar{t}$ background. The vertical lines correspond to the applied cuts in the final analysis.

169

Cut Description	Signal	ff→WW	$t\bar{t}$	W+jets	$\frac{S}{\sqrt{B}}$
$M_H = 200$ GeV/c^2 No Pileup					
Central Cuts	240.	421.	50665.	68397.	0.69
Tagging Mass	52.9	2.08	806.	593.	1.41
+Veto	46.9	1.03	112.	332.	2.22
+Veto+ΔM_H	38.7	0.53	63.9	194.	2.40
+Veto+Tagging P_T	26.4	0.27	57.8	71.0	2.32
+Veto+Tagging P_T+ΔM_H	21.4	0.15	32.8	29.2	2.71
$M_H = 200$ GeV/c^2 Low Luminosity Pileup					
Central Cuts	237.	422.	53238.	83140.	0.64
Tagging Mass	53.1	2.37	963.	890.	1.23
+Veto	45.0	1.01	149.	442.	1.85
+Veto+ΔM_H	37.4	0.57	85.4	242.	2.07
+Veto+Tagging P_T	26.1	0.24	65.6	77.9	2.17
+Veto+Tagging P_T+ΔM_H	21.3	0.13	38.2	29.2	2.59
$M_H = 200$ GeV/c^2 High Luminosity Pileup					
Central Cuts	2973.	15622.	939678.	6478670.	1.09
Tagging Mass	514.	135.	19108.	76617.	1.66
+Veto	388.	53.0	3131.	37309.	1.93
+Veto+ΔM_H	280.	25.0	1262.	19557.	1.94
+Veto+Tagging P_T	212.	7.84	1399.	3560.	3.01
+Veto+Tagging P_T+ΔM_H	151.	3.14	551.	1414.	3.40
$M_H = 1000$ GeV/c^2 No Pileup					
Central Cuts	11.9	17.7	142.	206.	0.62
Tagging Mass	3.89	0.04	3.75	1.99	1.62
+Veto	3.68	0.02	0.33	1.02	3.14
+Veto+ΔM_H	3.12	0.02	0.25	0.82	2.98
+Veto+Tagging P_T	3.68	0.02	0.33	1.02	3.14
+Veto+Tagging P_T+ΔM_H	3.12	0.02	0.25	0.82	2.98
$M_H = 1000$ GeV/c^2 Low Luminosity Pileup					
Central Cuts	11.7	17.6	146.	220.	0.60
Tagging Mass	3.96	0.03	3.47	1.85	1.71
+Veto	3.60	0.01	0.33	0.93	3.18
+Veto+ΔM_H	3.06	0.004	0.28	0.80	2.94
+Veto+Tagging P_T	3.60	0.01	0.33	0.93	3.18
+Veto+Tagging P_T+ΔM_H	3.06	0.004	0.28	0.80	2.94
$M_H = 1000$ GeV/c^2 High Luminosity Pileup					
Central Cuts	104.	166.	1779.	2760.	1.52
Tagging Mass	34.0	0.61	46.9	29.5	3.88
+Veto	29.3	0.45	4.44	15.0	6.57
+Veto+ΔM_H	24.9	0.32	3.89	11.9	6.21
+Veto+Tagging P_T	29.3	0.45	4.44	15.0	6.57
+Veto+Tagging P_T+ΔM_H	24.9	0.32	3.89	11.9	6.21

Table 5.17: Number of events remaining, and significances of the step 5 cuts. For a 200 GeV/c^2 and 1 TeV/c^2 Higgs boson. The rates for the no pileup and low luminosity pileup sections are calculated using 10 fb^{-1} of data, high luminosity is calculated using 100 fb^{-1}.

170

Luminosity	Muon Channels		Electron Channels		Comments
$(cm^{-2}s^{-1})$	10^{33}	10^{34}	10^{33}	10^{34}	
Single Lepton	20 GeV/c	20 GeV/c	20 GeV/c	30 GeV/c	$\eta_e^{trig} < 2.5$
trigger					$\eta_\mu^{trig} < 2.4$
$\not{E}_T$ +Jet	$\not{E}_T >$ 50 GeV/c	100 GeV/c	50 GeV/c	100 GeV/c	$\eta_{jet}^{trig} < 3.2$
trigger	$+P_T^{jet} >$ 50 GeV/c	100 GeV/c	50 GeV/c	100 GeV/c	

Table 5.18: A list of the triggers considered for the H→WW analysis.

5.5 H→WW Results

There were two different triggers considered for the H→WW analysis: a single lepton trigger and the $\not{E}_T$+jet trigger. The specific triggers considered can be found in table 5.18.

Tables 5.19, 5.20, 5.21, give the effects of the cuts discussed in section 5.4 on a 300 GeV/c^2 Higgs signal and the backgrounds for no pileup, low luminosity pileup and high luminosity pileup respectively. Similar tables have been produced for a Higgs boson of mass 200 GeV/c^2, 600 GeV/c^2 and 1 TeV/c^2 and can be found in appendix C.

Table 5.22 summarizes the total number of signal and background events expected after the application of all the previously discussed cuts. The invariant mass on the Higgs has been used as a discriminating variable up to a Higgs boson mass of 600 GeV/c^2 at which point the Higgs line shape is too large to get any benefit from such a cut.

Figure 5.23 plots the expected significance as a function of Higgs mass when all cuts have been applied except the tagging jet transverse momentum cuts. Figure 5.24 plots the significances when the cut on the transverse momentum of the tagging jets has been included. Both figures show that the expected significance is relatively flat for masses above 400 GeV/c^2. The efficiency of the cuts counteracts the factor of 10 reduction in cross-section that occurs when increasing the Higgs boson mass from 400 GeV/c^2 to 1 TeV/c^2.

The significance plots have a minimum at approximately M$_H$=250 GeV/c^2 with a rapid increase to the significance between 250 GeV/c^2 to 170 GeV/c^2. Figure 1.2 shows that the Higgs production cross-section increases as the Higgs mass decreases. The branching fraction H→WW increases to compensate for the drop in the H→ZZ rate below 2 M$_Z$ and has a value near 1 between 2M$_Z$ and 2M_W. This increase in branching fraction coupled with the strength of the azimuthal angle and tagging jet transverse momentum cuts give rise to the increase in significance in the H→WW channel below 250 GeV/c^2.

The reconstructed Higgs mass spectrum after 3 years of running at low luminosity

171

	Signal	W+jets	ff→ WW	t t̄	δ Back	$\frac{S}{\sqrt{B}}$
			$W\to \mu^{\pm}\nu_{\mu}$channel			
Expected	4160.70±6.390	48183300.	306210.	2141040.	5974.20	0.585±0.001
Precuts	3928.93±6.210	36841764.	241741.	2046704.	5226.40	0.628±0.001
Trigger	2758.38±5.210	11717199.	110961.	1344097.	2954.50	0.760±0.001
Central Cut	748.79±2.710	118779.	2727.60	162087.	312.00	1.406±0.005
M_H Window	586.50±2.400	53361.5	1045.20	77859.1	209.90	1.613±0.007
Jet Veto	407.19±2.000	27084.5	528.10	8537.89	143.20	2.142±0.011
Tagging Mass	126.59±1.120	227.31	1.700	234.61	13.50	5.879±0.100
+Tagging P_T	96.42±0.970	124.72	0.800	159.82	10.10	5.708±0.116
			$Z\to e^{+}e^{-}$channel			
Expected	4160.70±7.310	48180000.	308100.	2141040.	5812.30	0.585±0.001
Precuts	3857.29±7.040	34944592.	232219.	2019512.	4952.40	0.632±0.001
Trigger	2742.97±5.940	11600745.	111614.	1308472.	2859.10	0.760±0.002
Central Cut	749.10±3.100	115963.	2686.50	158962.	298.50	1.422±0.006
M_H Window	586.68±2.750	51933.3	1019.60	76379.5	200.40	1.631±0.008
Jet Veto	407.77±2.290	26269.2	513.40	8298.60	137.10	2.177±0.013
Tagging Mass	127.53±1.280	236.92	1.500	226.37	13.30	5.916±0.103
+Tagging P_T	96.43±1.110	133.49	0.800	154.93	10.10	5.670±0.118
			Combined Results			
Expected	8321.40±13.70	96363296.	614310.	4282080.	11786.5	0.827±0.001
Precuts	7786.22±13.25	71786352.	473960.	4066215.	10178.8	0.891±0.002
Trigger	5501.35±11.15	23317944.	222575.	2652569.	5813.60	1.075±0.002
Central Cut	1497.89±5.810	234742.	5414.10	321048.	610.50	1.999±0.009
M_H Window	1173.18±5.150	105295.	2064.80	154239.	410.30	2.294±0.012
Jet Veto	814.96±4.290	53353.7	1041.50	16836.5	280.30	3.054±0.022
Tagging Mass	254.12±2.400	464.23	3.200	460.98	26.80	8.340±0.199
+Tagging P_T	192.85±2.080	258.21	1.600	314.75	20.20	8.045±0.228

Table 5.19: M_H=300 GeV/c^2 . H→WW→ $l\nu$jj. Number of events expected after 3 years of running at the low luminosity setting (L=30 fb^{-1}). Pileup has not been included.

(10^{33} cm^{-2}s^{-1}) in the absence pileup, for varying Higgs boson masses, is presented in figure 5.25. When low luminosity pileup has been included, figure 5.26, a Higgs mass peak can be observed for M_H ≥180 GeV/c^2 . After gathering 100 fb^{-1}at the high luminosity setting (10^{34} cm^{-2}s^{-1}) figure 4.42 shows that a mass peak should be visible for a Higgs boson with a mass above ≈ 400 GeV/c^2 .

In this chapter we have outlined a method to search for a neutral scalar Higgs boson produced through vector boson fusion and decaying through the mixed leptonic/hadronic decays of the charged vector bosons: H→WW→lνjj. We have show that a neutral scalar Higgs boson can be observed in the charged Vector boson channel H→WW→lνjj when the Higgs boson mass is above 170 GeV/c^2 after 3 years of low luminosity running or 1 year of high luminosity running.

	Signal	W+jets	ff→ WW	t̄t	δ Back	$\frac{S}{\sqrt{B}}$
W→ $\mu^{\pm}\nu_{\mu}$channel						
Expected	4160.70±6.390	48183300.	306210.	2141040.	5974.20	0.585±0.001
Precuts	3928.93±6.210	36841764.	241741.	2046704.	5226.40	0.628±0.001
Trigger	2780.48±5.230	13007046.	115180.	1354683.	3111.50	0.731±0.001
Central Cut	718.43±2.660	123913.	2522.60	163223.	318.10	1.335±0.005
M_H Window	563.22±2.350	55187.4	973.80	78405.5	213.10	1.535±0.007
Jet Veto	379.98±1.930	27392.9	480.40	8451.42	144.00	1.994±0.011
Tagging Mass	119.02±1.080	257.57	1.600	226.85	14.30	5.399±0.093
+Tagging P_T	90.28±0.940	142.44	0.800	152.85	10.70	5.247±0.109
Z→ e^+e^- channel						
Expected	4160.70±7.310	48180000.	308100.	2141040.	5812.30	0.585±0.001
Precuts	3857.29±7.040	34944592.	232219.	2019512.	4952.40	0.632±0.001
Trigger	2767.59±5.970	12894045.	115894.	1318137.	3013.20	0.731±0.002
Central Cut	723.31±3.050	120588.	2482.70	159773.	303.90	1.360±0.006
M_H Window	566.38±2.700	53507.9	955.80	76746.6	203.20	1.564±0.008
Jet Veto	382.53±2.220	26490.1	471.50	8251.23	137.60	2.039±0.012
Tagging Mass	120.44±1.240	255.79	1.600	230.92	13.80	5.450±0.095
+Tagging P_T	90.23±1.080	133.49	0.800	156.29	10.10	5.293±0.111
Combined Results						
Expected	8321.40±13.70	96363296.	614310.	4282080.	11786.5	0.827±0.001
Precuts	7786.22±13.25	71786352.	473960.	4066215.	10178.8	0.891±0.002
Trigger	5548.07±11.20	25901092.	231073.	2672820.	6124.70	1.034±0.002
Central Cut	1441.74±5.710	244500.	5005.30	322995.	622.00	1.905±0.009
M_H Window	1129.60±5.050	108695.	1929.60	155152.	416.30	2.191±0.012
Jet Veto	762.51±4.150	53883.0	951.90	16702.7	281.60	2.851±0.021
Tagging Mass	239.46±2.320	513.36	3.200	457.77	28.10	7.671±0.185
+Tagging P_T	180.51±2.020	275.93	1.600	309.14	20.80	7.453±0.216

Table 5.20: M_H=300 GeV/c^2 . H→WW→ $l\nu$jj. Number of events expected after 3 years of running at the low luminosity setting (L=30 fb^{-1}). Pileup has been included.

173

	Signal	W+jets	ff→ WW	$t\bar{t}$	δ Back	$\frac{S}{\sqrt{B}}$
		$W \to \mu^{\pm}\nu_{\mu}$ channel				
Expected	13869.0±21.31	160611008.	1020700.	7136800.	19914.1	1.068±0.002
Precuts	13096.4±20.71	122805880.	805804.	6822346.	17421.2	1.147±0.002
Trigger	7852.27±16.03	32925082.	282443.	3684823.	9041.10	1.293±0.003
Central Cut	2267.71±8.620	938429.	14245.9	693869.	1564.30	1.767±0.007
M_H Window	1725.82±7.520	485782.	5975.20	378185.	1127.20	1.850±0.008
Jet Veto	1214.83±6.310	292488.	3506.20	61371.5	855.50	2.032±0.011
Tagging Mass	349.18±3.380	3102.13	16.20	1794.84	89.40	4.982±0.066
+Tagging P_T	274.24±3.000	1564.59	6.900	1175.03	63.90	5.233±0.084
		$Z \to e^+e^-$ channel				
Expected	13869.0±24.38	160600000.	1027000.	7136800.	19374.5	1.068±0.002
Precuts	12857.6±23.47	116481976.	774062.	6731705.	16508.0	1.155±0.002
Trigger	7332.36±17.73	26905910.	221145.	3080531.	7950.20	1.334±0.003
Central Cut	2166.55±9.640	890523.	13749.3	641026.	1477.50	1.743±0.008
M_H Window	1651.86±8.410	452470.	5658.90	341359.	1054.40	1.847±0.009
Jet Veto	1171.80±7.090	273041.	3357.40	56084.2	803.50	2.032±0.013
Tagging Mass	331.77±3.770	2751.30	14.90	1627.64	81.80	5.005±0.074
+Tagging P_T	264.01±3.360	1407.10	6.000	1071.78	58.80	5.296±0.092
		Combined Results				
Expected	27738.0±45.69	321211008.	2047700.	14273600.	39288.6	1.510±0.003
Precuts	25954.1±44.18	239287856.	1579867.	13554050.	33929.2	1.627±0.003
Trigger	15184.6±33.76	59830992.	503588.	6765354.	16991.3	1.854±0.004
Central Cut	4434.26±18.26	1828953.	27995.2	1334896.	3041.80	2.482±0.011
M_H Window	3377.68±15.93	938252.	11634.1	719544.	2181.60	2.614±0.014
Jet Veto	2386.63±13.40	565529.	6863.60	117456.	1659.00	2.873±0.020
Tagging Mass	680.95±7.150	5853.43	31.10	3422.48	171.20	7.058±0.139
+Tagging P_T	538.25±6.360	2971.69	12.90	2246.81	122.70	7.442±0.175

Table 5.21: M_H=300 GeV/c^2. H→WW→ $l\nu$jj. Number of events expected after 1 year of running at the high luminosity setting (L=100 fb^{-1}). Pileup has been included.

174
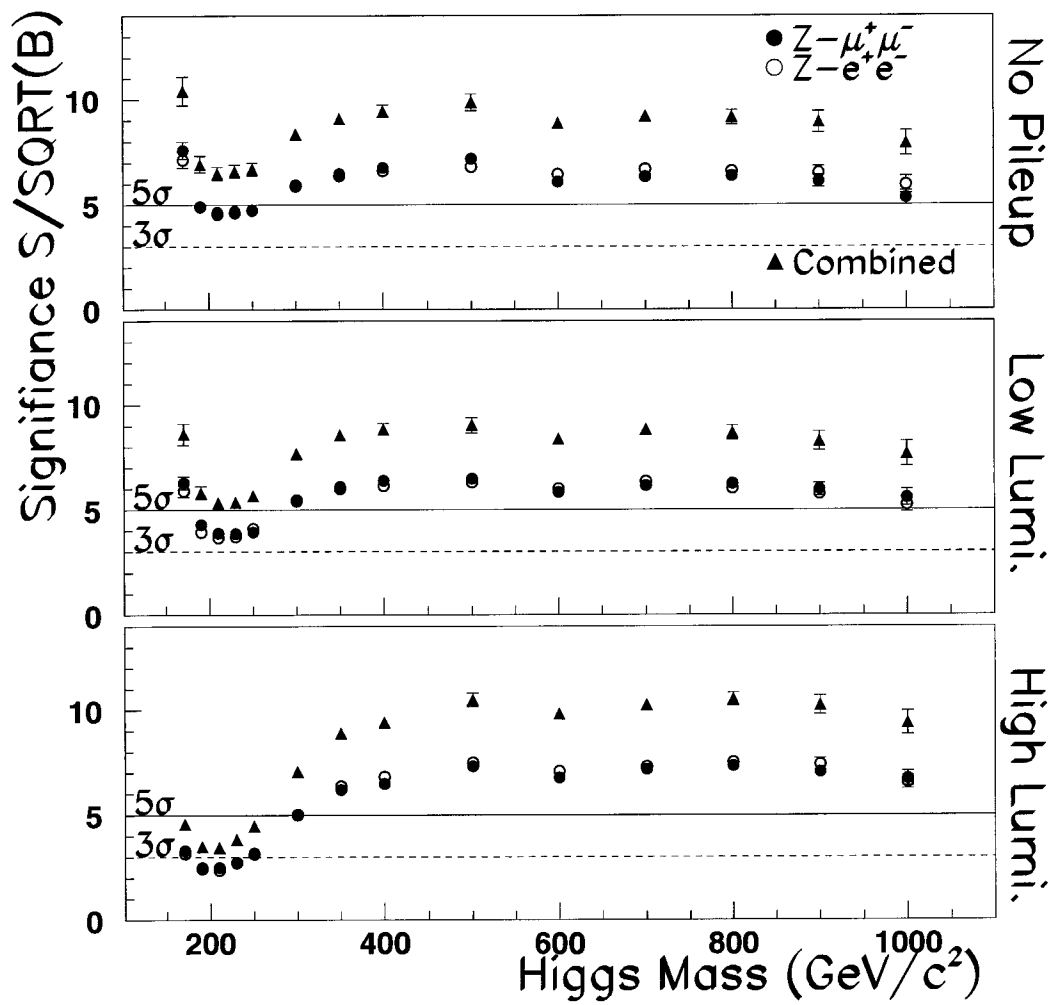
Figure 5.23: Significance (after all cuts excepted the tagging jet transverse momentum) as a function of Higgs mass (H→WW channel) for no luminosity pileup, low luminosity running and an integrated luminosity of 30fb^{-1}, and for high luminosity pileup with 100 fb^{-1}.

175

| Higgs Mass ($\frac{GeV}{c^2}$) | Low Luminosity ($10^{33} cm^{-2} s^{-1}$) | | | | | | High Luminosity ($10^{34} cm^{-2} s^{-1}$) | | |
| | w/o Pileup | | | w/ Pileup | | | w/ Pileup | | |
	Signal	Back.	$\frac{S}{\sqrt{B}}$	Signal	Back.	$\frac{S}{\sqrt{B}}$	Signal	Back.	$\frac{S}{\sqrt{B}}$
170	174.58±3.38	160.43±30.50	13.78±1.58	170.51± 3.34	250.10±43.50	10.78±1.15	290.69±7.96	1057.19 ±154.20	8.94±0.90
180	176.02±3.25	242.14±36.90	11.31±1.07	165.14± 3.15	318.09±46.10	9.26±0.85	302.87±7.77	1539.25 ±186.60	7.72±0.67
190	146.32±2.61	313.03±41.30	8.27±0.69	140.52± 2.57	407.69±52.10	6.96±0.57	271.68±6.50	1891.75 ±203.10	6.25±0.48
200	145.79±2.47	403.60±46.40	7.26±0.54	140.16± 2.41	512.61±56.60	6.19±0.45	262.68±6.03	2498.81 ±235.50	5.25±0.37
210	150.96±2.43	466.97±49.40	6.99±0.48	145.25± 2.38	581.66±59.50	6.02±0.41	275.95±5.97	2788.79 ±247.00	5.23±0.34
220	151.73±2.35	532.09±53.40	6.58±0.43	144.16± 2.29	570.43±55.40	6.04±0.39	279.35±5.80	2955.04 ±248.80	5.14±0.32
230	140.63±2.19	486.36±48.70	6.38±0.42	130.65± 2.11	541.19±52.80	5.62±0.36	279.43±5.62	3021.96 ±250.40	5.08±0.31
240	148.34±2.16	552.83±52.20	6.31±0.39	138.05± 2.09	620.02±57.90	5.54±0.34	278.59±5.41	3084.73 ±248.80	5.02±0.30
250	144.61±2.08	515.45±49.40	6.37±0.40	135.01± 2.01	590.42±56.70	5.56±0.35	277.87±5.24	3025.14 ±245.60	5.05±0.30
300	192.85±2.08	574.56±20.20	8.05±0.23	180.51± 2.02	586.67±20.80	7.45±0.22	538.25±6.36	5231.40 ±122.70	7.44±0.18
350	186.83±1.81	415.80±17.10	9.16±0.28	175.59± 1.75	413.18±17.00	8.64±0.26	519.87±5.48	3154.73 ± 92.00	9.26±0.23
400	171.09±1.47	319.88±15.30	9.57±0.31	160.91± 1.43	327.87±15.50	8.89±0.29	446.51±4.32	2133.75 ± 75.30	9.67±0.26
450	141.64±1.16	217.06±12.60	9.61±0.36	132.00± 1.12	238.14±13.60	8.55±0.32	373.10±3.43	1390.37 ± 60.30	10.01±0.31
500	120.19±0.95	147.12±10.20	9.91±0.42	112.61± 0.91	156.45±10.90	9.00±0.39	318.51±2.81	901.74 ± 48.00	10.61±0.38
550	108.24±0.82	120.50± 3.80	9.86±0.23	102.62± 0.79	120.79± 3.90	9.34±0.22	273.26±2.35	632.54 ± 16.20	10.87±0.23
600	72.28±0.60	66.28± 2.80	8.88±0.26	68.24± 0.58	66.52± 2.80	8.37±0.25	187.04±1.76	354.29 ± 12.10	9.94±0.26
650	94.43±0.63	85.03± 3.30	10.24±0.27	89.42± 0.61	84.77± 3.20	9.71±0.25	268.02±1.94	572.54 ± 15.50	11.20±0.23
700	77.44±0.52	71.03± 3.00	9.19±0.26	73.73± 0.52	69.85± 3.00	8.82±0.25	220.16±1.61	462.81 ± 13.80	10.23±0.23
750	65.85±0.44	51.67± 2.60	9.16±0.29	62.71± 0.43	51.66± 2.50	8.72±0.27	188.47±1.37	340.06 ± 12.00	10.22±0.25
800	52.32±0.37	32.71± 2.00	9.15±0.34	49.46± 0.35	32.53± 2.10	8.67±0.34	148.09±1.13	198.80 ± 9.10	10.50±0.32
850	37.64±0.29	17.34± 1.40	9.04±0.43	35.50± 0.28	18.46± 1.50	8.26±0.40	106.24±0.88	106.17 ± 6.70	10.31±0.41
900	33.49±0.24	14.07± 1.40	8.93±0.51	31.77± 0.24	14.72± 1.40	8.28±0.46	94.80±0.76	85.64 ± 6.10	10.24±0.45
950	31.11±0.22	12.58± 1.20	8.77±0.48	29.38± 0.22	13.17± 1.30	8.10±0.46	87.93±0.70	78.87 ± 5.80	9.90±0.44
1000	21.72±0.17	7.52± 1.00	7.92±0.59	20.68± 0.17	7.26± 1.00	7.68±0.59	62.21±0.54	43.86 ± 4.40	9.39±0.55

Table 5.22: Signal and background rates for the neutral vector boson channels (muon and electron channels included) after the application of all the previously discussed cuts.

176
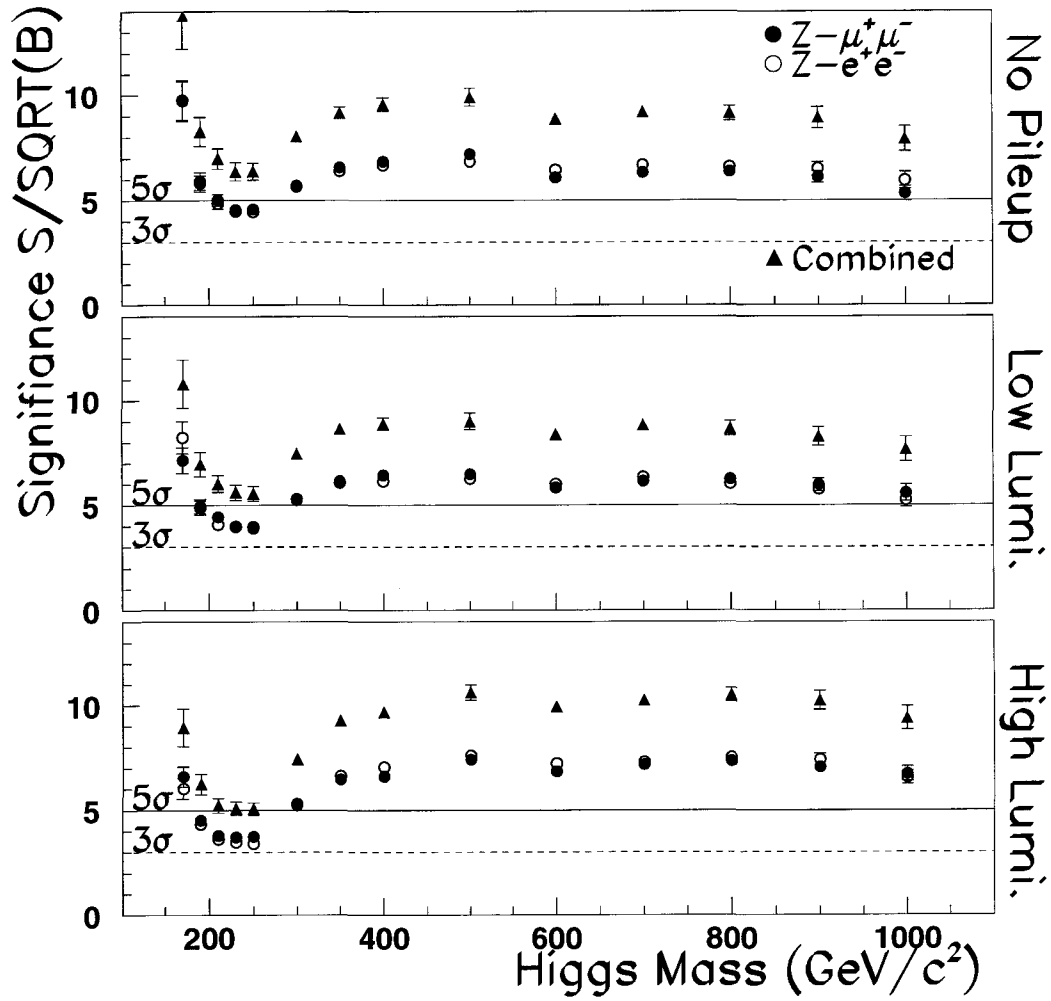
Figure 5.24: Significance (after all the cuts) as a function of Higgs mass(H→WW channel) for no luminosity pileup, low luminosity running and an integrated luminosity of 30fb^{-1}, and for high luminosity pileup with 100 fb^{-1}.

177
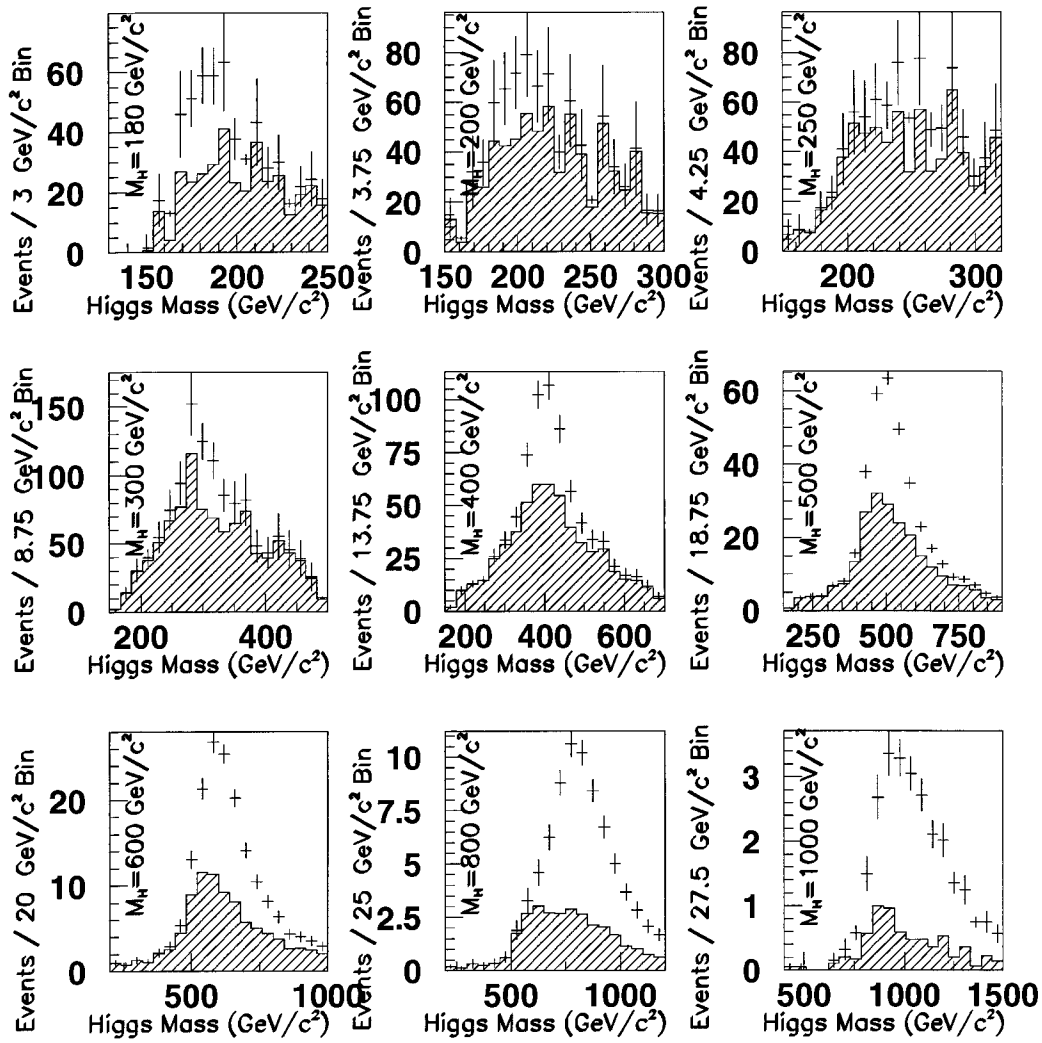
Figure 5.25: Higgs Reconstructed Mass peaks for the channel H→WW→lνjj with an integrated luminosity of 30 fb⁻¹. Pileup has not been included. The histogram gives the expected number of background events, the data points are the expected number of signal and background events. The histogram gives the expected number of background events, the data points are the expected number of signal and background events.

178
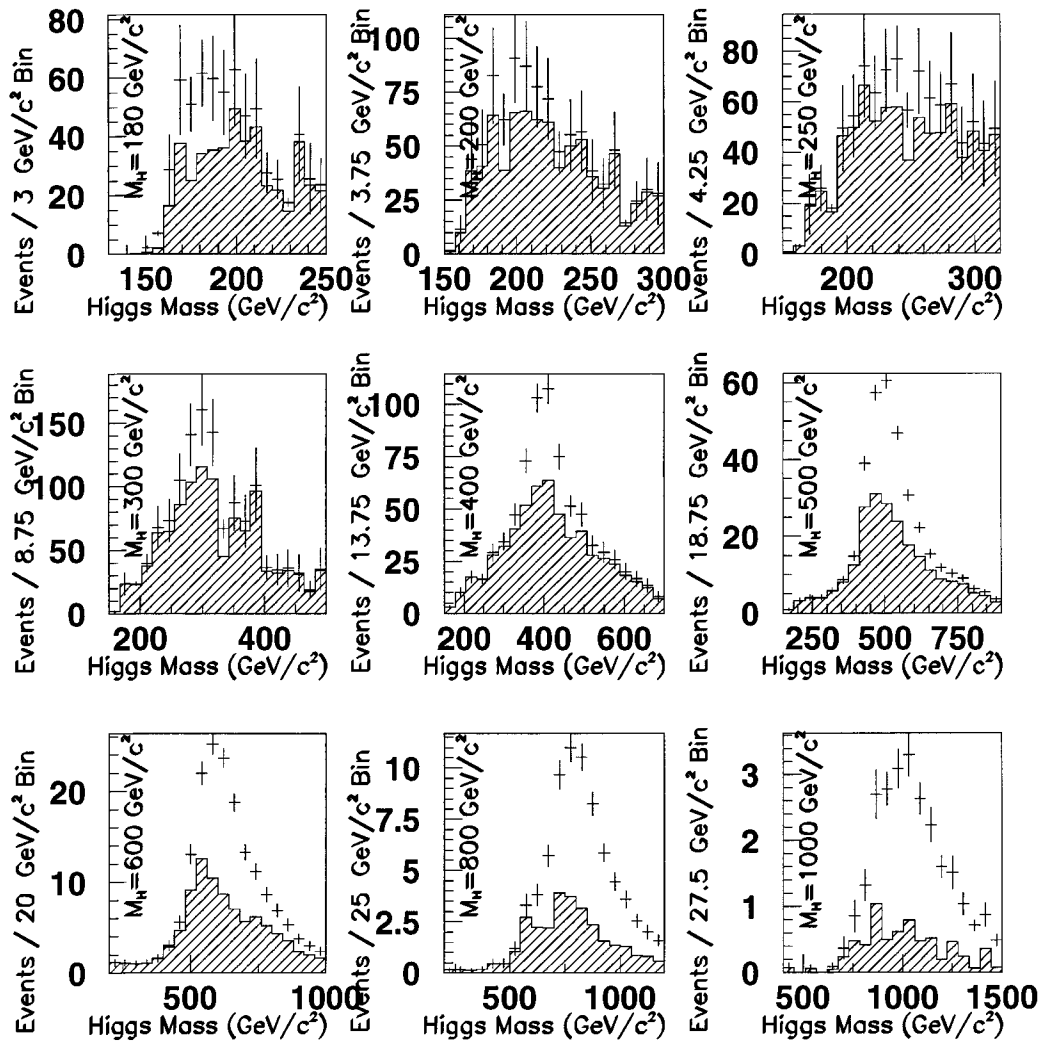
Figure 5.26: Higgs Reconstructed Mass peaks for the channel H→WW→lνjj with an integrated luminosity of 30 fb⁻¹. Low luminosity pileup has been included. The histogram gives the expected number of background events, the data points are the expected number of signal and background events.

179
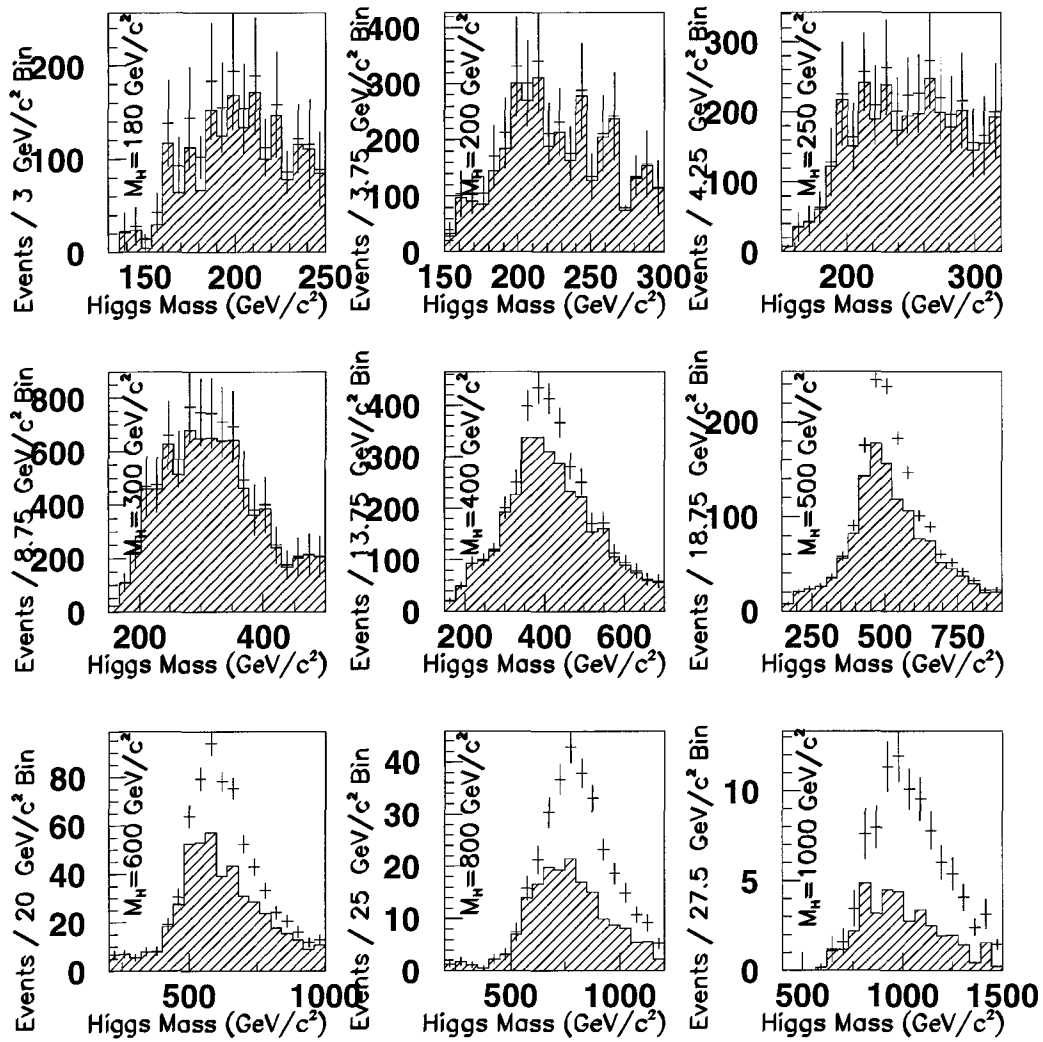
Figure 5.27: Higgs Reconstructed Mass peaks for the channel H→WW→lνjj with an integrated luminosity of 100 fb⁻¹. High luminosity pileup has been included. The histogram gives the expected number of background events, the data points are the expected number of signal and background events.

180

Chapter 6

Discussion of Results

6.1 Combined Results

The objective of this thesis is to develop an analysis method that could be applied to the search for a neutral scalar Higgs boson, produced through vector boson fusion, over a very large Higgs mass range (M_H=170 GeV/c² to 1 TeV/c²) and covering the four physics channels listed in equation 6.1.

$$q_1 q_2 \rightarrow \quad H q_3 q_4 \quad \begin{cases} H \rightarrow ZZ & \rightarrow e^+ e^- jj \\ & \rightarrow \mu^+ \mu^- jj \\ H \rightarrow WW & \rightarrow e^+ \nu_e jj \\ & \rightarrow \mu^+ \nu_\mu jj \end{cases} \qquad (6.1)$$

To produce the required statistics for this analysis we have utilized a modified version of the ATLAS fast simulation package ATLFAST. ATLFAST has been modified [1] to provide improved agreement with the full simulation package DICE/ATRECON[2]. To properly model the running conditions of the ATLAS detector electronic noise and luminosity pileup have been incorporated into this analysis.

The search for the Higgs boson through the neutral vector boson channel, H→ZZ→lljj, was discussed in length in chapter 4. The reconstruction of the Higgs using the charged vector boson channel, H→WW→lνjj was the subject of chapter 5. For both of these channels it was found that there is no significant deviation in signal significance between the muon and electron sectors. Figure 6.1 plots the expected significances for both the H→ZZ channel and the H→WW channel as well as the expected significance when both channels are combined[3]. Figure 6.1 shows that a neutral scalar Higgs boson with a mass above 170 GeV/c² and produced through vector boson fusion can be discovered using the ATLAS detector at

---

[1]Such as, but not limited to, jet reconstruction efficiencies and lepton resolutions etc. This software validation was the subject of chapter 3.

[2]There is a small 5% variation between the modified fast simulation and the full simulation results, which is much smaller than other systematics considered in this chapter so it is not addressed.

[3]The ZZ study only extended down to 190 GeV/c² so the results at the first data point, M_H=170 GeV/c² , is strictly calculated using the WW channel results.

181
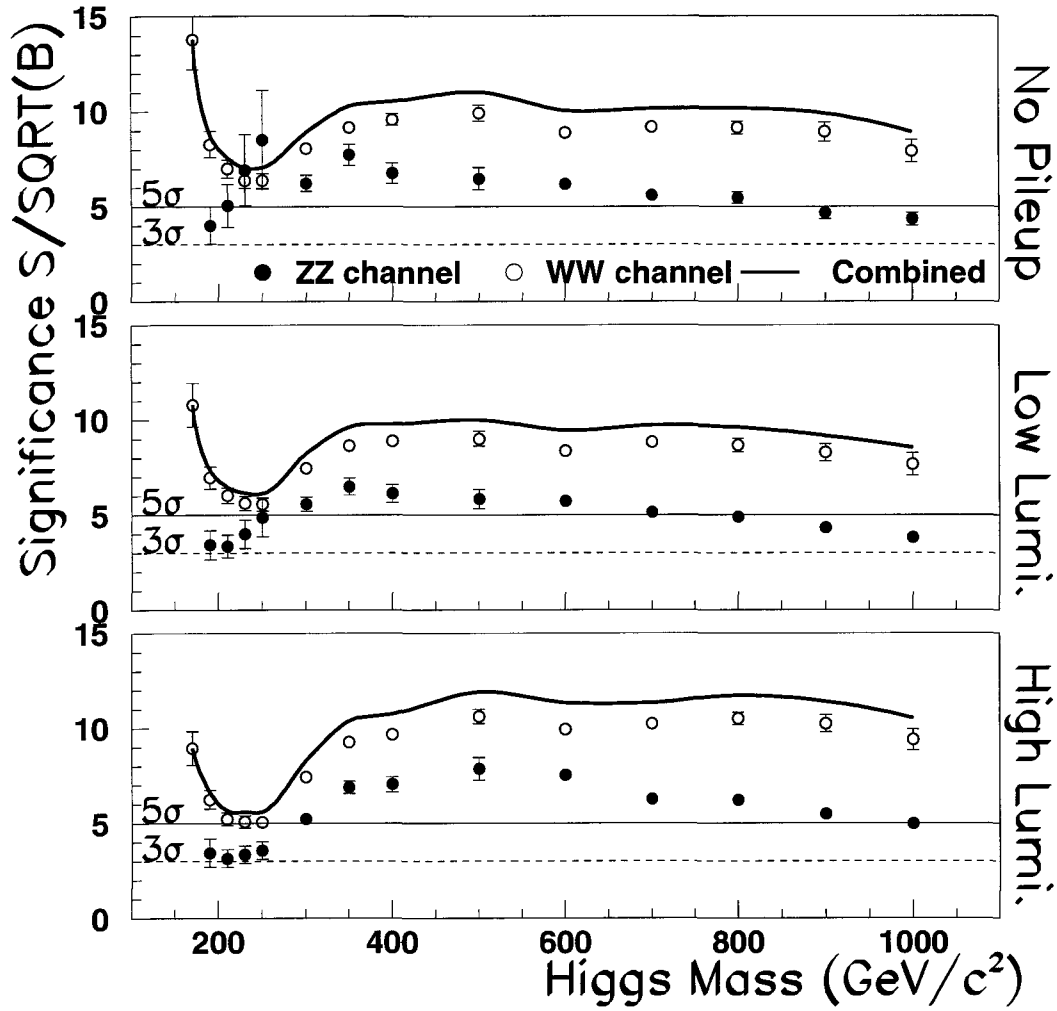
Figure 6.1: The significance as a function of Higgs boson mass for the H→ZZ channel (closed circles),H→WW channel (open circles). The solid line gives the combined results.The solid horizontal line gives the 5 σ discovery threshold and the horizontal dotted line gives the 3σ threshold.

the LHC after 3 years of low luminosity running (collecting 30 fb^{-1}at L=1×10^{33} cm^{-2}s^{-1}) or 1 year of running at high luminosity (collecting 100 fb^{-1}at L=1×10^{34} cm^{-2}s^{-1}).

6.2 Secondary Corrections

6.2.1 Profile Analysis

Conservation of 4-momentum states that for 2→2 background processes such as qj→Z^{0}q or qq→Z^{0}q, once we require the leptonically decaying Z^0 to have large transverse momentum, by demanding a large P$_T$ on the lepton pair, we force the second particle in the final state (in this case a quark or gluon) to have a large transverse momentum as well. This parton

182

Jet-Jet Core	Cells within a radius R(core) of *either jet.*	R(core)=0.2
Jet-Jet Centre	Cells within a radius R(centre) of *either jet.*	R(centre)=0.4
Full jet Pairs	Cells within a radius R(halo) of *either jet.*	R(halo)=0.6

Table 6.1: Jet-pair definitions for use in the profile analysis.
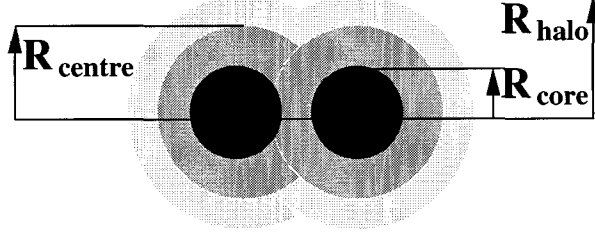
Figure 6.2: The jet-jet pair definitions for the Profile analysis.

may fragment via gluon bremsstrahlung, producing a jet-jet pair which resembles the signal.

The signal jet pair and the background jet pair have quite different origins. The former arises from the decay of a colour singlet Z boson while the later is produced in a colour non-singlet "parton shower". There is more hadronic activity around the jet-jet pair in the Z^0+jets background due to the excess bremsstrahlung. Field and Griffin [67][69] have shown for a 40 TeV proton-proton collider the signal of a heavy mass Higgs can be enhanced by placing a cut on this extra hadronic activity. Following their notation, table 6.1 and figure 6.2 define the profile analysis variables.

Field and Griffin define two complimentary profile variable cuts:

$$F_{E_T} = \frac{E_T(\text{Halo}) - E_T(\text{centre})}{E_T(\text{Halo})}$$

$$\Delta M_{jj} = M_{jj}(\text{Halo}) - M_{jj}(\text{centre})$$

(6.2)

The transverse energy E_T is calculated as the sum over all the cells within a specified radius R of either jet baricentre:

$$E_T = \sqrt{(\sum_{\Delta R \leq R} E_x^{cell})^2 + (\sum_{\Delta R \leq R} E_y^{cell})^2}$$

(6.3)

The invariant mass is calculated as:

$$M_{Halo}^2 = (\alpha E_{recon}^{R=0.6})^2 - (\beta(\alpha P_{recon}^{R=0.6}))^2$$

$$M_{centre}^2 = (\alpha E_{recon}^{R=0.4})^2 - (\beta(\alpha P_{recon}^{R=0.4}))^2$$

(6.4)

The energy calibration factor α (see section 4.2.1) and the momentum correction factor β (see section 4.2.2) are calculated using the reconstructed halo energy of the jet-jet pair

183

$(E_{recon}^{R=0.6})$.

Figure 6.3 compares the distribution of the profile variables, as determined in an ATL-FAST analysis, for the Z+jets background (dashed line) and the Higgs signal (solid line) events. These plots have been produced using data that has passed the central cuts, the central jet veto and possess both a forward and backward tagging jet. There is a clear difference between the line shape for the Higgs signal and the Z+jets background[4].

However, the measured profile of a jet is dependent on the hadronization of the parton prior to reaching the calorimeter **and** the shower spreading that occurs inside the calorimeter. Since ATLFAST does not model the transverse shower spreading that is included in full simulation it is important to validate this cut with fully simulated data.

Since full simulation is both time and memory intensive it is not feasible to evaluate the profile analysis at every Higgs mass studied in this analysis. The profile analysis is recognized as a beneficial cut in the analysis of a heavy Higgs boson so we limit our investigation of this variable to data points between M_H=500 GeV/c^2 and 800 GeV/c^2.

To determine which events were to be fully analyzed the events were first generated using PYTHIA 6.227 and analyzed using ATLFAST. Once it has been established, using ATLFAST, that a particular PYTHIA event has passed the central ZZ cuts (section 4.5) that event is then passed to full simulation. Although these selected events "passed" the central cuts as outlined in ATLFAST, they are still subject to the efficiencies and resolutions of the full simulation package. The output from the full simulation therefore does not automatically "pass" these central cuts.

In total we analyzed about 8,000 $Z^0(\rightarrow \mu\mu)$+jets background events using the M_H=500, 650 GeV/c^2 level cuts and 3500 signal (H$\rightarrow$ZZ$\rightarrow \mu\mu$jj) events at M_H=500, 600, 700, 800 GeV/c^2. An additional 5000 minimum bias events were analyzed with DICE/ATRECON to provide the reservoir from which to sample the pileup events. The two different Z^0+jets background data sets were meant to address the format change of the step 1 cut as outlined in section 4.5.1. At M_H=650 GeV/c^2 the step 1 switches from a cut on P_T^{pair} to a cut on $P_T^{Z\rightarrow jj}$ and $P_T^{Z\rightarrow ll}$.

Figure 6.4 compares the shape of the full and fast simulation profile variable ΔM_{jj}, as defined in equation 6.2, for a 600 GeV/c^2 Higgs (top two graphs) and the Z+jets background

---

[4]It should be noted that while this section discusses the profile analysis in term of the ZZ physics channels it can also be applied to the WW physics channels.
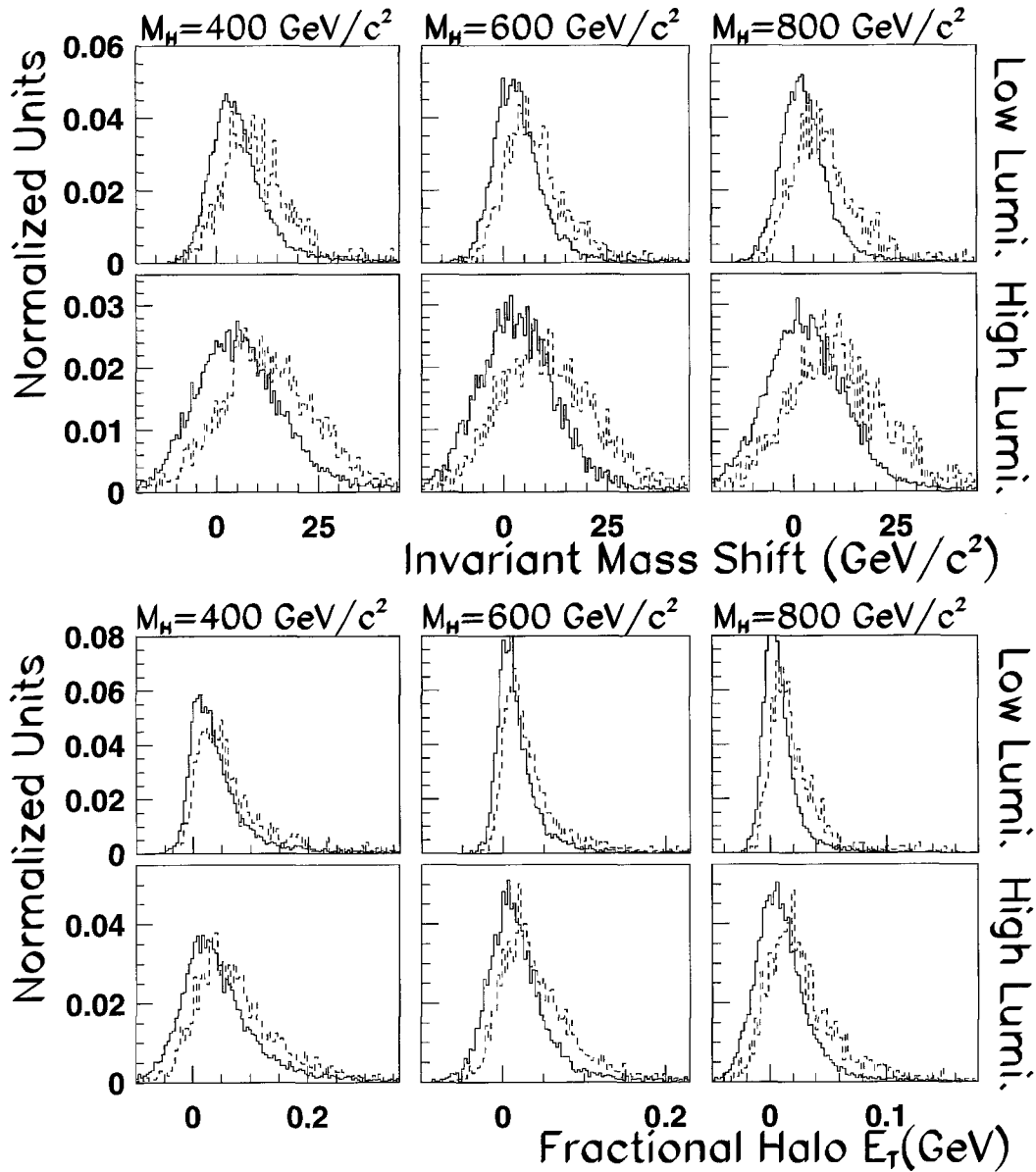
Figure 6.3: A comparison of the profile analysis variables in the low and high luminosity cases at a selection of different masses. The solid line is for the Higgs signal, the dashed line for the Z^0+jets background.

185

Higgs Mass (GeV/c^2)	Low Luminosity (10^{33} cm^{-2}s^{-1}) $\Delta M < 11\,\mathrm{GeV/c^2}$			High Luminosity (10^{34} cm^{-2}s^{-1}) $\Delta M < 15\ \mathrm{GeV/c^2}$		
	Signal	Z+jets	$\frac{S}{\sqrt{B}}$	Signal	Z+jets	$\frac{S}{\sqrt{B}}$
500	69.0%	51.4%	0.964	79.8%	72.9%	0.934
600	78.6%	45.0%	1.17	84.3%	66.7%	1.03
700	76.2%	43.5%	1.16	83.7%	65.6%	1.03
800	75.5%	44.0%	1.14	83.9%	61.4%	1.07
	Average Values					
	76.8	44.2	1.15	84.0	64.6	1.05

Table 6.2: The efficiencies (in %) of the profile analysis on fully simulated signal and background events. The value $\frac{S}{\sqrt{B}}$ is calculated as the efficiency at which the signal events pass the cut divided by the root of the efficiency at which background events pass the same cut.

(bottom two graphs) after the application of the central cuts, the central jet veto and requiring the presence of two tagging jets. The width of the invariant mass shift is similar between full and fast simulations, however the invariant mass shift peaks at a slightly higher value in full simulation. This is expected as the transverse showering in the full simulation will deposit more energy in the halo of the jet-jet pair.

To determine the optimal cut values on the profile variables we maximized the significance value, calculated as $\frac{S}{\sqrt{B}}$ where S is the number of signal events and B is the number of Z+jets background events, using fully simulated data. It was found that the significance was optimized by requiring that $\Delta M_{jj} < 11$ GeV/c^2 at low luminosity and $\Delta M_{jj} < 15$ GeV/c^2 at high luminosity. Including a cut on the second profile variable F_{E_T} improves the significance by less than 0.5%, but greatly reduces our statistics, and is therefore not considered in this analysis.

For the cuts mentioned in the previous paragraph the profile analysis efficiencies, as determined using full simulation, for the Z+jets and H$\rightarrow$ZZ physics channels are given in table 6.2. These full simulations studies show that a significance improvement of about 15% is possible at low luminosity for Higgs boson masses above 600 GeV/c^2. The improvement worsens to only 5% when running at high luminosity.

We can use the signal and background profile efficiencies from table 6.2 to estimate the profile efficiencies of all the processes addressed in this thesis. The efficiencies of the profile cut when applied to the ZZ(WW)-continuum and the $t\bar{t}$ $_W$[5] background processes will be similar to the signal since the jet-pairs in these cases do originate from a colour singlet vector boson. The two jets found in the $t\bar{t}$ $_Z$ background do not originate from a real vector

_____

[5]$t\bar{t}$ $_Z$ refers to the $t\bar{t}$ background of the H$\rightarrow$ZZ study. $t\bar{t}$ $_W$ refers to the $t\bar{t}$ background of the H$\rightarrow$WW study.

186
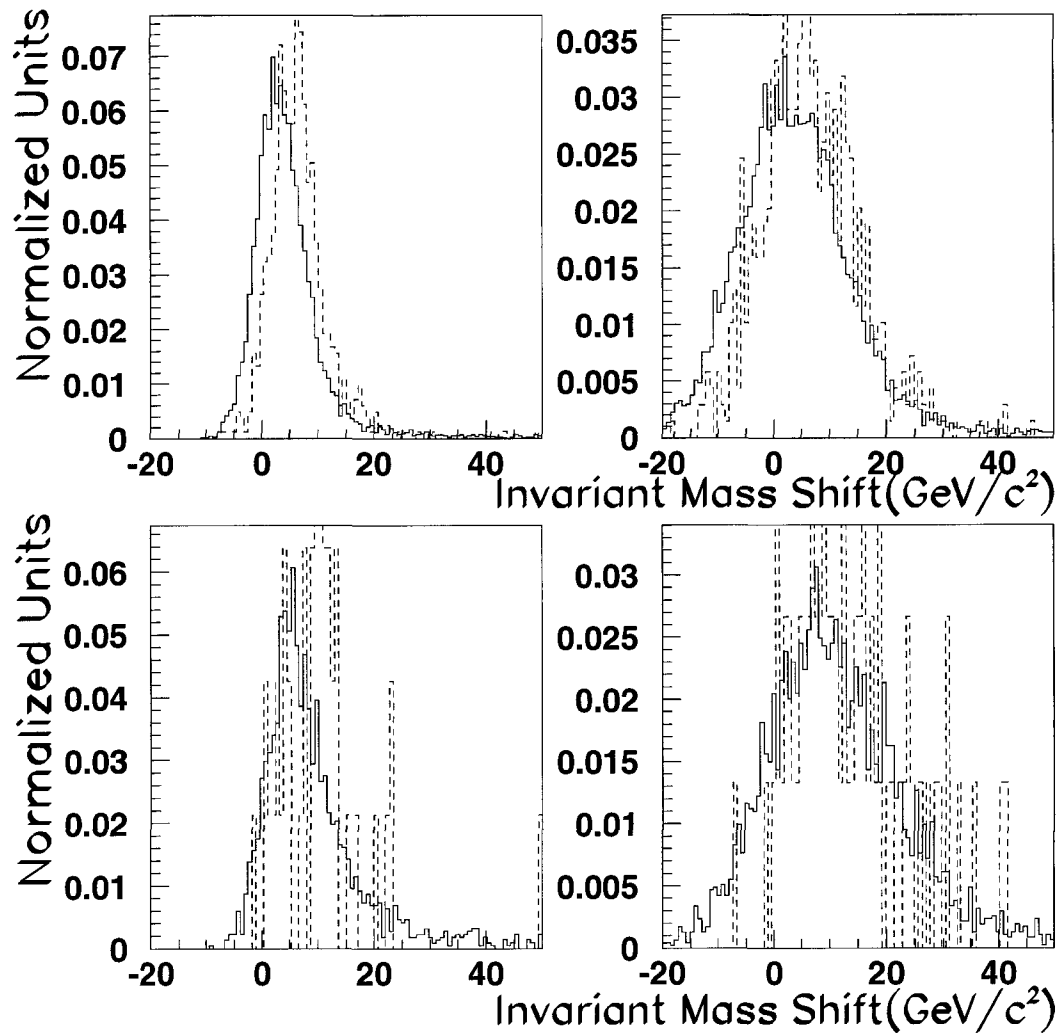
Figure 6.4: The top two plots compare the invariant mass shift of ATLFAST (solid line) to full simulation (dotted line) for a 600 GeV/c² Higgs sample. The plots on the left are in the absence of pileup, the plots on the right have included high luminosity pileup. The bottom two plots compare the Z+jets background.

187

Higgs Signal	Z/W+jets	ZZ/WW	$t\bar{t}_Z$	$t\bar{t}_W$
No Pileup and Low Luminosity (10^{33} cm^{-2}s^{-1})				
76.8	44.2	76.8	44.2	76.8
High Luminosity (10^{34} cm^{-2}s^{-1})				
84.0	64.6	84.0	64.6	84.0

Table 6.3: The efficiencies (in %) of the profile cuts as determined by a full simulation study. The profile analysis cut is conservatively considered for Higgs masses equal to or above 600 GeV/c^2. $t\bar{t}_Z$ is the $t\bar{t}$ background of the H→ZZ study and $t\bar{t}_W$ is the $t\bar{t}$ background of the H→WW study.

boson and will therefore have an efficiency similar to the W(Z)+jets backgrounds. These estimated efficiencies can be found in table 6.3.

Figure 6.5 plots the corrected significances after we have applied the efficiencies from table 6.3 to the results in figure 6.1. We see a noticeable improvement in the expected significance when the profile analysis is applied to the combined results in the no pileup and low luminosity scenarios. There is no noticeable improvement in the combined results at high luminosity. The combined results are not the best estimator in evaluating the benefits of the profile analysis. The profile analysis is a much more beneficial cut for the H→ZZ study versus the H→WW study. We can see in appendix C, that for the heavy Higgs analysis a considerable fraction of the expected background is due to the $t\bar{t}_W$ process. Since the jet-pair for this background process does originate from a colour singlet vector boson the profile analysis is *not* an effective tool in reducing this particular background. The $t\bar{t}$ background channel therefore diminishes the usefulness of the profile analysis in the H→WW studies.

We have demonstrated that placing a cut on the profile of a jet can improve the calculated significance at both the low and high luminosity settings when considering the Z+jets process as the main background. The use of the profile method to enhance the Higgs boson signal from vector boson fusion will be the subject of future studies.

6.3 Jet Reconstruction Efficiencies and their effect on the analysis

One of the differences between this analysis and the vector boson fusion studies previously performed is the inclusion of the jet reconstruction efficiency (previously discussed in section 3.3.4). This was introduced in order that the jet reconstruction rate in ATLFAST matched the jet reconstruction rate in full simulation. We generated and analyzed, with ATLFAST,
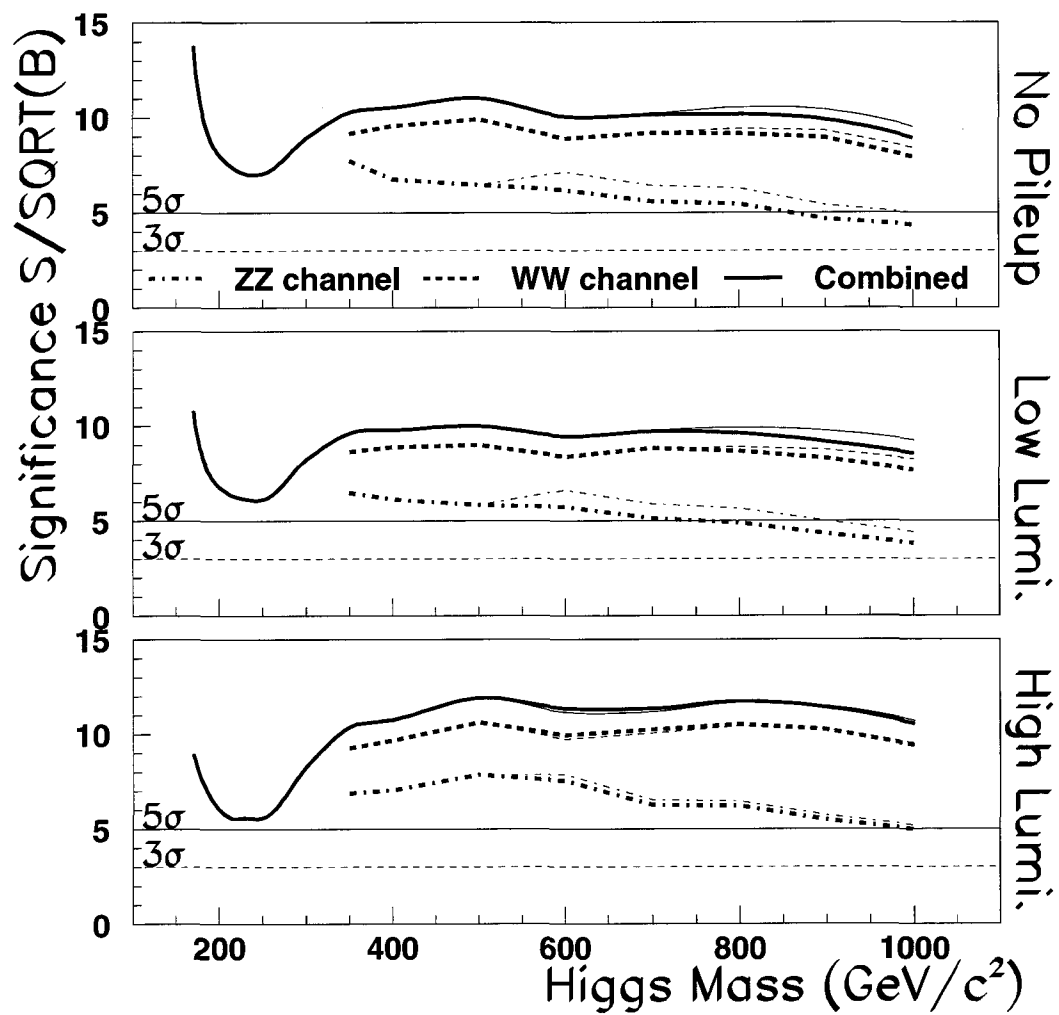
Figure 6.5: The solid line is the expected significance for the combined WW and ZZ physics channels. The dashed line is the expected significance for the WW channel, and the dashed-dotted line is the expected significance for the ZZ channel. The thick lines give the significances without the profile analysis, the thin lines are the significances with the profile analysis applied.

189

a small number of H→WW signal events and W+jets background events[6] without applying the jet reconstruction efficiency to evaluate this difference.

	No Applied Efficiency			Applied Jet Efficiency		
	ϵ(Signal)	ϵ(W+jets)	$\frac{S}{\sqrt{B}}$	ϵ(Signal)	ϵ(W+jets)	$\frac{S}{\sqrt{B}}$
	No Pileup (10^{33} cm^{-2}s^{-1})					
PreCuts	96.7	85.3		96.7	85.3	
M$_W$ Mass Cuts	58.5	14.1		55.9	11.6	
Step 1	33.6	0.675		33.3	0.617	
Step 2	22.4	0.238		22.6	0.237	
Step 3	18.6	0.126		18.7	0.130	
Step 4	18.5	0.126		18.7	0.130	
+Veto+M$_{tag}$ >1 TeV/c^2	7.3	0.00115	21.5	5.07	0.000589	20.89
	High Luminosity Pileup (10^{34} cm^{-2}s^{-1})					
PreCuts	96.6	85.3		96.6	85.3	
M$_W$ Mass Cuts	57.0	19.6		54.0	16.7	
Step 1	30.3	0.998		30.2	0.925	
Step 2	19.2	0.368		20.0	0.387	
Step 3	15.2	0.193		16.3	0.201	
Step 4	15.2	0.193		16.3	0.117	
+Veto+M$_{tag}$ >1 TeV/c^2	5.79	0.0025	11.58	4.27	0.0012	12.3

Table 6.4: A comparison of the cut efficiencies (in %) for the H→WW signal (M$_H$=600 GeV/c^2), and the W+jets backgrounds when jet efficiencies have been turned on/off. The significance estimator is calculated as $\epsilon(Signal)/\sqrt{\epsilon(W + jets)}$, where ϵ(Signal) is the efficiency of the signal and ϵ(W+jets) is the efficiency of the W+jets background.

Table 6.4 (table 6.5) compares the effectiveness of the WW analysis cuts for a 600 GeV/c^2 (300 GeV/c^2) Higgs sample and the W+jets background in the absence of pileup and in the presence of high luminosity pileup. Both tables show that when the jet reconstruction efficiency *is not* applied the rate at which events pass the M$_W$ mass cut is greater than that for when the efficiency *is* applied. This is to be expected as applying the jet efficiencies reduces the number of possible seed cells for consideration in the jet-jet pairing process (section 4.2).

When the central cuts are applied, steps 1 through to step 4, we are selecting events where the jets and muons have larger transverse momentums. The jet reconstruction efficiency, shown originally in figure 3.11, is greater for jets with larger transverse momentum. Thus, by selecting these higher jets we are reducing the differences between the two jet efficiency conditions being studied. After applying the central cuts the signal and background efficiencies (table 6.4, table 6.5), as calculated under these different conditions, are in good agreement at both Higgs masses and both luminosity settings studied.

Both table 6.4 and table 6.5 show that, after applying the central jet veto and a 1 TeV/c^2 invariant mass cut on the tagging jets, there is a significant difference in rate when compar-

---

[6]This study can be taken to represent the ZZ studies as well.

	No Applied Efficiency			Applied Jet Efficiency		
	ϵ(Signal)	ϵ(W+jets)	$\frac{S}{\sqrt{B}}$	ϵ(Signal)	ϵ(W+jets)	$\frac{S}{\sqrt{B}}$
	No Pileup (10^{33} cm^{-2}s^{-1})					
PreCuts	94.5	76.46		94.5	76.5	
M_W Mass Cuts	51.4	12.11		46.6	9.37	
Step 1	30.8	1.27		29.1	1.09	
Step 2	26.5	0.939		26.1	0.846	
Step 3	20.3	0.421		21.1	0.428	
Step 4	16.5	0.189		17.2	0.196	
+Veto+M_{tag} >1 TeV/c^2	4.46	0.0016	11.15	3.41	0.000850	11.7
+Tag Jet P_T cuts	3.56	0.00082	12.45	3.17	0.000751	11.56
	High Luminosity Pileup (10^{34} cm^{-2}s^{-1})					
PreCuts	94.5	76.5		94.4	76.46	
M_W Mass Cuts	50.1	17.0		46.4	13.87	
Step 1	28.1	2.06		27.2	1.8306	
Step 2	22.8	1.47		23.1	1.3815	
Step 3	17.6	0.755		18.6	0.787	
Step 4	16.5	0.622		17.5	0.647	
+Veto+M_{tag} >1 TeV/c^2	3.85	0.0084	4.19	3.03	0.003646	5.01
+Tag Jet P_T cuts	2.32	0.00183	5.41	2.29	0.001694	5.57

Table 6.5: A comparison of the cut efficiencies (in %) for the H→WW signal (M_H=300 GeV/c^2), and the W+jets backgrounds when jet efficiencies have been turned on/off. The significance estimator is calculated as ϵ(Signal)/$\sqrt{\epsilon\text{(W+jets)}}$, where ϵ(Signal) is the efficiency of the signal and ϵ(W+jets) is the efficiency of the W+jets background.

ing the two different jet reconstruction efficiency conditions. When the jet efficiencies are applied the rate at which the W+jets[7] background pass this cut drops more quickly than the H→WW signal. This is also to be expected as figure 4.35 shows that the "tagging" jets in the Z(W)+jets background have lower P_T than the tagging jets in the H→WW(ZZ) signal. Figure 4.35 also shows that the fake tagging jets introduced by pileup occur at very low P_T as well. The background tagging/fake tagging jets will therefore be rejected with a greater frequency than the signal tagging jets. Table 6.4 show that after the tagging jet invariant mass cut, in the absence of pileup, the significance decreases when jet reconstruction efficiency is included. However, since the "fake tags" due to pileup jets are rejected with a greater frequency than any signal or background '"tagging jet" there is an improvement in significance at high luminosity when the jet reconstruction efficiency is included.

It was shown in section 5.4.3 that applying a cut on the transverse momentum of our tagging jets can improve our signal significance at low Higgs masses. Table 6.5 shows that by applying this tagging jet P_T cut we can reduce the differences in calculated rates between the two jet efficiency conditions at low Higgs masses.

While the inclusion of jet efficiencies can significantly alter the number of signal and

---

[7]In this section we are directly addressing the W+jets and H→WW channels. It should be noted that the Z+jets, H→ZZ channels will have a similar behaviour in the cut efficiencies.

Physics Channel	CKIN Cut (GeV/c)	PYTHIA 5.7 (mb)	PYTHIA 6.227 (mb)
Z+jets→ll+jets	0	0.854×10^{-5}	0.107×10^{-4}
(l=e or μ)	40	0.194×10^{-6}	0.216×10^{-6}
	100	0.235×10^{-7}	0.243×10^{-7}
ff→ZZ→lljj	-	0.599×10^{-9}	0.600×10^{-9}
$t\bar{t}$ →llbb$\not{E}_T$	-	6.92×10^{-9}	5.77×10^{-9}
W+jets→lν+jets	0	0.328×10^{-4}	0.384×10^{-4}
	40	0.143×10^{-5}	0.161×10^{-5}
	100	0.177×10^{-6}	0.177×10^{-5}
ff→WW→lνjj	-	0.103×10^{-8}	0.102×10^{-8}
$t\bar{t}$ →lνjjbb (M_{top}=175GeV/c^2)	-	8.64×10^{-7}	5.932×10^{-8}
$t\bar{t}$ →lνjjbb (M_{top}=178GeV/c^2)			5.642×10^{-8}

Table 6.6: A comparison of the background cross-section between two versions of PYTHIA.

background events we would expect to see in the ATLAS detector, particularly at heavier Higgs masses, it does not significantly alter the expected significances.

6.4 Systematic Errors

6.4.1 Cross Section Calculations

The cross-section calculated for both the signal and background processes have large theoretical uncertainties. For example, they can depend on the particular version of PYTHIA being used. The bulk of the previous vector boson fusion studies were performed using PYTHIA 5.7, while this study implemented PYTHIA 6.227. The most significance change between these two versions, with regards to the cross-section, is the evolution of the Parton Distribution Function from CTEQ2L to CTEQ5L.

Table 6.6 shows that the dominant W/Z+jets background cross-section has increased and the $t\bar{t}$ background cross-section has decreased in the newer version of PYTHIA. Increasing the top quark mass from 175 GeV/c^2 to 178 GeV/c^2 does not appreciably change the kinematics of the $t\bar{t}$ process but it does reduce the cross-section by approximately 7%.

Table 6.7 shows that the signal cross-section has decreased for low Higgs masses and slightly increased at heavier Higgs masses for the newer version of PYTHIA. In PYTHIA there are two available methods whereby we can produce a Higgs through vector boson fusion, these processes are listed below.

- 2→3 process: qq→Hqq ; using ISUB=123(WW fusion) and 124(ZZ fusion).

- 2→1 process: WW/ZZ→H ; using ISUB=5(WW fusion) and 8(ZZ fusion).

192

The first method is preferred at low Higgs Masses where the narrow width approximation can be used, this is valid when the width of the particle is much less than its mass, M_H <400 GeV/c^2. The second method is preferred for heavy mass Higgs bosons above 700 GeV/c^2 [8], but is known to overestimate the production cross section for a low mass Higgs. Table 6.7 shows that these two methods predict significantly different cross-sections. For a 600 GeV/c^2 Higgs the 2→3 process calculates a cross-section 25% lower the than 2→1 process.

To evaluate the stability of the cross-sections used in this thesis Leading Order (LO) and Next to Leading Order (NLO) cross-section calculations were performed using VV2H[75] (the PDF used in this program is CTEQ6L) and the results are presented in table 6.7. The NLO cross-sections do not significantly differ from the LO values, but both LO and NLO differ substantially at heavy Higgs masses from the values determined by the LO calculations using PYTHIA 6.227. For this thesis we used the (conservative) cross-sections as calculated by PYTHIA 6.227 and using the 2→3 process.

Higgs Mass PDF (GeV/c^2)	σ(qq→Hqq)(pb)					
	PYTHIA 5.7		PYTHIA 6.227		VV2H[75]	
	CTEQ 2L		CTEQ 5L		CTEQ 6L	
	2→1	2→3	2→1	2→3	LO	NLO
200	4.542	2.76	4.028	2.41 pb	2.57	2.50
400	1.297	0.963	1.119	0.834 pb	0.872	0.860
600	0.452	0.372	0.432	0.352 pb	0.386	0.385
1000	0.0935	0.0787	0.107	0.090 pb	0.106	0.108

Table 6.7: A comparison of the Higgs production cross-section as calculated by different versions of PYTHIA and VV2H[75].

6.4.2 Z+jets/W+jets Monte-Carlo Generators

The largest theoretical uncertainty arises from the determination of the Z/W+jets cross-section. The Z/W+jets datasets used for this analysis were generated using PYTHIA 6.227. The Feynman diagram for the Z+jets process as modelled in PYTHIA is given in figure 6.6(a). PYTHIA can only produce Z + N jets (where N≥1) through the inclusion of: initial/final state radiation and multiple interactions[9]. A sample Feynman diagram for the Z + 4 jets process is given in 6.6(b). The PYTHIA authors recognize the inadequacies of their Monte-Carlo program when it comes to modelling the Z+N jets process by introducing a K-factor to account for the expected increase in cross section due to higher order QCD processes. The K-factor is a multiplicative factor that scales the calculated PYTHIA cross-

---

[8]Cavasinni et al. [62] have shown that there are no significant kinematic differences between these two methods.

[9]Multiple interactions are secondary parton collisions within the interacting proton-proton pair.
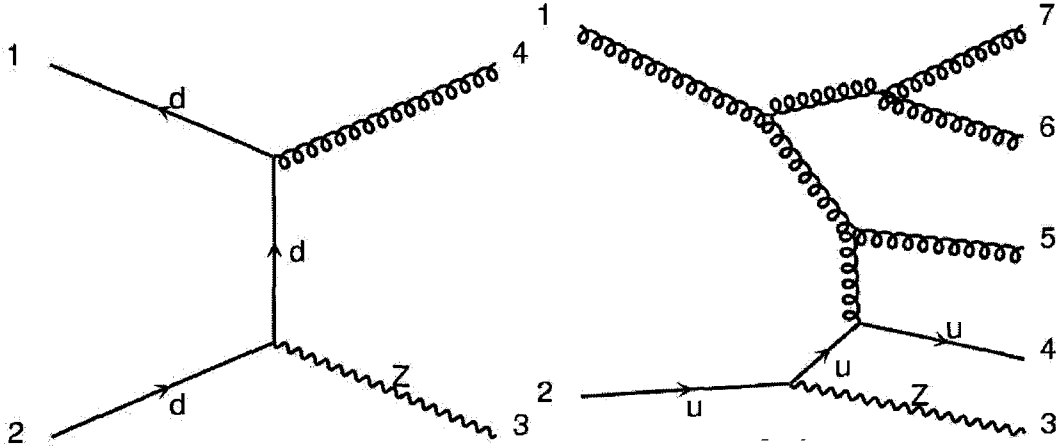
Figure 6.6: (a) The Feynman diagram for the Z+1 jet process. (b) The Feynman diagram for the Z+4 jets process.

Group	ME Generator	Z(W)+jets Correction	tt̄ correction
Savard et al. [15]	n/a	1.60	1.50
Cobal et al. [78]	VECBOS	2.0	-
Cavasinni et al. [62]	K-factor	1.5	1.5
Le Maner et al. [73]	MADGRAPH	4.0	-
Asai et al. [13]	COMPHEP	-	2.1

Table 6.8: The correction to the PYTHIA cross-sections due to higher order QCD diagrams contributing to the main background processes.

section.

Leading Order Matrix Element Monte-Carlo generators have been used in previous studies[15][62][78] to estimate the difference in cross-section for the higher order diagrams contributing to tche W/Z+jets (as well as tt̄) processes. Next to Leading Order corrections are expected to be small in comparison to the differences between PYTHIA and the Leading Order ME MC generators. Other studies[13][73][74] have linked the Matrix-Element Monte-Carlo generators directly to a shower program (such as PYTHIA/HERWIG) which is then processed by ATLFAST. Table 6.8 summarizes the differences between the Matrix-Element cross section and the default PYTHIA cross-section as estimated by these studies. The ME generator always predicts a bigger cross-section. The values in table 6.8 indicate a mean correction value of approximately 2.

6.4.3 Precut Bias

Limiting the time required to generate and analyze sufficient statistics for this analysis required the addition of generator level and cell level precuts. The form and efficiencies of
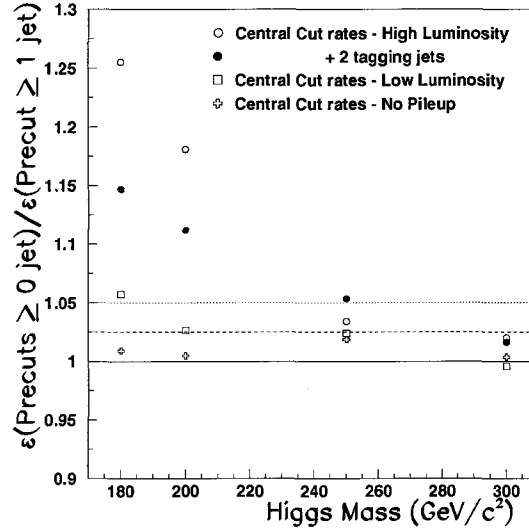
Figure 6.7: The fraction of events passing the central ZZ analysis cuts when the applied precut is ≥0 jets divided by the fraction of events passing that same cut when the precut requires ≥1 jet as a function of Higgs mass.

these precuts are detailed in the opening sections of chapter 4 and chapter 5. For example, to pass the precut that is implemented for the ZZ analysis requires an event to have 2 central leptons and greater than or equal to one reconstructed jet. Figure 4.4 shows that, for the H→ZZ signal, there is no difference in precut efficiency when this requirement is relaxed to be 2 central leptons and greater than or equal to zero jets. However, the precut efficiency increases (the rejection rate decreases) in the Z+jets background, for CKIN values less than 40 GeV/c, when the relaxed precut is applied. The concern is that an event which has 0 jets at the precut level, may actually have 4 jets when pileup is included. The strict precut will reject this event and we have therefore underestimated our actual background rate.

In this section we generated (and analyzed) a smaller sample of $Z(\rightarrow \mu^+\mu^-)$+jets background events (setting CKIN(3)=0 GeV/c) with these relaxed precuts ($\geq$ 0 jets) to prove there is no systematic bias introduced into the final analysis by using the stricter precuts ($\geq$ 1 jets). To validate this hypothesis we evaluate the expression[10]:

$$\frac{\epsilon(\geq 0\text{jets})}{\epsilon(\geq 1\text{jets})} \tag{6.5}$$

where $\epsilon(\geq 0jets)$ ($\epsilon(\geq 1jets)$) is the efficiency of the Z+jets background to pass a given cut when generated with the loose (strict) precuts. If no systematic bias was introduced we expect this ratio to be 1.

---

[10]Similar arguments can be made for the W+jets physics channel.

195

Figure 6.7 shows when no pileup is present the efficiency ratio of equation 6.5, after the application of the ZZ central cuts (section 4.5), is consistent with unity. Figure 6.7 also shows that when low or high luminosity pileup is included, the loose precut method predicts that a greater number of background events will pass the central cuts (versus the strict precut method). The loose precut method predicts that 25% more background events will pass the central cuts at the high luminosity setting and 5% more background events at the low luminosity setting. As the Higgs mass increases the central cuts select progressively higher E_T events, reducing the jet contribution from pileup, bringing the two precut methods into agreement at about M_H=300 GeV/c^2.

When tagging jets are identified[11] the difference at high luminosity shrinks to only 15% at M_H=180 GeV/c^2. While not shown on the graph the requirement of 2 tagging jets at low luminosity brings the two precut methods into agreement within statististical error. Requiring that the invariant mass of the two tagging jets be greater than 1 TeV/c^2 reduces the difference in efficiencies at high luminosity to be less than 6%. The reduced statistics produced for the loose precut dataset do not allow more restrictive cuts on the tagging jets to be investigated. In section 4.5.5 we introduced strong cuts on the transverse momentum of the tagging jets. Applying this cut should further reduce the difference between these two precut methods.

The strict precut requirement implemented in this analysis did not introduce any significant systematic bias into the final results.

6.4.4 Minimum Bias Events/Pileup Prescription

It is shown in this thesis that the rate at which the dominant Z^0+jets/W+jets backgrounds pass our analysis cuts is greatly affected by the addition of luminosity pileup. A number of different prescriptions for minimum bias events have been employed in ATLAS analyses. It is therefore necessary to evaluate the effect that changing the minimum bias prescription would have on our results. For this thesis we implemented the default MSEL=2 setting of PYTHIA. The relevant parameters for this minimum bias setting are given in the first column of table 6.9. To estimate the effect of changing the minimum bias prescription on this analysis we ran a smaller Z+jets background set that implemented the minimum bias prescription from [79], the parameters of which are given in the second column of table 6.9. The low P_T Z+jets background is the most sensitive to the introduction of pileup, so the Z+jets sample was generated without any cut on the hard P_T(CKIN(3)=0 GeV/c) of the

---

[11]Two tagging jets are found in opposite hemispheres with E_T > 15 GeV/c , but no mass or energy cuts are applied.

196

	Switch	Implemented	CDF Tuned[79]
Generated Processes	ISUB	91,92,93,94,95	92,93,94,95
Cross-Section(mb)		101.5	79.3
PDF		CTEQ5L	CTEQ5L
Multiple Interaction	MSTP(81)	1	1
Model	MSTP(82)	4	4
PT min	PARP(82)	2.0	1.8
	PARP(89)	1800	1000
	PARP(90)	0.25	0.16
Core Radius	PARP(84)	0.4	0.4
Gluon Production	PARP(85)	0.9	0.33
Mechanism	PARP(86)	0.95	0.66
α_s and K-factors	MSTP(2)	1	1
	MSTP(33)	0	0
Regulating Initial	PARP(67)	1	1
State Radiation			

Table 6.9: PYTHIA parameters for minimum bias pileup events.

process.

The biggest difference between these two prescriptions is which physics processes are included. The CDF tuned minimum bias definition excludes the proton-proton elastic scattering process (ISUB=91). In these interactions the protons remain intact (versus the diffractive process) scatter only slightly and continue down the beam pipe. The elastic scattering events therefore do not deposit any energy into the ATLAS calorimetry.

The TDR states that there will be, on average, 23 minimum bias[12] events per bunch crossing at high luminosity. However, the default PYTHIA process predicts 25.4 events per bunch, while the CDF tuned[79] setting predicts only 19.8 events/bunch. We wish to evaluate the effect on the background rate due to changing the process and not the mean number of events so for both settings in this analysis we will deposit the accepted value of 23 minimum bias events/bunch over the 24 bunch crossings that are included in the shaping functions. Since both process add the same number of pileup events, but on average 22% of the interactions in the events in case 1 are p-p elastic scattering, the second pileup scenario will deposit more energy and consequently give a higher fake tag rate than the MSEL=2 pileup setting.

Table 6.10 shows that for the two mass values studied (M_H=200, 300 GeV/c^2) the change in pileup prescription has a minimal effect on the low luminosity result, about 5% increase after the application of the level 4 central cuts, the central jet veto and a cut on

---

[12] It is actually a Poisson distribution with a mean value of 23 (2.3) at high (low) luminosity.

197

	Low Luminosity		High Luminosity	
	MSEL=2	CDF Tuned	MSEL=2	CDF Tuned
M_H=200 GeV/c² Cuts				
Pre-cuts	18.8	18.8	18.8	18.8
M_Z Mass Cuts	0.93	0.969	1.19	1.24
Step 1	0.375	0.384	0.574	0.597
Step 2	0.375	0.384	0.574	0.597
Step 3	0.125	0.124	0.258	0.262
Step 4	0.00967	0.00998	0.0308	0.0357
+Veto+$M_{tag} > 1TeV/c^2$	0.0000349	0.0000363	0.000186	0.000210
M_H=300 GeV/c² Cuts				
Pre-cuts	18.8	18.8	18.8	18.8
M_Z Mass Cuts	0.910	0.944	1.16	1.22
Step 1	0.0323	0.0332	0.0443	0.0456
Step 2	0.0233	0.0231	0.0349	0.0364
Step 3	0.00913	0.00914	0.0168	0.0178
Step 4	0.00354	0.00345	0.00736	0.00836
+Veto+$M_{tag} > 1TeV/c^2$	0.0000141	0.0000152	0.0000500	0.0000726

Table 6.10: A comparison of cut efficiencies (in%) at low and high luminosity for the Z+jets (CKIN(3)=0) background when different pileup prescriptions are used.

the tagging jet invariant mass (although the statistics limit the accuracy to be within about 10%). However at high luminosity we do see an increase in the background rate of 10% to 45%. This observed increase is an overestimate of the true change since for this analysis we have included 23 minimum bias events per bunch, but from cross-sectional considerations only expect 19.8. We estimate a systematic error of 30% associated with the minimum bias prescription.

6.4.5 Estimated Signal Significances including Systematic Errors

The most significant systematic errors are summarized as follows:

- The NLO signal cross-section calculated using VV2H is 10% larger than the cross-section determined with PYTHIA 6.227.

- The Z/W+jets and $t\bar{t}$ background cross-sections calculated using Matrix Element Monte-Carlo generators are, on average, a factor of 2 larger than those determined with PYTHIA 6.227.

- Changing the minimum bias prescriptions increases the background rate by 5% at low luminosity and approximtely 30% at High luminosity.

Figure 6.8 plots the expected signal significance, as a function of Higgs mass and luminosity, when the WW and ZZ studies are combined. The thin black band corresponds to the statistical error. The hatched band includes the statistical and systematic errors added in quadrature. The lower limit on this band was determined by using the conservative

198
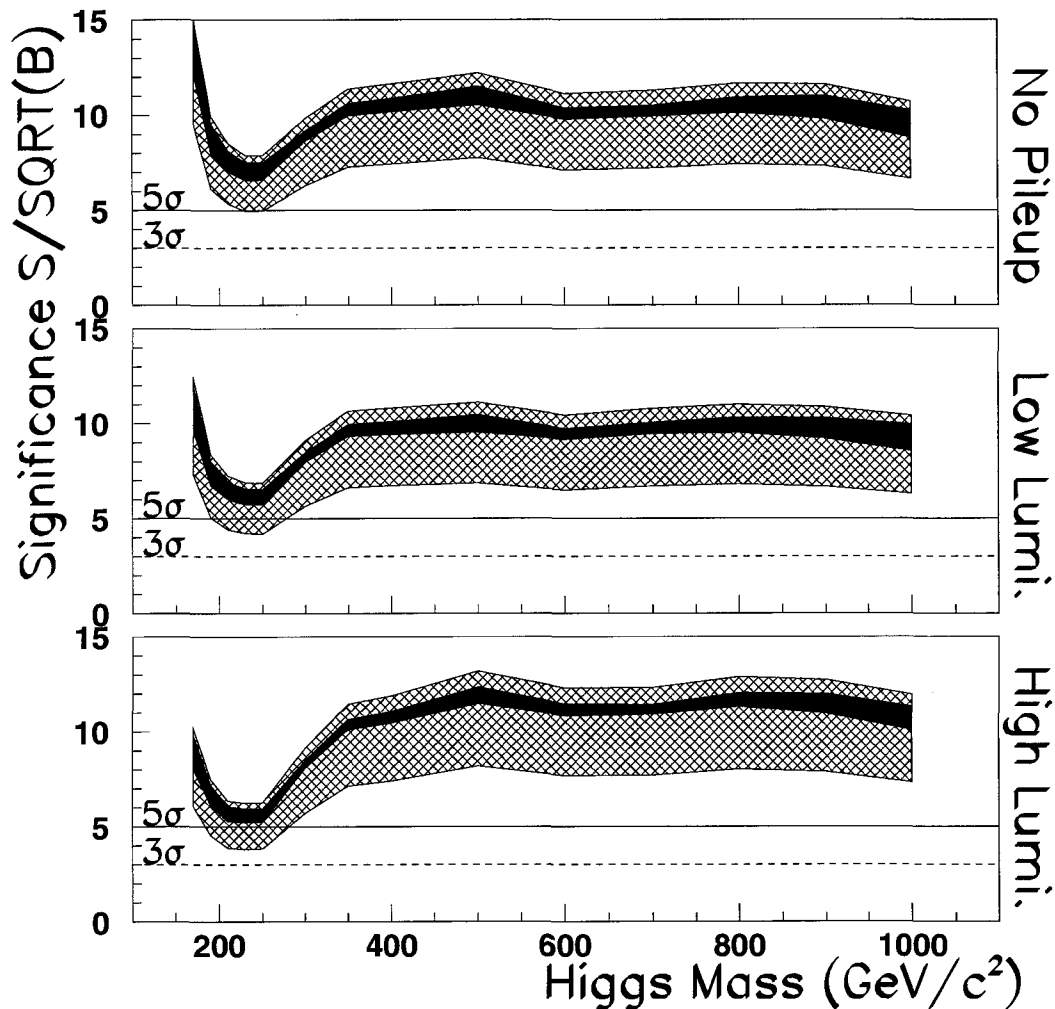
Figure 6.8: The expected signal significance for the combined ZZ and WW studies. The dark band gives the statistical error, the hatched band includes the systematic and statistical errors added in quadrature.

estimate for the signal cross-section and the strongest correction to the backgrounds. The upper limit of this band has been calculated using a 10% increase to the signal cross-section and no increase to the background rate.

Taking the lower limits of these significance plots in figure 6.8 to be a conservative estimate on the signal significance this analysis indicates that a Higgs boson can be discovered after :

1. 3 years at low luminosity (collecting 30 fb^{-1}at L=1×10^{33} cm^{-2}s^{-1}) if its mass were between 170 GeV/c^2 < M_H < 190 GeV/c^2 or above 280 GeV/c^2 ;

2. 1 year at high luminosity (collecting 100 fb^{-1}at L=1×10^{34} cm^{-2}s^{-1}) if its mass were

199

between 170 GeV/c^2 < M_H < 180 GeV/c^2 or above 290 GeV/c^2.

6.5   Previous Studies

The vector boson fusion Higgs' papers that currently exist in the High Energy Physics literature usually have limited scope, concentrating on either the ZZ or WW physics channels, or covering a very limited mass range. Furthermore, most are fast simulation studies that do not accurately model the response of the ATLAS detector, nor do they accurately model the effects of high luminosity pileup. This section summarizes these previous vector boson fusion studies.

Zmushko *et al.* [14] and Savard *et al.* [15], both using PYTHIA 5.7 as the Monte-Carlo generator, searched for a Higgs boson produced through vector boson fusion and examined the Higgs boson mass range M_H=600 GeV/c^2 to 1 TeV/c^2. Zmushko performed a fast simulation study that did not include jet reconstruction efficiencies but did include a default 90% lepton identification efficiency. To simulate pileup they overlayed 40 minimum bias events on top of their signal event. In this case their significance predictions at high luminosity are going to be conservative. Savard performed a fast simulation study that included full simulation jet and lepton reconstruction efficiencies and addressed pileup through the addition of "fake jets" to their fast simulation results. Cavasinni *et al.* [62] performed a fast simulation study with ATLFAST, also using PYTHIA 5.7 as a Monte-Carlo generator, and extended the explored Higgs boson mass range down from M_H=600 GeV/c^2 to 300 GeV/c^2. Cavasinni used the built-in ATLFAST energy smearing algorithms to model pileup. Their significances at high luminosity are therefore optimistic. Le Maner *et al.* [73] repeated the fast simulation Cavasinni study using a newer Monte-Carlo generator (PYTHIA 6.203). As in the Cavasinni study, Le Maner assumed a 90% lepton reconstruction efficiency and did not modify the jet reconstruction efficiency. Asai *et al.* [13] is a fast simulation study that incorporated jet and lepton reconstruction efficiencies to investigate the physics channel H→WW$^{(*)}$. A small subset of their study included a Higgs boson with mass between M_H=170-190 GeV/c^2 and decaying to 2 real W-bosons. The Le Maner and Asai studies were both performed in the absence of pileup[13].

The H→ZZ channel has been studied less frequently than the H→WW channel due to its smaller cross-section. Savard *et al.* [15] and Zmushko *et al.* [14] briefly addressed the ZZ channel for a Higgs with mass M_H > 600 GeV/c^2. Cranmer *et al.* performed

---

[13]The terminology in these papers is slightly different than that used in this thesis. The "low luminosity" studies referenced in these papers have actually been performed when pileup is *not* present. In the following tables we compare our results in the absence of pileup to the low luminosity results of these papers.

200

Group	Comments	Higgs Mass $\frac{GeV}{c^2}$	Efficiencies Lept.	Jet	Pileup	$\frac{S}{\sqrt{B}}$	This thesis
Savard *et al.* [15]	Efficiencies	1000	N	N	None	11.4	7.9
	Not Included	800	N	N	None	13.0	9.1
	Full sim	1000	Y	Y	None	10.3	7.9
	Corrected	800	Y	Y	None	11.8	9.1
	Corrected with	1000	Y	Y	High	11.6	9.4
	full sim. rates	800	Y	Y	High	13.2	10.5
Zmushko *et al.* [14]	H→WW	1000	Y	N	None	12.5	7.9
		800	Y	N	None	11.9	9.1
		600	Y	N	None	15.2	8.9
		1000	Y	N	High	11.3	9.3
		800	Y	N	High	11.4	10.5
		600	Y	N	High	14.3	9.9
Cavasinni *et al.* [62]	PYTHIA 5.7	600	Y	N	None	6.7	8.9
		300	Y	N	None	7.0	8.0
	Using ATLFAST	600	Y	N	High	14.0	9.9
	"pileup"	300	Y	N	High	7.5	7.4
Le Maner *et al.* [73]	PYTHIA 6.203	300	Y	N	None	9.2	8.0
	Mass Window					12.9	
Asai *et al.* [13]	PYTHIA 6.1	190	Y	Y	None	3.0	8.3
		180	Y	Y	None	3.5	11.3
		170	Y	Y	None	4.6	13.8

Table 6.11: A summary of previous Higgs studies for the H→WW physics channel. The thesis results presented in this table do not include the profile analysis cut.

a fast simulation study, excluding jet and leptons efficiencies, using PYTHIA 6.1 as the Monte-Carlo generator. One of the physics channels they studied was H→ZZ→qqll covering a Higgs boson mass range of 190 GeV/c² to 500 GeV/c². This study used a single set of cuts, optimized at M_H=300 GeV/c², and applied them to the full mass range studied.

The H→WW studies have been summarized in table 6.11 and the H→ZZ studies summarized in table 6.12. With the exception of the Cavasinni study[62], all the quoted studies searching for a Higgs boson with a mass equal to or below 300 GeV/c² utilized a mass ($M_H \pm 2\sigma$) window around the Higgs resonance peak to optimize the significance.

There is little internal consistency between the previous results presented in tables 6.11 and 6.12. Consider the WW physics channel in the absence of pileup. The Zmushko M_H=800 GeV/c² /1 TeV/c² predictions are similar to the Savard predictions but differ significantly (by a factor of 2) from the Cavasinni predictions at M_H=600 GeV/c². The Le Maner 300 GeV/c² results are close to the Cavasinni 300 GeV/c² results but still differ.

Group	Comments	Higgs Mass $\frac{GeV}{c^2}$	Efficiencies Lept.	Jet	Pileup	$\frac{S}{\sqrt{B}}$	This thesis
ATLAS TDR	Full simulation	1000	Y	Y	High	2.9	5.0
		800	Y	Y	High	3.3	6.2
Savard [15]	Modified ATLFAST	1000	Y	Y	High	3.4	5.0
		800	Y	Y	High	3.8	6.2
		1000	Y	Y	None	<3.0	4.3
		800	Y	Y	None	<3.0	5.5
Zmushko [14]	High Lumi	1000	Y	N	High	4.3	5.0
		800	Y	N	High	6.7	6.2
		600	Y	N	High	5.1	7.5
Cranmer[74]	PYTHIA 6.1	190	N	N	None	3.47	4.0
		200	N	N	None	3.76	4.3
		300	N	N	None	3.75	6.2
		500	N	N	None	1.98	6.5

Table 6.12: A summary of previous Higgs studies for the H→ZZ physics channel. The thesis results presented in this table do not include the profile analysis cut.

While there may be little consistency in the available data there are several trends that can be extracted, and are confirmed in the results of this thesis. Asai *et al.* show that for a Higgs boson with mass below 190 GeV/c² and decaying through the channel, H→WW, there is an increase in significance as the Higgs mass is lowered to 160 GeV/c². This increase is due to the increasing Higgs production cross-section at low M_H and the dominance of the H→WW decay below the 2 M_Z threshold. The Savard and Zmushko publications show that decreasing the Higgs mass from M_H=1000 GeV/c² to 600 GeV/c² is followed by an *increase* in significance, while Cranmer indicates that for Higgs bosons masses above 200 GeV/c² increasing the Higgs mass is followed by an increase in significance. At low Higgs masses the kinematics of the signal and the backgrounds are very similar giving a poor significance value. As the Higgs mass is increased the kinematics of the Higgs signal starts to significantly differentiate itself from the background allowing for the application of stronger analysis cuts that can improve the signal significance. As the Higgs mass increases, beyond about 600 GeV/c², the falling Higgs production cross-section dominates over any benefit obtainable by increasing the analytical cuts on the kinematics of the event and the significance will start to decrease.

Savard, Zmushko [15] have shown that for a heavy Higgs $M_H > 600$ GeV/c², 1 year at high luminosity running (collecting 100 fb⁻¹at 10³⁴ cm⁻²s⁻¹) will give a better significance value than 3 years at low luminosity (collecting 30 fb⁻¹at 10³³ cm⁻²s⁻¹). Naively, one would suggest that this increase in statistics would improve the significance by a factor of $\sqrt{3.3}$,

202

but we must remember that when increasing the luminosity the fake tag rate increases as well. The actual increase in significance is therefore less than that suggested by the simple statistical approach. None of these studies suggest what happens when the luminosity is increased for a low mass Higgs boson. The results presented in this thesis suggest that, for a low mass Higgs boson, 3 years at low luminosity gives a better significance value than 1 year at high luminosity. In this case, the increase in significance due to statistics is offset due to the increased sensitivity of the low mass Higgs studies to the presence of pileup jets.

For a heavier Higgs boson with a mass above 600 GeV/c^2, the signal significances obtained in this analysis, in the H→WW channel, are slightly lower than the previous Zmushko and Savard studies. Both the previous studies and the results presented in thesis give clear discovery potential for a heavy Higgs boson in this channel. The signal significances presented in this thesis for the H→ZZ channel are higher than the previous studies (in the same Higgs boson mass range). The cuts applied to the ZZ channels in the previous studies are not as strong (for example the cuts placed on $P_T^{Z→jj}$ were less than the equivalent cut on $P_T^{Z→jj}$) as the comparable WW channel suggesting that these previous studies have not been optimized. For the heavy Higgs masses studied by Zmushko and Savard (M_H >600 GeV/c^2) the small mass difference between the W/Z bosons should have a negligible effect on the kinematics of the events, resulting in kinematic cuts that should be similar between the two channels (see, for example, the cut values given in table 4.5 and table 5.8).

For a Higgs boson with a mass below 300 GeV/c^2 the signal significances determined in this thesis are higher than those presented by Asai[13] (H→WW) and Cranmer[74] (H→ZZ). This can be attributed to two factors. We have introduced in this several new analysis cuts that are optimally suited for a lighter Higgs: P_T^{pair}; the azimuthal angle cut between the reconstructed vector bosons; and, a much stronger cut on the transverse momentum of the tagging jets. Secondly, these previous studies have interfaced Matrix Element based Monte-Carlo generators to ATLFAST to analyze the dominant $t\bar{t}$ and Z/W+jets backgrounds. Asai *et al.* utilized COMPHEP and Cranmer *et al.* used MADGRAPH and ALPGEN. Matrix Element Monte-Carlo generators generally predict larger background cross sections than similar calculations using PYTHIA, and consequently predict a lower significance value.

Chapter 7

Conclusions

The origins of electroweak symmetry breaking and the generation of mass in the Standard Model has yet to be confirmed. The discovery of the Higgs boson is a key element in the confirmation of the Standard Model. Since the mass of the Higgs boson is not constrained by the Standard Model the search must extend from the experimental lower limit set by the LEP project of 114.4 GeV/c^2 (with 95% confidence[20]) to the 1 TeV/c^2 unitarity limit. The ATLAS experiment at the Large Hadron Collider is designed to search for a Higgs boson over the allowed mass range.

The objective of this thesis is to evaluate the discovery potential of a Higgs boson produced through vector boson fusion over a very large Higgs boson mass range, 170 GeV/c$^2 \leq$ M$_H \leq 1$ TeV/c^2, using an accurate model of the ATLAS detector that includes the effects of electronic noise and luminosity pileup. The analyses reported here were carried out using an upgraded version of the ATLAS fast simulation program, ATLFAST, modified to bring it into better agreement with the full simulation program DICE/ATRECON.

Higgs boson production was studied utilizing the mixed decay mode vector boson fusion channels: the H→WW→l$\nu_l$jj and the H→ZZ→l$^+$l$^-$jj channels(where l=e,μ). These mixed decay modes were chosen to exploit the cleanliness of the leptonic decay and the increased cross-section of the hadronic branching fractions.

As far as we are aware this is the first time these Higgs productions modes have been studied in a single analysis over the heavy Higgs mass range 170 GeV/c$^2 \leq$ M$_H \leq 1$ TeV/c^2, in the presence of low and high luminosity pileup. To facilitate such an analysis a jet-jet reconstruction and calibration method was developed that can be applied over the very large vector boson transverse momentum ranges studied in this thesis. Several cuts that were not applied in previous analyses in this area are shown to improve the signal significance measurement of a lighter Higgs boson with mass, in the range 170 GeV/c^2 to 300 GeV/c^2

, have been introduced. It is also shown that the signal significance can be enhanced for a heavy Higgs boson by introducing a cut on the profile of the reconstructed jet-jet pair.

If the Standard Model Higgs boson exists the theoretical uncertainties in the cross-section of the dominant Z/W+jets and $t\bar{t}$ backgrounds is the limiting factor in the determination of the signal significance. We have evaluated this, and other systematic uncertainties, to maximally reduce, within error, the signal significance and thus obtain a conservative significance estimate.

This thesis demonstrates that even when the large systematic uncertainties are taken into account a neutral scalar Higgs boson would be discovered using the vector boson channels studied in this thesis after 3 years of running at low luminosity (collecting 30 fb^{-1}at L=1×10^{33} cm^{-2}s^{-1}) if its mass were between 170 GeV/c^2 < M_H < 190 GeV/c^2 or above 280 GeV/c^2. The Higgs boson can also be discovered after running at 1 year at high luminosity (collecting 100 fb^{-1}at L=1×10^{34} cm^{-2}s^{-1}) if its mass were between 170 GeV/c^2 < M_H < 180 GeV/c^2 or above 290 GeV/c^2. An important caveat here is that it will, of course, be necessary to thoroughly understand and calibrate the ATLAS detector. This could no doubt add to the time estimates given above.

Bibliography

[1] J. Incandela [CDF Collaboration], Nuovo Cim. **109A**, 741 (1996).

[2] K. Kodama *et al.* [DONUT Collaboration], Phys. Lett. B **504**, 218 (2001) [arXiv:hep-ex/0012035].

[3] S. Eidelman *et al.* [Particle Data Group Collaboration], Phys. Lett. B **592** (2004) 1.

[4] S. Weinberg, Phys. Rev. Lett. **19**, 1264 (1967).

[5] S. L. Glashow, Nucl. Phys. **22** (1961) 579.

[6] H. Fritzsch, M. Gell-Mann and H. Leutwyler, Phys. Lett. B **47**, 365 (1973).

[7] S. N. Ahmed *et al.* [SNO Collaboration], Phys. Rev. Lett. **92**, 181301 (2004) [arXiv:nucl-ex/0309004].

[8] L. C. Tu, J. Luo and G. T. Gillies, Rept. Prog. Phys. **68**, 77 (2005).

[9] P. W. Higgs, Phys. Rev. Lett. **13**, 508 (1964).

[10] C. Quigg "Gauge Theories of the Strong,Weak, and Electromagnetic Interactions", 1997

[11] T. D. Lee and C. N. Yang, Phys. Rev. **104**, 254 (1956).

[12] D. L. Rainwater and D. Zeppenfeld, Phys. Rev. D **60**, 113004 (1999) [Erratum-ibid. D **61**, 099901 (2000)] [arXiv:hep-ph/9906218].

[13] S. Asai *et al.*, Eur. Phys. J. C **32S2**, 19 (2004) [arXiv:hep-ph/0402254].

[14] S. Zmushko, D. Froidevaux, L. Poggioli, ATLAS Internal Note ATL-PHYS-97-103, (1997)

[15] P. Savard, UMI-NQ35637

[16] A. Erdogan, D. Froidevaux, V. Klyukhin and V. Zmushko, Phys. Atom. Nucl. **57**, 274 (1994) [Yad. Fiz. **57**, 290 (1994)].

[17] M. Spira, arXiv:hep-ph/9711394.

[18] A. Djouadi, arXiv:hep-ph/9712334.

[19] T. Akesson *et al.* [ATLAS TRT Collaboration], Nucl. Instrum. Meth. A **412**, 200 (1998).

[20] R. Barate *et al.* [ALEPH Collaboration], Phys. Lett. B **565**, 61 (2003) [arXiv:hep-ex/0306033].

[21] S. H. Chuang [the CDF collaboration], FERMILAB-CONF-04-267-E *Prepared for 6th International Conference on Hyperons, Charm and Beauty Hadrons (BEACH 2004), Chicago, Illinois, 27 Jun - 3 Jul 2004*

[22] B. W. Lee, C. Quigg and H. B. Thacker, Boson Phys. Rev. Lett. **38**, 883 (1977).

[23] C. Quigg, Acta Phys. Polon. B **30**, 2145 (1999) [arXiv:hep-ph/9905369].

[24] A. Djouadi, Acta Phys. Polon. B **27**, 3837 (1996) [arXiv:hep-ph/9612361].

[25] G. Ridolfi, arXiv:hep-ph/0106300.

[26] [LEP Collaboration], arXiv:hep-ex/0312023.

[27] J. R. Ellis, A. B. Lahanas, D. V. Nanopoulos and K. Tamvakis, Phys. Lett. B **134**, 429 (1984).

[28] R. Barbieri, Riv. Nuovo Cim. **11N4**, 1 (1988).

[29] G. Weiglein, Nature **429** (2004) 613.

[30] t. L. E. Group, t. S. Electroweak and H. F. Groups [OPAL Collaboration], arXiv:hep-ex/0412015.

[31] P. Azzi *et al.* [CDF Collaborattion], arXiv:hep-ex/0404010.

[32] V. M. Abazov *et al.* [D0 Collaboration], Nature **429**, 638 (2004) [arXiv:hep-ex/0406031].

[33] M. S. Chanowitz, arXiv:hep-ph/0304199.

[34] M. E. Peskin and J. D. Wells, Phys. Rev. D **64**, 093003 (2001) [arXiv:hep-ph/0101342].

[35] G. P. Zeller *et al.* [NuTeV Collaboration], Phys. Rev. Lett. **88**, 091802 (2002) [Erratum-ibid. **90**, 239902 (2003)] [arXiv:hep-ex/0110059].

[36] CERN-AB-2003-008 *Prepared for 12th Chamonix LHC Performance Workshop, Chamonix, France, 3-8 Mar 2003*

[37] Engineering Data Management System, LHC Technical Committe
https://edms.cern.ch/cedar/plsql/cedarw.site_home
"LHC Parameters for Nominal Proton Performance Version 4.0 ", 7th LTC Meeting, 28/05/2003
"LHC Parameters for Ultimate Proton Performance Version 3.0 ", 14th LTC Meeting, 15/10/2003

[38] G. Jarlskog and D.. Rein, "Large Hadron Collider. Proceedings, Workshop, Aachen, Germnay, October 4-9 1990," CERN-90-10

[39] LHC Project Report 724

[40] W. W. Armstrong *et al.* [ATLAS Collaboration], "ATLAS: Technical proposal for a general-purpose p p experiment at the Large Hadron Collider at CERN," CERN-LHCC-94-43

[41] "ATLAS: Detector and physics performance technical design report. Volume 1," CERN-LHCC-99-14

[42] "ATLAS detector and physics performance. Technical design report. Vol. 2," CERN-LHCC-99-15

[43] [ATLAS Collaboration], CERN-LHCC-97-16

[44] [ATLAS Collaboration], CERN-LHCC-97-17

[45] The ATLAS Collaboration - ATLAS SCT - INDET-NO-085 int. rep (1995)
ATLAS: Technical propsal for a general purpose pp experiment at the Large Hadron Collider at CERN, CERN/LHCC 94-43, LHCC/P2(1994)

[46] Peter Loch, private communication. May, 2000.

[47] T. Sjostrand, L. Lonnblad and S. Mrenna, arXiv:hep-ph/0108264.

[48] E. Richter-Was, D. Froidevaux,L. Poggioli,
http://atlas.web.cern.ch/Atlas/GROUPS/PHYSICS/HIGGS/Atlfast.html

[49] The GEANT team, GEANT – Dectector Description and Simulation Tool, The CERN computing center. CERN Program Library Long Writeup W5013

[50] A. Amorim *ATGEN 2.0 Users Guide*, 1996 ,ATL-SOFT-96-033

[51] R. Brun and D. Lienart, CERN-Y250

[52] G. Azuelos et al. *Physics in ATLAS at a possible upgraded LHC* , ATLAS Internal Note, ATL-PHYS-2001-002(2000)

[53] J. Baines, Private Communication, Oct. 2003

[54] B. Andersson, G. Gustafson and B. Soderberg, Z. Phys. C **20**, 317 (1983).

[55] C. Peterson, D. Schlatter, I. Schmitt and P. M. Zerwas, Phys. Rev. D **27**, 105 (1983).

[56] H. L. Lai *et al.* [CTEQ Collaboration], Eur. Phys. J. C **12**, 375 (2000) [arXiv:hep-ph/9903282].

[57] M. H. Seymour, Phys. Lett. B **354**, 409 (1995) [arXiv:hep-ph/9505211].

[58] https://csr.phys.ualberta.ca/twiki/bin/view/Computing/THORLinuxCluster

[59] http://guide.westgrid.ca

[60] "ATLAS detector and physics performance. Technical design report. Vol. 2," CERN-LHCC-99-15, Figure 15-30

[61] M. Griffiths, B. Heinemann, G. Manca "Measurement of the Fake Rate of Electrons and Muons", CDF/ANAL/EXOTIC/CDFR/7479 (2005)

[62] V. Cavasinni,D. Costanzo,S. Lami,F. Spano, ATL-PHYS-98-127(1998)

[63] A. Erdogan, D. Froidevaux, S. Klioukhine, S. Zmushko, ATL-PHYS-92-008(1992)

[64] P. Savard The W-jetjet and Top Mass Reconstructions with the ATLAS Detector, ATLAS internal note CAL-NO-092,1997

[65] V. Cavasinni,D. Costanzo, I. Vivarelli "Forward Tagging and Jet Veto Studies for Higgs Events Produced via Vector Boson Fusion", ATL-PHYS-2002-008

[66] R. N. Cahn, S. D. Ellis, R. Kleiss and W. J. Stirling, Phys. Rev. D **35**, 1626 (1987).

[67] R. D. Field and P. A. Griffin, Phys. Rev. D **48**, 3167 (1993) [arXiv:hep-ph/9303289].

[68] N. Kauer, T. Plehn, D. L. Rainwater and D. Zeppenfeld, Phys. Lett. B **503**, 113 (2001) [arXiv:hep-ph/0012351].

[69] R. D. Field and P. A. Griffin, "Enhancing the heavy Higgs $\to$ W W signal at hadron hadron colliders," Phys. Rev. D **50**, 302 (1994).

[70] D. Espriu and J. Manzano, arXiv:hep-ph/0109059.

[71] T. R. Merz, "Monte Carlo studies for the hadronic calibration of the H1 calorimeter with HERA events. (In German),"

[72] T. Sjostrand, Comput. Phys. Commun. **82**, 74 (1994).

[73] C. Le Maner, L. Poggioli, H. Przysiezniak,E. Richter-Was Search for $qqH\to qqWW\to qql\nu jj$ (M_H=300 GeV/c^2) using the ATLAS detector", ATL-COM-PHYS-2003-028

[74] K.Cranmer,Y.Q. Fang, B. Mellado,S. Paganis,W. Quayle and Sau Lan Wu, Prospectes for Higgs Searches via VBF at the LHC with the ATLAS detector,ATL-PHYS-2004-005

[75] M. Spira,VV2H Program, http://people.web.psi.ch/spira/proglist.html

[76] A. Djouadi, J. Kalinowski and M. Spira, Comput. Phys. Commun. **108**, 56 (1998) [arXiv:hep-ph/9704448].

[77] F. Maltoni and T. Stelzer, MadEvent: Automatic Event Generation with MAD-GRAPH, hep-ph/0208156(2002)

[78] M. Cobal, D. Costanzo, S. Lami. ATLAS Internal Note PHYS-NO-84(1996)

[79] Brian Cox, Private Communication

Appendix A

H→ZZ Data Tables

	Signal	Z^0+jets	ff→ ZZ	$t\bar{t}$	δ Back	$\frac{S}{\sqrt{B}}$
		$Z \to \mu^+\mu^-$ channel				
Expected	879.30±1.880	320400000.	17988.	169740.	14289.6	0.050±0.000
Precuts	760.65±1.750	60243796.	12360.	154496.	6196.42	0.100±0.000
Trigger	645.65±1.610	10627444.	7799.0	116402.	2602.82	0.200±0.000
Central Cut	76.36±0.550	24933.0	68.2	101.16	126.06	0.480±0.004
M_H Window	67.46±0.520	7678.17	31.6	45.44	69.96	0.770±0.007
Jet Veto	37.42±0.390	2853.82	7.87	8.920	42.65	0.700±0.009
Tagging Mass	12.64±0.220	36.33	0.05	0.260	4.810	2.090±0.142
+Tagging P_T	6.630±0.160	4.460	0.01	0.110	1.690	3.100±0.576
		$Z \to e^+e^-$ channel				
Expected	879.30±1.790	320400000.	17988.	169740.	14795.0	0.050±0.000
Precuts	729.94±1.630	57660332.	11580.	150021.	6276.51	0.100±0.000
Trigger	587.74±1.460	9646750.	7136.6	108128.	2567.51	0.190±0.000
Central Cut	73.91±0.520	23443.3	65.9	124.08	126.56	0.480±0.004
M_H Window	65.13±0.490	7417.96	30.3	56.92	71.19	0.750±0.007
Jet Veto	37.18±0.370	2848.17	7.74	10.97	44.11	0.690±0.009
Tagging Mass	12.97±0.220	42.36	0.05	0.240	5.380	1.990±0.130
+Tagging P_T	6.900±0.160	5.470	0.01	0.080	1.930	2.930±0.514
		Combined Results				
Expected	1758.60±3.670	640800000.	35976.	339480.	29084.7	0.069±0.000
Precuts	1490.59±3.380	117904128.	23940.	304517.	12472.9	0.137±0.000
Trigger	1233.39±3.070	20274194.	14935.	224530.	5170.33	0.272±0.001
Central Cut	150.27±1.070	48376.3	134.1	225.24	252.62	0.681±0.007
M_H Window	132.59±1.010	15096.1	62.0	102.36	141.15	1.073±0.013
Jet Veto	74.60±0.760	5701.99	15.6	19.89	86.76	0.985±0.017
Tagging Mass	25.61±0.440	78.69	0.10	0.500	10.19	2.876±0.234
+Tagging P_T	13.53±0.320	9.930	0.02	0.190	3.620	4.249±0.859

Table A.1: M_H=200 GeV/c^2. H→ZZ→lljj. Number of events expected after 3 years of running at the low luminosity setting (L=30 fb^{-1}). Pileup has not been included.

211

	Signal	Z^0+jets	ff→ ZZ	t$\bar{t}$	δ Back	$\frac{S}{\sqrt{B}}$
			$Z\rightarrow \mu^+\mu^-$ channel			
Expected	879.30±1.880	320400000.	17988.	169740.	14289.6	0.050±0.000
Precuts	760.65±1.750	60243796.	12360.	154496.	6196.42	0.100±0.000
Trigger	647.03±1.610	12461291.	7982.5	117611.	2818.40	0.180±0.000
Central Cut	73.37±0.540	30278.7	71.4	115.35	138.92	0.420±0.003
M_H Window	64.33±0.510	10173.2	34.3	55.92	80.52	0.640±0.006
Jet Veto	33.71±0.370	3460.53	7.86	11.34	46.96	0.570±0.007
Tagging Mass	11.43±0.210	50.98	0.06	0.320	5.700	1.590±0.093
+Tagging P_T	6.090±0.160	5.740	0.01	0.080	1.910	2.520±0.419
			$Z\rightarrow e^+e^-$ channel			
Expected	879.30±1.790	320400000.	17988.	169740.	14795.0	0.050±0.000
Precuts	729.94±1.630	57660332.	11580.	150021.	6276.51	0.100±0.000
Trigger	587.49±1.460	11361744.	7294.5	109158.	2786.35	0.170±0.000
Central Cut	71.87±0.510	28650.5	69.7	139.49	139.91	0.420±0.003
M_H Window	62.76±0.480	9889.70	33.5	68.44	82.20	0.630±0.005
Jet Veto	34.05±0.350	3471.23	7.98	13.64	48.70	0.580±0.007
Tagging Mass	11.66±0.210	51.92	0.05	0.300	5.960	1.610±0.096
+Tagging P_T	6.070±0.150	8.200	0.01	0.080	2.370	2.110±0.306
			Combined Results			
Expected	1758.60±3.670	640800000.	35976.	339480.	29084.7	0.069±0.000
Precuts	1490.59±3.380	117904128.	23940.	304517.	12472.9	0.137±0.000
Trigger	1234.52±3.070	23823036.	15277.	226769.	5604.75	0.252±0.001
Central Cut	145.24±1.050	58929.2	141.2	254.84	278.83	0.596±0.006
M_H Window	127.09±0.990	20062.9	67.9	124.36	162.72	0.893±0.011
Jet Veto	67.76±0.720	6931.76	15.8	24.98	95.66	0.811±0.014
Tagging Mass	23.09±0.420	102.90	0.11	0.620	11.66	2.268±0.169
+Tagging P_T	12.16±0.310	13.94	0.02	0.160	4.280	3.236±0.573

Table A.2: M_H=200 GeV/c^2. H→ZZ→lljj. Number of events expected after 3 years of running at the low luminosity setting (L=30 fb^{-1}). Pileup has been included.

212

	Signal	Z^0+jets	ff$\rightarrow$ ZZ	$t\bar{t}$	δ Back	$\frac{S}{\sqrt{B}}$
			$Z\rightarrow \mu^+\mu^-$ channel			
Expected	2931.00±6.250	1068000000.	59960.	565800.	47632.0	0.090±0.000
Precuts	2535.49±5.820	200812656.	41200.	514985.	20654.8	0.180±0.000
Trigger	2120.26±5.320	37639816.	24501.	379089.	8943.09	0.340±0.001
Central Cut	242.51±1.800	319356.	388.2	1124.31	823.70	0.430±0.003
M_H Window	203.55±1.650	134759.	202.9	655.51	535.08	0.550±0.005
Jet Veto	111.56±1.220	61775.4	52.1	190.43	362.27	0.450±0.005
Tagging Mass	34.78±0.680	1193.87	0.75	4.480	50.36	1.000±0.029
+Tagging P_T	12.28±0.400	27.62	0.05	0.620	7.660	2.310±0.322
			$Z\rightarrow e^+e^-$ channel			
Expected	2931.00±5.970	1068000000.	59960.	565800.	49316.8	0.090±0.000
Precuts	2433.13±5.440	192201120.	38600.	500070.	20921.7	0.180±0.000
Trigger	1957.76±4.880	30460554.	21774.	337327.	8329.69	0.350±0.001
Central Cut	242.83±1.720	306962.	386.8	1610.38	836.13	0.440±0.003
M_H Window	202.07±1.570	130722.	203.3	935.23	545.65	0.560±0.004
Jet Veto	114.81±1.180	61934.8	54.1	272.99	375.57	0.460±0.005
Tagging Mass	35.26±0.650	1181.90	0.81	5.850	51.88	1.020±0.029
+Tagging P_T	12.94±0.400	20.50	0.04	1.150	6.840	2.780±0.446
			Combined Results			
Expected	5862.00±12.22	2136000000.	119920	1131600.	96948.8	0.127±0.000
Precuts	4968.62±11.26	393013760.	79800.	1015056.	41576.5	0.250±0.001
Trigger	4078.02±10.20	68100368.	46276.	716416.	17272.8	0.491±0.001
Central Cut	485.34±3.520	626318.	775.0	2734.69	1659.83	0.612±0.005
M_H Window	405.62±3.220	265481.	406.2	1590.74	1080.73	0.784±0.008
Jet Veto	226.37±2.400	123710.	106.3	463.42	737.84	0.642±0.009
Tagging Mass	70.04±1.330	2375.77	1.56	10.33	102.24	1.433±0.058
+Tagging P_T	25.22±0.800	48.12	0.09	1.770	14.50	3.567±0.631

Table A.3: M_H=200 GeV/c^2. H$\rightarrow$ZZ$\rightarrow$lljj. Number of events expected after 1 years of running at the high luminosity setting (L=100 fb^{-1}). Pileup has been included.

213

	Signal	Z^0+jets	ff→ ZZ	$t\bar{t}$	δ Back	$\frac{S}{\sqrt{B}}$
			$Z\to \mu^+\mu^-$ channel			
Expected	138.39±0.300	730290.	17988.	169740.	94.62	0.140±0.000
Precuts	130.55±0.290	559208.	12360.	154496.	85.05	0.150±0.000
Trigger	113.97±0.270	319487.	7799.0	116402.	67.59	0.170±0.000
Central Cut	25.18±0.130	704.42	22.8	0.820	2.470	0.930±0.005
M_H Window	20.81±0.120	411.95	11.8	0.460	1.890	1.010±0.006
Jet Veto	16.90±0.110	218.62	6.84	0.120	1.380	1.120±0.008
Tagging Mass	5.580±0.060	1.590	0.01	0.020	0.120	4.400±0.168
+Tagging P_T	5.580±0.060	1.590	0.01	0.020	0.120	4.400±0.168
			$Z\to e^+e^-$ channel			
Expected	138.39±0.300	730290.	17988.	169740.	93.29	0.140±0.000
Precuts	128.21±0.290	525844.	11580.	150021.	81.74	0.150±0.000
Trigger	115.79±0.270	297912.	7136.6	108128.	64.29	0.180±0.000
Central Cut	27.89±0.130	764.22	24.8	0.620	2.540	0.990±0.005
M_H Window	22.82±0.120	440.22	12.5	0.330	1.930	1.070±0.006
Jet Veto	18.54±0.110	232.58	7.21	0.030	1.400	1.200±0.008
Tagging Mass	6.090±0.060	1.920	0.02	0.000	0.130	4.380±0.150
+Tagging P_T	6.090±0.060	1.920	0.02	0.000	0.130	4.380±0.150
			Combined Results			
Expected	276.78±0.600	1460580.	35976.	339480.	187.91	0.204±0.000
Precuts	258.76±0.580	1085051.	23940.	304517.	166.79	0.218±0.001
Trigger	229.76±0.540	617399.	14935.	224530.	131.88	0.248±0.001
Central Cut	53.07±0.260	1468.64	47.6	1.440	5.010	1.362±0.009
M_H Window	43.63±0.240	852.17	24.4	0.790	3.820	1.473±0.011
Jet Veto	35.44±0.220	451.20	14.0	0.150	2.780	1.643±0.015
Tagging Mass	11.67±0.120	3.510	0.03	0.020	0.250	6.185±0.281
+Tagging P_T	11.67±0.120	3.510	0.03	0.020	0.250	6.185±0.281

Table A.4: M_H=600 GeV/c². H→ZZ→lljj. Number of events expected after 3 years of running at the low luminosity setting (L=30 fb⁻¹). Pileup has not been included.

214

	Signal	Z^0+jets	ff$\to$ ZZ	$t\bar{t}$	δ Back	$\frac{S}{\sqrt{B}}$
			$Z\to \mu^+\mu^-$ channel			
Expected	138.39±0.300	730290.	17988.	169740.	94.62	0.140±0.000
Precuts	130.55±0.290	559208.	12360.	154496.	85.05	0.150±0.000
Trigger	113.96±0.270	337245.	7982.5	117611.	68.85	0.170±0.000
Central Cut	24.45±0.130	744.87	22.6	0.930	2.540	0.880±0.005
M_H Window	20.31±0.120	437.29	11.7	0.460	1.950	0.960±0.006
Jet Veto	15.96±0.100	232.11	6.79	0.110	1.420	1.030±0.007
Tagging Mass	5.290±0.060	1.680	0.01	0.020	0.120	4.060±0.152
+Tagging P_T	5.290±0.060	1.680	0.01	0.020	0.120	4.060±0.152
			$Z\to e^+e^-$ channel			
Expected	138.39±0.300	730290.	17988.	169740.	93.29	0.140±0.000
Precuts	128.21±0.290	525844.	11580.	150021.	81.74	0.150±0.000
Trigger	115.75±0.270	314191.	7294.5	109158.	65.47	0.180±0.000
Central Cut	26.88±0.130	806.01	24.2	0.570	2.610	0.930±0.005
M_H Window	22.01±0.120	465.84	12.2	0.360	1.980	1.010±0.006
Jet Veto	17.36±0.110	246.11	7.11	0.080	1.440	1.090±0.007
Tagging Mass	5.630±0.060	1.900	0.01	0.000	0.130	4.080±0.142
+Tagging P_T	5.630±0.060	1.900	0.01	0.000	0.130	4.080±0.142
			Combined Results			
Expected	276.78±0.600	1460580.	35976.	339480.	187.91	0.204±0.000
Precuts	258.76±0.580	1085051.	23940.	304517.	166.79	0.218±0.001
Trigger	229.71±0.540	651436.	15277.	226769.	134.32	0.243±0.001
Central Cut	51.33±0.260	1550.88	46.8	1.500	5.150	1.284±0.009
M_H Window	42.32±0.240	903.13	23.9	0.820	3.930	1.389±0.011
Jet Veto	33.32±0.210	478.22	13.9	0.190	2.860	1.502±0.014
Tagging Mass	10.92±0.120	3.580	0.02	0.020	0.250	5.739±0.261
+Tagging P_T	10.92±0.120	3.580	0.02	0.020	0.250	5.739±0.261

Table A.5: M_H=600 GeV/c^2. H$\to$ZZ$\to$lljj. Number of events expected after 3 years of running at the low luminosity setting (L=30 fb^{-1}). Pileup has been included.

215

	Signal	Z^0+jets	ff→ ZZ	$t\bar{t}$	δ Back	$\frac{S}{\sqrt{B}}$
Z→ $\mu^+\mu^-$ channel						
Expected	461.30±1.000	2434300.	59960.	565800.	315.41	0.260±0.001
Precuts	435.17±0.970	1864026.	41200.	514985.	283.50	0.280±0.001
Trigger	380.27±0.910	1098815.	24501.	379089.	226.43	0.310±0.001
Central Cut	77.33±0.410	3603.79	76.8	5.160	10.21	1.270±0.007
M_H Window	64.06±0.370	2139.69	40.8	2.680	7.870	1.370±0.008
Jet Veto	52.35±0.340	1289.16	26.2	0.720	6.100	1.440±0.010
Tagging Mass	17.00±0.190	11.95	0.04	0.100	0.590	4.890±0.132
+Tagging P_T	15.27±0.180	8.810	0.02	0.100	0.510	5.110±0.158
Z→ e^+e^- channel						
Expected	461.30±0.990	2434300.	59960.	565800.	310.96	0.260±0.001
Precuts	427.36±0.960	1752812.	38600.	500070.	272.48	0.280±0.001
Trigger	387.75±0.910	1033554.	21774.	337327.	214.24	0.330±0.001
Central Cut	87.31±0.430	3965.15	83.5	3.250	10.56	1.370±0.007
M_H Window	71.78±0.390	2321.50	42.8	2.150	8.080	1.480±0.008
Jet Veto	58.60±0.350	1389.09	27.5	0.300	6.250	1.560±0.010
Tagging Mass	18.82±0.200	13.08	0.07	0.000	0.610	5.190±0.132
+Tagging P_T	16.67±0.190	9.020	0.05	0.000	0.500	5.540±0.166
Combined Results						
Expected	922.60±1.990	4868600.	119920	1131600.	626.37	0.373±0.001
Precuts	862.53±1.930	3616837.	79800.	1015056.	555.98	0.397±0.001
Trigger	768.02±1.820	2132369.	46276.	716416.	440.67	0.451±0.001
Central Cut	164.64±0.840	7568.94	160.3	8.410	20.77	1.872±0.012
M_H Window	135.84±0.760	4461.19	83.6	4.830	15.95	2.014±0.015
Jet Veto	110.95±0.690	2678.25	53.7	1.020	12.35	2.122±0.018
Tagging Mass	35.82±0.390	25.03	0.11	0.100	1.200	7.130±0.247
+Tagging P_T	31.94±0.370	17.83	0.07	0.100	1.010	7.528±0.298

Table A.6: M_H=600 GeV/c^2. H→ZZ→lljj. Number of events expected in 1 year of high luminosity running(L=100 fb^{-1}). High luminosity pileup has been included.

216

	Signal	Z^0+jets	ff→ ZZ	t$\bar{\text{t}}$	δ Back	$\frac{S}{\sqrt{B}}$
Z→ $\mu^+\mu^-$ channel						
Expected	38.85±0.080	730290.	17988.	169740.	94.62	0.040±0.000
Precuts	37.18±0.080	559208.	12360.	154496.	85.05	0.040±0.000
Trigger	31.74±0.080	319487.	7799.0	116402.	67.59	0.050±0.000
Central Cut	6.050±0.030	91.72	3.96	0.030	0.890	0.620±0.004
M$_H$ Window	6.050±0.030	91.72	3.96	0.030	0.890	0.620±0.004
Jet Veto	5.220±0.030	46.31	2.12	0.020	0.630	0.750±0.007
Tagging Mass	1.890±0.020	0.380	0.00	0.000	0.060	3.050±0.232
+Tagging P$_T$	1.890±0.020	0.380	0.00	0.000	0.060	3.050±0.232
Z→ e^+e^- channel						
Expected	38.85±0.080	730290.	17988.	169740.	93.29	0.040±0.000
Precuts	36.70±0.080	525844.	11580.	150021.	81.74	0.040±0.000
Trigger	33.25±0.080	297912.	7136.6	108128.	64.29	0.050±0.000
Central Cut	7.000±0.040	102.35	4.39	0.000	0.930	0.680±0.005
M$_H$ Window	7.000±0.040	102.35	4.39	0.000	0.930	0.680±0.005
Jet Veto	6.110±0.030	52.17	2.40	0.000	0.660	0.830±0.007
Tagging Mass	2.210±0.020	0.500	0.01	0.000	0.060	3.120±0.203
+Tagging P$_T$	2.210±0.020	0.500	0.01	0.000	0.060	3.120±0.203
Combined Results						
Expected	77.70±0.160	1460580.	35976.	339480.	187.91	0.057±0.000
Precuts	73.88±0.160	1085051.	23940.	304517.	166.79	0.062±0.000
Trigger	64.99±0.160	617399.	14935.	224530.	131.88	0.070±0.000
Central Cut	13.05±0.070	194.07	8.35	0.030	1.820	0.917±0.009
M$_H$ Window	13.05±0.070	194.07	8.35	0.030	1.820	0.917±0.009
Jet Veto	11.33±0.060	98.48	4.52	0.020	1.290	1.116±0.013
Tagging Mass	4.100±0.040	0.880	0.01	0.000	0.120	4.346±0.335
+Tagging P$_T$	4.100±0.040	0.880	0.01	0.000	0.120	4.346±0.335

Table A.7: M_H=1000 GeV/c^2. H→ZZ→lljj. Number of events expected after 3 years of running at the low luminosity setting (L=30 fb^{-1}). Pileup has not been included.

217

	Signal	Z^0+jets	ff→ ZZ	$t\bar{t}$	δ Back	$\frac{S}{\sqrt{B}}$
		$Z \to \mu^+\mu^-$ channel				
Expected	38.85±0.080	730290.	17988.	169740.	94.62	0.040±0.000
Precuts	37.18±0.080	559208.	12360.	154496.	85.05	0.040±0.000
Trigger	31.82±0.080	337245.	7982.5	117611.	68.85	0.050±0.000
Central Cut	5.910±0.030	94.71	3.92	0.060	0.910	0.590±0.004
M_H Window	5.910±0.030	94.71	3.92	0.060	0.910	0.590±0.004
Jet Veto	4.920±0.030	47.48	2.05	0.020	0.640	0.700±0.006
Tagging Mass	1.760±0.020	0.440	0.00	0.000	0.060	2.640±0.186
+Tagging P_T	1.760±0.020	0.440	0.00	0.000	0.060	2.640±0.186
		$Z \to e^+e^-$ channel				
Expected	38.85±0.080	730290.	17988.	169740.	93.29	0.040±0.000
Precuts	36.70±0.080	525844.	11580.	150021.	81.74	0.040±0.000
Trigger	33.22±0.080	314191.	7294.5	109158.	65.47	0.050±0.000
Central Cut	6.790±0.040	107.59	4.24	0.000	0.950	0.640±0.004
M_H Window	6.790±0.040	107.59	4.24	0.000	0.950	0.640±0.004
Jet Veto	5.690±0.030	54.70	2.32	0.000	0.680	0.750±0.006
Tagging Mass	2.040±0.020	0.550	0.00	0.000	0.070	2.750±0.172
+Tagging P_T	2.040±0.020	0.550	0.00	0.000	0.070	2.750±0.172
		Combined Results				
Expected	77.70±0.160	1460580.	35976.	339480.	187.91	0.057±0.000
Precuts	73.88±0.160	1085051.	23940.	304517.	166.79	0.062±0.000
Trigger	65.04±0.160	651436.	15277.	226769.	134.32	0.069±0.000
Central Cut	12.70±0.070	202.30	8.16	0.060	1.860	0.875±0.009
M_H Window	12.70±0.070	202.30	8.16	0.060	1.860	0.875±0.009
Jet Veto	10.61±0.060	102.18	4.37	0.020	1.320	1.028±0.012
Tagging Mass	3.800±0.040	0.990	0.00	0.000	0.130	3.819±0.291
+Tagging P_T	3.800±0.040	0.990	0.00	0.000	0.130	3.819±0.291

Table A.8: M_H=1000 GeV/c^2. H→ZZ→lljj. Number of events expected in 3 years of running at the low luminosity setting (L=30 fb^{-1}). Pileup has been included.

218

	Signal	Z^0+jets	ff$\to$ ZZ	$t\bar{t}$	δ Back	$\frac{S}{\sqrt{B}}$
		$Z\to \mu^+\mu^-$ channel				
Expected	129.50±0.280	2434300.	59960.	565800.	315.41	0.070±0.000
Precuts	123.95±0.280	1864026.	41200.	514985.	283.50	0.080±0.000
Trigger	106.31±0.260	1098815.	24501.	379089.	226.43	0.090±0.000
Central Cut	18.62±0.110	429.83	12.8	0.360	3.530	0.880±0.006
M_H Window	18.62±0.110	429.83	12.8	0.360	3.530	0.880±0.006
Jet Veto	15.97±0.100	250.45	7.75	0.150	2.690	0.990±0.008
Tagging Mass	5.510±0.060	2.680	0.04	0.000	0.280	3.340±0.174
+Tagging P_T	5.510±0.060	2.680	0.04	0.000	0.280	3.340±0.174
		$Z\to e^+e^-$ channel				
Expected	129.50±0.280	2434300.	59960.	565800.	310.96	0.070±0.000
Precuts	122.32±0.270	1752812.	38600.	500070.	272.48	0.080±0.000
Trigger	111.51±0.260	1033554.	21774.	337327.	214.24	0.090±0.000
Central Cut	21.81±0.120	495.51	14.7	0.000	3.730	0.970±0.006
M_H Window	21.81±0.120	495.51	14.7	0.000	3.730	0.970±0.006
Jet Veto	18.90±0.110	288.64	9.28	0.000	2.850	1.090±0.008
Tagging Mass	6.530±0.060	3.140	0.03	0.000	0.300	3.670±0.175
+Tagging P_T	6.530±0.060	3.140	0.03	0.000	0.300	3.670±0.175
		Combined Results				
Expected	259.00±0.560	4868600.	119920	1131600.	626.37	0.105±0.000
Precuts	246.27±0.550	3616837.	79800.	1015056.	555.98	0.113±0.000
Trigger	217.82±0.520	2132369.	46276.	716416.	440.67	0.128±0.000
Central Cut	40.43±0.230	925.34	27.5	0.360	7.260	1.309±0.012
M_H Window	40.43±0.230	925.34	27.5	0.360	7.260	1.309±0.012
Jet Veto	34.87±0.210	539.09	17.0	0.150	5.540	1.478±0.016
Tagging Mass	12.04±0.120	5.820	0.07	0.000	0.580	4.961±0.294
+Tagging P_T	12.04±0.120	5.820	0.07	0.000	0.580	4.961±0.294

Table A.9: M_H=1000 GeV/c^2. H$\to$ZZ$\to$lljj. Number of events expected in 1 year of high luminosity running(L=100 fb^{-1}). High luminosity pileup has been included.

219

Appendix B

Bipolar Weighting Functions

Bunch Crossing	Time(ns)	Hadronic LAr $0.0< |\eta| \leq 1.5$	EM LAr $1.5< |\eta| \leq 3.2$	FCAL2 $3.2< |\eta| \leq 5.0$
1	25	0.52	0.48	0.440
2	50	1.00	1.0	1.00
3	75	0.70	0.68	0.607
4	100	0.26	0.25	-0.166
5	125	-0.01	-0.008	-0.561
6	150	-0.15	-0.12	-0.536
7	175	-0.20	-0.17	-0.365
8	200	-0.22	-0.18	-0.208
9	225	-0.23	-0.19	-0.106
10	250	-0.23	-0.19	-0.050
11	275	-0.23	-0.19	-0.022
12	300	-0.23	-0.19	-0.010
13	325	-0.23	-0.19	-0.004
14	350	-0.23	-0.19	-0.002
15	375	-0.22	-0.19	-0.001
16	400	-0.15	-0.19	0.0
17	425	-0.08	-0.18	0.0
18	450	-0.05	-0.13	0.0
19	475	-0.01	-0.07	0.0
20	500	-0.005	-0.03	0.0
21	525	-0.002	-0.01	0.0
22	550	-0.0006	-0.003	0.0
23	575	0.0	-0.001	0.0
24	600	0.0	0.00	0.0

Table B.1: The shaping function values used to weight the bunch energy in different pseudo-rapidity regions of the calorimetry.

221

Appendix C

H→WW Data Tables

	Signal	W+jets	ff→ WW	t t̄	δ Back	$\frac{S}{\sqrt{B}}$
W→ $\mu^{\pm}\nu_{\mu}$ channel						
Expected	7852.50±11.95	1153200000.	306210.	2141040.	83017.2	0.231±0.000
Precuts	7268.48±11.49	417316512.	241741.	2046704.	49940.8	0.355±0.001
Trigger	4631.17±9.170	72613960.	110961.	1344097.	20833.5	0.538±0.001
Central Cut	732.24±3.650	182321.	1144.90	151839.	1048.20	1.265±0.007
M_H Window	568.63±3.210	88644.6	609.60	86042.7	731.40	1.358±0.008
Jet Veto	334.88±2.470	30837.1	181.70	7170.44	429.80	1.714±0.016
Tagging Mass	125.00±1.510	537.86	1.700	235.20	56.80	4.491±0.173
+Tagging P_T	72.74±1.150	89.64	0.500	112.65	23.30	5.108±0.304
Z→ e^+e^- channel						
Expected	7852.50±13.64	1153200000.	308100.	2141040.	82658.2	0.231±0.000
Precuts	7103.42±12.97	405481024.	232219.	2019512.	49014.5	0.352±0.001
Trigger	4598.80±10.44	73964440.	111614.	1308472.	20935.1	0.530±0.001
Central Cut	737.74±4.180	178995.	1123.60	149074.	1033.50	1.286±0.008
M_H Window	570.45±3.680	87625.1	599.00	84432.9	723.50	1.373±0.009
Jet Veto	338.76±2.830	30197.8	180.90	7014.04	423.40	1.752±0.018
Tagging Mass	125.40±1.720	521.37	1.600	233.05	55.70	4.561±0.179
+Tagging P_T	73.05±1.320	88.87	0.400	111.54	23.10	5.155±0.310
Combined Results						
Expected	15705.0±25.59	2306400000.	614310.	4282080.	165675.	0.327±0.001
Precuts	14371.9±24.46	822797568.	473960.	4066215.	98955.3	0.500±0.001
Trigger	9229.97±19.61	146578400.	222575.	2652569.	41768.6	0.755±0.002
Central Cut	1469.98±7.830	361316.	2268.50	300913.	2081.70	1.803±0.012
M_H Window	1139.08±6.890	176270.	1208.60	170476.	1454.90	1.931±0.016
Jet Veto	673.64±5.300	61034.9	362.60	14184.5	853.20	2.450±0.033
Tagging Mass	250.40±3.230	1059.23	3.300	468.25	112.50	6.400±0.318
+Tagging P_T	145.79±2.470	178.51	0.900	224.19	46.40	7.257±0.540

Table C.1: M_H=200 GeV/c^2. H→WW→ $\mu\nu$jj. Number of events expected after 3 years of running at the low luminosity setting (L=30 fb^{-1}). Pileup has not been included.

223

	Signal	W+jets	ff→ WW	t t̄	δ Back	$\frac{S}{\sqrt{B}}$
W→ $\mu^{\pm}\nu_{\mu}$ channel						
Expected	7852.50±11.95	1153200000.	306210.	2141040.	83017.2	0.231±0.000
Precuts	7268.48±11.49	417316512.	241741.	2046704.	49940.8	0.355±0.001
Trigger	4690.33±9.230	86251432.	115180.	1354683.	22705.4	0.501±0.001
Central Cut	722.89±3.620	225625.	1200.40	158723.	1165.30	1.164±0.006
M_H Window	563.02±3.200	113589.	646.10	91450.9	827.20	1.241±0.007
Jet Veto	320.38±2.410	37064.2	179.00	7593.97	471.10	1.513±0.014
Tagging Mass	119.93±1.480	723.12	1.900	265.62	65.90	3.810±0.135
+Tagging P_T	70.45±1.130	119.52	0.400	125.95	26.90	4.493±0.256
Z→ e^+e^- channel						
Expected	7852.50±13.64	1153200000.	308100.	2141040.	82658.2	0.231±0.000
Precuts	7103.42±12.97	405481024.	232219.	2019512.	49014.5	0.352±0.001
Trigger	4649.00±10.49	88208312.	115894.	1318137.	22861.9	0.491±0.001
Central Cut	728.10±4.150	220390.	1191.80	155345.	1146.10	1.186±0.007
M_H Window	562.02±3.650	109303.	640.40	89567.4	807.50	1.258±0.009
Jet Veto	325.46±2.780	35571.4	178.50	7409.39	459.50	1.567±0.016
Tagging Mass	120.10±1.690	853.15	1.800	251.60	71.20	3.610±0.127
+Tagging P_T	69.71±1.280	148.12	0.500	118.12	29.70	4.268±0.251
Combined Results						
Expected	15705.0±25.59	2306400000.	614310.	4282080.	165675.	0.327±0.001
Precuts	14371.9±24.46	822797568.	473960.	4066215.	98955.3	0.500±0.001
Trigger	9339.33±19.72	174459744.	231073.	2672820.	45567.3	0.701±0.002
Central Cut	1450.99±7.770	446015.	2392.20	314068.	2311.40	1.662±0.011
M_H Window	1125.04±6.850	222893.	1286.50	181018.	1634.70	1.767±0.014
Jet Veto	645.84±5.190	72635.7	357.50	15003.4	930.60	2.177±0.029
Tagging Mass	240.03±3.170	1576.27	3.700	517.22	137.10	5.241±0.241
+Tagging P_T	140.16±2.410	267.64	0.900	244.07	56.60	6.191±0.448

Table C.2: M_H=200 GeV/c^2. H→WW→ $\mu\nu$jj. Number of events expected after 3 years of running at the low luminosity setting (L=30 fb^{-1}). Pileup has been included.

224

	Signal	W+jets	ff→ WW	$t\bar{t}$	δ Back	$\frac{S}{\sqrt{B}}$
			$W\to \mu^{\pm}\nu_{\mu}$channel			
Expected	26175.0±39.82	3844000000.	1020700.	7136800.	276724.	0.422±0.001
Precuts	24228.3±38.31	1391055104.	805804.	6822346.	166469.	0.648±0.001
Trigger	12677.9±27.71	207382672.	282443.	3684823.	64280.1	0.872±0.002
Central Cut	2672.01±12.72	4747196.	12223.6	818272.	9732.90	1.131±0.005
M_H Window	1956.07±10.88	2872928.	7148.10	475579.	7571.30	1.068±0.006
Jet Veto	1173.62±8.430	1542272.	2692.90	63834.9	5544.00	0.925±0.007
Tagging Mass	357.31±4.650	22211.5	35.50	2122.44	665.50	2.289±0.043
+Tagging P_T	138.53±2.900	717.14	1.600	602.12	120.00	3.811±0.191
			$Z\to e^+e^-$channel			
Expected	26175.0±45.45	3844000000.	1027000.	7136800.	275528.	0.422±0.001
Precuts	23678.1±43.23	1351603456.	774062.	6731705.	163382.	0.642±0.001
Trigger	10448.5±28.72	141217760.	221145.	3080531.	52814.7	0.869±0.002
Central Cut	2260.62±13.36	3504532.	10059.9	679073.	8326.20	1.104±0.007
M_H Window	1660.78±11.45	2049425.	5736.60	386186.	6367.00	1.063±0.007
Jet Veto	1005.37±8.910	1102335.	2169.50	52143.8	4666.80	0.935±0.008
Tagging Mass	307.50±4.930	17517.1	28.50	1761.97	588.40	2.213±0.049
+Tagging P_T	124.15±3.130	671.46	1.700	504.79	115.50	3.617±0.199
			Combined Results			
Expected	52350.0±85.27	7688000000.	2047700.	14273600.	552252.	0.596±0.001
Precuts	47906.3±81.54	2742658560.	1579867.	13554050.	329851.	0.912±0.002
Trigger	23126.4±56.43	348600448.	503588.	6765354.	117095.	1.226±0.003
Central Cut	4932.63±26.08	8251728.	22283.5	1497346.	18059.1	1.578±0.010
M_H Window	3616.85±22.33	4922353.	12884.7	861765.	13938.3	1.502±0.011
Jet Veto	2178.99±17.34	2644607.	4862.40	115979.	10210.8	1.310±0.013
Tagging Mass	664.81±9.580	39728.6	64.00	3884.41	1253.90	3.181±0.092
+Tagging P_T	262.68±6.030	1388.60	3.300	1106.91	235.50	5.255±0.368

Table C.3: M_H=200 GeV/c^2 . H→WW→ $\mu\nu$jj. Number of events expected after 1 year of running at the high luminosity setting (L=100 fb^{-1}). Pileup has been included.

225

	Signal	W+jets	ff→ WW	t̄t	δ Back	$\frac{S}{\sqrt{B}}$
W→ $\mu^{\pm}\nu_{\mu}$channel						
Expected	893.49±1.390	5313000.	306210.	2141040.	690.60	0.321±0.000
Precuts	862.86±1.360	4532046.	241741.	2046704.	647.80	0.330±0.001
Trigger	625.34±1.160	2043489.	110961.	1344097.	463.00	0.334±0.001
Central Cut	162.13±0.590	6693.32	396.80	7272.12	29.60	1.353±0.005
M_H Window	133.50±0.540	4212.20	204.70	5397.05	24.50	1.348±0.006
Jet Veto	111.15±0.490	2313.36	121.40	594.93	13.70	2.019±0.010
Tagging Mass	35.50±0.280	17.49	0.300	16.04	1.400	6.101±0.139
+Tagging P_T	35.50±0.280	17.49	0.300	16.04	1.400	6.101±0.139
Z→ $e^{+}e^{-}$ channel						
Expected	893.49±1.590	5313000.	308100.	2141040.	704.10	0.321±0.001
Precuts	853.08±1.560	4343848.	232219.	2019512.	647.10	0.332±0.001
Trigger	632.57±1.340	1973251.	111614.	1308472.	458.30	0.343±0.001
Central Cut	165.88±0.690	6672.91	401.40	7060.96	29.00	1.395±0.006
M_H Window	136.42±0.620	4176.27	202.70	5249.42	23.90	1.390±0.007
Jet Veto	113.83±0.570	2281.08	119.50	568.23	14.00	2.089±0.012
Tagging Mass	36.78±0.320	17.69	0.300	14.46	1.400	6.455±0.152
+Tagging P_T	36.78±0.320	17.69	0.300	14.46	1.400	6.455±0.152
Combined Results						
Expected	1786.98±2.980	10626000.	614310.	4282080.	1394.70	0.454±0.001
Precuts	1715.94±2.920	8875894.	473960.	4066215.	1294.90	0.468±0.001
Trigger	1257.91±2.500	4016740.	222575.	2652569.	921.30	0.479±0.001
Central Cut	328.01±1.280	13366.2	798.20	14333.1	58.60	1.943±0.010
M_H Window	269.92±1.160	8388.47	407.40	10646.5	48.40	1.936±0.011
Jet Veto	224.98±1.060	4594.44	240.90	1163.16	27.70	2.905±0.020
Tagging Mass	72.28±0.600	35.18	0.600	30.50	2.800	8.878±0.261
+Tagging P_T	72.28±0.600	35.18	0.600	30.50	2.800	8.878±0.261

Table C.4: M_H=600 GeV/c². H→WW→ $\mu\nu$jj. Number of events expected after 3 years of running at the low luminosity setting (L=30 fb^{-1}). Pileup has not been included.

226

	Signal	W+jets	ff→ WW	$t\bar{t}$	δ Back	$\frac{S}{\sqrt{B}}$
W→ $\mu^{\pm}\nu_{\mu}$channel						
Expected	893.49±1.390	5313000.	306210.	2141040.	690.60	0.321±0.000
Precuts	862.86±1.360	4532046.	241741.	2046704.	647.80	0.330±0.001
Trigger	630.41±1.170	2181582.	115180.	1354683.	473.30	0.330±0.001
Central Cut	159.10±0.590	7180.01	396.30	7415.13	30.20	1.299±0.005
M_H Window	130.70±0.530	4456.69	203.40	5470.88	24.90	1.299±0.006
Jet Veto	105.79±0.480	2445.03	121.50	588.73	14.00	1.883±0.009
Tagging Mass	33.68±0.270	16.26	0.400	16.76	1.400	5.829±0.134
+Tagging P_T	33.68±0.270	16.26	0.400	16.76	1.400	5.829±0.134
Z→ e^+e^-channel						
Expected	893.49±1.590	5313000.	308100.	2141040.	704.10	0.321±0.001
Precuts	853.08±1.560	4343848.	232219.	2019512.	647.10	0.332±0.001
Trigger	637.62±1.350	2106170.	115894.	1318137.	469.30	0.339±0.001
Central Cut	162.04±0.680	7100.49	396.00	7215.94	29.70	1.336±0.006
M_H Window	132.56±0.610	4405.39	199.80	5301.29	24.30	1.332±0.006
Jet Veto	107.73±0.550	2416.19	118.50	561.71	14.30	1.936±0.011
Tagging Mass	34.56±0.310	17.98	0.200	14.92	1.400	6.006±0.141
+Tagging P_T	34.56±0.310	17.98	0.200	14.92	1.400	6.006±0.141
Combined Results						
Expected	1786.98±2.980	10626000.	614310.	4282080.	1394.70	0.454±0.001
Precuts	1715.94±2.920	8875894.	473960.	4066215.	1294.90	0.468±0.001
Trigger	1268.03±2.520	4287752.	231073.	2672820.	942.60	0.473±0.001
Central Cut	321.14±1.270	14280.5	792.30	14631.1	59.90	1.863±0.009
M_H Window	263.26±1.140	8862.08	403.20	10772.2	49.20	1.860±0.010
Jet Veto	213.52±1.030	4861.22	240.00	1150.44	28.30	2.700±0.019
Tagging Mass	68.24±0.580	34.24	0.600	31.68	2.800	8.367±0.247
+Tagging P_T	68.24±0.580	34.24	0.600	31.68	2.800	8.367±0.247

Table C.5: M_H=600 GeV/c^2. H→WW→ $\mu\nu$jj. Number of events expected after 3 years of running at the low luminosity setting (L=30 fb^{-1}). Pileup has been included.

	Signal	W+jets	ff→ WW	t$\bar{t}$	δ Back	$\frac{S}{\sqrt{B}}$
			W→ $\mu^{\pm}\nu_\mu$channel			
Expected	2978.30±4.630	17710000.	1020700.	7136800.	2301.90	0.586±0.001
Precuts	2876.22±4.550	15106821.	805804.	6822346.	2159.40	0.603±0.001
Trigger	1923.48±3.720	5879070.	282443.	3684823.	1420.60	0.613±0.001
Central Cut	478.63±1.860	34335.8	1241.20	28986.2	115.10	1.884±0.007
M$_H$ Window	395.76±1.690	22300.0	651.80	21296.4	95.40	1.881±0.008
Jet Veto	330.72±1.540	13851.9	430.70	3212.59	60.50	2.500±0.012
Tagging Mass	103.34±0.860	129.61	1.600	100.98	6.900	6.782±0.116
+Tagging P$_T$	91.67±0.810	92.98	0.900	85.68	6.100	6.841±0.131
			Z→ e^+e^-channel			
Expected	2978.30±5.310	17710000.	1027000.	7136800.	2347.00	0.586±0.001
Precuts	2843.61±5.190	14479495.	774062.	6731705.	2157.10	0.606±0.001
Trigger	1940.31±4.290	5544662.	221145.	3080531.	1365.50	0.652±0.001
Central Cut	493.21±2.160	34740.6	1279.50	28961.2	115.40	1.935±0.009
M$_H$ Window	404.74±1.960	22484.7	662.90	21306.5	95.10	1.920±0.010
Jet Veto	338.82±1.790	13929.4	439.70	3149.10	62.50	2.560±0.014
Tagging Mass	107.24±1.010	134.82	1.200	93.54	7.000	7.078±0.126
+Tagging P$_T$	95.37±0.950	96.40	0.800	77.53	6.000	7.216±0.144
			Combined Results			
Expected	5956.60±9.940	35420000.	2047700.	14273600.	4648.90	0.828±0.001
Precuts	5719.83±9.740	29586316.	1579867.	13554050.	4316.50	0.855±0.001
Trigger	3863.79±8.010	11423732.	503588.	6765354.	2786.10	0.894±0.002
Central Cut	971.84±4.020	69076.5	2520.70	57947.4	230.50	2.700±0.014
M$_H$ Window	800.50±3.650	44784.7	1314.70	42602.9	190.50	2.688±0.015
Jet Veto	669.54±3.330	27781.2	870.40	6361.69	123.00	3.578±0.024
Tagging Mass	210.58±1.870	264.43	2.800	194.52	13.90	9.800±0.235
+Tagging P$_T$	187.04±1.760	189.38	1.700	163.21	12.10	9.937±0.263

Table C.6: M$_H$=600 GeV/c^2. H→WW→ $\mu\nu$jj. Number of events expected after 1 year of running at the high luminosity setting (L=100 fb^{-1}). Pileup has been included.

228

	Signal	W+jets	ff→ WW	t t̄	δ Back	$\frac{S}{\sqrt{B}}$
			W→ $\mu^{\pm}\nu_\mu$ channel			
Expected	244.90±0.380	5313000.	306210.	2141040.	690.60	0.088±0.000
Precuts	238.54±0.380	4532046.	241741.	2046704.	647.80	0.091±0.000
Trigger	169.48±0.320	2043489.	110961.	1344097.	463.00	0.091±0.000
Central Cut	33.97±0.140	589.75	51.10	353.34	7.700	1.077±0.006
M$_H$ Window	33.97±0.140	589.75	51.10	353.34	7.700	1.077±0.006
Jet Veto	30.07±0.130	307.10	27.30	29.58	4.700	1.576±0.012
Tagging Mass	10.58±0.080	2.930	0.100	0.950	0.500	5.322±0.338
+Tagging P$_T$	10.58±0.080	2.930	0.100	0.950	0.500	5.322±0.338
			Z→ e^+e^- channel			
Expected	244.90±0.440	5313000.	308100.	2141040.	704.10	0.088±0.000
Precuts	236.38±0.430	4343848.	232219.	2019512.	647.10	0.092±0.000
Trigger	174.38±0.370	1973251.	111614.	1308472.	458.30	0.095±0.000
Central Cut	35.14±0.170	591.38	53.90	337.56	7.800	1.121±0.007
M$_H$ Window	35.14±0.170	591.38	53.90	337.56	7.800	1.121±0.007
Jet Veto	31.25±0.160	312.90	29.30	27.05	4.900	1.626±0.014
Tagging Mass	11.14±0.090	2.680	0.100	0.760	0.500	5.945±0.412
+Tagging P$_T$	11.14±0.090	2.680	0.100	0.760	0.500	5.945±0.412
			Combined Results			
Expected	489.80±0.820	10626000.	614310.	4282080.	1394.70	0.124±0.000
Precuts	474.92±0.810	8875894.	473960.	4066215.	1294.90	0.130±0.000
Trigger	343.86±0.690	4016740.	222575.	2652569.	921.30	0.131±0.000
Central Cut	69.11±0.310	1181.13	105.00	690.90	15.50	1.554±0.013
M$_H$ Window	69.11±0.310	1181.13	105.00	690.90	15.50	1.554±0.013
Jet Veto	61.32±0.290	620.00	56.60	56.63	9.600	2.265±0.026
Tagging Mass	21.72±0.170	5.610	0.200	1.710	1.000	7.920±0.589
+Tagging P$_T$	21.72±0.170	5.610	0.200	1.710	1.000	7.920±0.589

Table C.7: M$_H$=1000 GeV/c^2. H→WW→ $\mu\nu$jj. Number of events expected after 3 years of running at the low luminosity setting (L=30 fb^{-1}). Pileup has not been included.

229

	Signal	W+jets	ff→ WW	$t\bar{t}$	δ Back	$\frac{S}{\sqrt{B}}$
			W→ $\mu^{\pm}\nu_{\mu}$channel			
Expected	244.90±0.380	5313000.	306210.	2141040.	690.60	0.088±0.000
Precuts	238.54±0.380	4532046.	241741.	2046704.	647.80	0.091±0.000
Trigger	171.30±0.320	2181582.	115180.	1354683.	473.30	0.090±0.000
Central Cut	33.25±0.140	631.17	50.80	364.85	8.000	1.028±0.006
M_H Window	33.25±0.140	631.17	50.80	364.85	8.000	1.028±0.006
Jet Veto	28.53±0.130	328.23	27.40	30.00	4.800	1.453±0.011
Tagging Mass	10.12±0.080	2.540	0.000	0.720	0.500	5.583±0.390
+Tagging P_T	10.12±0.080	2.540	0.000	0.720	0.500	5.583±0.390
			Z→ e^+e^-channel			
Expected	244.90±0.440	5313000.	308100.	2141040.	704.10	0.088±0.000
Precuts	236.38±0.430	4343848.	232219.	2019512.	647.10	0.092±0.000
Trigger	176.00±0.370	2106170.	115894.	1318137.	469.30	0.094±0.000
Central Cut	34.58±0.170	631.46	52.50	350.81	8.000	1.075±0.007
M_H Window	34.58±0.170	631.46	52.50	350.81	8.000	1.075±0.007
Jet Veto	29.69±0.150	335.30	28.60	27.51	5.100	1.501±0.012
Tagging Mass	10.56±0.090	3.190	0.000	0.810	0.500	5.251±0.342
+Tagging P_T	10.56±0.090	3.190	0.000	0.810	0.500	5.251±0.342
			Combined Results			
Expected	489.80±0.820	10626000.	614310.	4282080.	1394.70	0.124±0.000
Precuts	474.92±0.810	8875894.	473960.	4066215.	1294.90	0.130±0.000
Trigger	347.30±0.690	4287752.	231073.	2672820.	942.60	0.130±0.000
Central Cut	67.83±0.310	1262.63	103.30	715.66	16.00	1.487±0.013
M_H Window	67.83±0.310	1262.63	103.30	715.66	16.00	1.487±0.013
Jet Veto	58.22±0.280	663.53	56.00	57.51	9.900	2.089±0.023
Tagging Mass	20.68±0.170	5.730	0.000	1.530	1.000	7.675±0.592
+Tagging P_T	20.68±0.170	5.730	0.000	1.530	1.000	7.675±0.592

Table C.8: M_H=1000 GeV/c². H→WW→ $\mu\nu$jj. Number of events expected after 3 years of running at the low luminosity setting (L=30 fb⁻¹). Pileup has been included.

230

	Signal	W+jets	ff→ WW	t$\bar{t}$	δ Back	$\frac{S}{\sqrt{B}}$
W→ $\mu^{\pm}\nu_{\mu}$channel						
Expected	816.32±1.270	17710000.	1020700.	7136800.	2301.90	0.161±0.000
Precuts	795.13±1.260	15106821.	805804.	6822346.	2159.40	0.167±0.000
Trigger	529.30±1.030	5879070.	282443.	3684823.	1420.60	0.169±0.000
Central Cut	100.28±0.450	2611.72	159.30	1512.37	29.50	1.532±0.009
M$_H$ Window	100.28±0.450	2611.72	159.30	1512.37	29.50	1.532±0.009
Jet Veto	88.53±0.420	1571.80	101.10	182.29	19.50	2.055±0.015
Tagging Mass	30.22±0.250	15.39	0.400	4.370	2.100	6.735±0.348
+Tagging P$_T$	30.22±0.250	15.39	0.400	4.370	2.100	6.735±0.348
Z→ e^+e^-channel						
Expected	816.32±1.460	17710000.	1027000.	7136800.	2347.00	0.160±0.000
Precuts	787.94±1.440	14479495.	774062.	6731705.	2157.10	0.168±0.000
Trigger	545.04±1.200	5544662.	221145.	3080531.	1365.50	0.183±0.000
Central Cut	105.05±0.530	2672.65	169.00	1487.24	30.00	1.597±0.010
M$_H$ Window	105.05±0.530	2672.65	169.00	1487.24	30.00	1.597±0.010
Jet Veto	93.02±0.490	1610.55	107.80	171.41	20.50	2.140±0.016
Tagging Mass	31.99±0.290	18.85	0.300	4.550	2.300	6.566±0.325
+Tagging P$_T$	31.99±0.290	18.85	0.300	4.550	2.300	6.566±0.325
Combined Results						
Expected	1632.64±2.730	35420000.	2047700.	14273600.	4648.90	0.227±0.000
Precuts	1583.07±2.700	29586316.	1579867.	13554050.	4316.50	0.237±0.000
Trigger	1074.34±2.230	11423732.	503588.	6765354.	2786.10	0.248±0.001
Central Cut	205.33±0.980	5284.37	328.30	2999.61	59.50	2.213±0.018
M$_H$ Window	205.33±0.980	5284.37	328.30	2999.61	59.50	2.213±0.018
Jet Veto	181.55±0.910	3182.35	208.90	353.70	40.00	2.967±0.031
Tagging Mass	62.21±0.540	34.24	0.700	8.920	4.400	9.393±0.553
+Tagging P$_T$	62.21±0.540	34.24	0.700	8.920	4.400	9.393±0.553

Table C.9: M$_H$=1000 GeV/c^2. H→WW→ $\mu\nu$jj. Number of events expected after 1 year of running at the high luminosity setting (L=100 fb^{-1}). Pileup has been included.

231